

THE UNIVERSITY OF MICHIGAN  
7848-1-F

AFAL-TR-68-114

STUDY AND INVESTIGATION OF A UHF-VHF ANTENNA

Prepared by

John A. M. Lyon, Nicholas G. Alexopoulos, Chao-Chun Chen,  
James C. Parker, Jr., Dean L. Smith and Pei-Rin Wu

This document is subject to special export controls and each transmittal to foreign governments or foreign nationals may be made only with the prior approval of AFAL (AVPT), Wright-Patterson Air Force Base, Ohio 45433

# THE UNIVERSITY OF MICHIGAN

7848-1-F

## FOREWORD

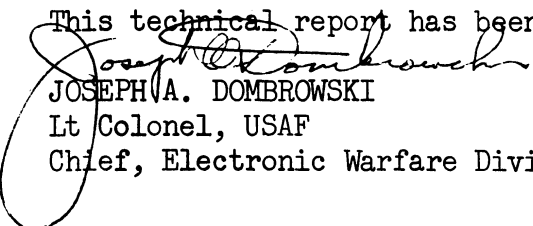
This report AFAL-TR-68-114 (7848-1-F) was prepared by The University of Michigan Radiation Laboratory, Department of Electrical Engineering, under the direction of Professor Ralph E. Hiatt and Professor John A.M. Lyon, on Air Force Contract AF33(6p5)-3609, Task 627801 of Project 6278 "Study and Investigation of UHF-VHF Antennas". The work was administered under the direction of the Air Force Avionics Laboratory, Wright-Patterson AFB, Ohio. The Task Engineer was Mr. Olin E. Horton.

This report covers the period 1 April 1966 through 29 February 1968.

The experimental assistance of Mr. R. Carducci, Mr. U.E. Gilreath, Mr. J.B. Hutt, Mr. T.B. Lewis, Mr. K.A. Pitcher and Mr. B.C. Vrieland is gratefully acknowledged.

Dr. George G. Rassweiler contributed to the material reported herein.

This technical report has been reviewed and is approved.

  
JOSEPH A. DOMBROWSKI  
Lt Colonel, USAF  
Chief, Electronic Warfare Division

# THE UNIVERSITY OF MICHIGAN

7848-1-F

## ABSTRACT

This final report describes the results of a program to reduce the size of antennas while still maintaining the usual frequency operating range for each type of antenna involved. The work described has been in part theoretical analysis and in other parts largely experimental. The work has been divided into four tasks.

Task I on ferrite loaded conical spirals has dealt with the development of a ferrite loaded conical spiral antenna covering a range from 200 to 600 MHz. Several design procedures have been considered. Under this task an appropriate type of design has resulted which will fulfill the original task requirement.

In Task II the objective has been to use ferrite loaded slot elements in an array and to utilize the control possible with such elements associated with a biasing magnetic field. Time has permitted only a preliminary assembly of the array without any complete determination of the functional possibilities. A novel antenna of reduced size, the "interdigital array", has been developed.

Under Task III a detailed analysis has been made of ferrite rod antennas. Numerous experiments have been performed. The studies therein indicate that a ferrite tube or hollow rod antenna has more desirable characteristics than the solid rod antenna.

Under Task IV detailed studies have been made of various loading and miniaturization techniques suitable for frequencies down to 30 MHz. The studies under this task indicate the influence of the various techniques of winding, loading and fabrication upon the antenna characteristics.

The need for further work on some of the tasks is clearly recognized in this report. Much of the required future work is covered in the renewal contract (F33615-68-C-1381).

THE UNIVERSITY OF MICHIGAN  
7848-1-F

TABLE OF CONTENTS

I	INTRODUCTION AND SUMMARY	1
II	FERRITE LOADED CONICAL SPIRALS	3
	2.1 Background	3
	2.2 Recommended Antenna	5
	2.3 Partial Core Ferrite Loading	8
	2.4 Transmit-Receive Mode Feasibility	14
	2.5 Complementary Helix Antenna	14
	2.6 Ferrite Coated Windings	32
	2.7 Ferrite Loaded Coiled Conductor	36
	2.8 Discrete Inductance Loading	45
	2.9 Anisotropic Ferrite Loaded Helix Antenna	57
III	SLOT ARRAYS	60
	3.1 Introduction	60
	3.2 Cavity Backed Slot Array	61
	3.3 Properties of Elements	67
	3.4 Interdigital Antennas	72
	3.4.1 Summary	72
	3.4.2 Ferrite Loading	85
	3.5 Power Capability of Ferrite Loaded Slot Antennas	105
	3.6 Waveguide Slot Arrays	107
IV	HE <sub>11</sub> MODE FERRITE ROD AND TUBE ANTENNAS	114
	4.1 General Discussion	114
	4.1.1 Introduction	114
	4.1.2 Review of the Existing Approaches	115
	4.1.3 Discussion of the Problem	116
	4.1.4 Some Comments on the Existing Analyses	119
	4.1.5 Revised Method in this Report	120
	4.2 Ferrite Rod Antennas	122
	4.2.1 General Solution of the Field Equation in Terms of the Electric Polarization Current and Magnetization Current	122
	4.2.2 Ferrite Rod Waveguide	125
	4.2.3 Radiation Due to the Polarization Current and Magnetization Current in the Rod	129
	4.2.4 Radiation Due to the Loaded Waveguide	136
	4.2.5 Far Field Pattern of the Ferrite Rod Antenna and a Class of Degenerate Antennas	138
	4.2.6 Operating Range of the Solid Rod Antenna	140

# THE UNIVERSITY OF MICHIGAN

7848-1-F

## Table of Contents (cont'd)

4.3	Ferrite Tube Antennas	141
	4.3.1 Choice of the Mathematical Approaches	141
	4.3.2 Ferrite Tube Waveguide	142
	4.3.3 Radiation from the Open End of the Ferrite Tube	149
	4.3.4 The Far Field Pattern of the Ferrite Tube Antenna	154
	4.3.5 Advantages of the Tube Antenna Over the Solid Rod Antenna	155
4.3	Experimental Results	156
	4.4.1 Ferrite Tube Excited by a Quadrifilar Helix	156
	4.4.2 Ferrite Tube Excited by Quadropole	160
	4.4.3 Ferrite Tube with a Conical Tapered End Excited by a Cylindrical Cavity	160
	4.4.4 Ferrite Tube with an Open End Excited by a Cylindrical Cavity	165
4.5	Conclusions	173
<b>V</b>	<b>LOW FREQUENCY FERRITE ANTENNAS</b>	<b>183</b>
5.1	Introduction	183
5.2	General Properties of Loaded Linear Elements	185
	5.2.1 Radiation Patterns	185
	5.2.2 Radiation Efficiency	186
	5.2.3 Impedance Bandwidth	187
	5.2.4 Helical Slow Structure	189
5.3	Advantages of Using Multiple Linear Elements	190
	5.3.1 Analysis of the Two Parallel Elements	191
	5.3.2 Input Impedance for a Generalized Folded Dipole	198
	5.3.3 Experimental Results	205
5.4	Multiple Resonance Behavior of Composite Structures	214
	5.4.1 Experimental Evidence	215
	5.4.2 Approximate Mathematical Analysis	217
	5.4.3 Generalization and Improved Analysis	223
<b>VI</b>	<b>FERRITE MATERIALS</b>	<b>235</b>
6.1	Introduction	235
6.2	Loading Materials	235
	6.2.1 Useful Materials	236
	6.2.2 Possible Useful Materials	236
	6.2.3 Non-useful Materials	237
	6.2.4 Summary	237
6.3	Measurement of Dielectric Constant	237

THE UNIVERSITY OF MICHIGAN  
7848-1-F

Table of Contents (cont'd)

6. 3. 1 Measurement Technique	238
6. 3. 2 Results	238
6. 3. 3 Conclusions	240
6. 3. 4 Theory of Measurement	240
6. 4 Q of Lossy Ferrites	241
VII CONCLUSIONS	244
APPENDIX A: GAIN MEASUREMENT BY COMPARISON	246
APPENDIX B: DETERMINATION OF COEFFICIENTS AND DERIVATION OF THE DETERMINENTAL EQUATION OF THE FERRITE TUBE WAVEGUIDE	250
APPENDIX C: DESIGN CURVES FOR A HELICAL SLOW WAVE STRUCTURE	254
APPENDIX D: INPUT IMPEDANCE TO A HELICAL DIPOLE	273
REFERENCES	287
DD FORM 1473	

THE UNIVERSITY OF MICHIGAN  
7848-1-F

LIST OF FIGURES

2-1	Proposed Antenna Design.	6
2-2a	Alternate Design.	7
2-2b	Alternate Design.	7
2-3	Layer Loading Effectiveness.	10
2-4	Theoretical and Experimental Diametral Reduction Factors for a Helix Antenna Loaded with K-10 Dielectric and EAF-2 Ferrite Powder.	11
2-5	Circuit for Testing Simultaneous Use of Transmit and Receive Mode.	15
2-6	Radiation Patterns of a Complementary Helical Antenna.	17
2-7	Near Field Amplitude of a Complementary Helical Antenna Without Loading.	18
2-8	Near Field Amplitude of a Complementary Helical Antenna With Dielectric Loading.	20
2-9	Arrangement for Phase Velocity Measurement.	21
2-10	Axial Phase Shift of a Complementary Helical Antenna with Various Loadings.	22
2-11	A Bifilar Complementary Helical Antenna.	23
2-12	A Balanced Feed of the Antenna.	23
2-13	The Experimental Set-up for the Impedance Measurement	24
2-14	Unloaded Complementary Helix Antenna.	25
2-15	K-10 Loaded Complementary Helix Antenna.	27
2-16	EAF-2 Loaded Complementary Helix Antenna.	28
2-17	Q-3 Loaded Complementary Helix Antenna.	29
2-18	Metal Loaded Complementary Helix Antenna.	30
2-19	The Input Resistances for Various Loading Materials.	31
2-20	Plot of the Reduction Factor ( $V_g/C$ ) vs $t/d$ for a Two Wire Transmission Line Loaded with EAF-2 Ferrite.	33
2-21	Plot of the Reduction Factor ( $V_g/C$ ) vs $t/d$ for a Two Wire Transmission Line Loaded with Indiana General Q-3 Ferrite.	35
2-22	Antenna 228; A $14^\circ$ Bifilar Helix with a Helical Winding.	38
2-23	Far Field Power Patterns of Antenna 228.	39
2-24	Antenna 232; A Bifilar Helix Antenna with a Helix Slow Wave Structure Winding Filled with EAF-2 Powdered Ferrite.	40
2-25	Longitudinal Cross Section Drawing of Antenna 232 with the Winding Helix Filled with EAF-2 Ferrite Powder Showing all Pertinent Dimensions.	41
2-26	Linear Power Radiation Patterns of Antenna 232. Cut 1 is in the Plane of the Feed; Cut 2 is perpendicular to Cut 1.	42
2-27	VSWR with Respect to $100\Omega$ for Antenna 232.	44
2-28	Relative Amplitude and Phase of the Current along Antenna 232 at 170 MHz.	46

THE UNIVERSITY OF MICHIGAN  
7848-1-F

List of Figures (cont'd)

2-29	Relative Amplitude and Phase of the Current Along Antenna 232 at 190 MHz.	47
2-30	Antenna 232; Showing the Location of the Loop Probe with Respect to Antenna 232.	48
2-31	Antenna 238; A Bifilar Helix Antenna with Shorted Transmission Line Inductors Used as Loading.	50
2-32	Dimensions of Inductances of Inductance Loaded Antenna.	52
2-33	Coordinate System Assumed for the Helix Antenna.	53
2-34a	Linear Power Patterns of Antenna 238; 455 to 800 MHz.	54
2-34b	Linear Power Patterns of Antenna 238; 820 to 1300 MHz	55
2-35	VSWR of Antenna 238.	56
3-1	Feed Network for Ferrite Filled Rectangular Cavity Backed Slot Array.	62
3-2	Mounting Configuration and Ground Plane for Ferrite Filled Rectangular Cavity Backed Slot Array.	63
3-3	Beamwidth of a 3-element $.534\lambda$ (350 MHz) Broadside Array Fed with a Hybrid-Double Stub Tuner Network.	64
3-4	Sidelobe Levels and Angles and Mainlobe Angle of a 3-element $.534\lambda$ (350 MHz) Broadside Array Fed with a Hybrid-Double Stub Tuner Network.	65
3-5	Coordinate System Assumed for Radiation Pattern Measurements of Ferrite Filled Rectangular Cavity Backed Slot Array.	66
3-6	Cavity Backed Slots, 107, 108 and 109.	68
3-7	Impedance of Cavity Backed Slot 107.	69
3-8	Impedance of Cavity Backed Slot 108.	70
3-9	Impedance of Cavity Backed Slot 109.	71
3-10a	H-Plane Power Radiation Patterns of Ferrite Filled Rectangular Cavity Backed Slot 107; 330 - 345 MHz.	73
3-10b	H-Plane Power Radiation Patterns of Ferrite Filled Rectangular Cavity Backed Slot 107; 350 - 365 MHz.	74
3-11	Beamwidth of Rectangular Cavity Backed Slots, 107, 108 and 109.	75
3-12	The Geometry of the Conducting Array Elements.	76
3-13	The Interdigital Array Antenna A-1.	77
3-14	The Interdigital Array Antenna A-2.	77
3-15	The Interdigital Array Antenna A-3.	78
3-16	The Interdigital Array Antenna B-1.	78
3-17	The Interdigital Array Antenna B-2.	79
3-18	Theoretical and Measured Dispersion Characteristics.	81
3-19a	Far Field H-Plane $E_y$ -Pattern for Antenna A-1 (350 - 500 MHz).	82
3-19b	Far Field H-Plane $E_y$ -Pattern for Antenna A-1 (550 - 700 MHz).	83
3-19c	Far Field H-Plane $E_y$ -Pattern for Antenna A-1 (750 - 850 MHz).	84



THE UNIVERSITY OF MICHIGAN  
7848-1-F

List of Figures (cont'd)

3-20	Input Impedance for Antenna A-1.	86
3-21a	Far Field H-Plane Power Pattern for Antenna C-2 Fed at Left End of the Array; 450 - 550 MHz.	87
3-21b	Far Field H-Plane Power Pattern for Antenna C-2 Fed at Left End of the Array; 600 - 750 MHz.	88
3-21c	Far Field H-Plane Power Pattern for Antenna C-2 Fed at Left End of the Array; 800 - 950 MHz.	89
3-22a	Far Field Patterns of Antenna A-1 Loaded and Unloaded with EAF-2 Ferrites; 250 - 400 MHz.	90
3-22b	Far Field Patterns of Antenna A-1 Loaded and Unloaded with EAF-2 Ferrite; 450 - 600 MHz.	91
3-22c	Far Field Patterns of Antenna A-1 Loaded and Unloaded with EAF-2 Ferrite; 650 - 800 MHz.	92
3-23a	Far Field Patterns of Antenna A-2 Loaded and Unloaded with EAF-2 Ferrite; 250 - 400 MHz.	93
3-23b	Far Field Patterns of Antenna A-2 Loaded and Unloaded with EAF-2 Ferrite; 450 - 600 MHz.	94
3-23c	Far Field Patterns of Antenna A-2 Loaded and Unloaded with EAF-2 Ferrite; 650 - 800 MHz.	95
3-24a	Far Field Patterns of Antenna A-3 Loaded and Unloaded with EAF-2 Ferrite; 250 - 400 MHz.	96
3-24b	Far Field Patterns of Antenna A-3 Loaded and Unloaded with EAF-2 Ferrite; 450 - 600 MHz.	97
3-24c	Far Field Patterns of Antenna A-3 Loaded and Unloaded with EAF-2 Ferrite; 650 - 800 MHz.	98
3-25a	Far Field Patterns of Antenna B-1 Loaded and Unloaded with EAF-2 Ferrite; 250 - 400 MHz.	99
3-25b	Far Field Patterns of Antenna B-1 Loaded and Unloaded with EAF-2 Ferrite; 450 - 600 MHz.	100
3-25c	Far Field Patterns of Antenna B-1 Loaded and Unloaded with EAF-2 Ferrite; 650 - 800 MHz.	101
3-26a	Far Field Patterns of Antenna B-2 Loaded and Unloaded with EAF-2 Ferrite; 250 - 400 MHz.	102
3-26b	Far Field Patterns of Antenna B-2 Loaded and Unloaded with EAF-2 Ferrite; 450 - 600 MHz.	103
3-26c	Far Field Patterns of Antenna B-2 Loaded and Unloaded with EAF-2 Ferrite; 650 - 800 MHz.	104
3-27	Temperature vs Position in Cavity at Thermal Equilibrium	106
3-28	Experimental Set-Up.	108
3-29	Increase in Temperature vs Time (150 watts)	109
3-30	°F vs Watts.	110

THE UNIVERSITY OF MICHIGAN  
7848-1-F

List of Figures (cont'd)

3-31	VSWR of the 11.5 cm x 1.0 cm Cross Section Q-3 Ferrite Filled Waveguide with a Feeding Loop Located approximately 1/4 Guide Wavelength from the Shorting End.	111
3-32	Wave Attenuation Along the Longitudinal Direction of the 11.5cm x 1.0 cm Cross Section Q-3 Ferrite Filled Waveguide.	113
4-1	Scattering from a Dielectric Material.	117
4-2	Transmission Line Analog of the Dielectric Rod Antenna.	118
4-3	Volume and Surface Sources of the Ferrite Rod Antenna.	121
4-4	Coordinate System assumed for the Ferrite Rod Antenna.	130
4-5	Coordinate System Assumed for the Ferrite Tube Antenna	143
4-6	Coordinate System Assumed for the Ferrite Tube Antenna and the Radiation Plane Defined.	157
4-7a	Linear Power Patterns from the Dipole Excited Metal Cup with the Balsa Wood Core and the Phenolic Shell without EAF-2 Ferrite Powder (E-Plane).	158
4-7b	Linear Power Patterns from the Dipole Excited Metal Cup with the Balsa Wood Core and the Phenolic Shell without EAF-2 Ferrite Powder (H-Plane).	159
4-8	Linear Power Patterns from a Quadrifilar Helix Excited Ferrite Tube Antenna.	161
4-9a	Linear Power Patterns from a Quadrupole Excited Ferrite Tube Antenna (Monopole inside Circumference of Ferrite Tube).	162
4-9b	Linear Power Patterns from a Quadrupole Excited Ferrite Tube Antenna (Monopole outside Circumference of Ferrite Tube).	163
4-10	Geometry of the Ferrite Tube Antenna with a Conical End.	164
4-11a	Linear Power Patterns of the Ferrite Tube Antenna with a Conical End (H-plane).	166
4-11b	Linear Power Patterns of the Ferrite Tube Antenna with a Conical End (E-plane).	167
4-12a	Near Field Measurement, Relative Amplitude and Phase of $E_{\rho}$ Against Coordinate Angle $\phi$ (Taken at 5 cm from Feed End).	168
4-12b	Near Field Measurement, Relative Amplitude and Phase of $E_{\rho}$ Against Coordinate Angle $\phi$ (Taken at 5 cm from Free End).	169
4-13a	Near Field Measurement, Relative Amplitude and Phase of $E_{\rho}$ Against Ferrite Tube Axis at 600 MHz in $\phi=\pi/2$ Plane.	170
4-13b	Near Field Measurement, Relative Amplitude and Phase of $E_{\rho}$ Against Ferrite Tube Axis at 900 MHz in $\phi=\pi/2$ Plane.	171
4-14	Geometry of the Ferrite Tube Antenna.	172
4-15a	Linear Power Patterns from a Dipole Excited Ferrite Tube (E-Plane).	174
4-15b	Linear Power Patterns from a Dipole Excited Ferrite Tube (H-Plane).	175

THE UNIVERSITY OF MICHIGAN  
7848-1-F

List of Figures (cont'd)

4-16	Variation of Beamwidth with Frequency (E- and H-Plane) .	176
4-17	Position of First Sidelobe Varying with Frequency (E- and H-Plane).	177
4-18	Maximum Sidelobe or Backlobe Level vs Frequency.	178
4-19a	Input Impedance of the Dipole Excited Ferrite Tube Antenna (length = 36 cm).	179
4-19b	Input Impedance of the Dipole Excited Ferrite Tube Antenna (Length - 71.5 cm).	180
5-1	Element Excitation Decomposition and Fundamental Equations.	193
5-2	Input Resistance R and Reactance X for Folded Dipole Structure where $p_s=1.0$ , $p_a=1.0$ .	199
5-3	Input Resistance R and Reactance X for folded Dipole Structure where $p_s=1.0$ , $p_a=0.8$ .	200
5-4	Input Resistance R and Reactance X for Folded Dipole Structure where $p_s=1.0$ and $p_a=0.6$ .	201
5-5	Input Resistance R and Reactance X for Folded Dipole Structure where $p_s=1.0$ , $p_a=0.4$ .	202
5-6	Input Resistance R and Reactance X for Folded Dipole Structure where $p_s=0.8$ $p_a=0.8$ .	203
5-7	Input Resistance R and Reactance X for Folded Dipole Structure where $p_s=0.8$ , $p_a=0.6$ .	204
5-8	Construction of Folded Helical Monopole with Ferrite Core.	206
5-9	Magnitude of Reflection Coefficient vs Frequency for Various Hollow Core and Ferrite Core Helical Element Configurations.	207
5-10	Effect of Magnetic Biasing on Magnitude of Reflection Coefficient vs Frequency for two Different Element Ferrite Core Configurations.	211
5-11	Construction of Helical Monopole with Ferrite and Copper Core.	213
5-12	Multiple Resonance Behavior of Various Composite Element Structures.	216
5-13	Geometry of Corresponding Dipole Configuration with Analogous Transmission Line.	219
5-14	Current Distribution for General Result when $Z_2 < Z_1$ .	221

THE UNIVERSITY OF MICHIGAN

7848-1-F

List of Figures (cont'd)

6-1	Test Arrangement for Measuring the Dielectric Constant of Indiana General Q-4 Ferrite.	239
6-2	Coaxial Line with Specimen in Position.	242
C-1	Solution of the Characteristic Equation for Helix Having Core Parameters $\epsilon_r=1.00$ , $\mu_r=1.00$ (Air).	256
C-2	Solution of the Characteristic Equation for Helix Having Core Parameters $\epsilon_r=3.77$ , $\mu_r=1.00$ (EAF-2 Powder Ferrite Biased into Saturation).	257
C-3	Solution of the Characteristic Equation for Helix Having Core Parameters $\epsilon_r=7.88$ , $\mu_r=1.00$ (Q-3 Ferrite at 150 MHz Biased into Saturation).	258
C-4	Solution of the Characteristic Equation for Helix Having Core Parameters $\epsilon_r=22.0$ , $\mu_r=1.00$ (Eccosorb CR at 300 MHz Biased into Saturation).	259
C-5a	Solution of the Characteristic Equation for Helix Having Core Parameters $\epsilon_r=3.77$ , $\mu_r=2.10$ (EAF-2 Powder Ferrite).	260
C-5b	Solution of the Characteristic Equation for Helix Having Core Parameters $\epsilon_r=3.77$ , $\mu_r=2.10$ (EAF-2 Powder Ferrite).	261
C-6a	Solution of the Characteristic Equation for Helix Having Core Parameters $\epsilon_r=7.96$ , $\mu_r=12.4$ (Q-3 Ferrite at 100 MHz).	262
C-6b	Solution of the Characteristic Equation for Helix Having Core Parameters $\epsilon_r=7.96$ , $\mu_r=12.4$ (Q-3 Ferrite at 100 MHz).	263
C-7a	Solution of the Characteristic Equation for Helix Having Core Parameters $\epsilon_r=7.88$ , $\mu_r=13.2$ (Q-3 Ferrite at 150 MHz).	264
C-7b	Solution of the Characteristic Equation for Helix having Core Parameters $\epsilon_r=7.88$ , $\mu_r=13.2$ (Q-3 Ferrite at 150 MHz).	265
C-8a	Solution of the Characteristic Equation for Helix Having Core Parameters $\epsilon_r=7.81$ , $\mu_r=14.3$ (Q-3 Ferrite at 200 MHz).	266
C-8b	Solution of the Characteristic Equation for Helix Having Core Parameters $\epsilon_r=7.81$ , $\mu_r=14.3$ (Q-3 Ferrite at 200 MHz).	267
C-9a	Solution of the Characteristic Equation for Helix Having Core Parameters $\epsilon_r=22.0$ , $\mu_r=4.51$ (Eccosorb CR at 300 MHz).	268
C-9b	Solution of the Characteristic Equation for Helix Having Core Parameters $\epsilon_r=22.0$ , $\mu_r=4.51$ (Eccosorb CR at 300 MHz).	269

THE UNIVERSITY OF MICHIGAN  
7848-1-F

List of Figures (cont' d)

D-1a	R vs $\beta_s h$ for the Parameter $p_s$ (EMF Method).	277
D-1b	Expanded R vs $\beta_s h$ for the Parameter $p_s$ (EMF Method).	278
D-2a	$X_1$ vs $\beta_s h$ for the Parameter $p_s$ (EMF Method).	279
D-2b	Expanded $X_1$ vs $\beta_s h$ for the Parameter $p_s$ (EMF Method).	280
D-3a	$X_2 p_s$ vs $\beta_s h$ for the Parameter $h/a$ (EMF Method).	281
D-3b	Expanded $X_2 p_s$ vs $\beta_s h$ for the Parameter $h/a$ (EMF Method).	282



I

INTRODUCTION AND SUMMARY

This final report describes the activities and accomplishments associated with each of four assigned technical tasks of this project. A separate section considers the activity under each task.

Section II deals with the task of showing the design feasibility of a ferrite loaded conical spiral antenna of reduced size capable of operating over the frequency range 200 to 600 MHz. A design appropriate to the requirements is shown in Fig. 2-1. Additional possibilities for the design are also shown in Fig. 2-2. A design objective has been to handle 100 watts of cw power; the design shown satisfies this requirement. Experimental investigations have indicated that it is possible both to transmit and to receive at the same time over this antenna. Such experimental verification has been made using the backfire cylindrical helix filled with ferrite. It has been convenient throughout most of the experimentation to use the cylindrical helix rather than the conical helix. It has been well established however, that information so obtained is applicable to the conical helix at that frequency where the center of the active region has a diameter equivalent to that of the cylindrical helix. Several exploratory studies on loading techniques have been made under this task in order to provide the necessary background information. The details of these studies are included in the main body of the report.

Task II (Section III) has as its objective, the study of the utilization of ferrite loaded slot elements in an array. The studies under this task have been devoted to providing an elementary array of such elements. Initial work only has been accomplished. This initial work has consisted of obtaining ferrite loaded slot elements which are reasonably matched. The actual utilization of these elements in a simple linear array, together with studies of the performance as an array, will be included in one of the requested tasks under a succeeding contract. However, an unforeseen accomplishment has been made in the development of an entirely

THE UNIVERSITY OF MICHIGAN  
7848-1-F

new type of antenna, the interdigital array, suitable for flush mounting. This antenna is operable over a 2:1 frequency range. It is of reduced size and there is prospect of reducing the size still more; this will be attempted as part of the effort on the succeeding contract. This antenna consists of an arrangement of toppled monopoles; all but one of these is parasitic.

Under Task III (Section IV) extended studies have been made of the ferrite rod radiator. These studies have emphasized a very large amount of mathematical analysis. This analysis has provided a detailed comparison of mathematical methods available to date. One result of this work has been to provide an improved mathematical model. Also, it has been found by such analysis, as well as verified experimentally, that a ferrite tube radiator has more desirable characteristics than a ferrite rod radiator. Details on the advantages of the tube radiator as compared with the rod radiator are given in Section IV. The mathematical methods used for this task have been supplemented by a substantial machine computation effort. In the experimental phase of the work, many radiation patterns have been obtained.

Under Task IV (Section V) studies have been made on a very wide basis of numerous methods of designing and constructing antennas suitable for operation for frequencies down to 30 MHz. Such methods have included the folding of elements, the coiling of elements, the use of ferrite and dielectric core materials, and the use of segments providing lumped reactance parameters. Although the methods studies showed the various advantages to be had by one technique over another, the work described here does not treat intensively the matter of radiation efficiency. However, during the latter stages of the work, appropriate reference material has been found indicating the radiation efficiencies that can be expected by at least one of the methods. In the provision for the continuance of these studies in the next contract, it is expected that further exploration of radiation efficiencies will be made in this area. The general discussions of techniques and methods are described in some detail in the succeeding sections of this report.



II

FERRITE LOADED CONICAL SPIRALS

2.1 Background

The objective of this task is to develop a ferrite filled conical spiral antenna that will cover the 200 - 600 MHz range and reduce to approximately one-third the size of an unloaded conical spiral antenna. The antenna is to have circular polarization with a broad forward directional main beam. The antenna should also be capable of employing both the transmit and receive modes simultaneously.

Throughout the course of this study, emphasis has been placed on size reduction of helix antennas instead of conical spiral antennas. The reasons are two-fold: 1) a helix is a special case of a conical spiral antenna that occurs when the cone angle is  $0^\circ$  and 2) helix antennas are much easier to construct and analyze mathematically. Therefore, more investigations can be made into reduction techniques with the time and money available.

During the course of the contract, several ferrite loading techniques have been investigated to determine which adaptation of ferrite to the antenna would be the most advantageous from the standpoint of weight, effectiveness, cost of fabrication and practicality. Such techniques as full and partial loading of the interior of a conical helix with ferrite; coating the windings with ferrite; ferrite loaded coiled windings; anisotropic ferrite loading, and discrete inductance loading have been investigated.

All of these techniques are either effective to some degree or look as though additional effort could make them so. However, for the requirements of the feasibility study, partial interior loading of ferrite proved to be the most advantageous. Thick shells inside of the windings can give almost the same reduction as full core loadings, which is equal to

$$R = \sqrt{\frac{1 + 1/\mu_r}{1 + \epsilon_r}}, \quad (2.1)$$

# THE UNIVERSITY OF MICHIGAN

7848-1-F

where  $R$ , the reduction factor, is the radial ratio of the dimension of the loaded to the unloaded antenna. Yet, partial core loading saves considerable weight over full core loading. Small reduction factors (less than 0.50) can be readily achieved, provided material is available. Efficiency remains very good. The biggest drawback is weight.

A theoretical study of an approximate model of ferrite coated windings indicates that moderate reduction factors (greater than 0.50) can be achieved. The loading is relatively lightweight, and probably will not reduce antenna efficiency. However, it is difficult to fabricate. So difficult, in fact, that no experiments were conducted.

A ferrite coiled winding exhibits the same desirable features as a ferrite coated winding, and in addition high reduction factors can be obtained. However, it results in an extremely inefficient radiator. The radiation efficiency may be improved by the techniques discussed in Section 2.7.

Discrete inductance loading looks very promising for lower VHF frequencies where good low frequency inductors can be wound on ferrite cores. Ferrite loaded shorted transmission line stubs might prove acceptable alternates at high VHF and low UHF frequencies, but neither technique could be completely explored due to limitations of materials.

Investigation of anisotropic ferrite loading had not progressed far when the contract expired. Whether it would introduce any special advantages over isotropic ferrites other than its low loss characteristics at microwave frequencies remains to be seen.

In addition to loading techniques, two peripheral subjects were also covered in this task: 1) demonstrating the feasibility of using interior loading techniques on "complementary" conical helices (i.e. conical helices with magnetic current "conductors" instead of electric current conductors), and 2) demonstrating the feasibility of using the transmit and receive modes simultaneously. Both appear entirely feasible and the tests on both transmit-receive mode capability and material loading of "complementary" conical helices is covered in this report.

## 2.2 Recommended Antenna

An antenna capable of meeting the specifications appears to be feasible. Most of the concepts of the proposed design have been verified experimentally, although the model itself has not been built or tested. The design is depicted in Fig. 2-1.

The conical helix shown should have a half-power beamwidth of about  $60^\circ$  at the high frequency limit of its operation and have a beamwidth of about  $80^\circ$  at the low frequency limit of its operation. The beamwidth could be made more uniform over its frequency range of operation by using the shape denoted in Fig. 2-2a and 2-2b. The shape in Fig. 2-2b gives the most uniform beamwidth. It should be kept in mind when designing an antenna as shown in Figs. 2-2a, b, that the reduction factor formula (Eq. 2.1) applies only to the diameter; not the length.

The proposed design should be capable of handling 100 watts of power since there are no small gaps over which breakdown could occur. The transmit and receive modes have been simultaneously used successfully on a backfire helix fully filled with ferrite material.

On this basis it is expected that the proposed conical helix will be capable of operating in these modes simultaneously also.

Experiments performed on ferrite loaded helices and conical helices indicate that the patterns will have a broad forward direction beam and that the radiation will be circularly polarized.

Because of the ferrite loading, the proposed antenna is able to operate down to 200 MHz, even though the dimensions of the base are those of an antenna operating down to about 550 MHz. It has been determined both theoretically and experimentally that a half diameter loading of material will give almost the same diameter reduction loading as a full core loaded helix (Rassweiler, 1966). The success of a tapered loading in a conical helix has also been demonstrated (Ferris et al 1966). Thus, a half-core loading of ferrite at the base will give almost the full core reduction predicted by Eq. (2.1) (Rassweiler, 1966). In this case, the

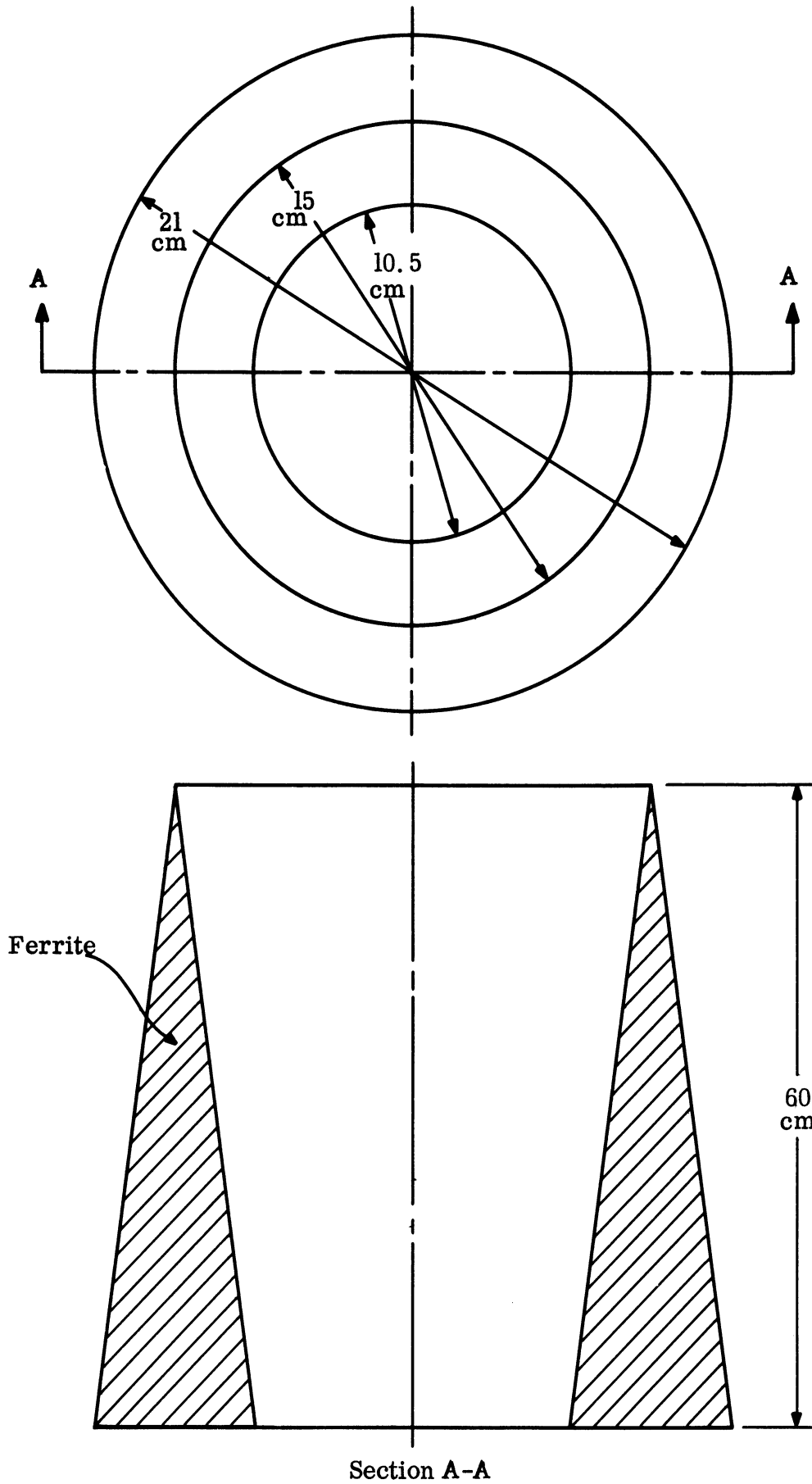


FIG. 2-1: PROPOSED ANTENNA DESIGN

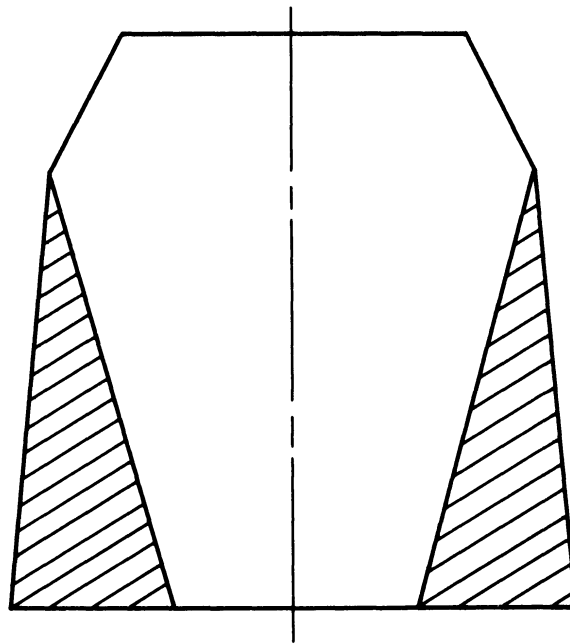


FIG. 2-2a: ALTERNATE DESIGN

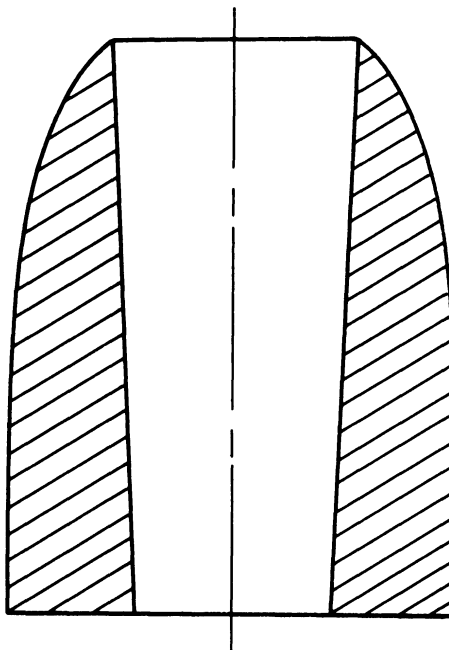


FIG. 2-2b: ALTERNATE DESIGN

reduction needed is 0.365. The tapering reduces the weight of the antenna and, in this particular frequency range, also improves the efficiency of the antenna at the higher frequencies since most ferrites become very lossy in the 200 - 600 MHz range.

The ferrite should preferably be low loss in the frequency range of interest or have a high loss only at the high end of the frequency range so that power is not lost heating the ferrite. This material should also be lightweight. The relative permeability and permittivity should be as high as possible so that a thinner shell of material can be used and a weight saving can be obtained. Unfortunately, high permeabilities and permittivities seem to conflict with a material being lightweight. Similarly, high permeabilities are associated with high loss.

Another consideration is that the relative permeability and permittivity should be about the same to improve the radiation rate (Rassweiler, 1966). Unfortunately, there is no certainty about what the relationship between the relative permeability and relative permittivity should be to produce the highest radiation rate. The correct combination must be determined by numerical or experimental studies for a given ferrite.

Several materials (some of which are not ferrites) are commercially available at present that will give a reduction factor of at least 0.365. These include; Emerson and Cuming Eccosorb CR, MF-124, MF-117, MF-116 and MF-114. If Eccosorb MF-114 is used as the loading material, the weight of the material alone would be 30.6 Kg (67.4 lbs) .

One other consideration in the design of the antenna is that the windings should be in as close contact with the ferrite as possible. Even a small spacing between the windings and the material will reduce the reduction that can be obtained with the material. Preferably, the material should be scored and the winding placed in the surface of the material.

### 2.3 Partial Core Ferrite Loading

Both experimental and theoretical work have indicated the practicability of ferrite loaded cylindrical and conical helix antennas. An analysis of the sheath

helix transmission line operating in the -1 mode (Hong and Rassweiler, 1966) indicates that the diameter of a helix transmission line wound with many turns per wavelength, can be reduced in diameter by Eq. (2. 1) where  $\epsilon_r$  is the relative dielectric constant and  $\mu_r$  is the relative permeability of the ferrite loading material. Equation (2. 1) is applicable for  $\mu_r \epsilon_r$  products less than 10, but is probably a good approximation for  $\mu_r \epsilon_r$  products greater than 10.

A variational analysis of a tape helix with a material core indicates the same diameter reduction, if the equations are solved for the reduction factor (Bulgakov, et al, 1960). Again nothing is said about reduction in length, although the transmission line mode (no angular variation in the fields) is assumed.

Another analysis of the sheath helix was done by Rassweiler (1966) to investigate the effects of partial loadings of ferrite on the backfire mode (-1) of a sheath helix transmission line. It was shown that a layer of ferrite inside the windings of a sheath that was a quarter radius thick would produce almost the same reduction in diameter as would a full core loading. Figure 2-3 shows theoretical curves, based on this model, of the effectiveness of  $\mu_r$  and  $\epsilon_r$  in partial core loading for various thicknesses of material and for various combinations of  $\mu_r$  and  $\epsilon_r$ ;  $\beta$  is the wave number for the helical guide;  $a$  is the outer radius and  $b$  the inner radius.

Experimental investigations tend to support the theory as is indicated in Fig. 2-4. This figure shows the results of several full and partial core loadings of various materials. The experimental reductions were determined by comparing the loaded and unloaded antenna patterns. Good agreement is apparent between experiment and theory. The diameter size reduction formula applies both to backfire and forward-fire helices.

Because the radiation mechanism is believed to be different for the forward fire and backward fire helix antennas, the problem of reduction of length of these two antennas is quite different (Chen, 1967). In the forward fire helix, energy propagates down the helix from the feed in a traveling wave and diffracts off the end of the structure.

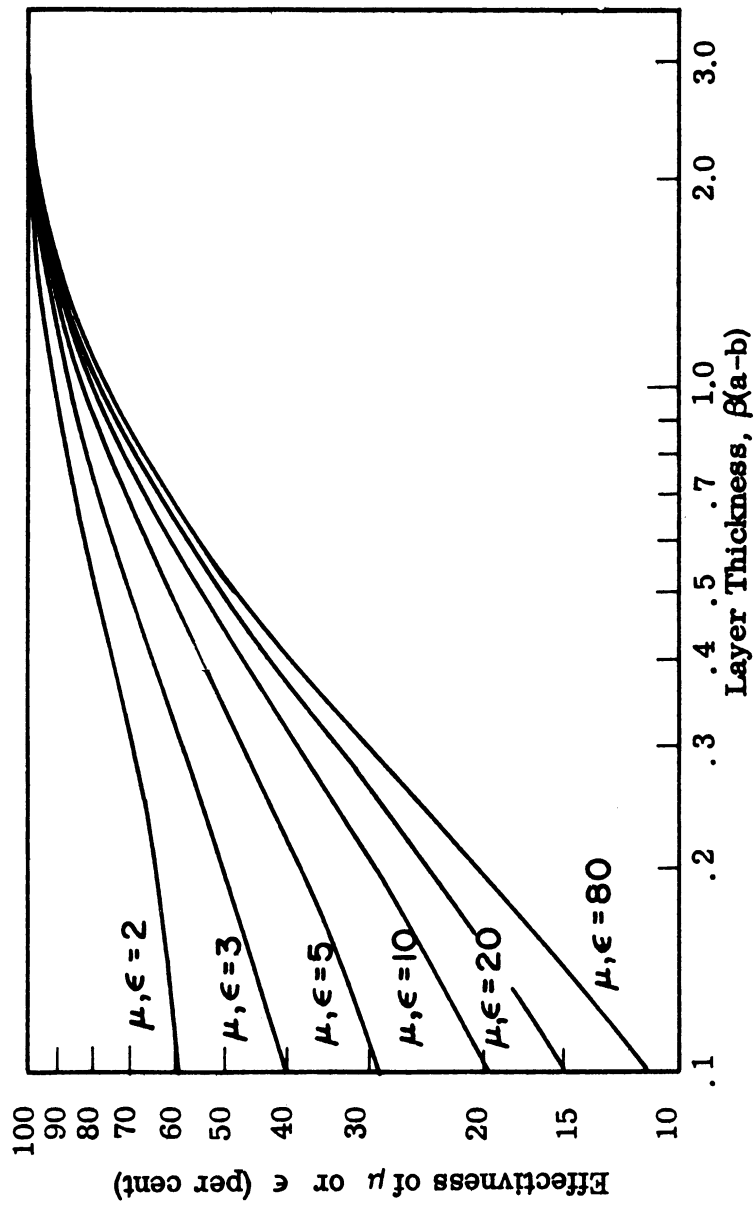


FIG. 2-3: LAYER LOADING EFFECTIVENESS



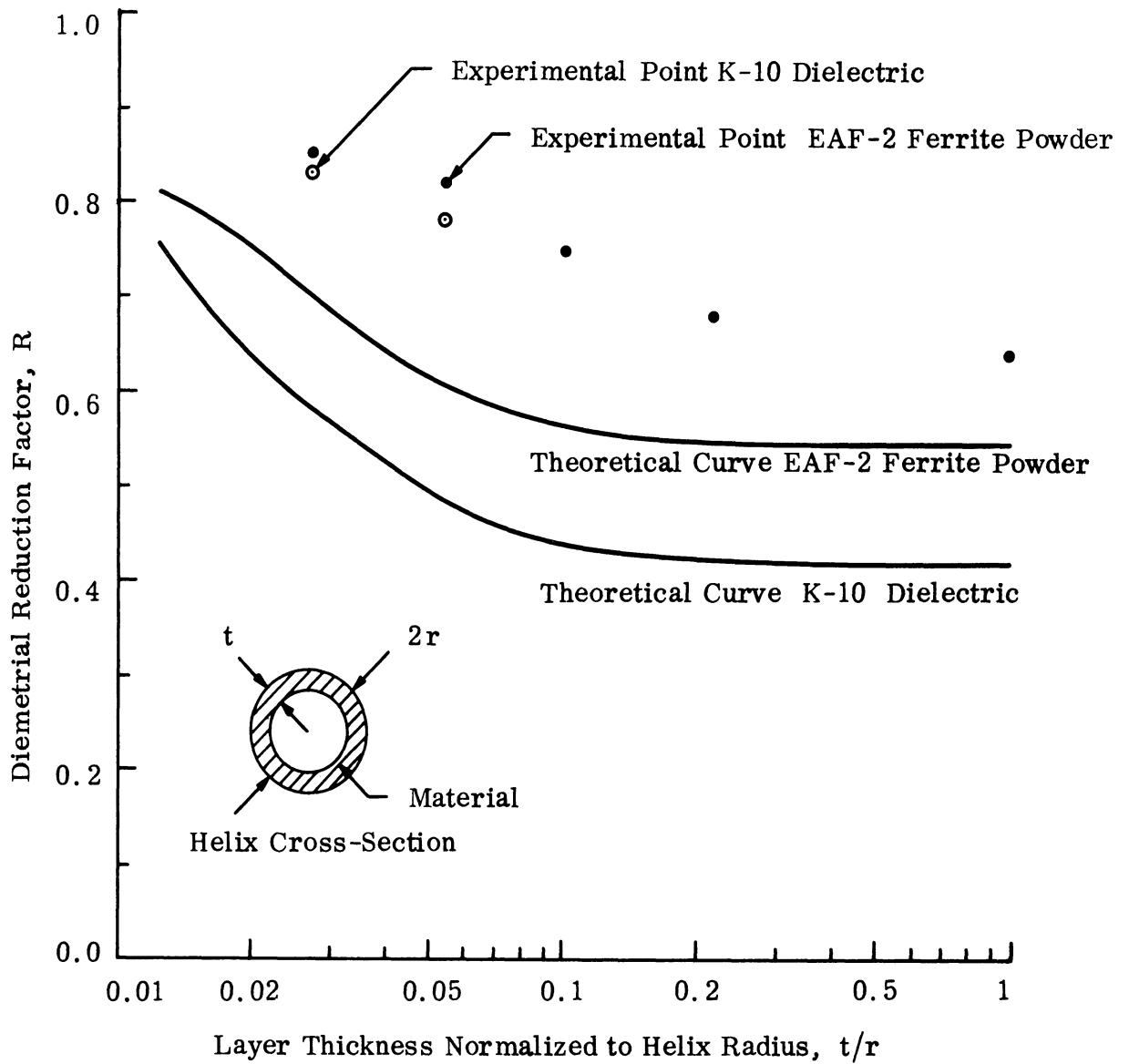


FIG. 2-4: THEORETICAL AND EXPERIMENTAL DIAMETRAL REDUCTION FACTORS FOR A HELIX ANTENNA LOADED WITH K-10 DIELECTRIC AND EAF-2 FERRITE POWDER.

For the backfire helix, the currents decay from the feed as they propagate toward the back of the antenna, and energy radiates in the opposite direction, back towards the feed. A backfire helix is a surface wave antenna. Thus, if the radiation rate can be increased by a material loading, then the length can be reduced. A variational solution assuming complex exponential variation with length and  $-1$  angular variation in the polar angle for the field has been obtained. From this solution the radiation rate, or real part of the complex exponential variation, has been analyzed (Rassweiler, 1966).

This tape helix analysis indicates that the diametral reduction factor given earlier is still valid for small tape widths. It was not possible to produce a relation showing how the radiation rate was effected by the choice of  $\mu_r$  and  $\epsilon_r$ , but the characteristic equation of the problem was solved numerically and the results plotted for various  $\mu_r$  and  $\epsilon_r$ .

These conclusions can be drawn from Rassweiler's study: 1) the width of the winding and the pitch angle affect the radiation rate very little; 2) there appears to be a trend of higher  $\epsilon_r$  to reduce the radiation rate and higher  $\mu_r$  to increase the radiation rate. No attempt was made to find an optimum ratio between  $\mu_r$  and  $\epsilon_r$ , as was done by Adams (1967), nor were any theoretical calculations of efficiency made. However, some  $\mu_r \epsilon_r$  combinations studied did increase the radiation rate.

It is interesting to note that although a convenient expression for determining the optimum relationship of  $\mu_r$  to  $\epsilon_r$  for a given reduction factor was not obtained, an optimum probably does exist. This optimum is probably the relationship that will give the equivalent helical waveguide the same wave impedance as free space, if previous experience can be extended (Kalafus and Lyon, 1961; Adams, 1967).

Experimental calculations of efficiency were made, however, for several full and partial core loadings and one exterior loading of the EAF-2 powdered ferrite. The diametral reduction factors and efficiencies measured are indicated in Table I (Lyon et al 1966). The magnetic  $Q$  of the ferrite material is also indicated for the purposes of comparison. The reduction of radiation rate with

# THE UNIVERSITY OF MICHIGAN

7848-1-F

TABLE I: EFFICIENCY OF HELIX ANTENNA WITH SEVERAL FERRITE LOADINGS

Frequency (MHz)	Loading	Efficiency (Percent)	Comments	Magnetic Q
750	Air	60	Center of Operation	—
550	3/8" Inside Layer of EAF-2	61.2	Center of Operation	25
550	1" Inside Layer of EAF-2	41	Above Center of Operation	25
550	Air	31.8	Below Center of Operation	—
550	3/4" Outside Layer of EAF-2	54.5	Center of Operation	25

plain dielectric loading was also observed on near field measurements of the antennas. Rassweiler calculates the maximum radiation rate for a full core loading of EAF-2 for this same antenna to be about one-third that of the unloaded antenna. Thus, it appears that moderate reductions can be accomplished without much sacrifice in efficiency.

Because of the reduction in radiation rate for some choices of  $\mu_r$  and  $\epsilon_r$  the backlobe tends to rise as a result of the unradiated energy either being diffracted off the back of the antenna or being reflected from the back of the antenna and radiating in a backfire mode while trying to propagate towards the tip.

The extension of the backfire cylindrical helix work to the conical helix work is easily done by considering a backfire cylindrical helix antenna as the special case of a conical helix antenna with zero cone angle. Several experiments performed with dielectric and ferrite loading confirm both the experimental and theoretical findings on backfire helices concerning reduction of the diameter.

Near field measurements of the conical helix antennas exhibited slower decay of the currents in the radiation region of the antenna. On very wideband conical helices, far field patterns indicated the presence of the -2 mode as a result of not all the energy being radiated in the -1 mode.

If a poor selection of materials is made when loading the base of conical helix antennas with a ferrite material, so that the radiation rate is reduced, then it is possible that some energy will not be radiated in the desired backfire mode, but will interact with the base of the antenna to produce high backlobes. The back-lobe can be reduced by any (or a combination) of the following techniques: 1) select a material that has a higher radiation rate; 2) increase the number of turns per inch, and 3) use absorber across the back of the antenna to absorb the backlobe.

#### 2.4 Transmit-Receive Mode Feasibility

To test the usability of a ferrite loaded antenna with both the transmit and receive modes, a bifilar backfire helix antenna with its interior filled with EAF-2 powder was tested. The experimentally determined properties were reported earlier in a quarterly report under this contract (Rassweiler, 1966). Since the antenna seems to operate most efficiently at 450 MHz, this frequency was chosen as the transmit frequency. The equipment available restricted the reception frequency to 595 MHz. Figure 2-5 shows the diplexer circuit used to protect the receiver front end from being overloaded by the transmitter.

A 80 mw signal was fed to the antenna and this is approximately the input power to the antenna since the reflected power was negligible. The test was conducted on the 50-foot North Campus range of the Radiation Laboratory with the test antenna placed in the field of a 595 MHz signal. Observation of the 595 MHz signal on the receiver was made. The first harmonic addition frequency, as a result of possible mixing of the transmitted and received signals (1045 MHz), was not observed. The attenuation of the band pass filter was less than 10 db at this frequency; it is doubtful if this would prevent reception of a 1045 MHz signal if it did exist. Hence, simultaneous transmit and receive mode operation appears to be entirely feasible and harmonic generation should not be a problem for low power levels.

#### 2.5 Complementary Helix Antenna

The so-called complementary helix antenna, one with very broad flat conductors, produces the same results as the wire wound helix antennas. Thus

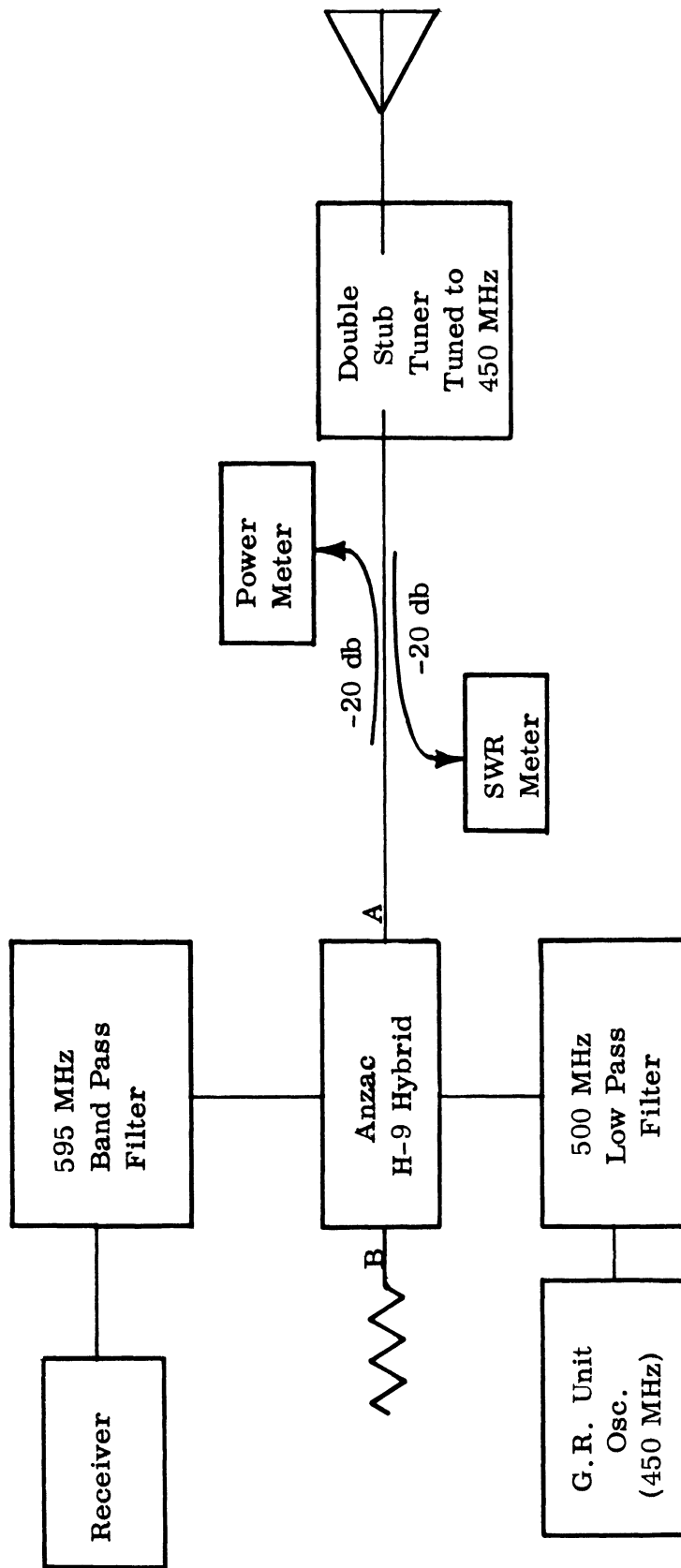


FIG. 2-5: CIRCUIT FOR TESTING SIMULTANEOUS USE OF TRANSMIT AND RECEIVE MODES.

THE UNIVERSITY OF MICHIGAN  
7848-1-F

reductions for very thin and very thick conductors can be predicted fairly accurately with the formula given earlier (Eq. 2. 1). However, the complementary helix antenna does offer the advantage of easily measuring reductions obtained with loadings.

A bifilar complementary helix (or narrow gap helix) was constructed and its property as an antenna was investigated. The specifications are as follows:

Diameter: 13 cm	Length: 40 cm	Gap Width: 0.1 cm
Pitch Angle: $10^{\circ}$	Construction: bifilar, balanced or unbalanced feed.	

The radiation pattern in Fig. 2-6 shows that the unloaded antenna has good patterns from 600 MHz up to around 900 MHz, which is quite comparable to the equivalent wire helix (its dual).

The radiation pattern of a loaded case is also shown. The EAF-2 ferrite shell  $1/2''$  thick was loaded inside and under the gap. The radiation pattern indicated in Fig. 2-6 seems to give a useful frequency range from 450 MHz up to around 700 MHz, which gives about 0.75 reduction in the resonant frequency. This is also very close to the value obtained from its dual.

The complementary antenna was placed inside an anechoic chamber for the near field amplitude measurement. Since it is a dual of the wire helix, an E-probe was used instead of the H-probe that was used in the wire helix measurement. The E-probe was made from a 0.084 cm coaxial line. The protruding inner conductor has a length of 0.4 cm and is bent  $90^{\circ}$  with respect to the feeding coaxial line. A small disk of 1.2 cm diameter was attached to the outer conductor and it was perpendicular to the protruded inner conductor. This unbalanced probe was then placed  $\lambda/10$  above the antenna with its inner conductor parallel to the axial direction of the antenna.

The near field amplitude is shown in Fig. 2-7. The general shape and the trend is very similar to those of the wire helix previously used and discussed (Lyon et al, 1966). The best near field pattern is at 600 MHz (which also gives best far field pattern).

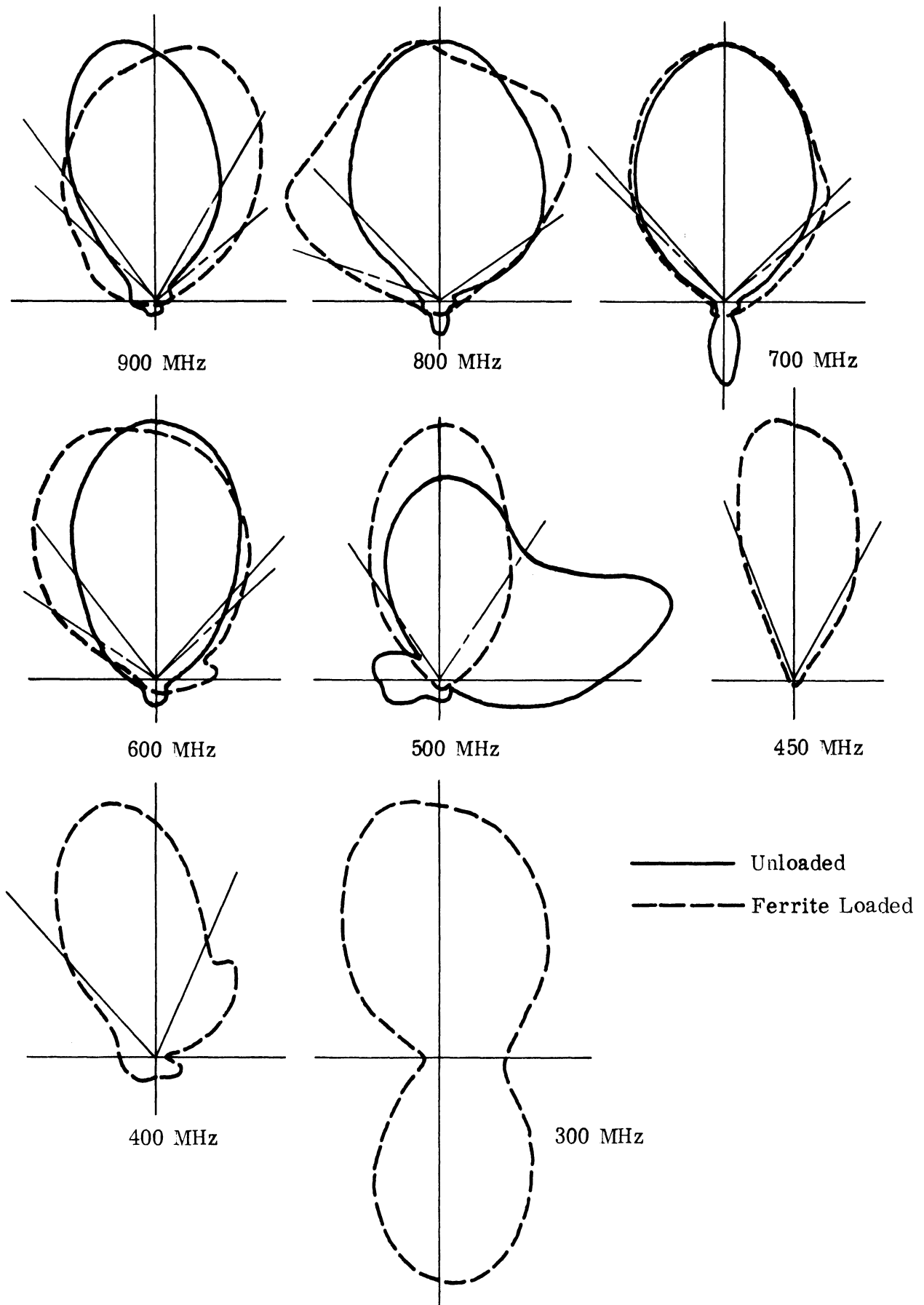


FIG. 2-6: RADIATION PATTERNS OF A COMPLEMENTARY HELICAL ANTENNA

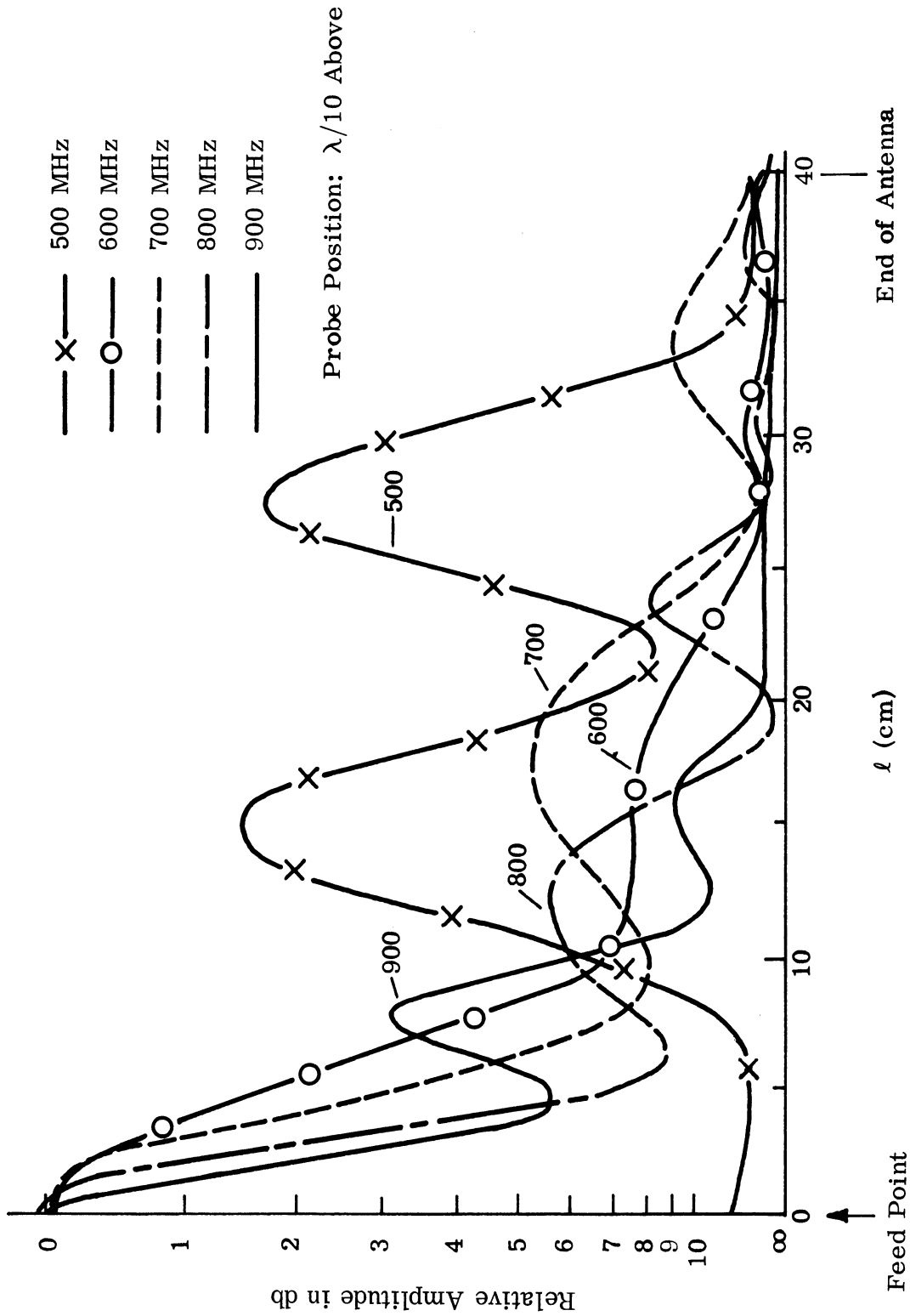


FIG. 2-7: NEAR FIELD AMPLITUDE OF A COMPLEMENTARY HELICAL ANTENNA WITHOUT LOADING.



THE UNIVERSITY OF MICHIGAN  
7848-1-F

The near field amplitude was also taken with 1/2" shell loading of K-10 dielectric, and as shown in Fig 2-8, seems to indicate the best near field pattern at 700 MHz.

The phase velocity along the gap can be measured accurately if the phase shift along the axial direction is measured by a typical phase measurement arrangement. However, it is a very time-consuming and painstaking measurement. Therefore, a very crude and easy method was devised. As shown in Fig. 2-9, the antenna is fed through a PRD standing wave detector with a standard VSWR measurement set-up. The shorting copper ring was moved to obtain a minimum reading on the amplitude meter. Then the ring was moved to obtain a second minimum. The distance between the two minima was recorded for several trials and the average value taken. This should be a half wavelength along the axial direction. This value was then converted to the distance along the gap by dividing by the sine of the pitch angle. With the frequency known, it is then possible to obtain a phase velocity along the gap for different types of loadings at different frequencies. The measurement at or near the resonant frequency is very difficult (if not impossible) because most of the energy is radiated before traveling very far down the helix. Therefore, the phase velocity at the resonant frequency must be obtained approximately by extrapolating the results at other frequencies. The measurement was taken for the unloaded, the metal (cylinder of 4" dia) loaded, the K-10 dielectric shell (1/2" thick) and the EAF-2 ferrite shell (1/2" thick) loaded cases. The results are shown in Fig. 2-10. The resonant frequency can be read out from the intersection of the zero phase shift axis and the straight lines connecting measured points (i.e. 630 MHz for the unloaded, 650 MHz for the loaded, 500 MHz for the K-10 dielectric loaded, and 520 MHz for the ferrite loaded cases).

The input impedance of a bifilar complementary helical antenna was measured for various loading materials. The antenna is shown in Figs. 2-11 and 2-12. The experimental set-up for the measurement is shown in Fig. 2-13. The antenna was fed by an unbalanced feed across the gap at the center of the feed point of the antenna. The input impedance for the unloaded antenna is shown in Fig. 2-14 and

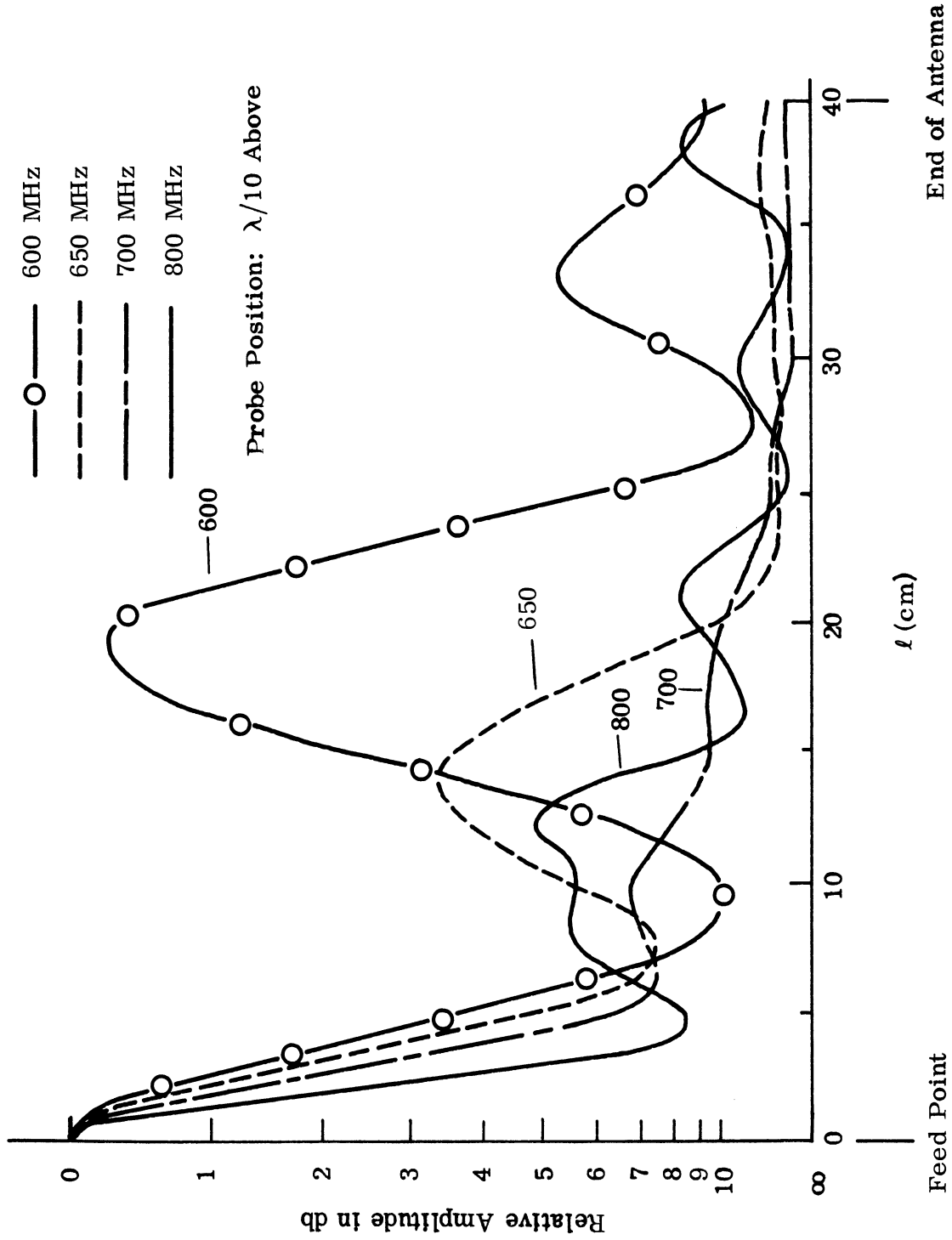


FIG. 2-8: NEAR FIELD AMPLITUDE OF A COMPLEMENTARY HELICAL ANTENNA WITH DIELECTRIC LOADING.

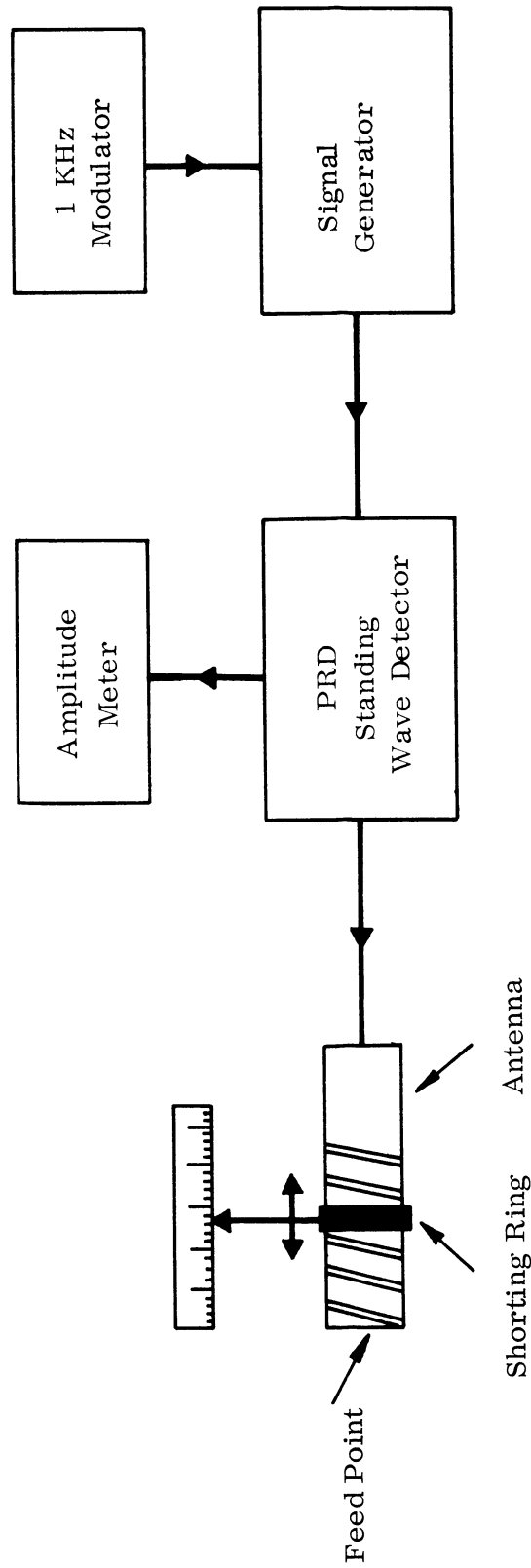


FIG. 2-9: ARRANGEMENT FOR PHASE VELOCITY MEASUREMENT.

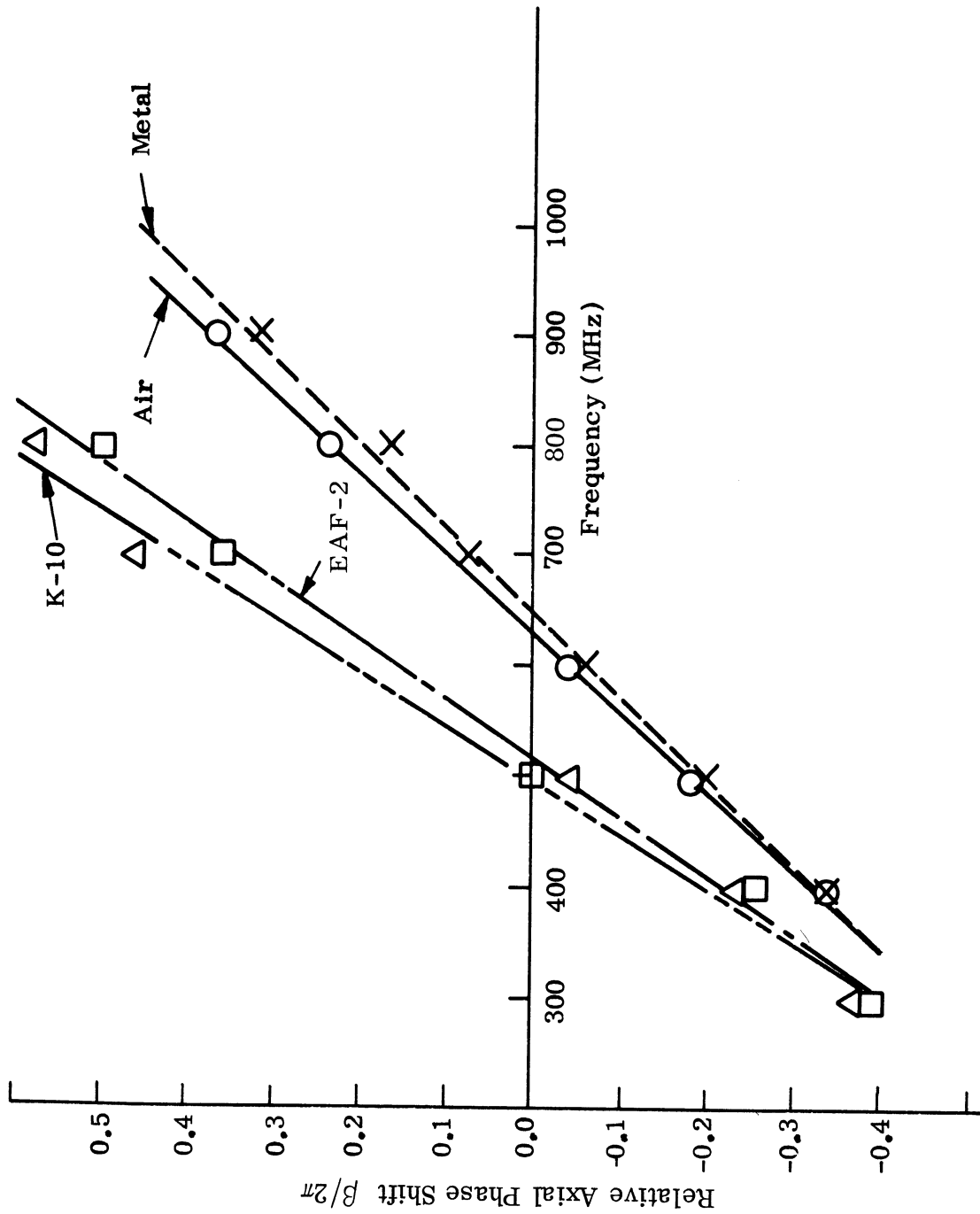


FIG. 2-10: AXIAL PHASE SHIFT OF A COMPLEMENTARY HELICAL ANTENNA WITH VARIOUS LOADINGS.

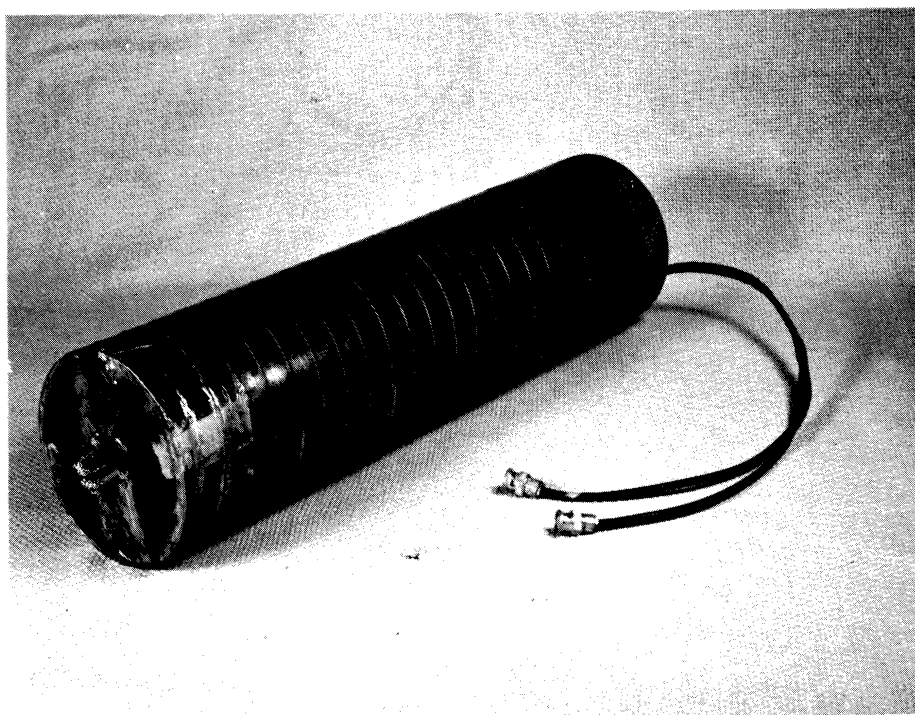


FIG. 2-11: A BIFILAR COMPLEMENTARY HELICAL ANTENNA

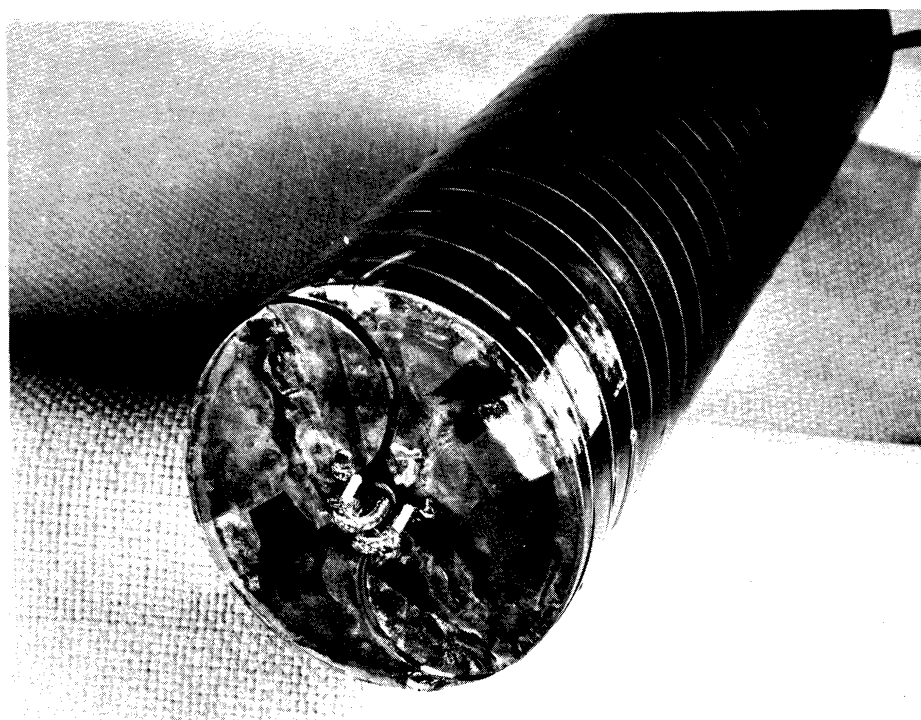


FIG. 2-12: A BALANCED FEED OF THE ANTENNA

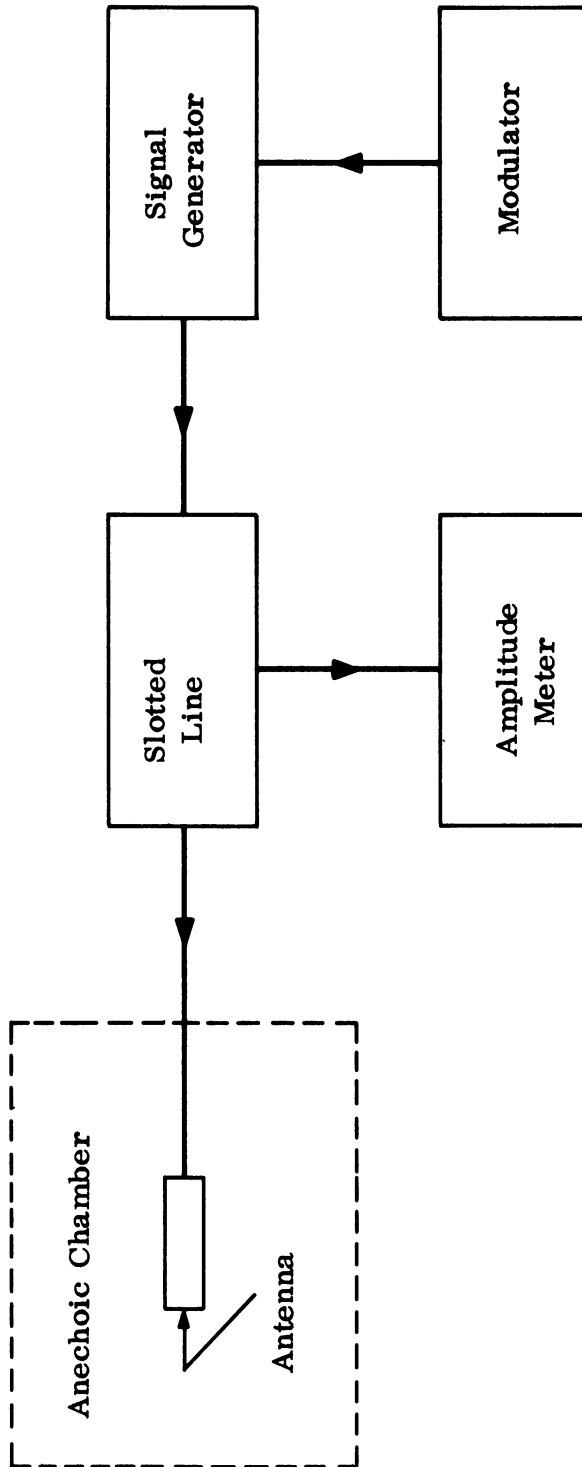


FIG. 2-13: THE EXPERIMENTAL SET-UP FOR THE IMPEDANCE MEASUREMENT

THE UNIVERSITY OF MICHIGAN  
7848-1-F

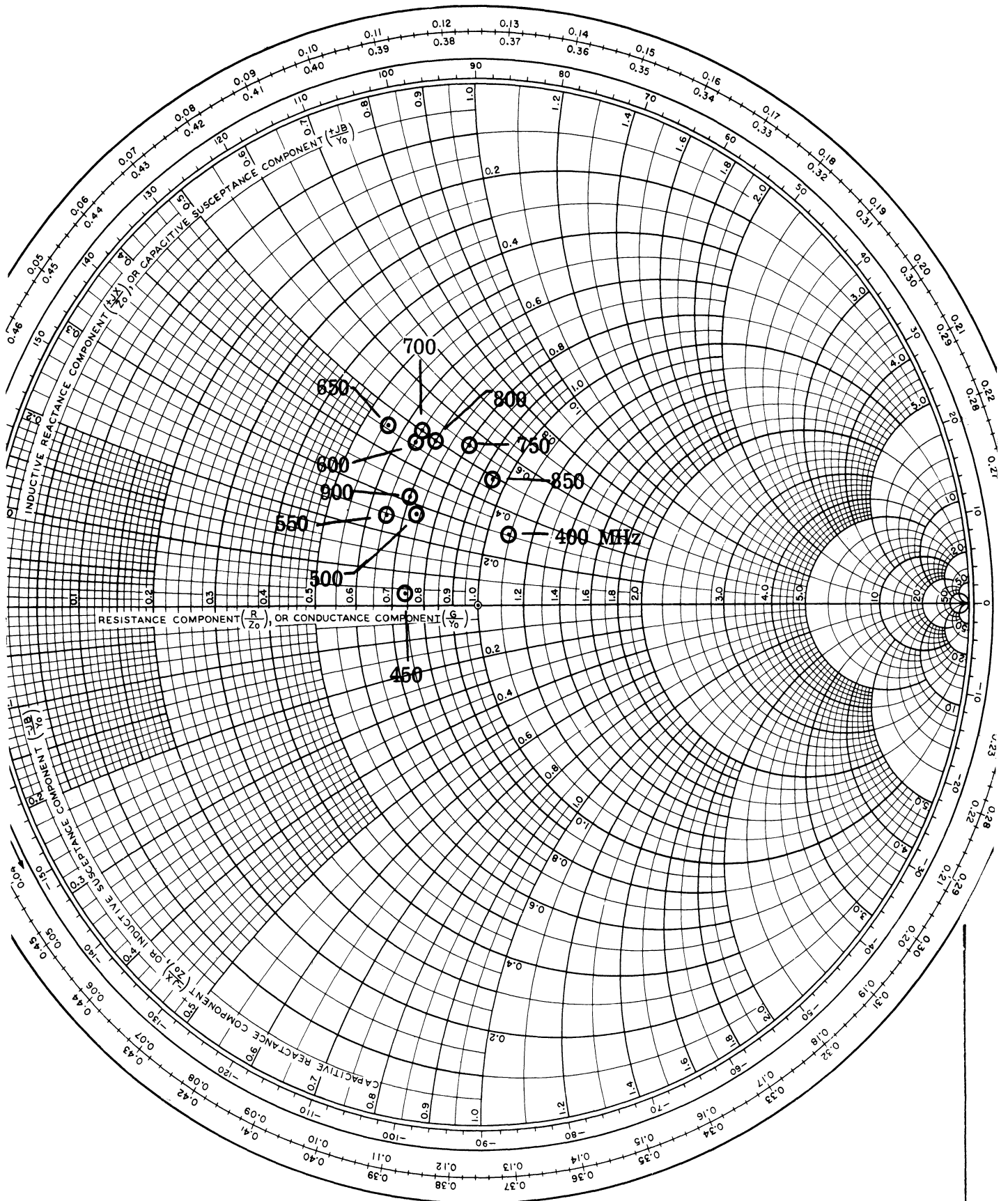


FIG. 2-14: UNLOADED COMPLEMENTARY HELIX ANTENNA

it is seen that the impedance stays fairly constant over the frequency range. The bandwidth determined from the far field and near field patterns is from 600 to 900 MHz. The variation of the input impedance in this range is 28 to 47.5  $\Omega$  for the real part and j 15 to j 28  $\Omega$  for the imaginary part. It is interesting to note that the input reactance is inductive within the frequency range. As will be discussed later, this property has a very interesting result when the antenna is loaded with a dielectric or a ferrite material.

The input impedance for a K-10 dielectric loaded antenna is shown in Fig. 2-15. The general pattern is not changed significantly, due to the fact that the antenna is inductive within the frequency range. The loading of the dielectric material will move the frequency range (determined by the near and the far field pattern) down but the input impedance does not seem to be affected much except for some marginal frequencies. However, the input impedance of the antenna is affected by a ferrite loading precisely for the same reason; that is, the inductive nature of the antenna is further affected by the ferrite loading. The input impedance seems to cluster and thus becomes less dependent on the frequency. This is shown in Fig. 2-16 where EAF-2 ferrite was placed inside the antenna. The trend of less frequency dependence of the input impedance due to a ferrite loading is further evidenced by Fig. 2-17 where Q-3 ferrite was used; Q-3 has a much higher relative permeability. The input impedance seems to converge toward 38 + j 15  $\Omega$  with a small variation as the frequency is changed (31 to 42  $\Omega$  for the real part and j 10 to j 22  $\Omega$  for the imaginary part over the frequency range; 400 - 900 MHz). A metal loaded helix was also measured; the effect is not very significant (Fig. 2-18).

From the above observations it can be said that the input impedance of a bifilar complementary helical antenna is affected by the loading materials in a very interesting way. Since the antenna is inductive over the frequency range, the loading of the dielectric material is not as effective as the ferrite material. It is also noted that the input resistance of the antenna is very low compared to that of the wire helix antenna, as it should be, corresponding to the usual reciprocal relationship of impedances of two complementary antennas. It can be observed from Fig. 2-19 that



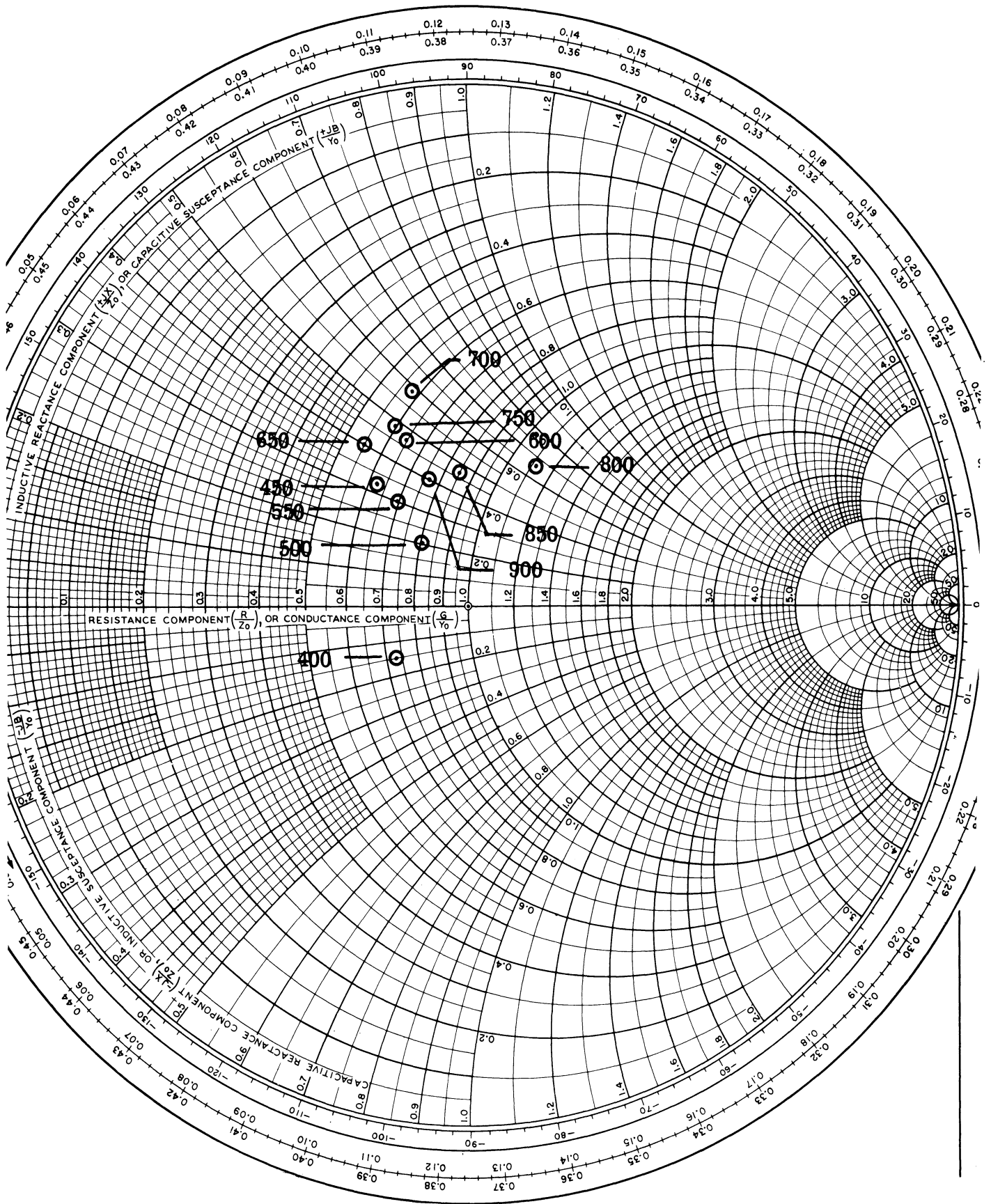


FIG. 2-15: K-10 LOADED COMPLEMENTARY HELIX ANTENNA

THE UNIVERSITY OF MICHIGAN  
7848-1-F

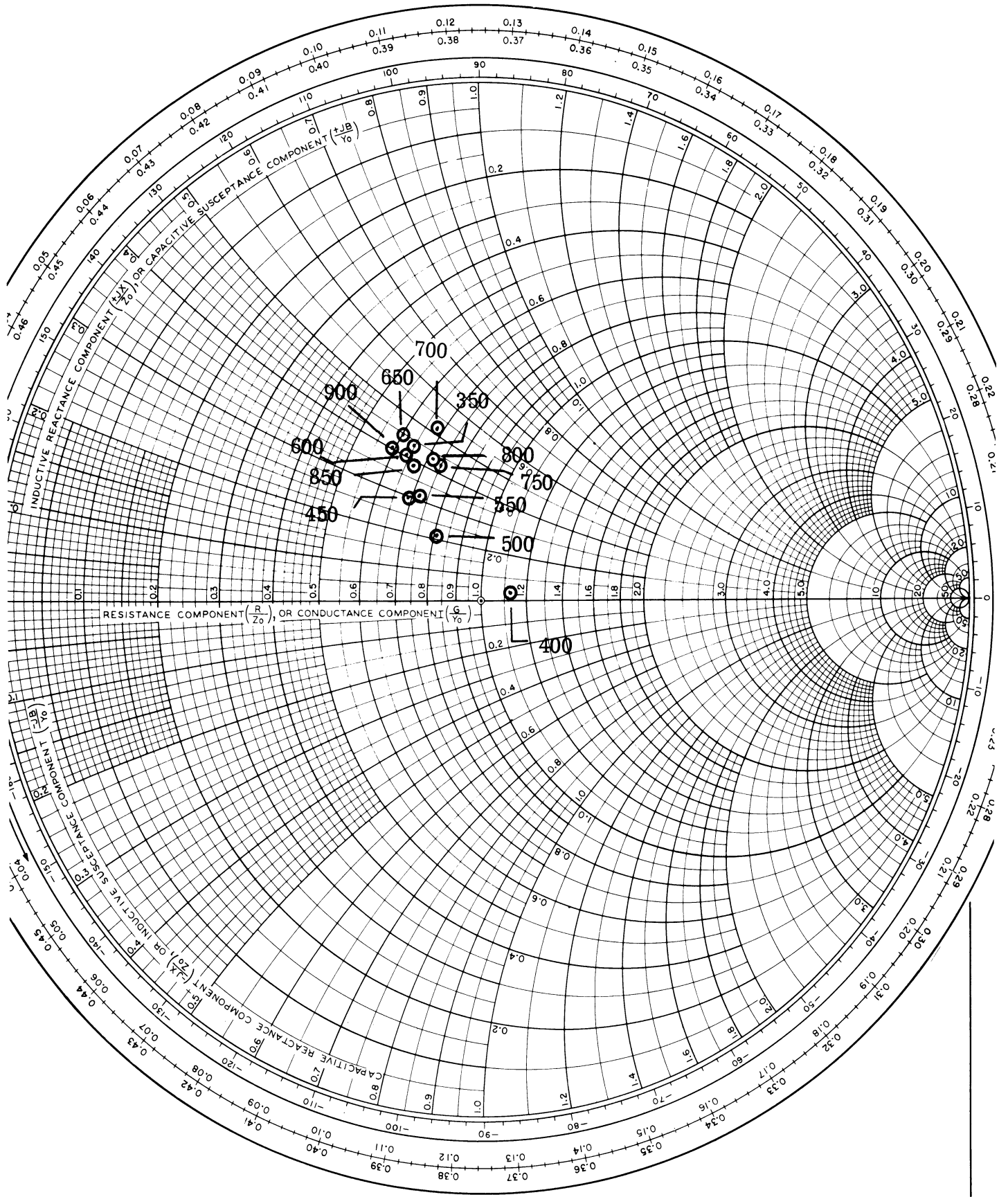


FIG. 2-16; EAF-2 LOADED COMPLEMENTARY HELIX ANTENNA

THE UNIVERSITY OF MICHIGAN  
7848-1-F

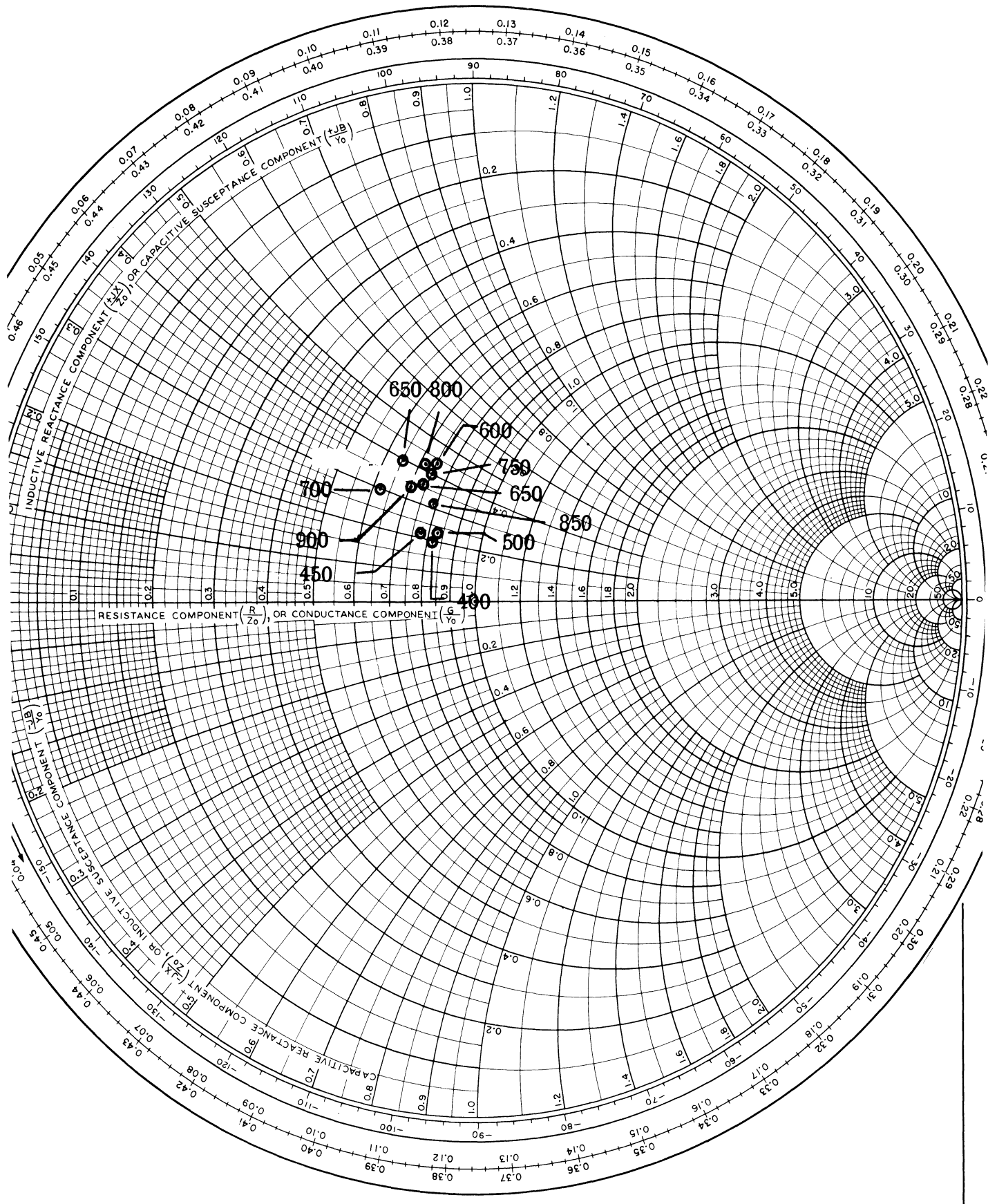


FIG. 2-17: Q-3 LOADED COMPLEMENTARY HELIX ANTENNA

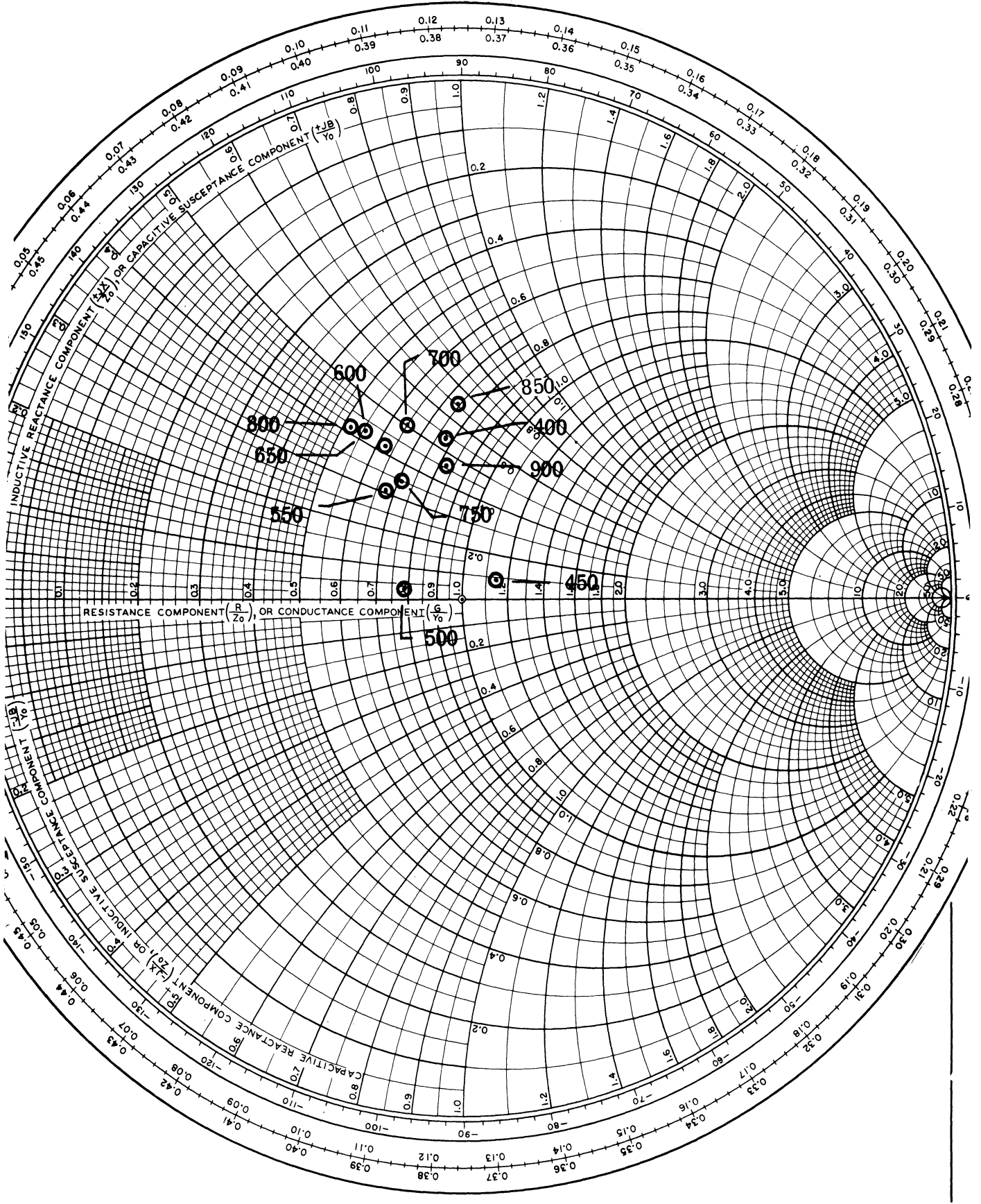


FIG. 2-18: METAL LOADED COMPLEMENTARY HELIX ANTENNA

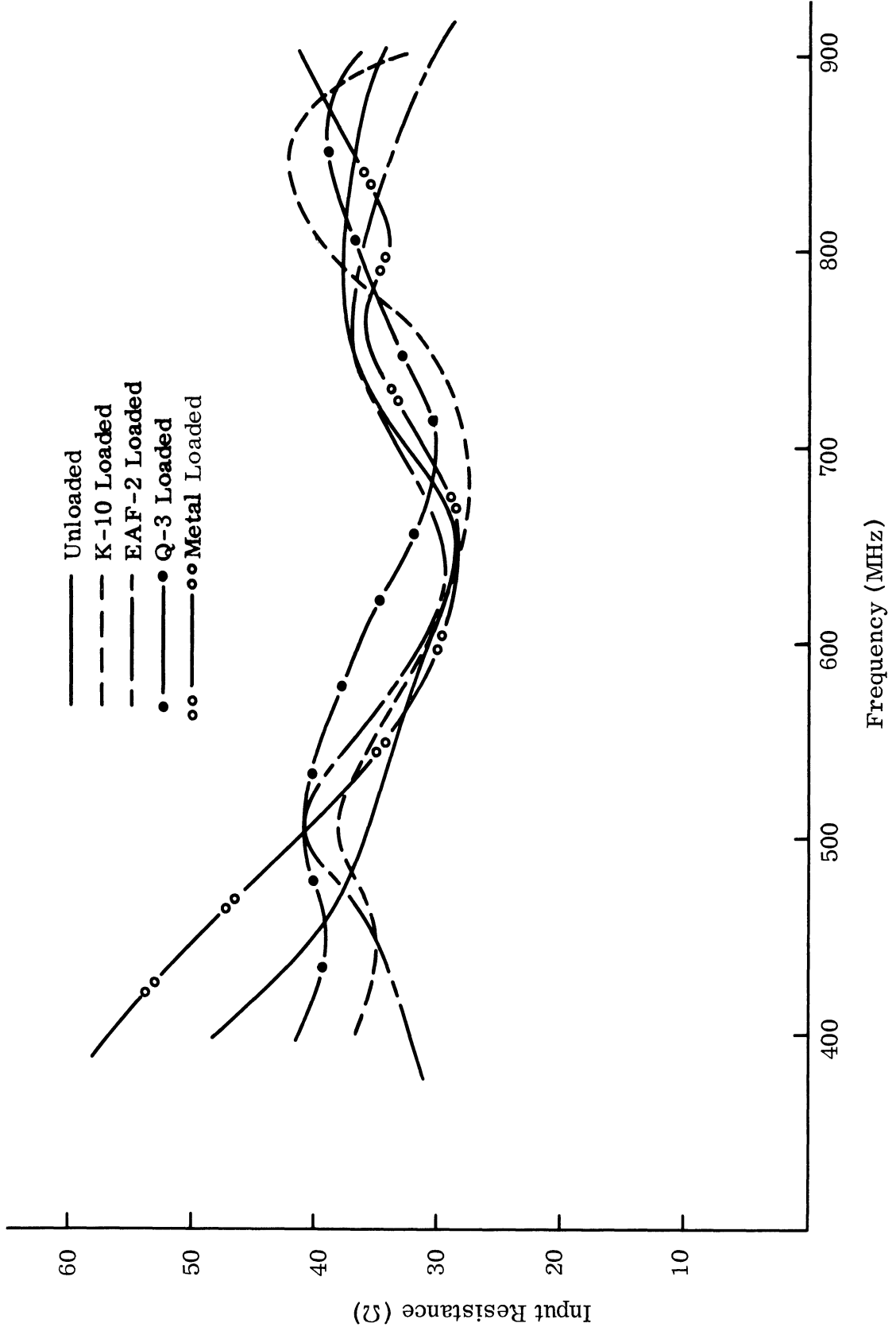


FIG. 2-19: THE INPUT RESISTANCES FOR VARIOUS LOADING MATERIALS

the most efficient radiation takes place around 650 MHz for all cases . This seems to imply that the input resistance of the antenna is not affected by the loading materials quite as much as the resonant frequency except at the marginal frequencies where the effect seems to be a little greater.

## 2.6 Ferrite Coated Windings

Because of the construction difficulties associated with incorporating the Radiation Laboratory's supply of ferrites into a ferrite coated winding, a simple theoretical analysis of the problem was done. It indicated that a size reduction multiplicative factor of less than 0.50 can be obtained under favorable conditions. However, this alone would not be sufficient to obtain the 0.365 reduction factor needed to build a conical helix covering 200 - 600 MHz with the above dimensions.

The analysis is based on an observation as reported by Rassweiler (1966) who considers a helix or conical helix antennas as a two-wire transmission line wrapped around a cone. Judging from his work it appears that this is a fair approximation for the loading effects of ferrite around each antenna wire. Of course, for the two-wire transmission line model to be realistic, the ferrite coating of the wires cannot be too thick; otherwise, the coating is really closer to a layer of ferrite covering the surface of the windings.

Using a conventional approach to determine the capacitance and inductance per unit length of the two-wire transmission line cross section depicted in Fig. 2-20, (e. g. , Johnson, 1950, p. 82), it can readily be shown that the inductance per unit length  $L$  and the capacitance per unit length  $C$  are given by the expressions

$$C \approx \frac{\pi}{\frac{1}{\epsilon} \ln \frac{t}{d} + \frac{1}{\epsilon_0} \ln \frac{2D}{t}} \quad \text{and} \quad L \approx \frac{\mu}{\pi} \ln \frac{t}{d} + \frac{\mu_0}{\pi} \ln \frac{2D}{t} . \quad (2.2)$$

Thus, it follows that the phase velocity (and group velocity, since the medium is assumed non-dispersive and the transmission line is assumed to be lossless) is given by the expression:

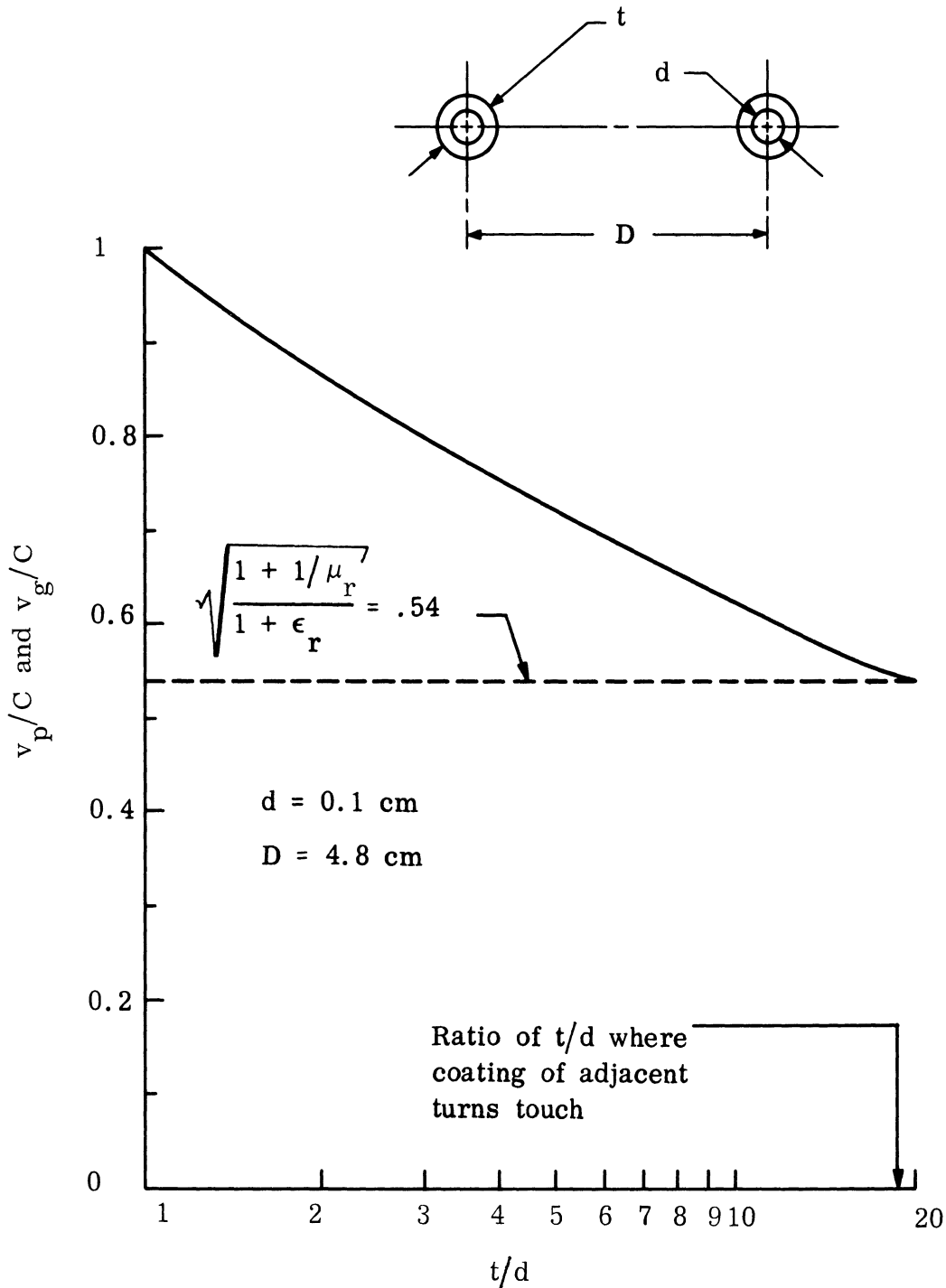


FIG. 2-20: PLOT OF THE REDUCTION FACTOR ( $v_p/C$ ) VS.  $t/d$  FOR A TWO WIRE TRANSMISSION LINE LOADED WITH EAF-2 FERRITE ( $\mu_r = 2.2$ ,  $\epsilon_r = 3.8$ ).

$$v_p = v_g = c \sqrt{\frac{\frac{1}{\epsilon_r} \ln \frac{t}{d} + \ln \frac{2D}{t}}{\mu_r \ln \frac{t}{d} + \ln \frac{2D}{t}}} \quad (2.3)$$

The above formula (2.3) indicated a very interesting property of ferrite coating. For small  $t/d$  ratios, most of the reduction is produced by the relative permeability. The relative dielectric constant provides a greater influence at large  $t/d$  ratios.

This would mean that the coating would have to be tightly bound to the conductor. If there were a small gap between the coating and the conductor, the effectiveness of the coating would be greatly reduced.

Let us now look at two cases of a ferrite coating on the winding of a helix antenna. The first is illustrated in Fig. 2-20. In this case, the ferrite is assumed to be powdered EAF-2. The dimensions used correspond to a 4.8 cm dia., bifilar,  $14^\circ$  helix wound with No. 18 copper wire. The diameter corresponds to that needed at 600 MHz for a helix to radiate in the axial mode assuming a 0.365 reduction factor. (This reduction factor corresponds to the reduction needed to obtain a conical helix fitting the dimensions described in the technical guidelines.) The object of assuming the reduction factor was to see if, indeed, the reduction was possible with a thin coating of this ferrite.

Notice that the dashed line in Fig. 2-20 corresponds to the reduction factor expected with EAF-2 ferrite if the core of the helix were completely filled with the material. Note also the marking that indicates the ferrite diameter to wire diameter ratio that corresponds to the touching of the ferrite coating of successive turns. It is interesting to note that if the antenna were buried in a medium consisting of nothing but EAF-2, the reduction factor should be 0.346.

The second case consists of a coating of Indiana General Q-3 Ferrite. (see Fig. 2-21). The dimensions used correspond to a 14.4 cm dia.,  $14^\circ$ , bifilar helix wound with  $1/4"$  O.D. copper tubing. This particular helix diameter corresponds



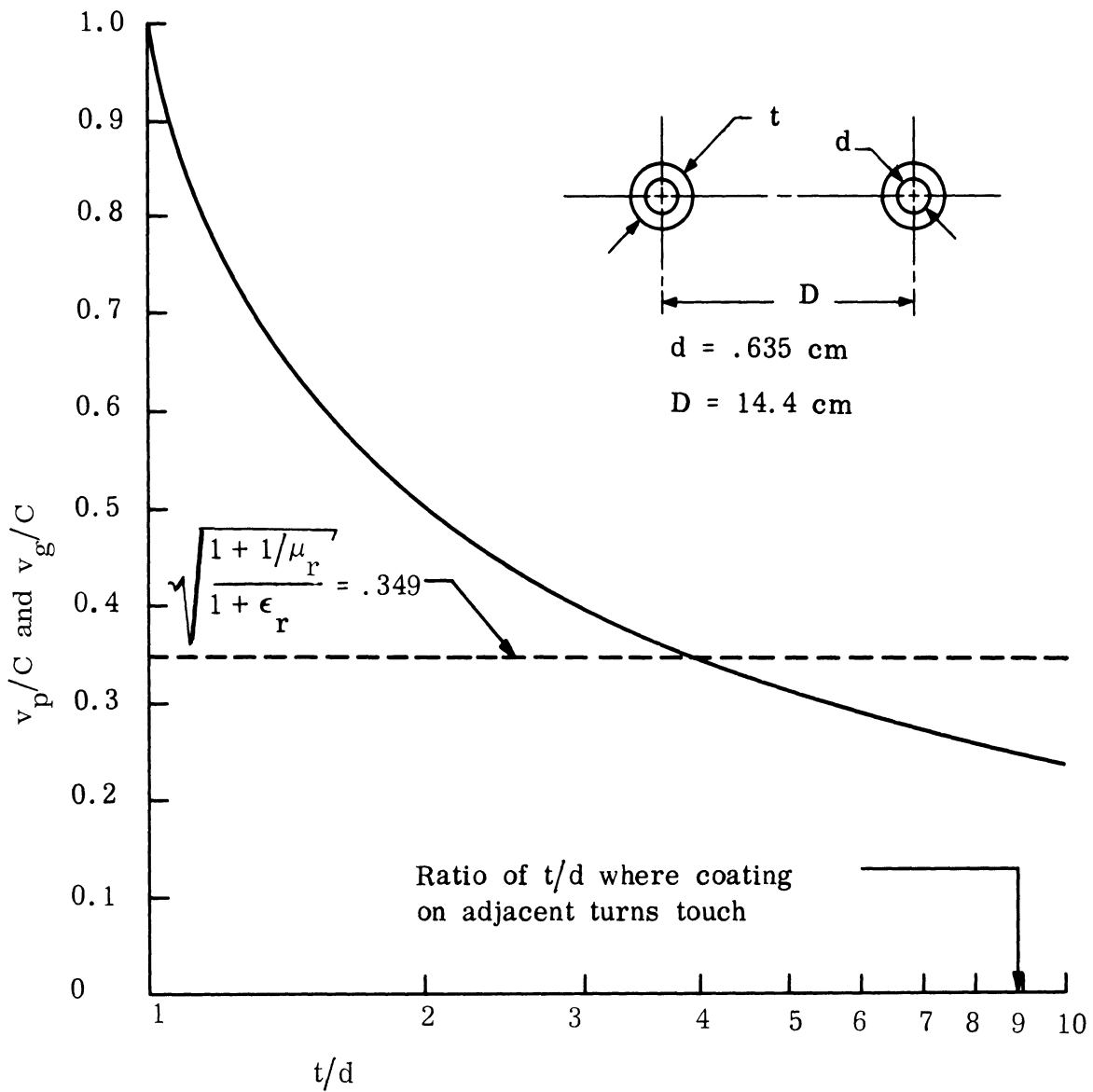


FIG. 2-21: PLOT OF THE REDUCTION FACTOR ( $v_p/C$ ) VS.  $t/d$  FOR A TWO WIRE TRANSMISSION LINE<sup>g</sup> LOADED WITH INDIANA GENERAL Q-3 FERRITE ( $\mu_r = 14$ ,  $\epsilon_r = 7.8$ ).

to that needed for axial radiation at 200 MHz, assuming a 0.365 reduction factor. The reduction factor was assumed in this case for the same reason as in the previous case.

The dashed line in Fig. 2-21 corresponds to the reduction factor obtainable with a full core loading of Q-3. Again the ferrite-to-wire diameter corresponding to the coating of adjacent turns touching is indicated on the graph. If the antenna were buried in a medium consisting entirely of Q-3, the reduction factor should be 0.096.

For the Q-3 example, it appears that a ferrite coating diameter between four and five times the wire diameter should give the desired reduction. However, for thicknesses this great the requirement that  $t/D \ll 1$  is most certainly violated, and, indeed, the reduction factor may not be possible after all.

## 2.7 Ferrite Loaded Coiled Conductor

A helix antenna with a winding consisting of a ferrite filled helical slow wave structure was studied. Tests performed on this antenna indicate that it has good helix antenna patterns from 160 - 210 MHz corresponding approximation to a 4:1 reduction of the diameter of this antenna. The input impedance over this frequency range centers around  $400 - j200 \Omega$ . However, the gain measurements indicate that the antenna is very lossy. Current distribution measurements indicate that a standing wave current distribution exists on the antenna instead of a traveling wave distribution attenuating rapidly from the tip as occurs for the conventional unloaded backward-fire helix antenna current. Thus, the helix antenna wound with a ferrite filled helical slow wave structure is a reduced size helix antenna of rather low efficiency. A higher magnetic Q of the ferrite filling could considerably improve the efficiency.

It is well known that a helix is a slow wave structure. It would seem that if a helical antenna were wound with a small coiled conductor, then the size of the antenna wound with such a coiled conductor could be reduced. This experiment has been tried by several workers, but unfortunately, no one has been completely satisfied with the results (Turner, 1966). The device acts as an antenna and appears to radiate quite well. However, the far field patterns do not resemble those of a regular helical antenna. Apparently, the interaction of a turn with other turns produces unusual results.

THE UNIVERSITY OF MICHIGAN  
7848-1-F

Since a magneto-dielectric material has a confining effect on electromagnetic fields, it was hoped that if the interior of a coiled conductor were filled with ferrite, the interaction might be reduced enough for the antenna with the coiled conductor to operate successfully.

Figure 2-22 shows a bifilar helix constructed for this experiment. The coiled conductor is wound on a  $3/4''$  O.D x  $3/32''$  thick piece of Tygon tubing using No. 20 enameled copper wire with a pitch of  $1/3''$ . This coiled conductor should give a slowing factor of about 0.25 based on the data presented by Okubo (1965). The antenna itself has a pitch of  $4''$ . The antenna winding proper is wound on a  $3\ 1/8''$  O.D. by  $1/16''$  thick piece of NEMA Grade XXX paper phenolic tubing. The antenna is fed at the tip through a two-wire shielded transmission line from a hybrid.

Figure 2-23 shows the far field patterns for this antenna. The center frequency of operation, if the antenna were wound with a simple wire on a cylindrical form of the same mean diameter as the antenna, would be about 800 MHz.

Unfortunately, the plastic tubing used to construct the coiled conductor started to decompose before the antenna could be loaded with ferrite. Rather than risk contaminating the irreplaceable EAF-2 ferrite, a second antenna, identical to the first was constructed. Figure 2-24 depicts the antenna with the windings filled with EAF-2 powdered ferrite. Figure 2-25 shows a cross section of the antenna and gives the dimensions.

Using the largest diametral dimension of the antenna ( $4\ 5/8''$ ) and the approximate formula that the center frequency of operation occurs when the circumference is approximately a wavelength, then the size of this antenna would correspond to a conventional helix operating at 800 MHz. This is the reference frequency used in the reduction figures given later on.

The far field radiation patterns between 160 - 210 MHz for Antenna 232 were very close to those observed for a conventional helix antenna, as is indicated in Fig. 2-26. Using the arithmetic average of 160 and 210, or 185 as the center frequency of operation, this would indicate a multiplicative size reduction factor of 0.231. Based on the center frequency of 185 MHz, the bandwidth of operation of

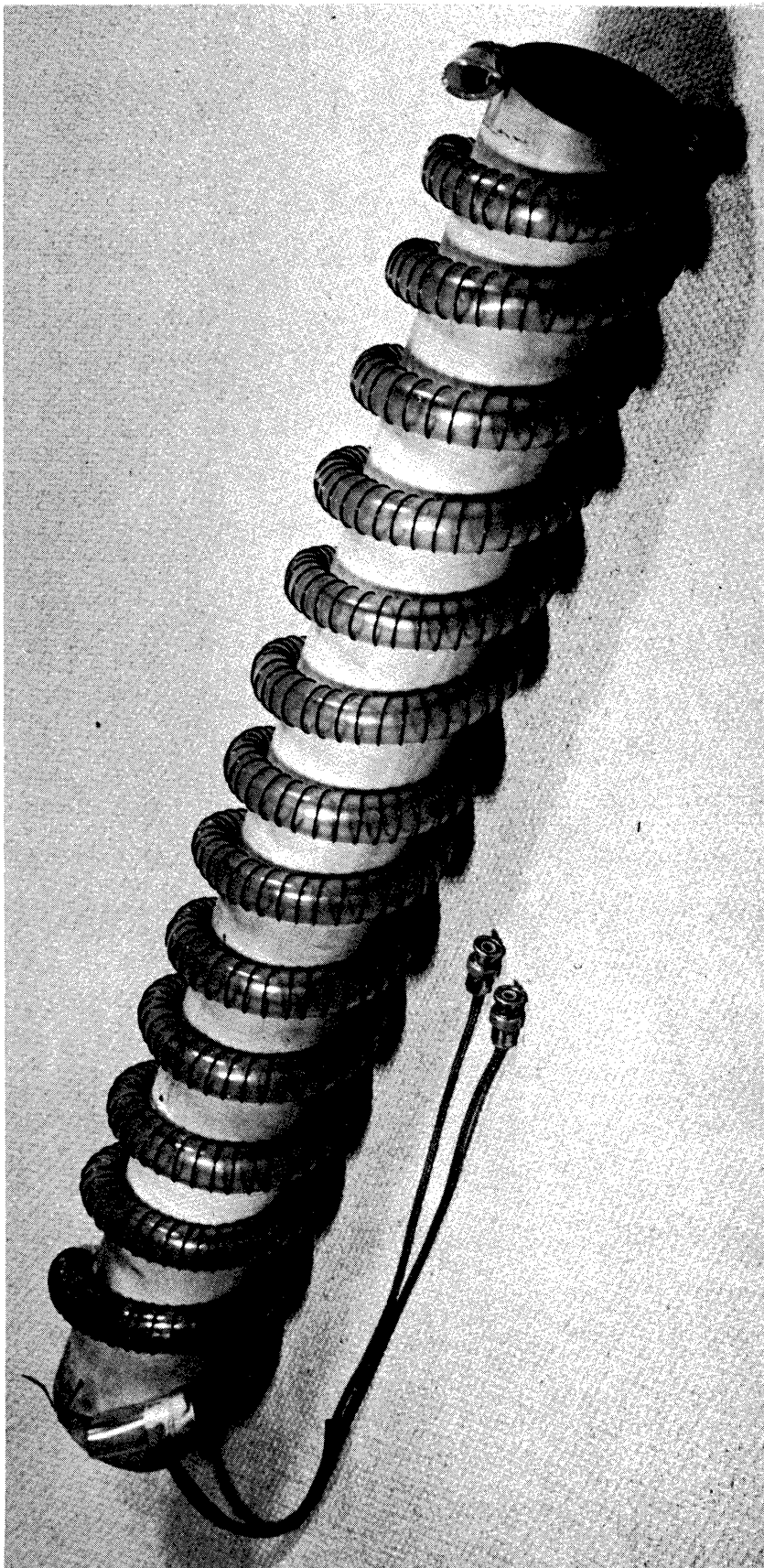


FIG. 2-22: ANTENNA 228, A  $14^\circ$  BIFILAR HELIX WITH A HELICAL WINDING.

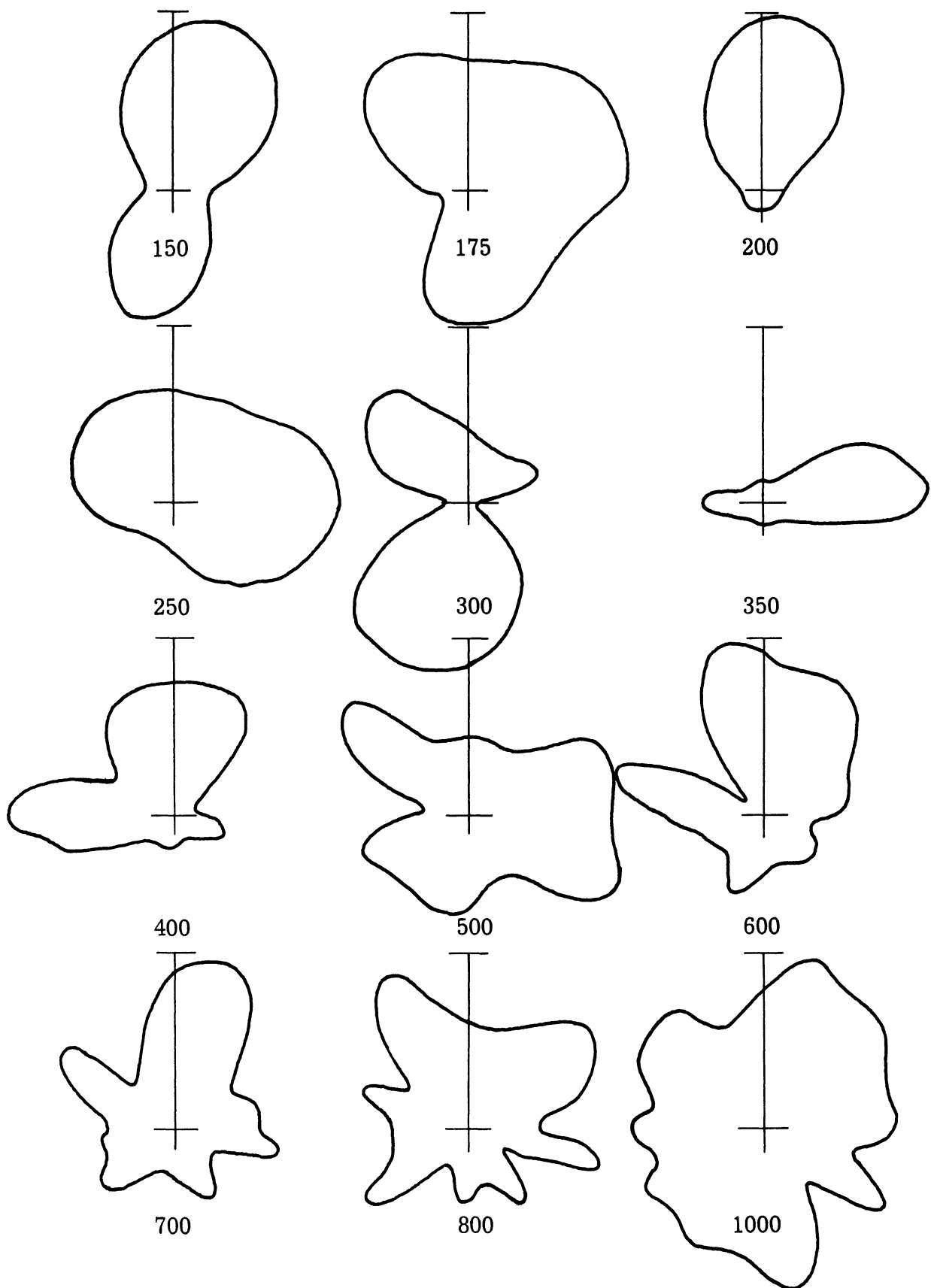


FIG. 2-23: FAR FIELD POWER PATTERNS OF ANTENNA 228,  
A BIFILAR  $14^\circ$  HELIX WITH A HELICAL WINDING.



FIG. 2-24; ANTENNA 232; A BIFILAR HELIX ANTENNA WITH A HELIX SLOW WAVE  
STRUCTURE WINDING FILLED WITH EAF-2 POWDERED FERRITE.

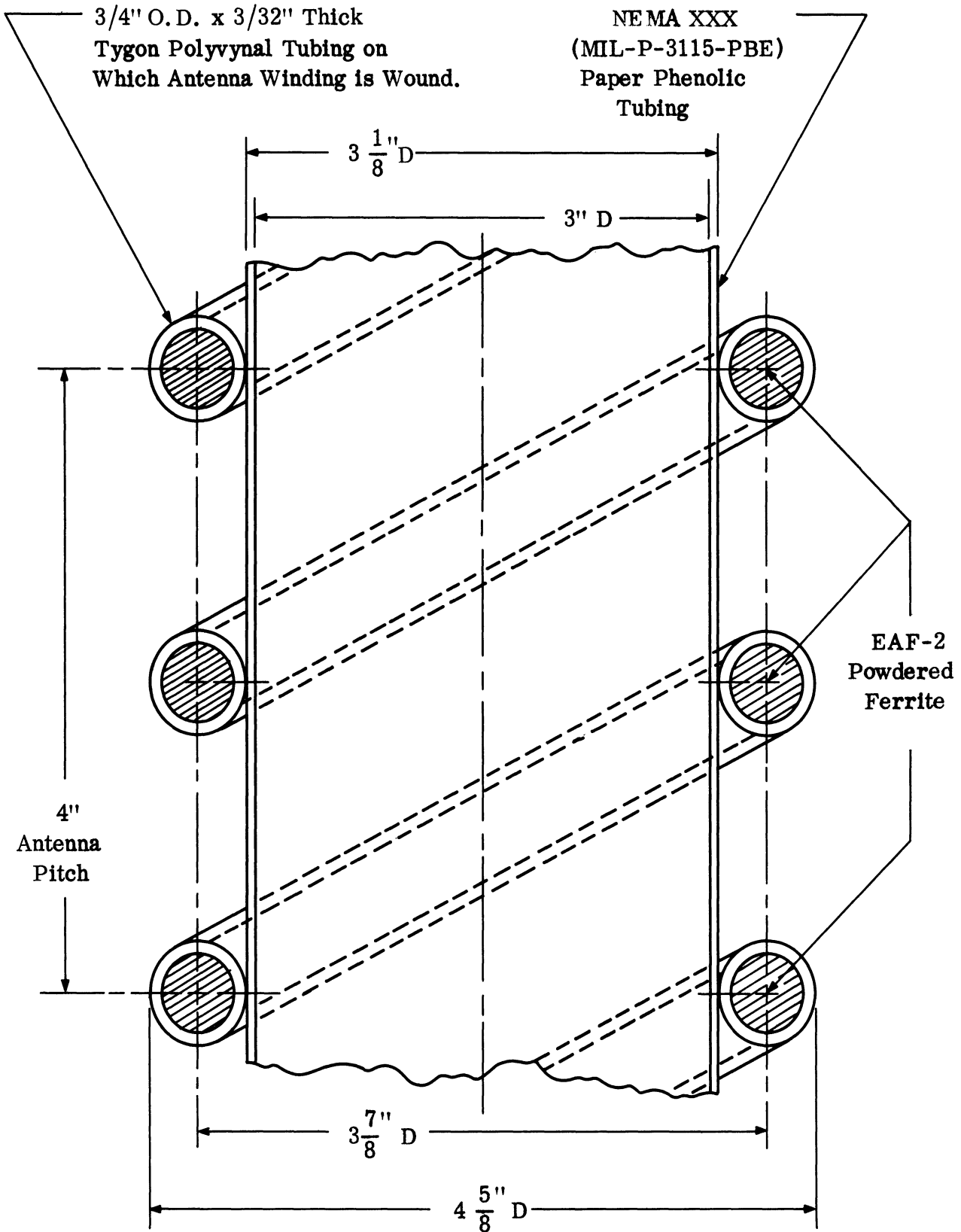


FIG. 2-25: LONGITUDINAL CROSS-SECTION DRAWING OF ANTENNA 232 WITH THE WINDING HELIX FILLED WITH EAF-2 FERRITE POWDER SHOWING ALL PERTINENT DIMENSIONS.

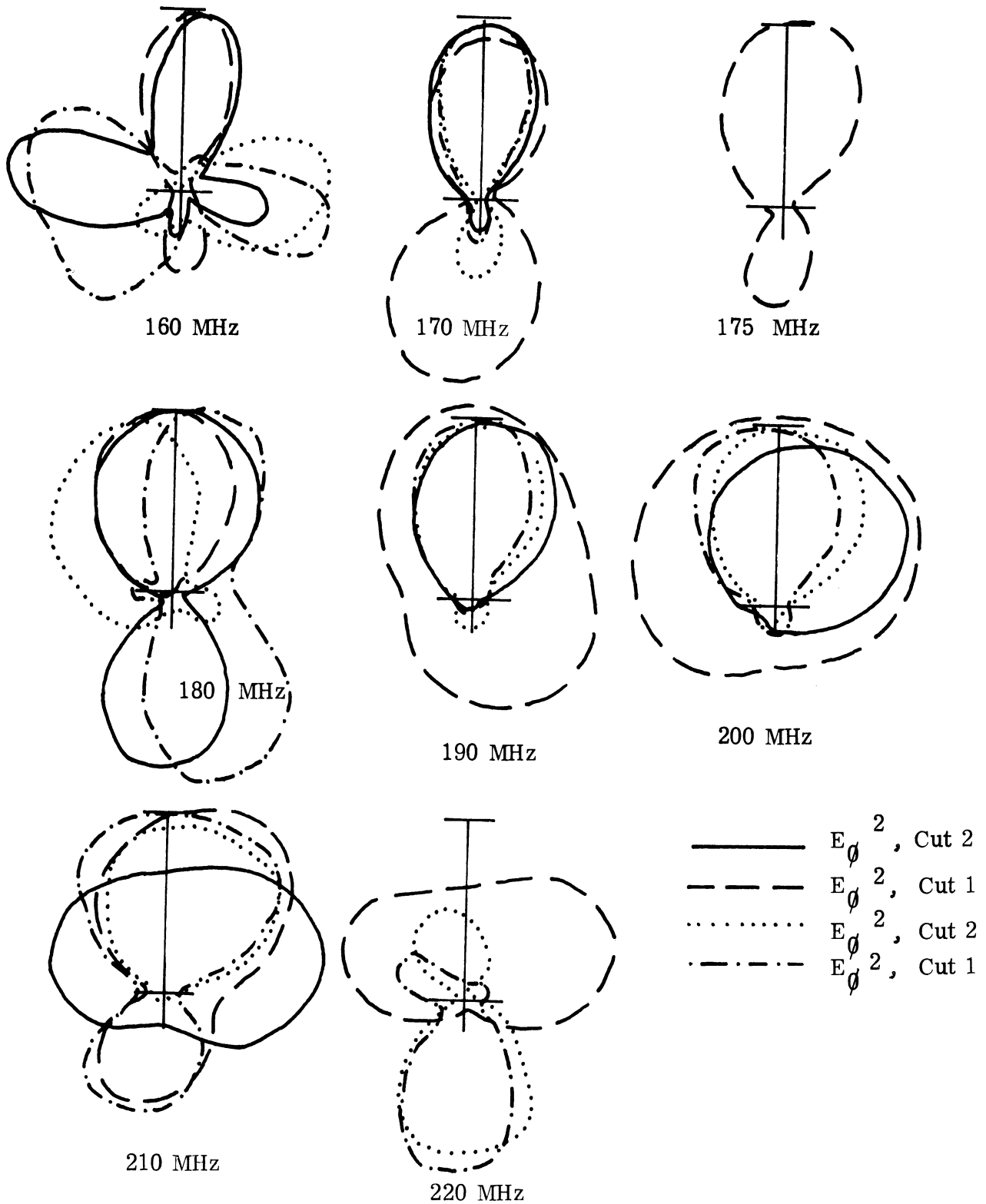


FIG. 2-26: LINEAR POWER RADIATION PATTERNS OF ANTENNA 232, A BIFILAR HELIX WITH A EAF-2 POWDER FERRITE FILLED HELICAL WINDING. CUT 1 IS IN THE PLANE OF THE FEED, CUT 2 IS PERPENDICULAR TO CUT 1.



THE UNIVERSITY OF MICHIGAN  
7848-1-F

Antenna 232 is 27 percent. This compares with a value of 50 percent frequently claimed for a conventional helix antenna.

According to Li and Beam (1957) the slowing factor for the coiled winding used on Antenna 232 is 0.28. Thus, the patterns are consistent with what is known about the problem.

A Smith Chart of the input impedance is illustrated in Fig. 2-27. The impedance was measured with a Hewlett-Packard Vector Voltmeter. Corrections were made in the data for the phase shift caused by the reference in the Vector Voltmeter arrangement not being at the tip of the antenna. No corrections were made for the attenuation of the cable between the reference and the antenna. The resultant inaccuracy in the magnitude of the reflection should be very small since the cable loss was less than 0.4 db.

Notice that the input impedance of Antenna 232 is higher than for a conventional helix. This would be expected from the transmission line analogy used to describe some of the properties of a helix antenna, since the coiled conductor is an inductive loading (see Section 2.8).

The results of the gain measurements on the antenna were not very encouraging. The gain was -12.3 db at 170 MHz and -4.2 db at 190 MHz with respect to an isotropic source. A summary of the calculations are given in Appendix A. The loss in the RG-58/U coaxial cable (2 feet) was not used to correct the measured reflection coefficient. At frequencies from 170 to 190 MHz this loss is insignificant.

The polarization ratio was measured at 170 MHz and was 4.5 db; at 190 MHz it was 2.5 db. In both cases, the range of error is  $\pm 1$  db.

In these last two sets of measurements, the polarization ratio could have been adversely affected by the antenna being only four feet above a metal turret. This is 0.68 of a wavelength at 170 MHz and could have contributed to a slight degradation in the value of the polarization ratio measured. The measured values were not, however, at all unusual for conventional helix antennas. Since the construction of the antenna was not very precise, irregularities may have been the cause of the ellipticity of the polarization.

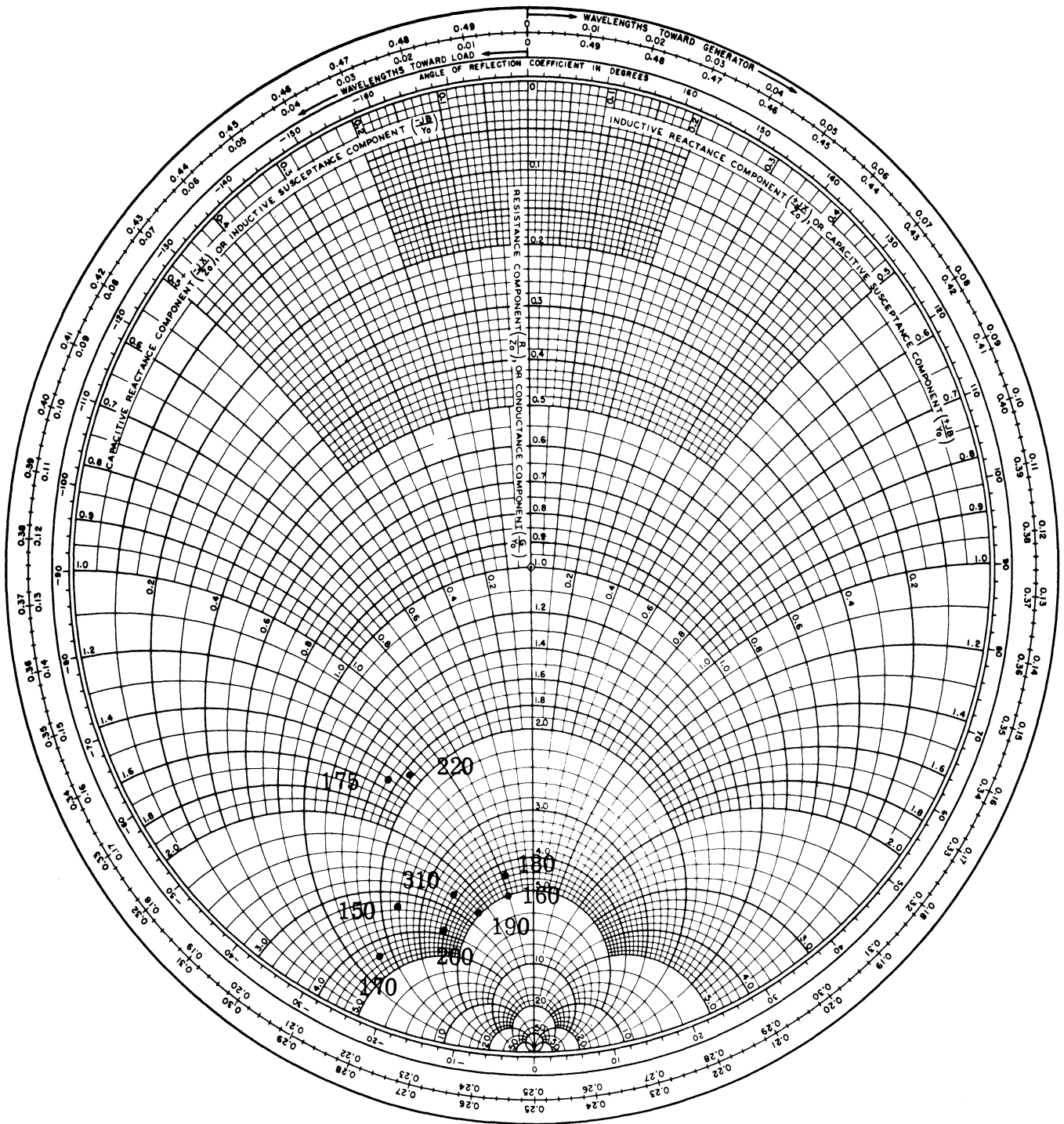


FIG. 2-27: VSWR WITH RESPECT TO 100 Ω FOR ANTENNA 232 WITH THE WINDING FILLED WITH POWDERED EAF-2 FERRITE.

One reason for the low efficiency of the antenna is apparent from the measured current distribution on the antenna which indicates a standing wave. Figure 2-28 shows the current distribution on the antenna at 170 MHz and Fig. 2-29 shows the current distribution at 190 MHz. In both cases relative amplitude and relative phase were measured.

A small loop (0.131" dia.) was used to measure the magnetic field at the exterior of the winding as is illustrated in Fig. 2-30. The probe was centered above each winding with the plane of the loop perpendicular to the axis of the antenna as illustrated. A Hewlett-Packard Vector Voltmeter was used to measure the relative phase and amplitude of the voltage induced in the probe; the voltage is, of course, proportional to the current in the winding.

As is seen from Figs. 2-28 and 2-29, a standing wave current distribution exists along the antenna with some loss present which fills in the nulls of the amplitude curve and smooths out the phase curve. The numbers along the abscissa of the plots indicate the locations of the winding at each point of intersection as the probe was moved down the axis of the antenna from the tip to the opposite end. Point 1 corresponds to the tip (feed point) and Point 14 corresponds to the end of the winding.

## 2.8 Discrete Inductance Loading.

If the equations for an ideal transmission line are solved for the inductance per unit length,  $L$ , and capacitance per unit length,  $C$ , in terms of the characteristic impedance,  $Z_0$ , and the phase velocity,  $V_p$ , the following expressions result:  $C = (1/Z_0)V_p$ , and  $L = Z_0/V_p$ . Since a helix or conical helix antenna can be reasonably approximated by a two-wire transmission line having the same wire diameter as the winding of the helix antenna and a wire spacing equal to the diameter of the helix (Rassweiler, 1966) it seems reasonable that if the helix antenna has inductance **inserted in series** with the winding, then the phase velocity of a wave propagating **along the helix** and hence the size of the helix, can be reduced.

It follows that if the antenna size is to be reduced by a factor  $R$  and the capacitance is to remain unchanged, then the inductance per unit length must be changed by  $L/R^2$ , where  $L$  is the original inductance per unit length. In addition,

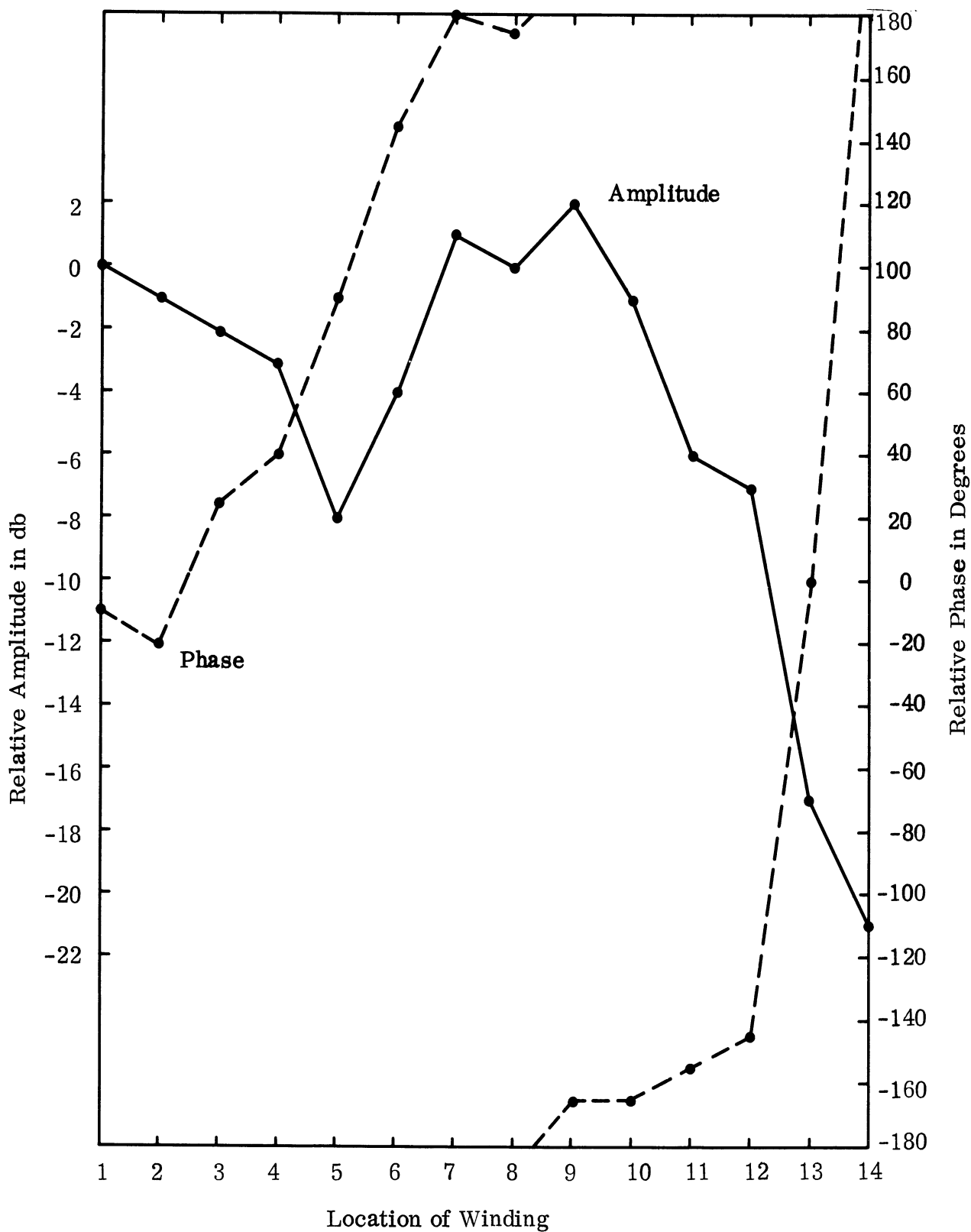


FIG. 2-28: RELATIVE AMPLITUDE AND PHASE OF THE CURRENT ALONG ANTENNA 232 WITH THE WINDING FILLED WITH EAF-2 POWDERED FERRITE AT 170 MHz.

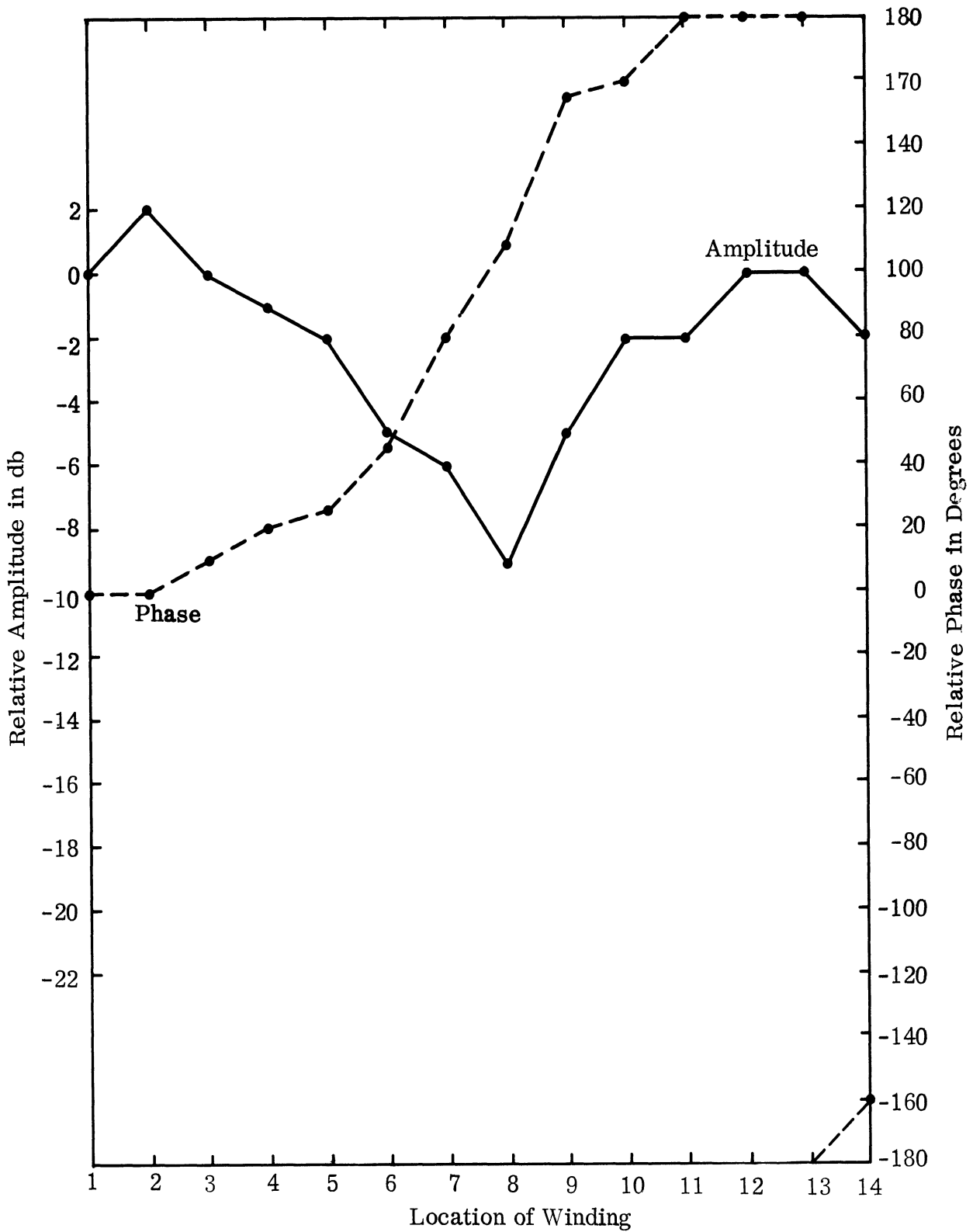


FIG. 2-29: RELATIVE AMPLITUDE AND PHASE OF THE CURRENT ALONG ANTENNA 232 WITH THE WINDING FILLED WITH EAF-2 POWDERED FERRITE AT 190 MHz.



FIG. 2-30: ANTENNA 232, A BIFILAR HELIX ANTENNA WITH A FERRITE FILLED HELICAL WINDING SHOWING THE LOCATION OF THE LOOP PROBE WITH RESPECT TO ANTENNA 232.

THE UNIVERSITY OF MICHIGAN  
7848-1-F

the characteristic impedance will be increased to  $Z_0/R$ . (Note, since  $R$  is the ratio of the lineal dimensions of the loaded to the unloaded antenna,  $R$  is always less than one.)

To check out this theory, a helix antenna was constructed and tested that had additional inductance inserted in series with the winding. The inductances were shorted coaxial transmission line stubs. The object of the experiment was to check out the concept of using inductors made out of shorted sections of coaxial transmission line. If the concept were substantiated, then a ferrite loaded stub would be used. The advantages of ferrite are that smaller stubs could be used for a given inductance and that more stubs could be used per winding, hence making the discrete inductances approximate more closely a distributed inductance.

Unfortunately, due to an error in calculating the inductance needed, the inductances inserted were too small, and the anticipated performance was not realized. However, the experimental results were so favorable that they are reported here in the hope that the antenna may be useful to someone else. A backward-fire pattern is obtained over almost a 3 : 1 band (475 - 1250 MHz), and the VSWR is close to 3 : 1 with respect to a 50  $\Omega$  load over this band, except for a band of 80 MHz centered around 800 MHz. Yet a helix antenna of the same size would have a center of operation around 710 MHz.

The antenna in Fig. 2-31, is a bifilar helix, fed at the tip with a hybrid via a twin lead consisting of two pieces of RG-58/U coaxial cable on the axis of the antenna. The inductances are inserted every quarter turn, and were designed to produce a 4 : 1 reduction in size assuming the diameter of the two wire line model is the diameter of the helix antenna, and that the diameter of the wire of the parallel wire line is that of the winding of the helix. However, the miscalculation altered this relationship.

The formulas used to calculate the inductance needed to accomplish the reduction are restated here:

$$L = Z_0/V_p \qquad L' = L/R$$

where  $R$  is the multiplicative reduction factor (0.25 in this case),  $L$  is the original



-31: ANTENNA 238, A BIFILAR HELIX ANTENNA WITH SHORTED TRANSMISSION INDUCTORS USED AS LOADING.



THE UNIVERSITY OF MICHIGAN  
7848-1-F

inductance per unit length,  $L'$  the new inductance per unit length,  $Z_0$  the characteristic impedance and  $V_p$  the phase velocity.

The antenna was wound on a 4" I.D. x 1/16" thick piece of NEMA Grade XXX (Mil-P-3115-PBE) paper phenolic tubing. The pitch angle of the helix is  $14^\circ$  and there are five turns on the antenna. The winding was cut at the intervals shown in Fig. 2-32. Part of the dielectric and outer shield was removed, and one end of the remaining part of the shield was soldered to the center conductor to produce the inductor.

A helix antenna of this size would have a center frequency of operation of about 710 MHz as can readily be calculated from Fig. 8-20 (p. 333) of Walter (1965). The antenna described there, however, was designed to have a center frequency of operation of 227 MHz, since 910 MHz was assumed to be the unloaded center frequency.

The radiation patterns taken measuring  $|E_\theta|^2$  on the  $\phi=0$  cut as in Fig. 2-33 show the usual backward-fire radiation patterns, (low backlobe and sidelobes, a well-developed main lobe) from 475 - 760 MHz and from 840 - 1250 MHz as can be seen in Fig. 2-34: This gives geometrical mean center frequencies of operation of 600 and 1025 MHz respectively, with corresponding bandwidths of 79 and 67 percent.

Between 760 and 840 MHz, the signal amplitude was so small that it was difficult to record patterns. Those that could be recorded were not satisfactory backward-fire helix patterns.

The VSWR of the antenna was measured with respect to the input port of the hybrid used to feed the antenna with swept frequency equipment as is indicated in Fig. 2-35. In the lower band, the VSWR was centered around 2.5 with respect to  $100 \Omega$  and the variation from this was within  $\pm 0.5$  over most of the band. In the high band, the VSWR centered around 3.0 and the variation from this was less than  $\pm 0.5$  over most of the band. At about 790 MHz the reflection coefficient was almost 1.0. A check of the design indicated that at this frequency, the coaxial stub should be about one-quarter wavelength long, and hence the winding should be effectively open-circuited.

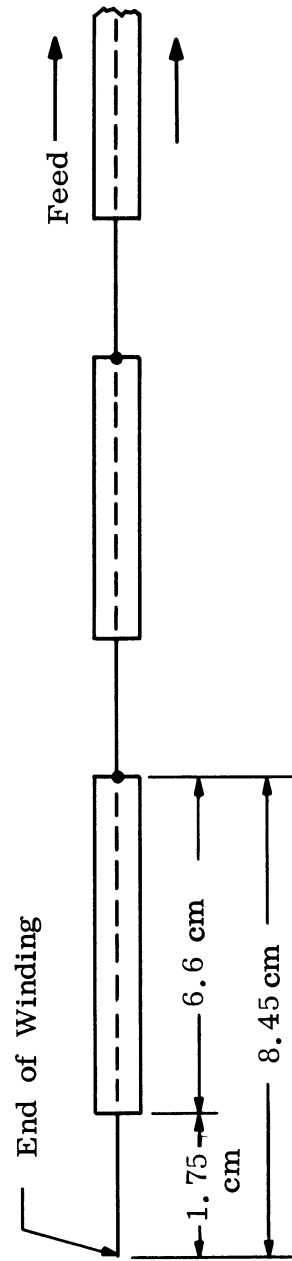


FIG. 2-32: DIMENSIONS OF INDUCTANCES OF INDUCTANCE LOADED ANTENNA.

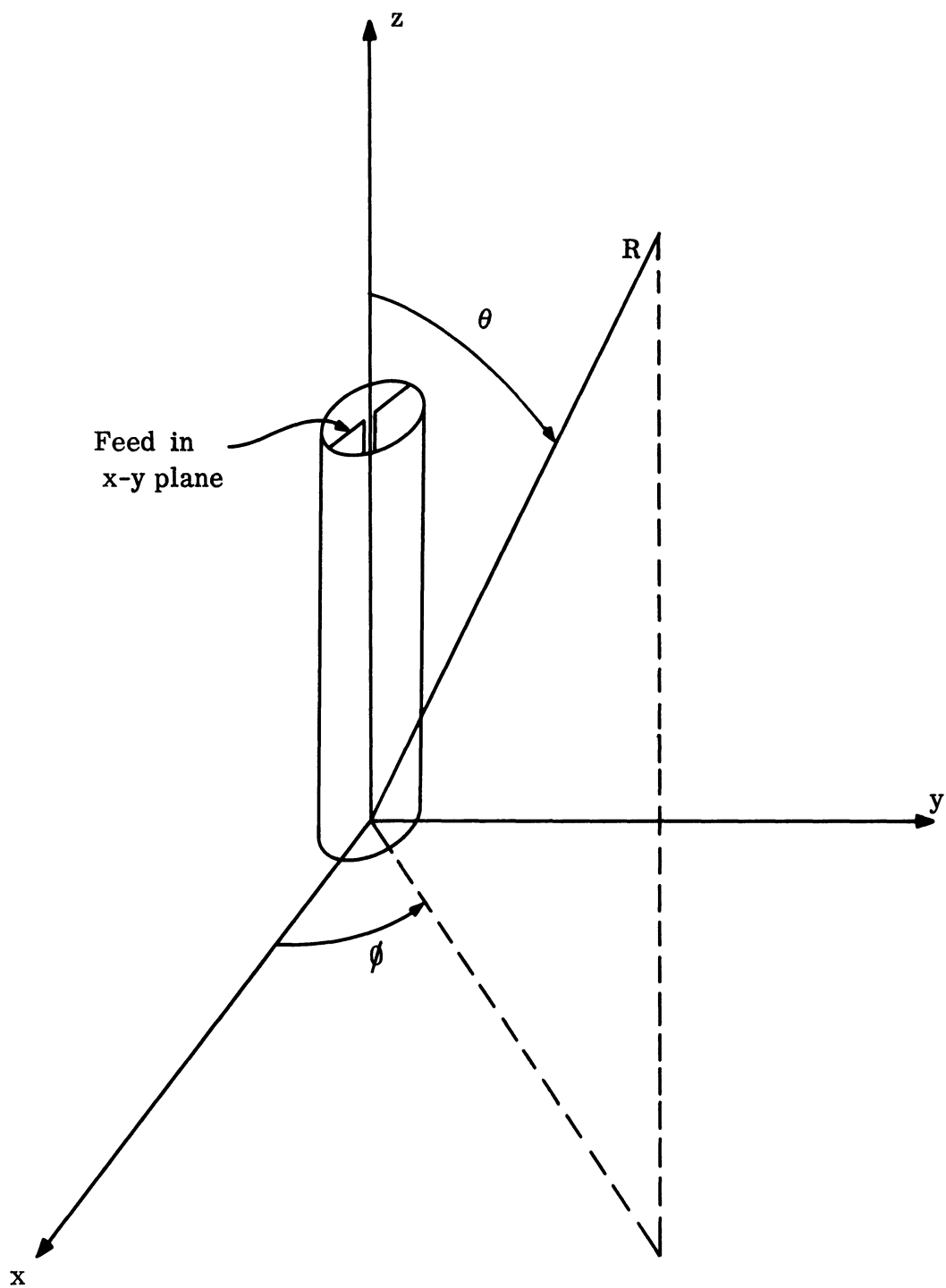


FIG. 2-33: COORDINATE SYSTEM ASSUMED FOR THE HELIX ANTENNA.

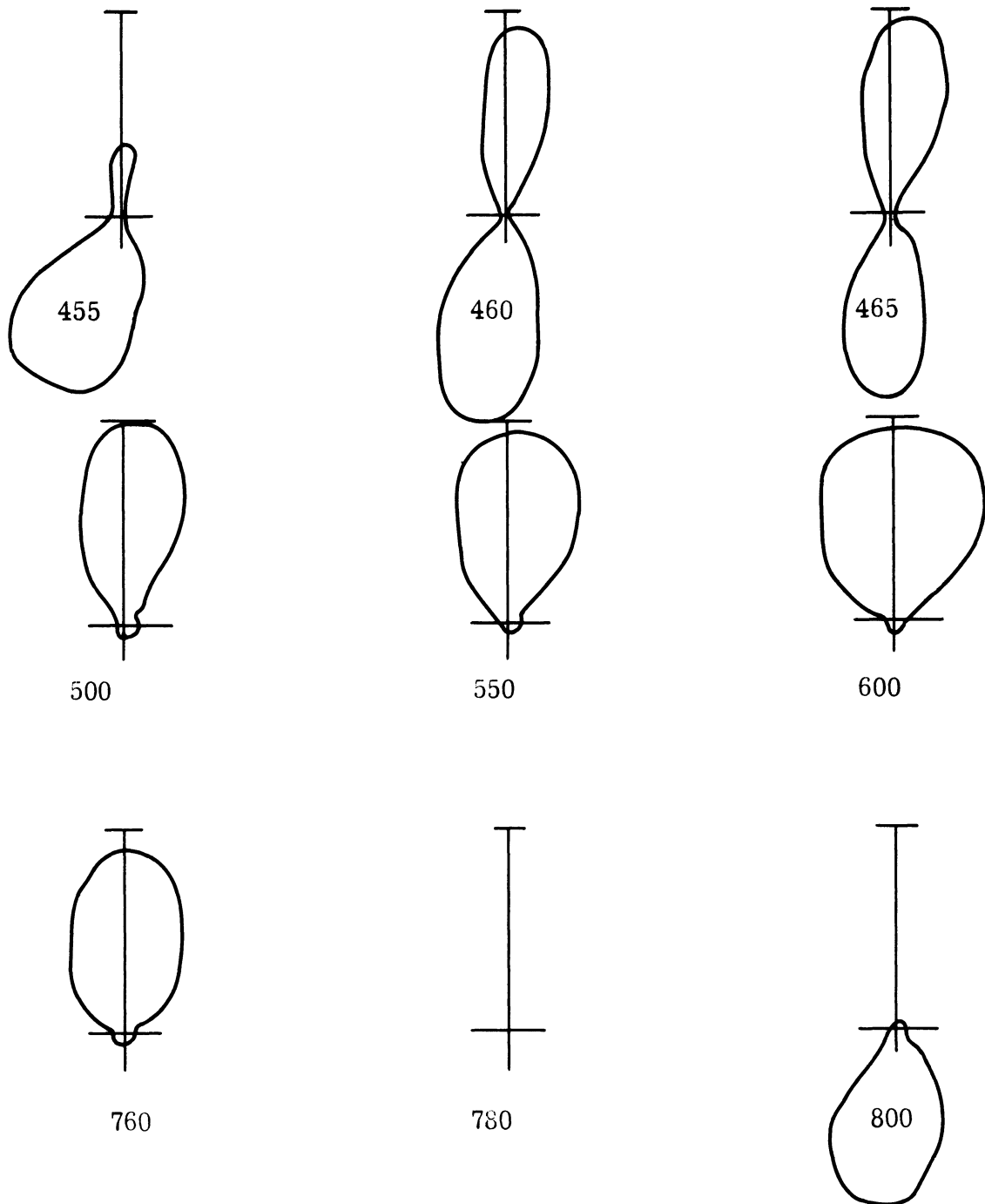


FIG. 2-34a: LINEAR POWER PATTERNS OF ANTENNA 238, AN INDUCTOR LOADED BIFILAR HELIX. ( $|E_\theta|^2$  Patterns in the  $\phi = 0$  plane.)

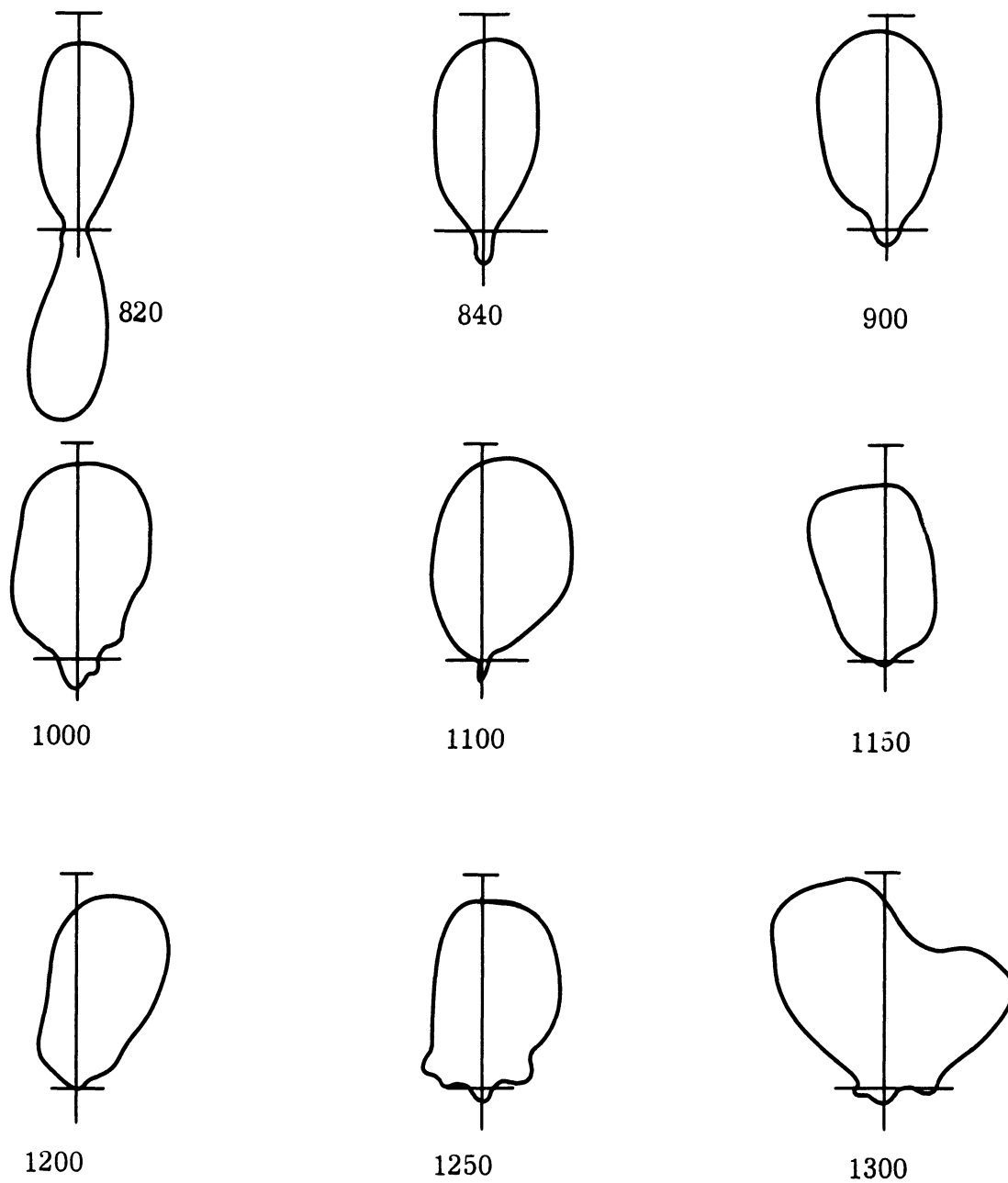


FIG. 2-34b: LINEAR POWER PATTERNS OF ANTENNA 238, AN INDUCTOR LOADED BIFILAR HELIX. ( $E_\theta^2$  Patterns in the  $\phi = 0$  Plane.)

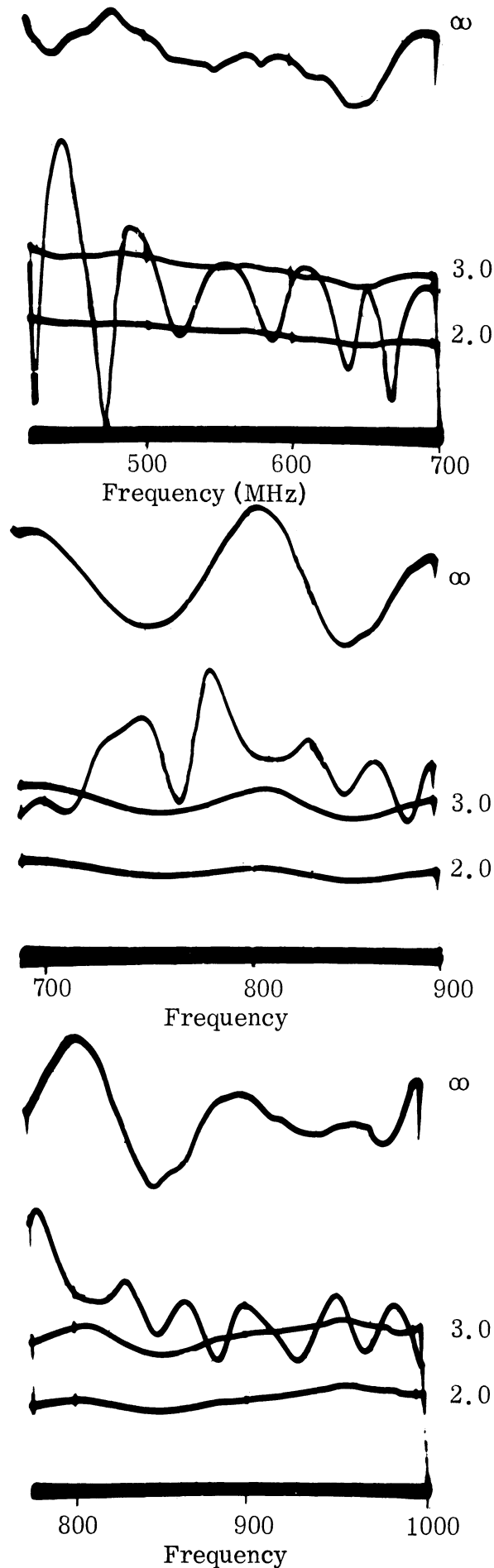


FIG. 2-35: VSWR OF ANTENNA 238, A BIFILAR HELIX WITH INDUCTANCE LOADING.

These conclusions can be drawn:

1) The transmission line model of the helix antenna presented by Rassweiler (1966) is apparently not quite correct. Assuming that the lower band of operation was caused by the inductive loading and working backwards from its frequency range to find the characteristic impedance of the corresponding transmission line produced a characteristic impedance of  $110 \Omega$ . The input impedance of a helix antenna is usually in the range of  $100 - 150 \Omega$ . Thus, apparently using the input impedance of a helix antenna in the transmission line analogy correctly predicts the experimental results.

2) Even by itself, Antenna 238 is a very interesting antenna. It covers almost the entire frequency range from  $475 - 1250$  MHz, except for a band of  $80$  MHz centered around  $800$  MHz.

3) Series inductance tends to reduce the size of a helix antenna but series capacitive loading will increase the size for a given frequency range of operation. (In the  $840 - 1250$  MHz range, the stubs were capacitive.)

4) The average impedance values measured, however, do not tend to support the transmission line analogy. The impedance was higher in the high band and lower in the low band; not the other way around as would be expected from the transmission line relation  $Z_0 = \sqrt{L/C}$ . (Note, that in the high band the capacitance introduced would tend to reduce the inductance in the above formula.)

## 2.9 Anisotropic Ferrite Loaded Helix Antenna

There are several reasons for examining anisotropic ferrite loading in helix antennas. All of these reasons are a consequence of the steady unidirectional magnetic field in the material. First of all, at higher frequencies, a magnetic bias of the ferrite makes a low loss material possible (Hach, 1966). Second, if a helix is magnetically tuned by adjusting the magnetic field, then the properties of the antenna would be affected by the changes in the characteristics of the material. Third, because a plane wave propagating through a saturated ferrite exhibits circular polarization, precisely the polarization produced by a helix antenna, it

may be possible to use anisotropic loading as a mode filter to reduce the high side and backlobes that sometimes result from isotropic loading materials.

Because a saturated ferrite can be expected to represent one limit in the range of operation of a magnetic field tuned ferrite loaded antenna, it poses an interesting special case to study. Fortunately, the anisotropy of the permeability tensor of such a material is relatively simple and can be readily predicted by classical electromagnetic theory. The permeability tensor can be described by the following tensor:

$$\bar{\mu} = \mu_0 \begin{pmatrix} \mu & j\kappa & 0 \\ -j\kappa & \mu & 0 \\ 0 & 0 & 1 \end{pmatrix} \quad (2.4)$$

where

$$\mu = \left( 1 + \frac{\gamma \omega_0 M_0}{\omega_0^2 - \omega^2} \right),$$

$$\kappa = \left( \frac{\omega \gamma M_0}{\omega_0^2 - \omega^2} \right),$$

and  $M_0$  is approximately  $M_s$ , the saturated magnetization (provided the amplitude of the time varying fields is small),  $\gamma$  is the gyromagnetic ratio,  $\omega_0$  is the Larmor frequency and is equal to  $\gamma B_0$ ,  $B_0$  is the dc magnetic field, and  $\mu_0$  is the permeability of free space (Collin, 1960). The dielectric constant of the material is the same as when no bias is applied.

The permeability tensor, like any tensor, may be transformed to another coordinate system. For the helix antenna, circular cylindrical coordinates are appropriate. Since the transformation matrix from rectangular to circular cylindrical coordinates is

$$\bar{C}_{CR} = \begin{pmatrix} \cos\phi & \sin\phi & 0 \\ -\sin\phi & \cos\phi & 0 \\ 0 & 0 & 1 \end{pmatrix} \quad (2.5)$$



then the permeability tensor in the new system is:

$$\bar{\bar{\mu}}_C = \bar{\bar{C}}_{CR} \cdot \bar{\bar{\mu}}_R = \begin{pmatrix} \mu \cos\phi & -j\kappa \sin\phi & j\kappa \cos\phi + \mu_r \sin\phi & 0 \\ -\mu_r \sin\phi & -j\kappa \cos\phi & -j\kappa \sin\phi + \mu \cos\phi & 0 \\ 0 & 0 & 0 & 1 \end{pmatrix} \quad (2.6)$$

which makes the permeability tensor a function of the coordinates. This is true, in general, for any common coordinate system, except rectangular. This dependence on one of the coordinate variables complicates the mathematical solution of any saturated ferrite problem in any coordinate system except rectangular. However, this does not make the situation hopeless, and some insight may be obtained by a mathematical analysis.

III

SLOT ARRAYS

3.1 Introduction

The purpose of this task is to investigate the feasibility of using physically small slot antennas at 300 MHz as elements in an antenna array system. Specifically, the following parameters are to be determined: 1) beamwidth and gain as a function of frequency, 2) bandwidth as a function of magnetic tuning, and 3) sidelobe levels and angles as a function of power distribution. The possibility of adapting such arrays to electronic scan and steerable beam systems is also to be considered.

As originally envisioned, the arrays would consist of ferrite filled slots in a ferrite filled waveguide. However, above 200 MHz, this type of array was completely infeasible at present due to the high loss of commercially available ferrites. Spaces between the ferrite sticks used in the array also posed a problem. The resulting inhomogeneity reduced the effectiveness of the ferrite and the cutoff frequency of the waveguide was higher than predicted. Several attempts were made to produce a waveguide that had a low enough propagation loss above 200 MHz so that a realistic array could be built. However, as the data in Section 3.6 shows, the effort was unsuccessful.

The array testing program was restructured to use rectangular cavity backed slot antennas. Two additional slots similar to one tested earlier (Adams, 1964, 1967) were built and individually tested to insure their similarity. The test results, which are presented in Section 3.3, indicate that the elements are very similar. Preliminary results for one array of these cavity backed slots are included in Section 3.2.

Another physically small array developed under this task was the interdigital array. A separate report was issued covering its properties (Wu, 1967a). Hence, only a summary of its properties is included here (Section 3.4).

Finally, a ferrite filled cavity backed slot was tested to determine how much power it could successfully handle. The test results, in Section 3.5, indicated that 50 watts of power could be continuously fed to the slot. Higher powers could be tolerated for shorter periods of time.

### 3.2 Cavity Backed Slot Array

The first array tested was a broadside array with  $0.534\lambda$  spacing. The hybrid network depicted in Fig. 3-1 was used to feed the slots. Measurements on each output port with all the other ports terminated in matched loads indicated that the amplitudes of the outputs were within 5 percent of each other and the phases were within 2 percent of each other. Each slot had a double stub tuner at its terminals and each slot was tuned to resonance at 350 MHz, with the other slots unexcited. Care was taken to insure identical feed lines and connectors were used in all parts of the feed network so that electrical symmetry was maintained. The ground plane used for the test and the location of the slots on the ground plane are shown in Fig. 3-2.

A summary of the test results on the patterns of the array are shown in Figs. 3-3 and 3-4. Figure 3-3 gives 3 db and 10 db beamwidths as a function of frequency and Fig. 3-4 gives the sidelobe level and angle of the most prominent sidelobe and the angle of the mainlobe as a function of frequency. All the data were taken from H-plane patterns with pen deflection proportional to  $|E|^2$ . Figure 3-5 shows the assumed coordinate system.

One prominent characteristic of all the patterns of power vs frequency is the asymmetry of the patterns. The sidelobe levels were much higher for  $-\theta$  in the x-z plane than for  $+\theta$ . The asymmetry of the patterns is probably due to the unequal distribution of energy reflected by the slots as a result of the asymmetry of the feed network. However, other feed networks will be used in the future to insure the phenomena are not inherent in the properties of ferrite slots.

To give some indication of what radiation pattern properties can be expected from array theory (e. g. Kraus, Ch. 4, 1950), for a uniform array of omnidirectional

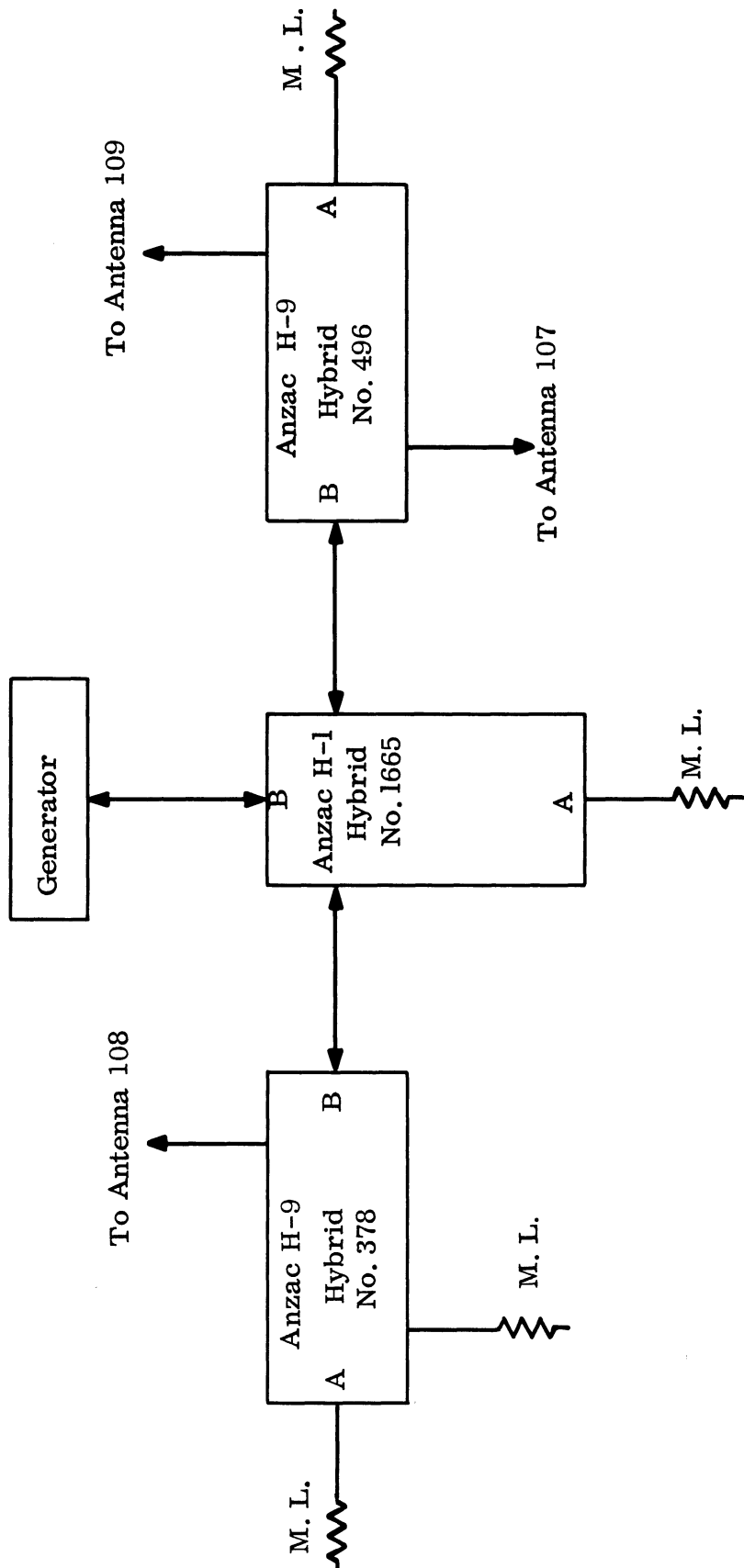


FIG. 3-1: FEED NETWORK FOR FERRITE FILLED RECTANGULAR CAVITY BACKED SLOT ARRAY.

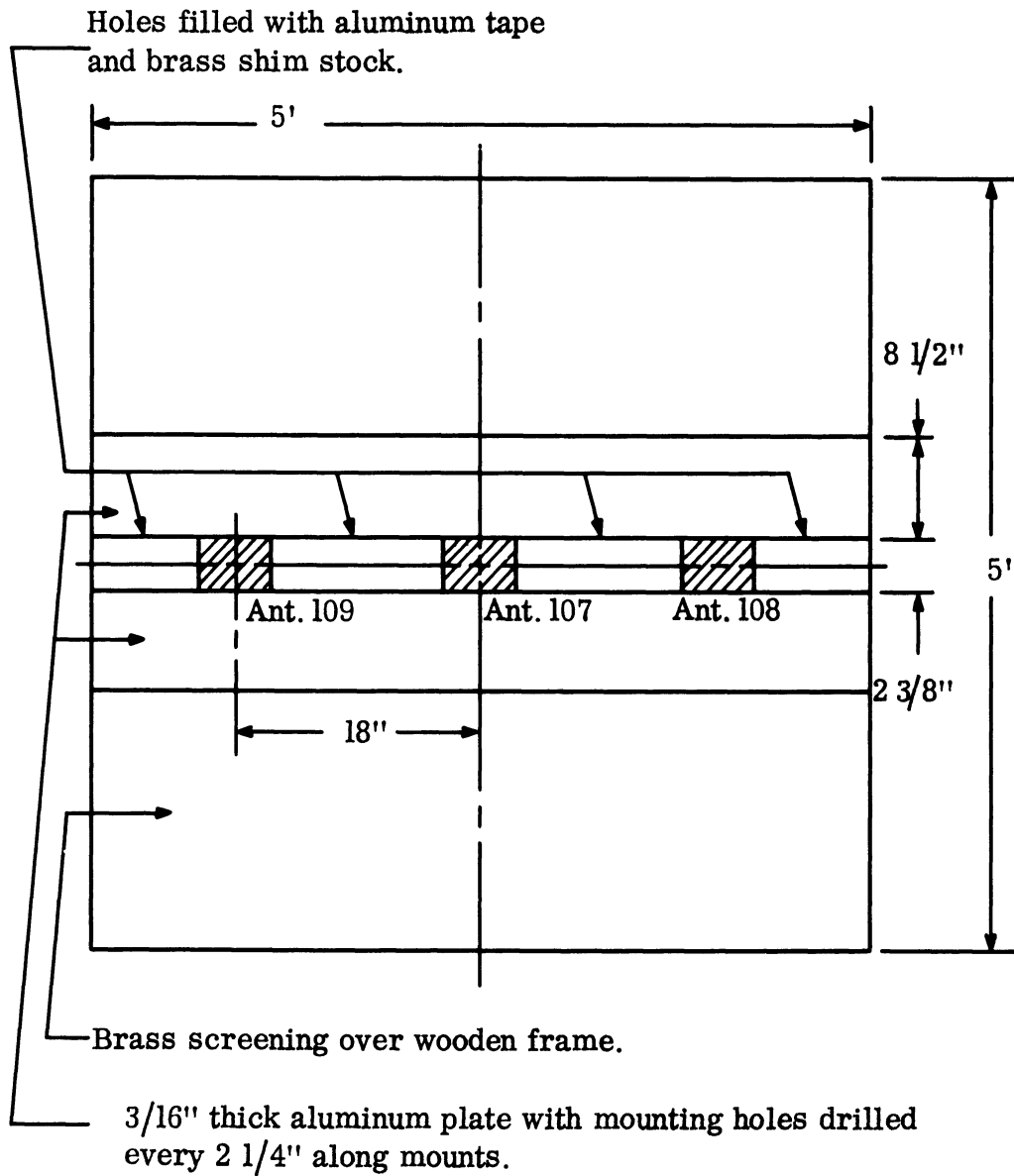
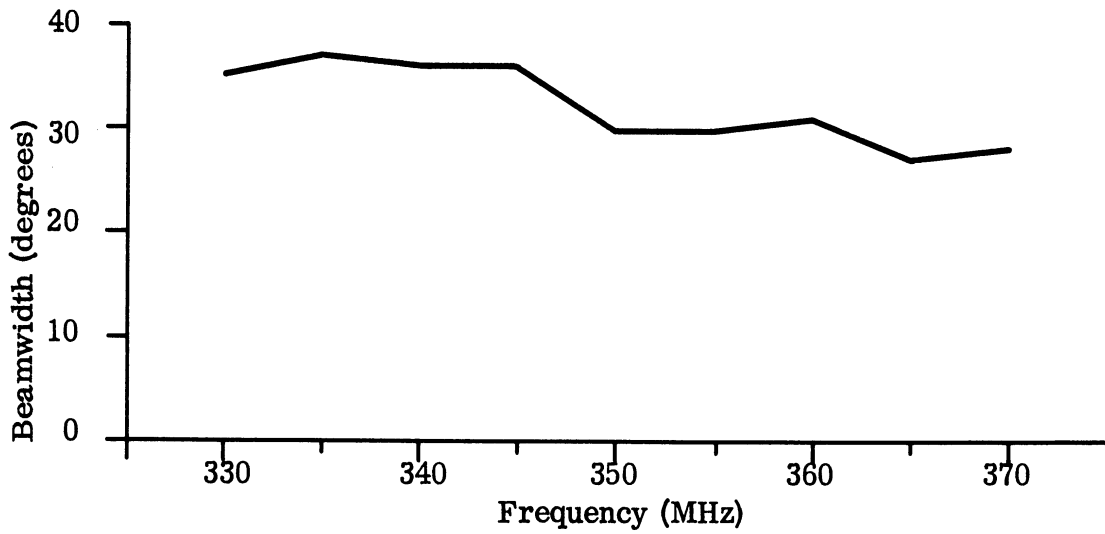
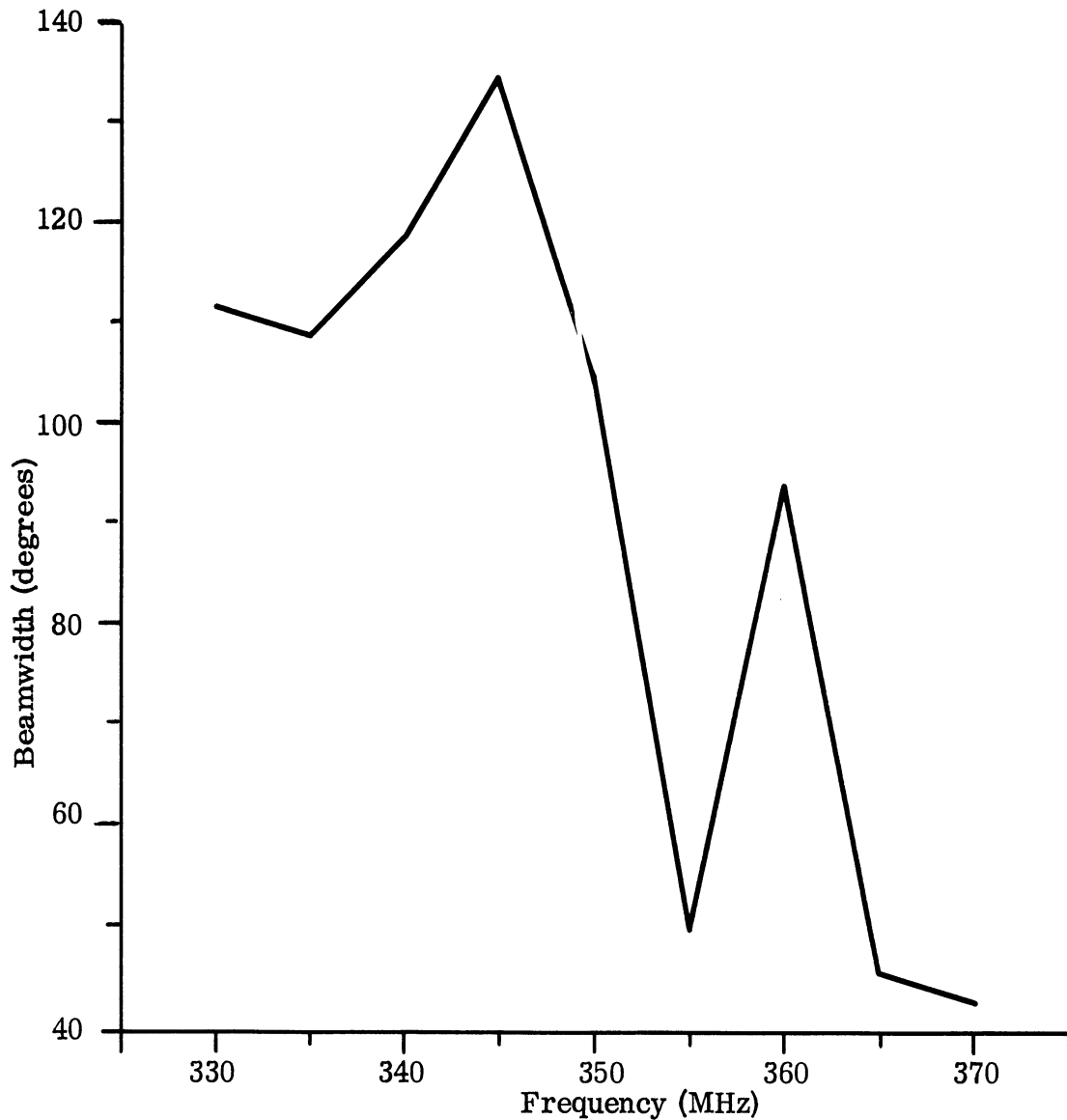


FIG. 3-2: MOUNTING CONFIGURATION AND GROUND PLANE FOR  
FERRITE FILLED RECTANGULAR CAVITY BACKED  
SLOT ARRAY.



(a) 3 db Beamwidth



(b) 10 db Beamwidth

FIG. 3-3: BEAMWIDTH OF A 3-ELEMENT  $.534\lambda$  (AT 350 MHz) BROADSIDE ARRAY FED WITH A HYBRID-DOUBLE STUB TUNER NETWORK.

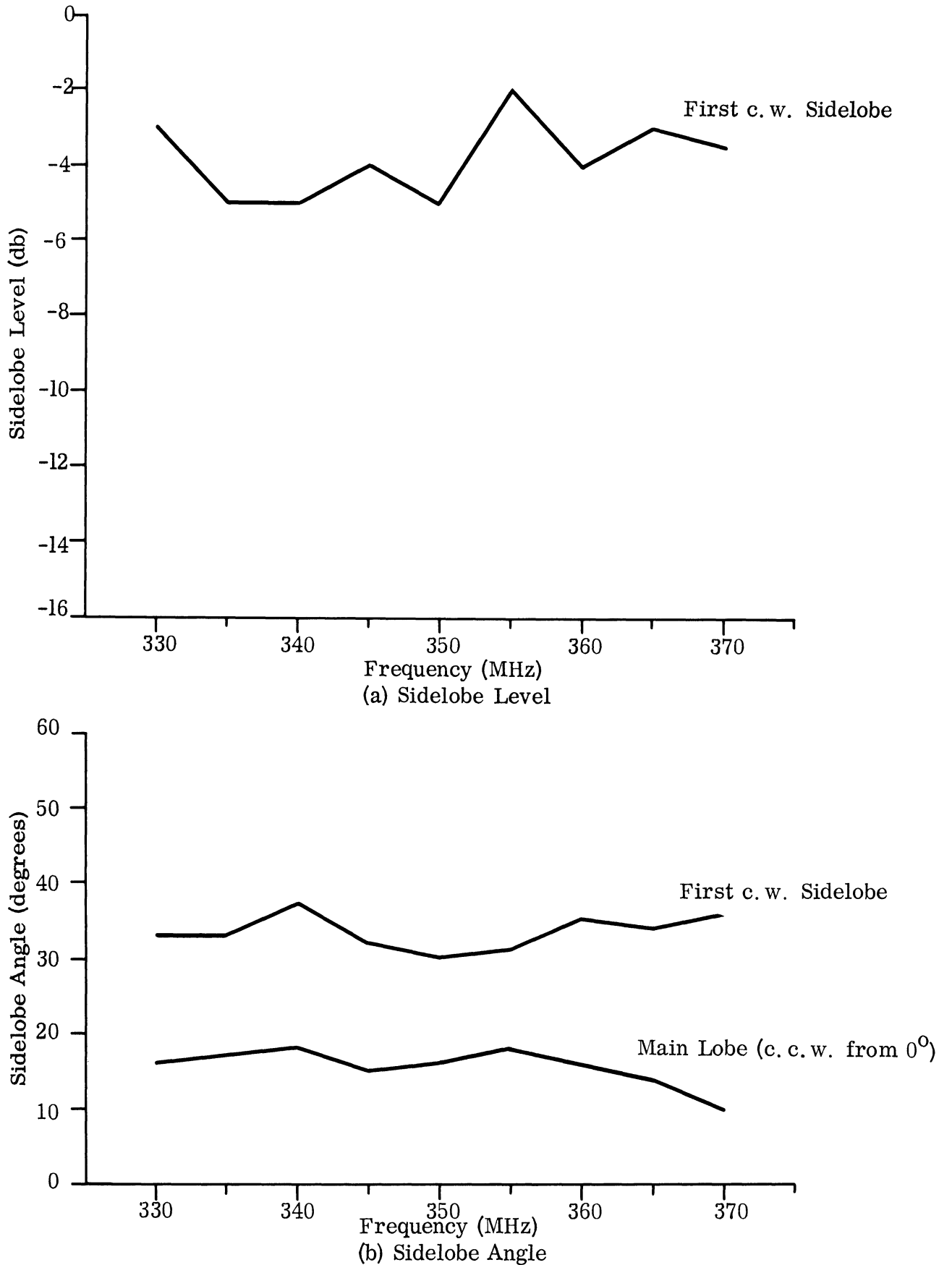


FIG. 3-4: SIDELOBE LEVELS AND ANGLES AND MAINLOBE ANGLE OF A 3-ELEMENT  $.534\lambda$  (AT 350 MHz) BROADSIDE ARRAY FED WITH A HYBRID-DOUBLE STUB TUNER NETWORK.

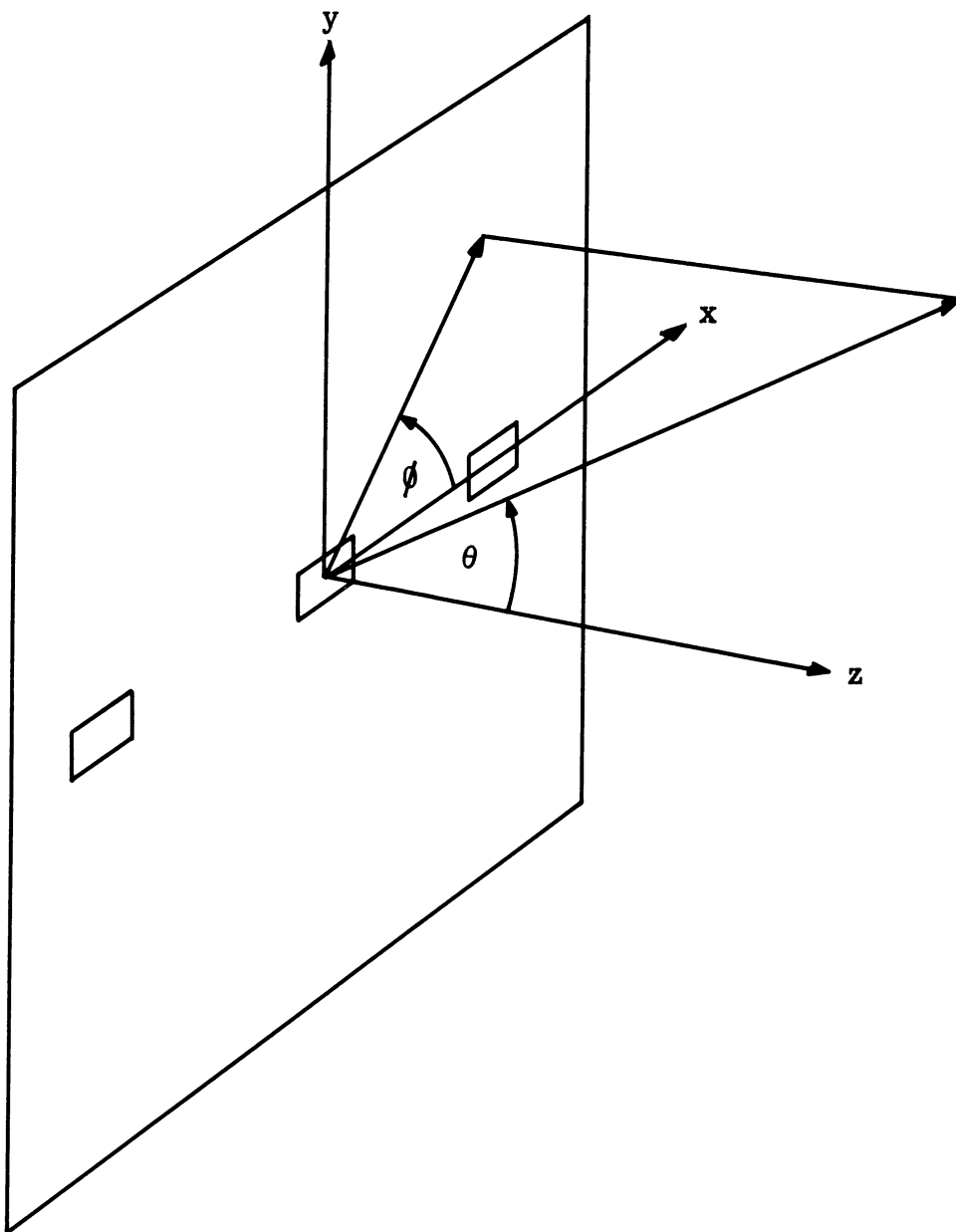


FIG. 3-5: COORDINATE SYSTEM ASSUMED FOR RADIATION  
PATTERN MEASUREMENTS OF FERRITE FILLED  
RECTANGULAR CAVITY BACKED SLOT ARRAY.



THE UNIVERSITY OF MICHIGAN  
7848-1-F

elements spaced 0.534 wavelengths apart, a symmetrical pattern can be expected with a half-power beamwidth of  $34^\circ$  and the first sidelobes would be 9.5 db down at angles of  $\pm 70^\circ$ . For the ferrite slot array, the beamwidth should be somewhat smaller and the sidelobe levels further down because of the higher directivity of the element pattern. The measured beamwidth is in accord with theory, although the sidelobe levels and amplitudes are not.

### 3.3 Properties of Elements

When it became apparent that a waveguide slot array was not feasible, an array of three cavity backed slot antennas was chosen that operates close to 350 MHz.

One element used was an experimental ferrite filled cavity backed slot antenna originally described by Adams (1964, 1967). Two other ferrite filled cavity backed slot antennas almost identical to it were constructed to permit tests on a three element array. The antennas are shown in Fig. 3-6, and a table summarizing their important properties is shown in Table II.

The discrepancy in the appearance between Adams' original slot (107) and the two copies (108, 109) is a result of the placement of the ferrite in the slots. The bars of ferrite (Motorola EAF-2 solid) were placed parallel to the long dimension of the cavity in antennas 108 and 109 since this configuration resulted in the least amount of waste material. The bars were inserted perpendicular to the aperture and cut off flush with the aperture in antenna 107.

Before constructing an array of the elements, it was felt that each slot should be thoroughly tested to determine how similar the slots were to each other. Figures 3-7 through 3-9 show the input impedance of slots 107, 108 and 109 with respect to a  $50 \Omega$  load, as measured on a 5 ft square ground plane. The ground plane consisted of brass screening with a 20"x27" aluminum plate mounted in the center and in which the slots were mounted. To insure electrical continuity, the joint formed by the slot and the ground plane was taped with Scotch Brand No. 425 3UALK3791 aluminum tape.

The resonant frequencies listed in Table II are based on the minimum reflection coefficient observed.

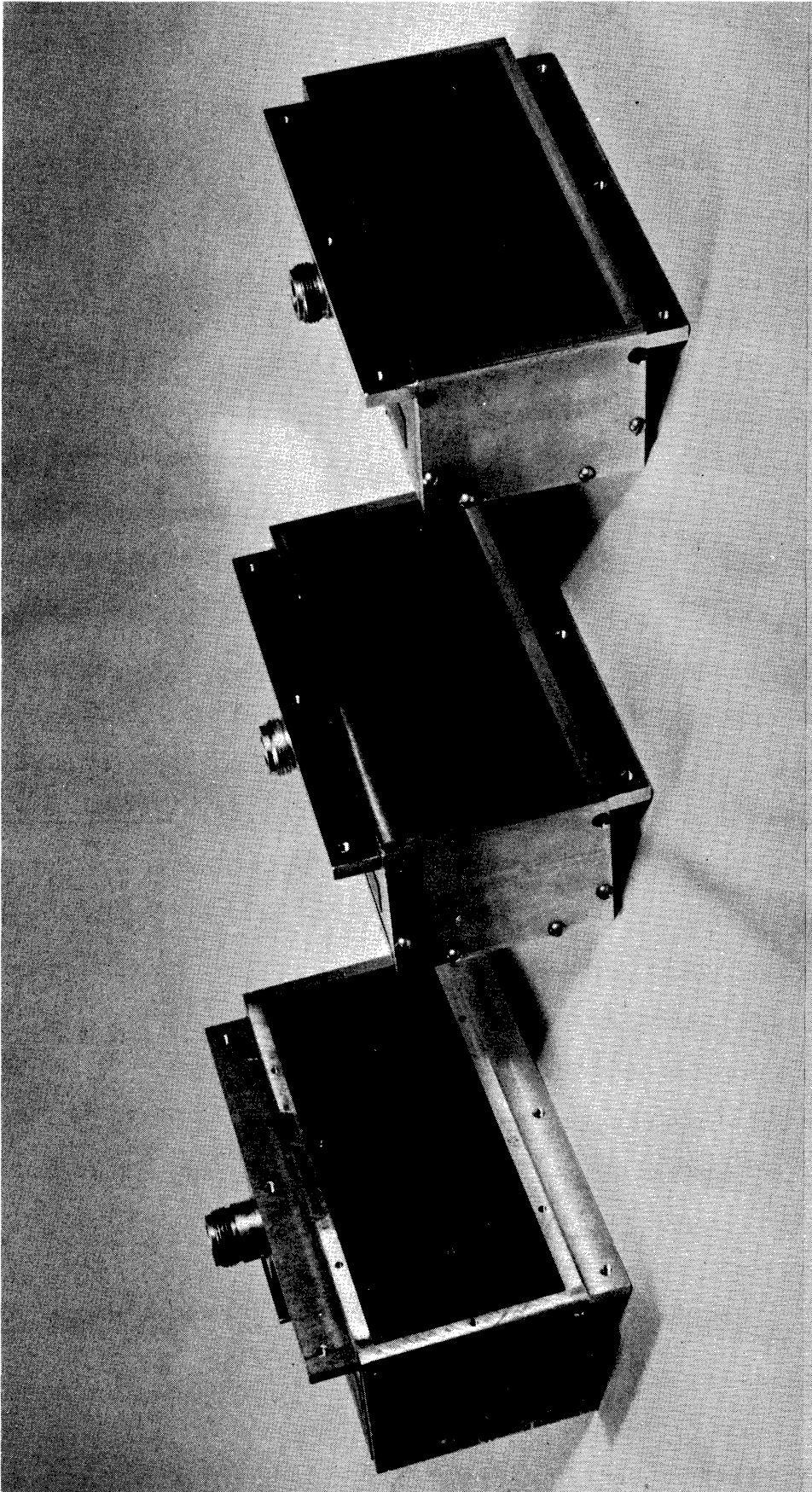


FIG. 3-6: CAVITY BACKED SLOTS 107, 108, and 109

THE UNIVERSITY OF MICHIGAN  
7848-1-F

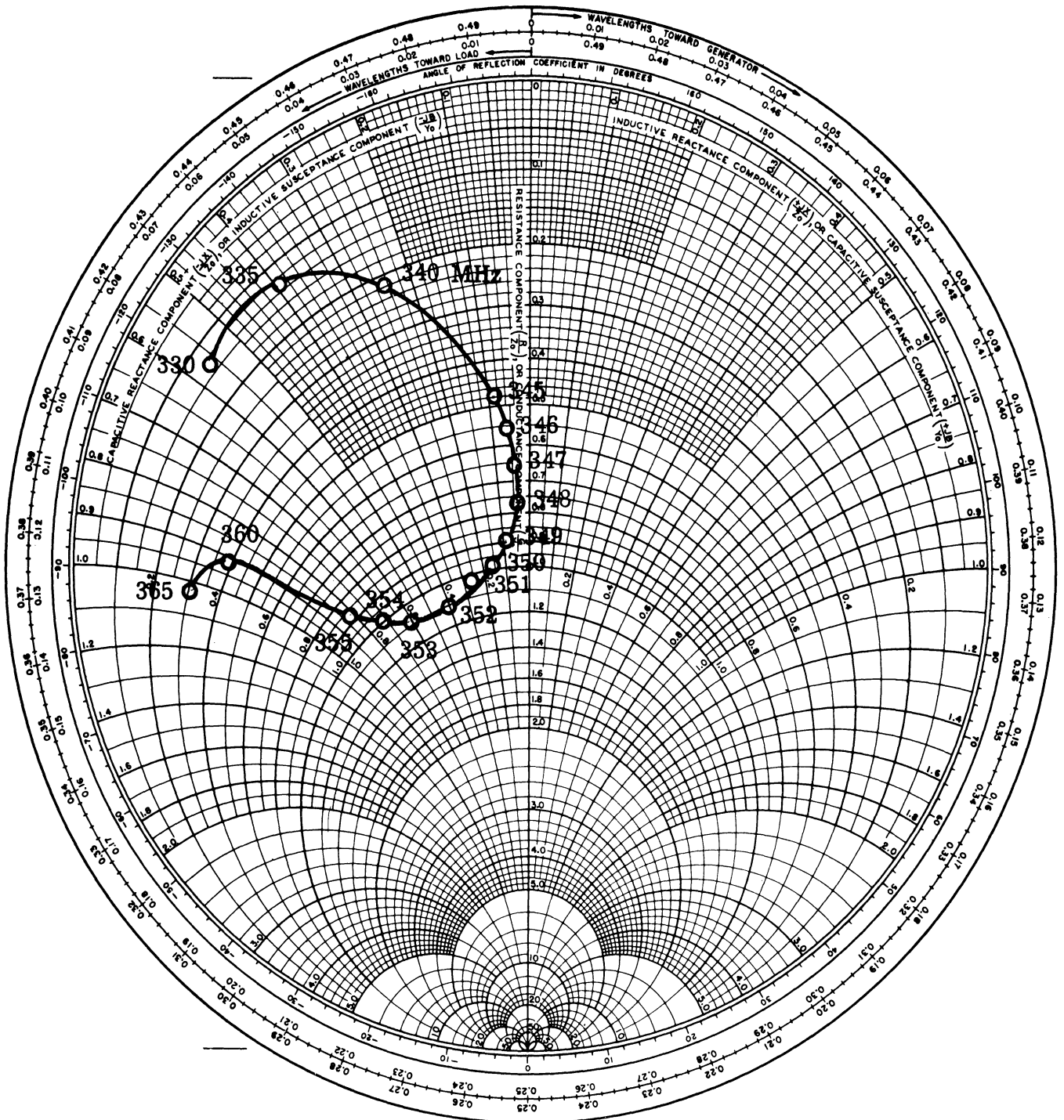


FIG. 3-7: IMPEDANCE OF CAVITY BACKED SLOT 107.  
( $Z_0 = 50$  ohms)

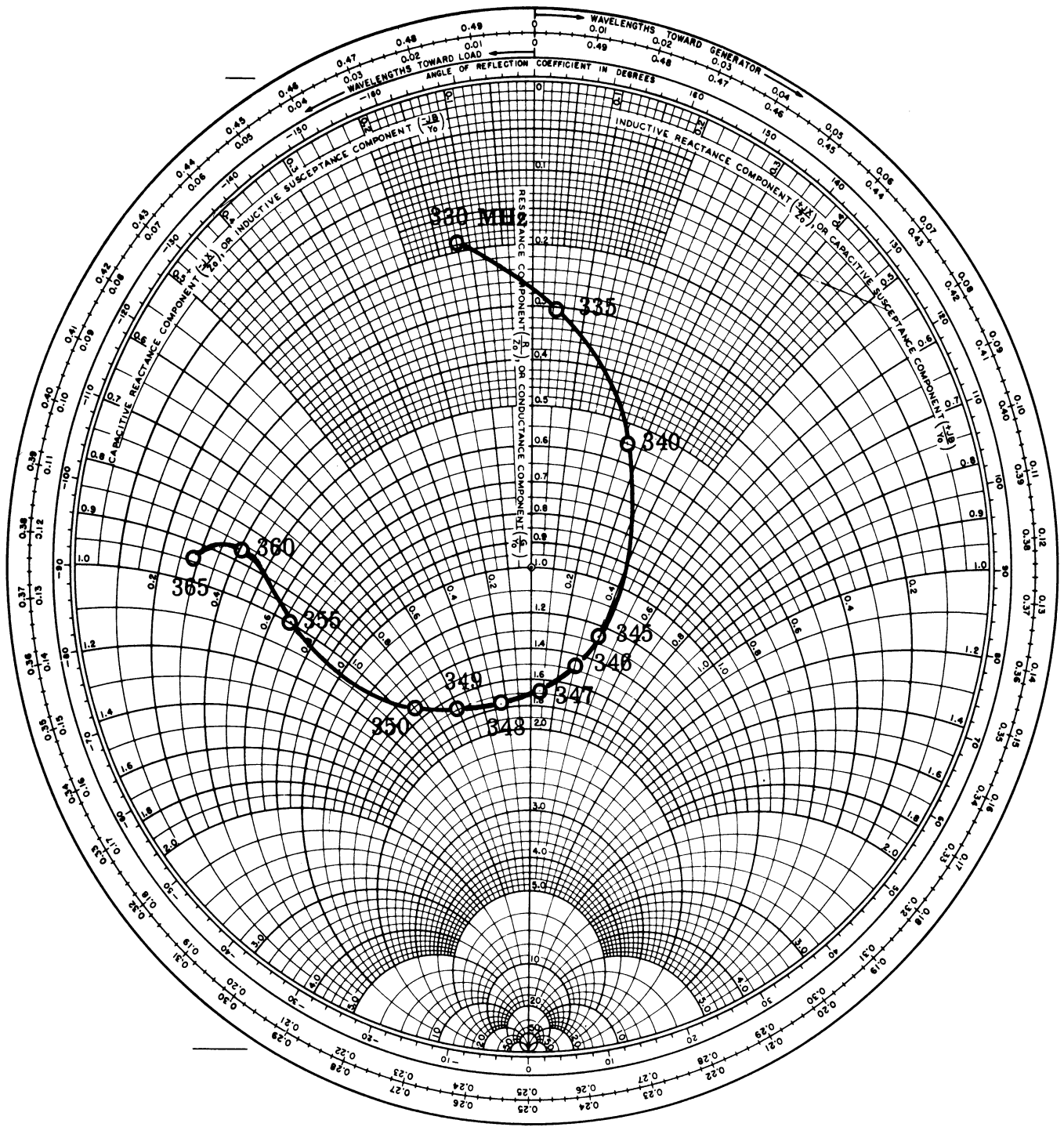


FIG. 3-8: IMPEDANCE OF CAVITY BACKED SLOT 108.

( $Z_0 = 50$  ohms)

THE UNIVERSITY OF MICHIGAN  
7848-1-F

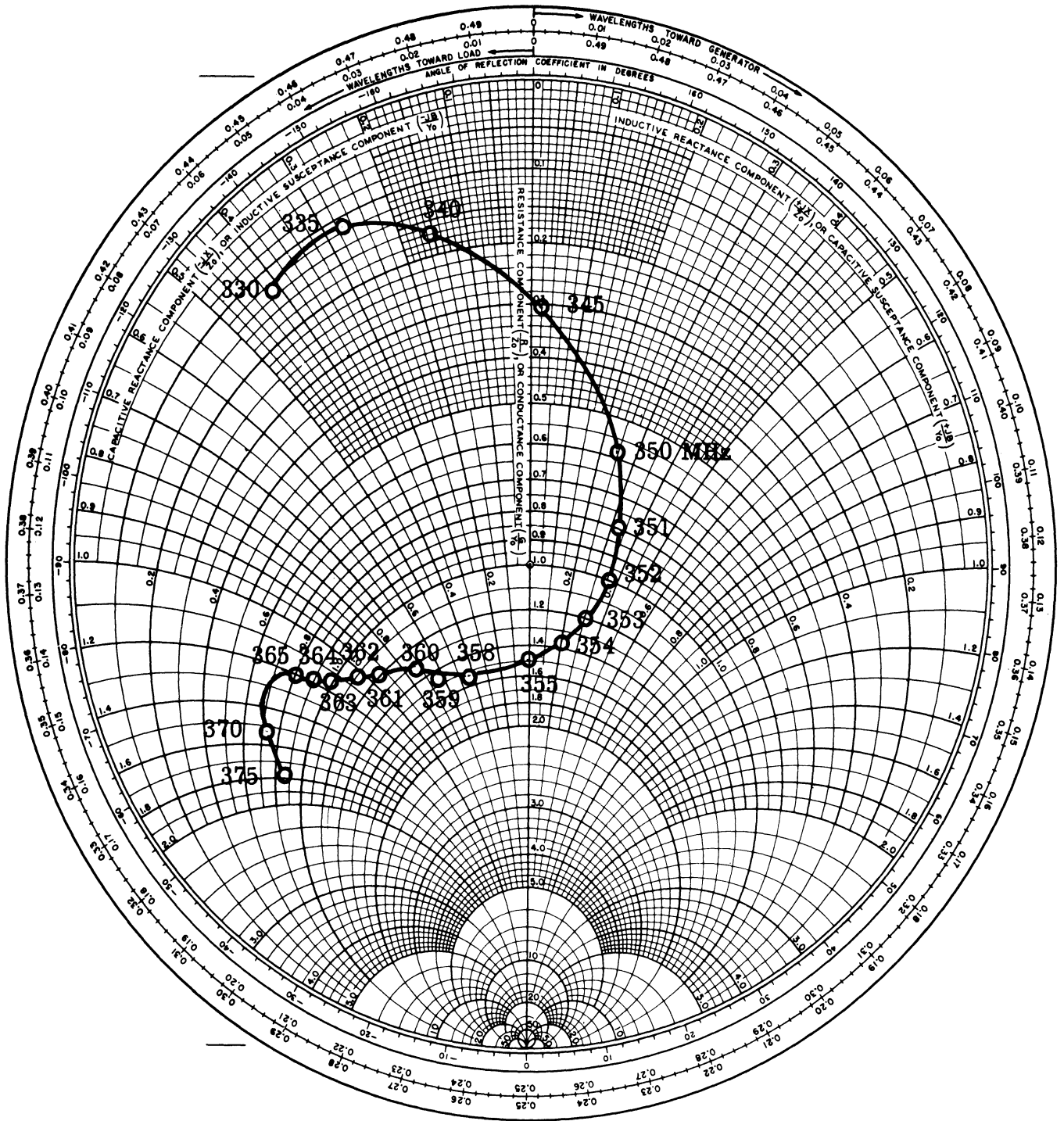


FIG. 3-9: IMPEDANCE OF CAVITY BACKED SLOT 109.  
( $Z_0 = 50$  ohms)

THE UNIVERSITY OF MICHIGAN  
7848-1-F

TABLE II: PROPERTIES OF CAVITY BACKED SLOTS

Cavity No.	Antenna 107	Antenna 108	Antenna 109
Size of Aperture	2.0"x5.0"	2.0"x5.0"	2.0"x5.0"
Cross Section of Cavity	2.0"x5.0"	2.0"x5.0"	2.0"x5.0"
Depth of Cavity	1.5"	1.5"	1.5"
Diameter of Probe	0.25"	0.25"	0.25"
Resonant Frequency (based on minimum reflection)	350 MHz	346 MHz	355 MHz

Radiation patterns were also taken to insure the similarity of the slots.

Figure 3-10 shows the patterns of antenna 107, which are typical of slots 108 and 109 too. Except for 350 and 355 MHz, where the patterns tend to develop "ears", the patterns are fairly good representations of a magnetic dipole radiating into half space. Figure 3-11 compares the 3 db and 10 db beamwidths of the patterns of all three slots and shows there is very close agreement.

The patterns were measured on the same 5'x5' ground plane used to measure the array patterns of the previous section (see Fig. 3-2). The antennas were mounted in the center of the ground plane and the remainder of the channel was filled with brass stock and aluminum tape.

Thus, it appears that for practical purposes, the three slots are identical.

### 3.4 Interdigital Antennas

As was pointed out earlier, a special report was issued covering the theory and experiments on the interdigital array (Wu, 1967a ). This section presents a summary of the many properties of an interdigital array and discusses experiments on ferrite loading the interdigital array.

#### 3.4.1 Summary

The interdigital array (Wu, 1967a) is a small flush mounted broadband antenna that, depending on the feed used, will produce either a broadside beam, a backfire beam, or a forward fire beam. Figure 3-12 illustrates the geometry of the array, and Figs. 3-13 through 3-17 illustrate an actual antenna that was constructed from

THE UNIVERSITY OF MICHIGAN  
7848-1-F

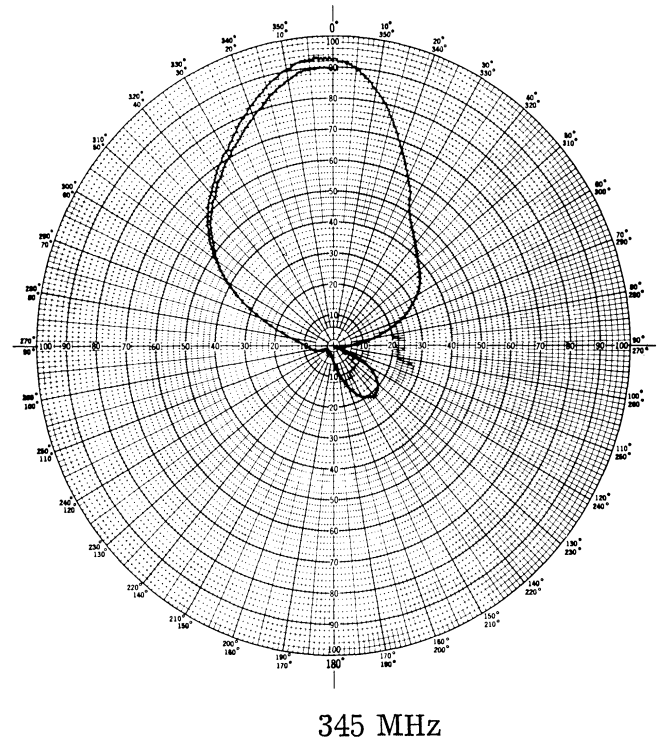
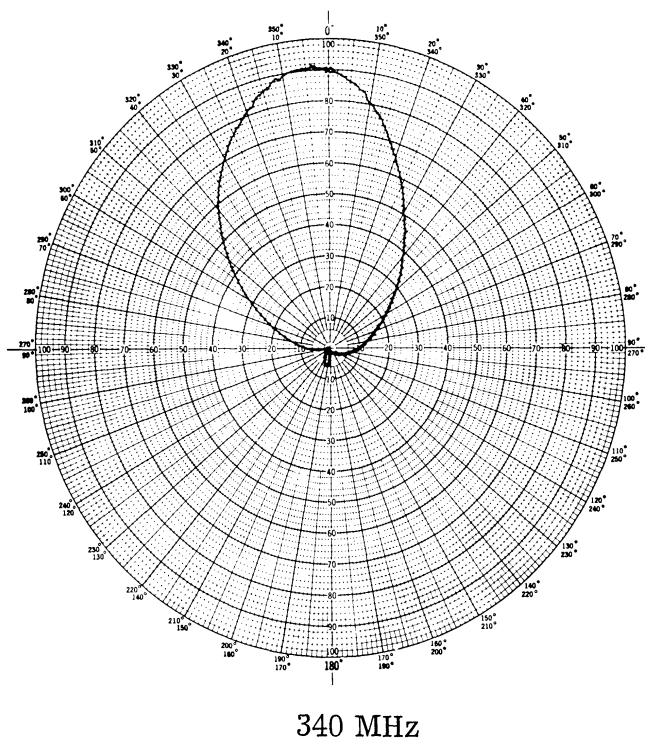
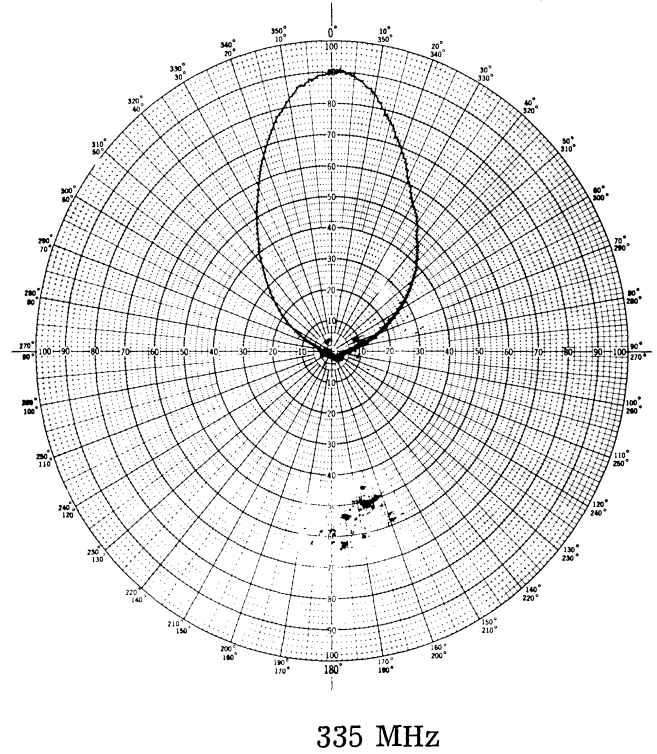
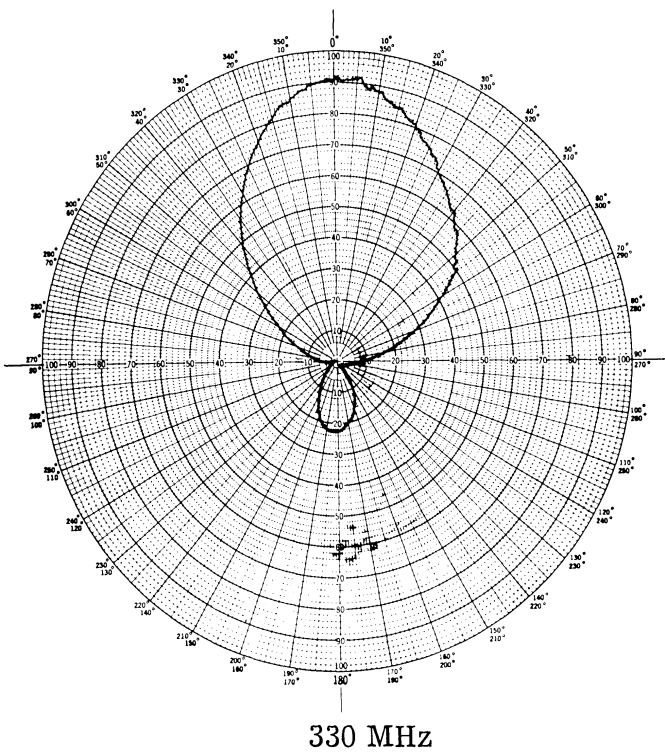
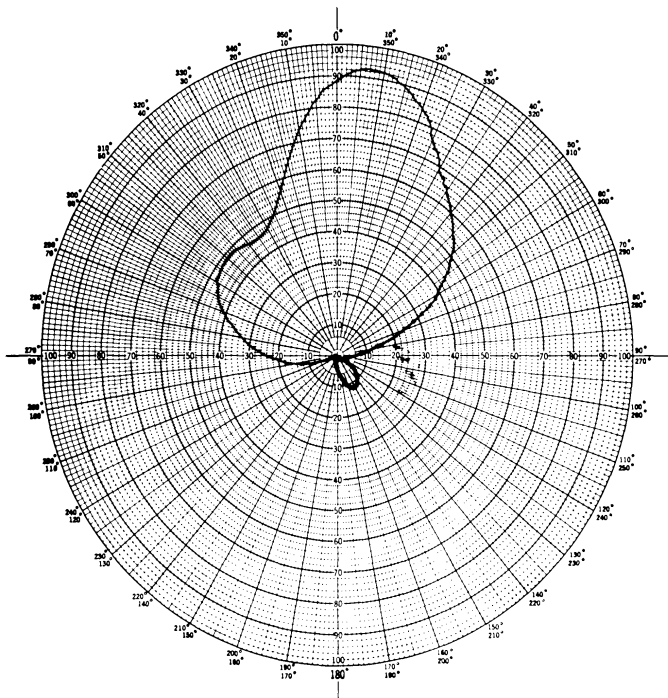
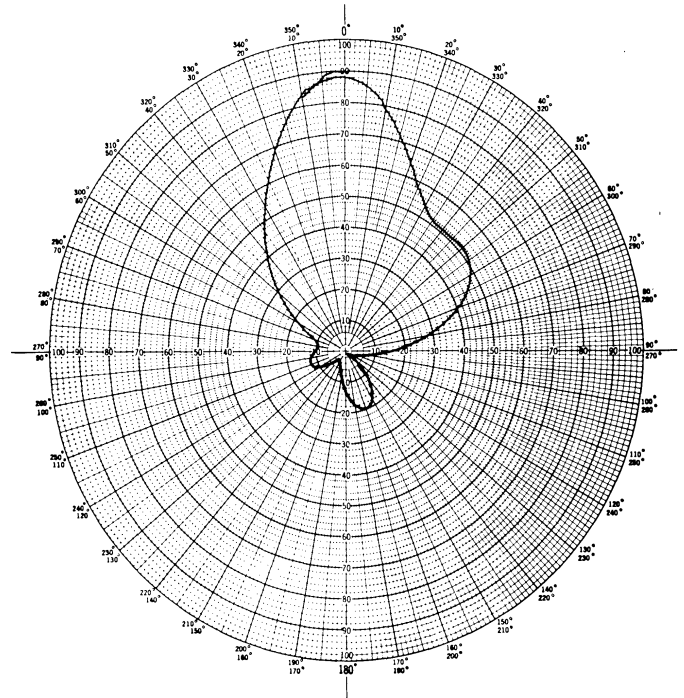


FIG. 3-10a: H-PLANE POWER RADIATION PATTERNS OF FERRITE FILLED  
RECTANGULAR CAVITY BACKED SLOT 107.

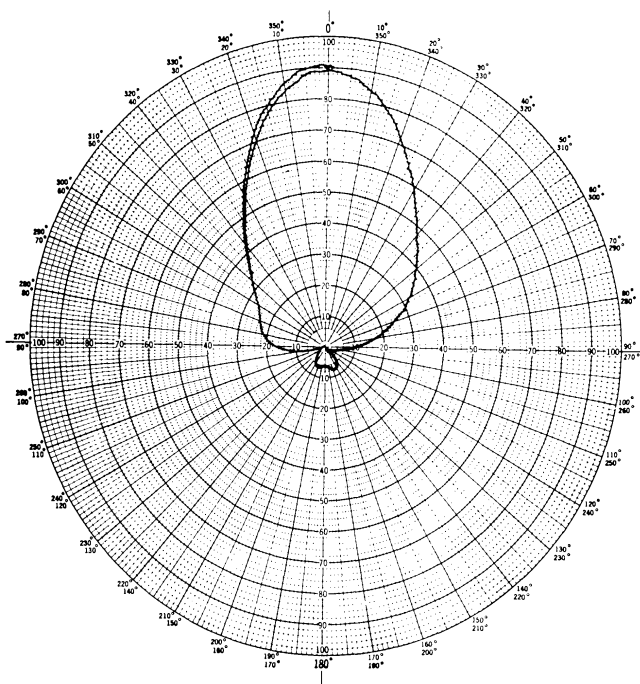
THE UNIVERSITY OF MICHIGAN  
7848-1-F



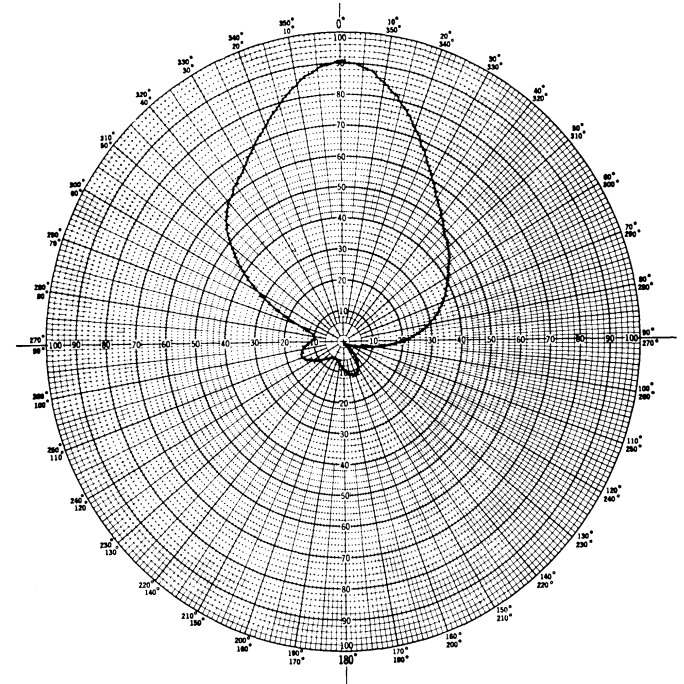
350 MHz



355 MHz



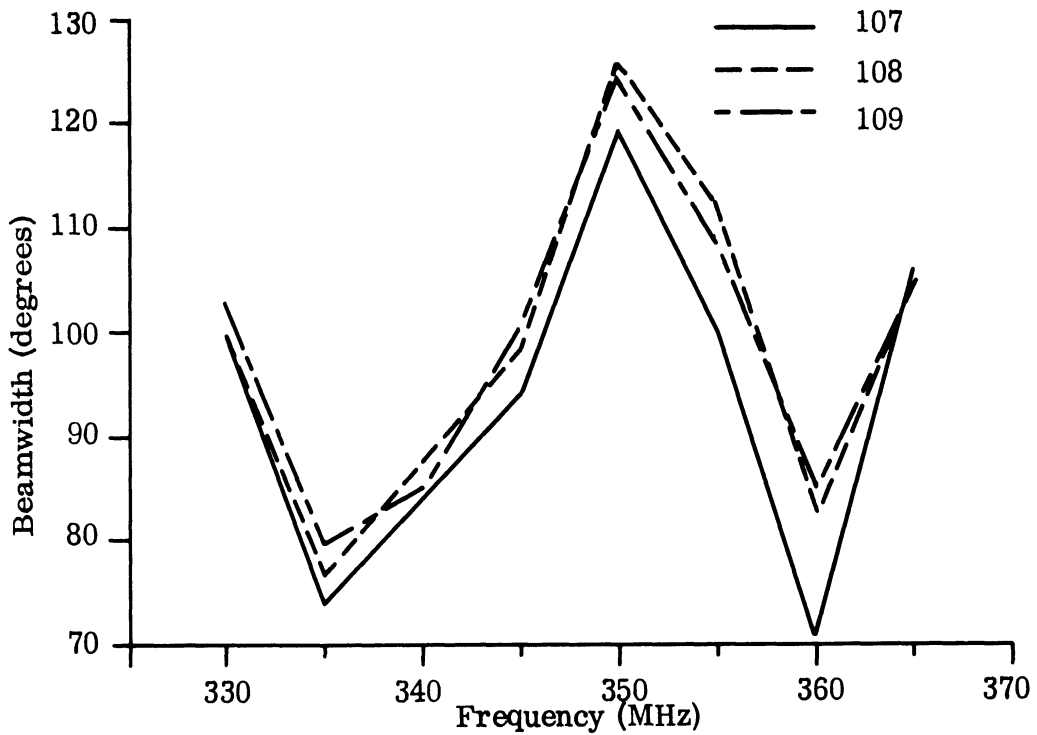
360 MHz



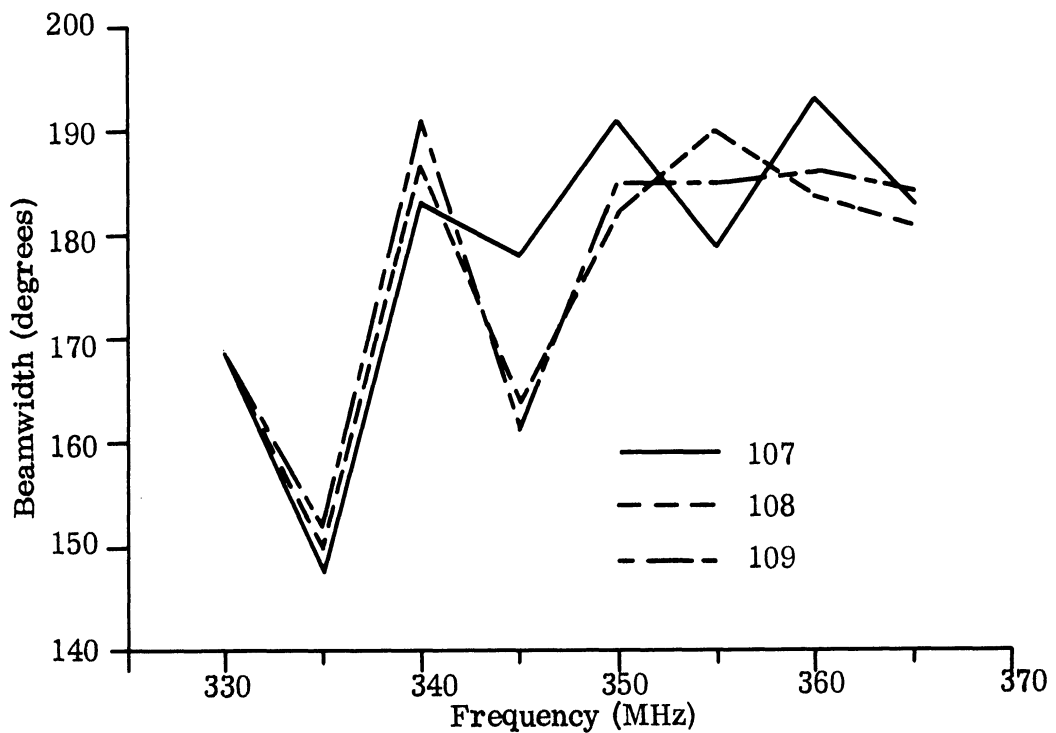
365 MHz

FIG. 3-10b: H-PLANE POWER RADIATION PATTERNS OF FERRITE FILLED RECTANGULAR CAVITY BACKED SLOT 107.





(a) 3 db Beamwidth



(b) 10 db Beamwidth

FIG. 3-11: BEAMWIDTH OF RECTANGULAR CAVITY BACKED SLOTS 107, 108 AND 109.

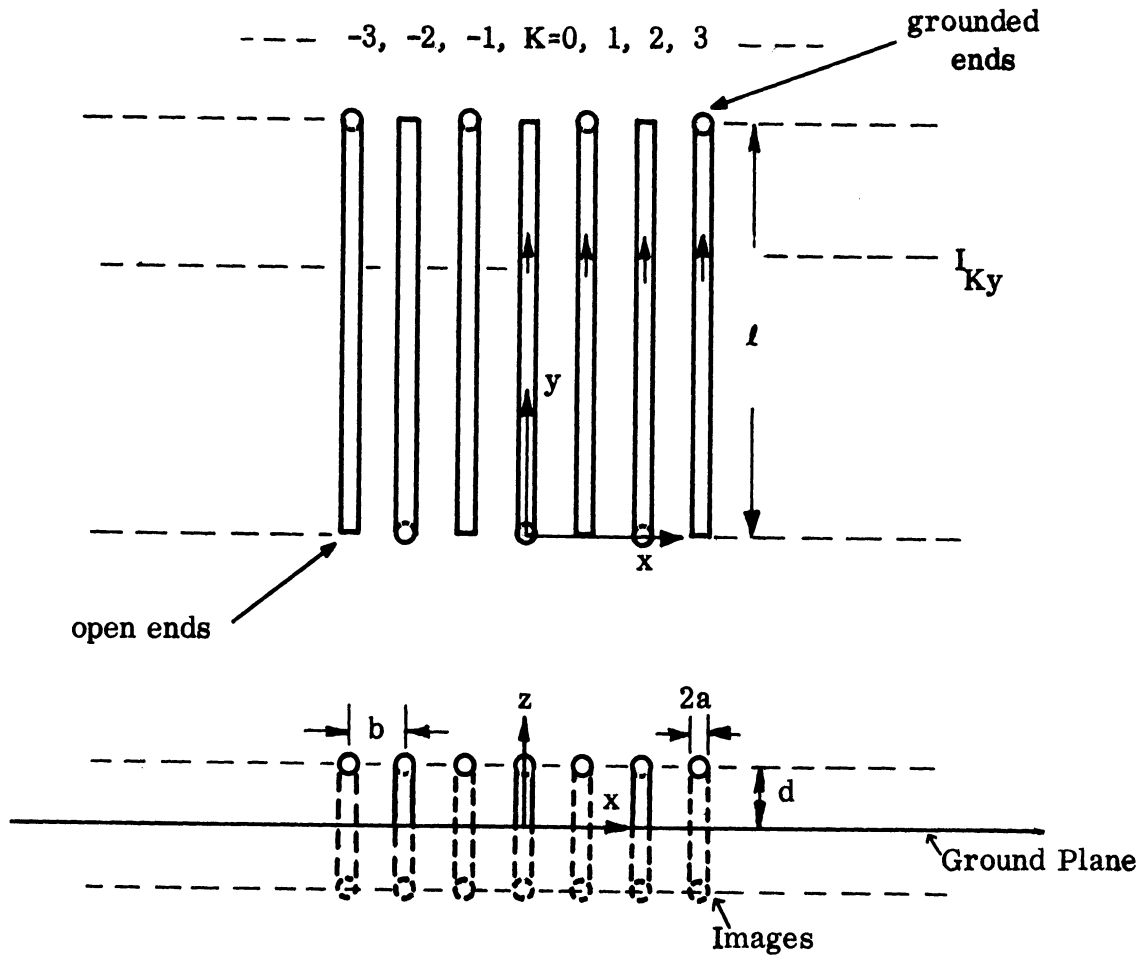


FIG. 3-12: THE GEOMETRY OF THE CONDUCTING ARRAY ELEMENTS.

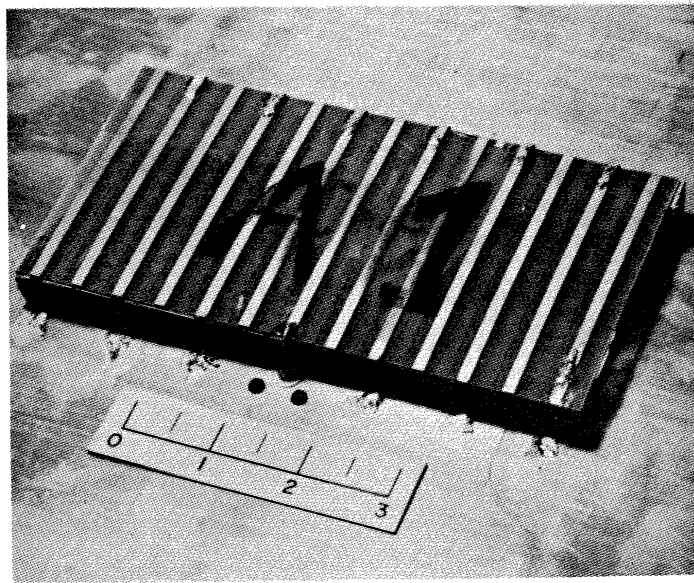


FIG. 3-13: THE INTERDIGITAL ARRAY ANTENNA A-1.  
 $\ell = 8$  cm,  $d/\ell = 0.125$ ,  $b/\ell = 0.15$ ,  $a/\ell = 0.01$ ,  $N = 6$ .

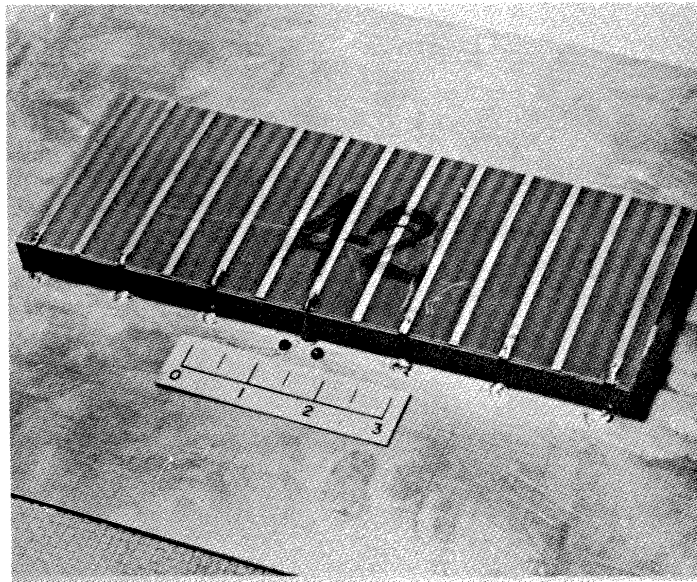


FIG. 3-14: THE INTERDIGITAL ARRAY ANTENNA A-2.  
 $\ell = 8$  cm,  $d/\ell = 0.125$ ,  $b/\ell = 0.225$ ,  $a/\ell = 0.01$ ,  $N = 6$ .

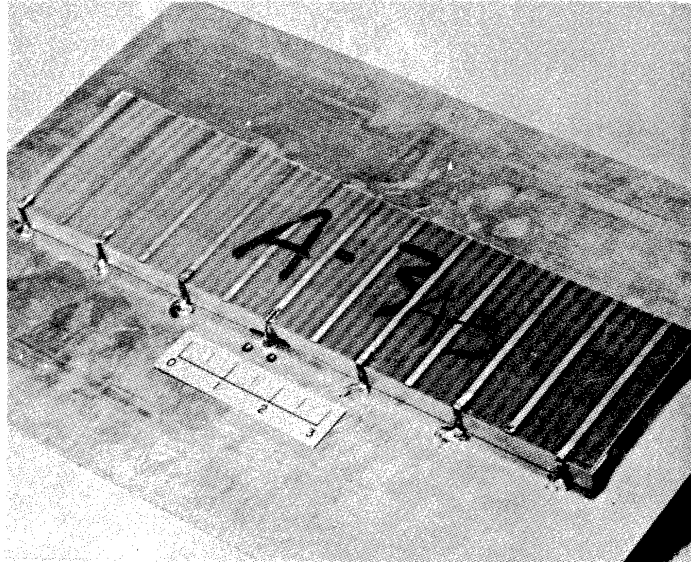


FIG. 3-15: THE INTERDIGITAL ARRAY ANTENNA A-3.  
 $\ell = 8\text{ cm}$ ,  $d/\ell = 0.125$ ,  $b/\ell = 0.30$ ,  $a/\ell = 0.01$ ,  $N = 6$ .

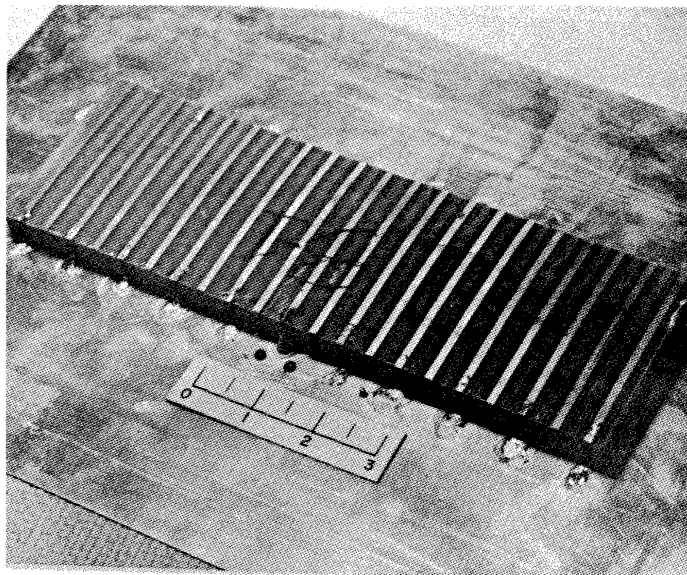


FIG. 3-16: THE INTERDIGITAL ARRAY ANTENNA B-1.  
 $\ell = 8\text{ cm}$ ,  $d/\ell = 0.125$ ,  $b/\ell = 0.15$ ,  $a/\ell = 0.01$ ,  $N = 0$ .

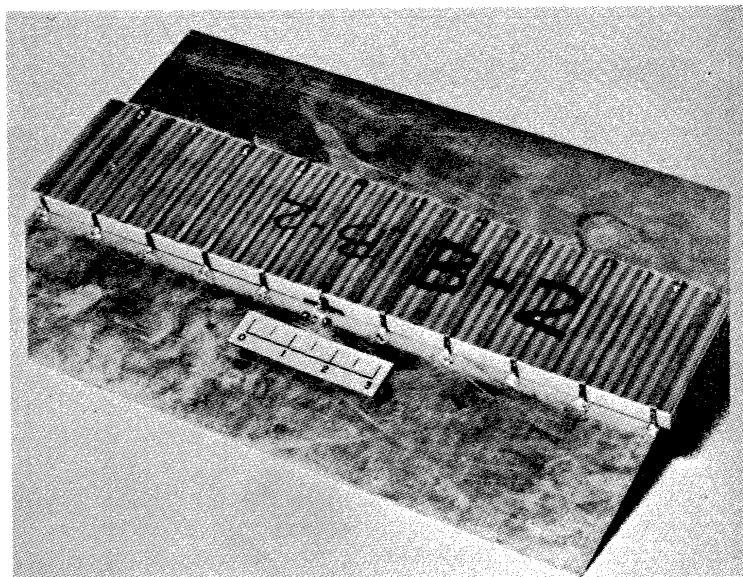


FIG. 3-17: THE INTERDIGITAL ARRAY ANTENNA B-2.  
 $l = 8$  cm,  $d/l = 0.125$ ,  $b/l = 0.225$ ,  $a/l = 0.01$ ,  
 $N = 10$ .

copper clad laminate. Notice that the geometry is similar to the interdigital geometry used in traveling wave tubes and filters. The antenna in Fig. 3-13 covers a frequency range of 350 - 900 MHz. At 350 MHz, the lowest frequency of operation, the antenna is approximately  $0.0935\lambda$  wide by  $0.182\lambda$  long.

Wu (1967 a) did a theoretical analysis of both the open interdigital structure and of an interdigital antenna excited by a source. Test results from many experimental models are in close agreement with the theory. Propagation of a wave along an infinitely long interdigital structure can be represented by the  $k-\psi$  diagram shown in Fig. 3-18 where  $\psi$  is the phase shift per element spacing. Experimental points measured on the models are also shown. The dashed line in the fast wave region of the diagram shows a mathematical solution for the wave that cannot exist physically. Thus the wave travels down the array with about the speed of light (actually, slightly faster) until  $kl$  is about  $\pi/2$ , where a slow wave region is entered. The slow wave region can be made quite small, depending on the parameters of the antenna.

Figure 3-19 shows the far field patterns for the antenna depicted in Fig. 3-13. The antenna is fed in the center of the array, as is shown in the picture. For a short array like this, very good broadside patterns are obtained over most of the frequency range of the antenna. E-plane cut patterns are similar to those shown for the H-plane, except low level sidelobes appear as a result of the contribution of the small sections of elements that are in the  $z$ -direction (Wu, 1967 b). The reasons are that below frequencies corresponding to  $kl = \pi/2$  the endfire components of the wave propagating from the feed cancel and only broadside radiation results. Above this turning point, slow waves would be expected to produce a rabbit ear pattern. However, since the array is sufficiently short so that slow waves do not have enough length to form, the radiation is still broadside. For longer arrays, it was observed that the split beam pattern does occur for frequencies above  $kl = \pi/2$  and below the end of the slow wave region which is not shown in Fig. 3-18. Broadside radiation is resumed as the next region is entered where the phase velocity is approximately that of light.

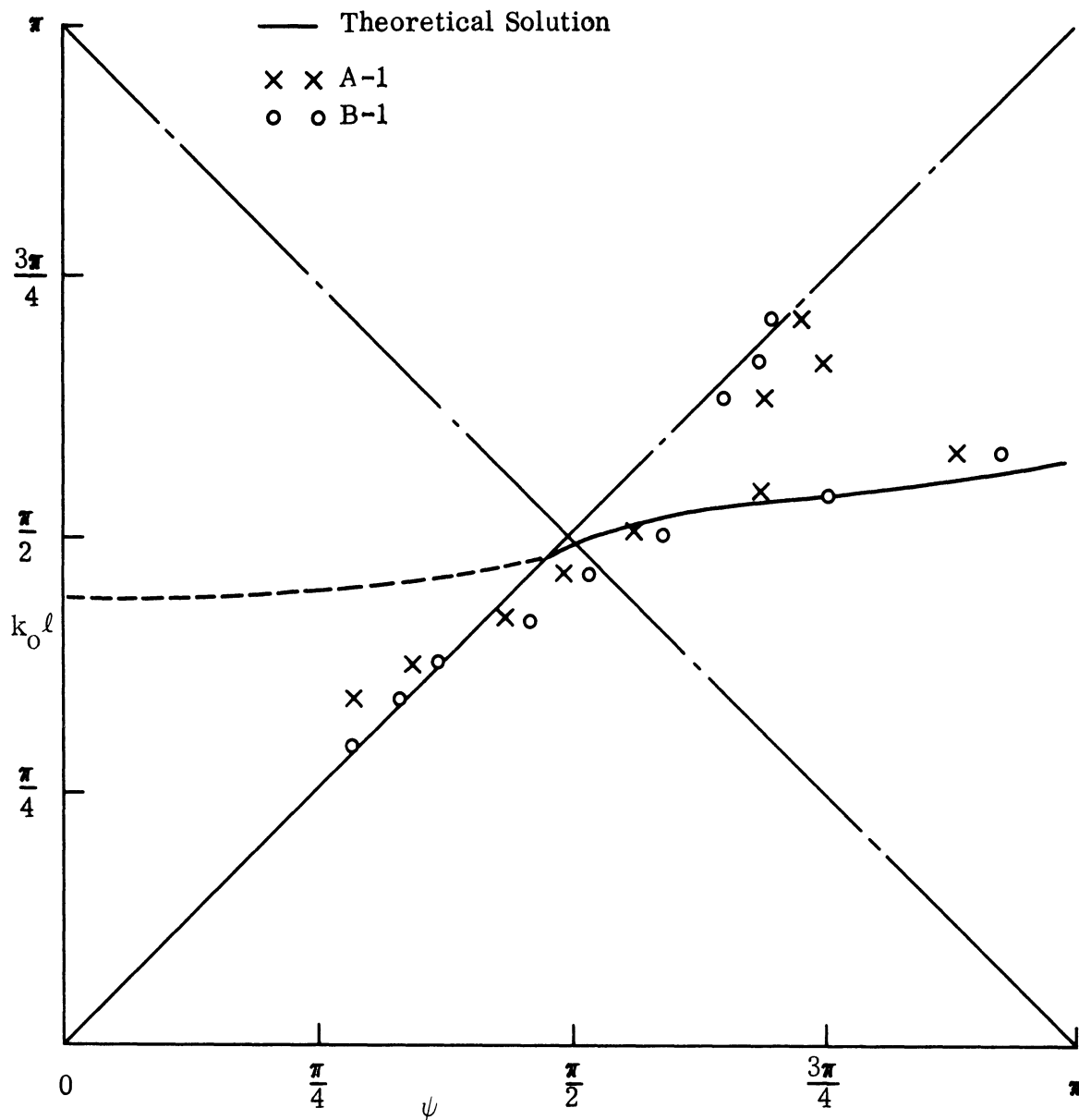


FIG. 3-18; THEORETICAL AND MEASURED DISPERSION CHARACTERISTICS.

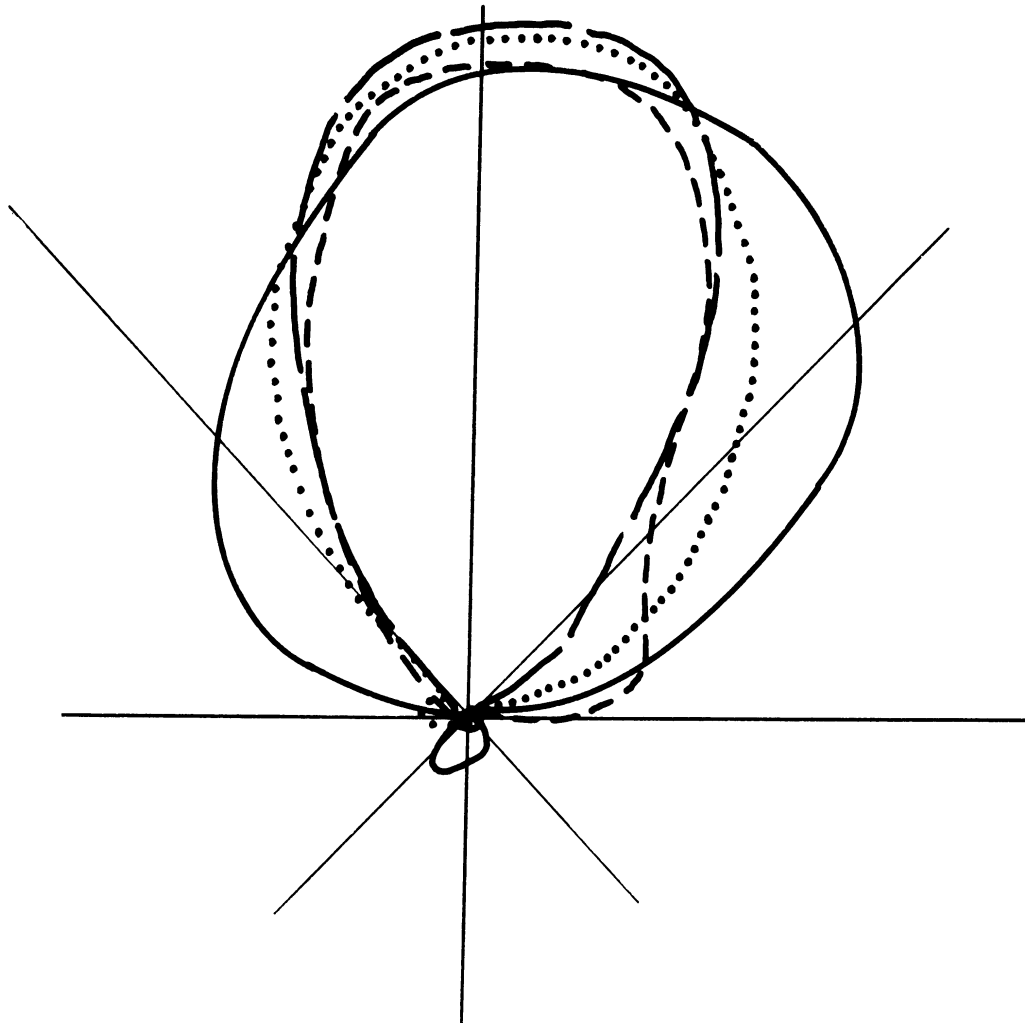


Fig. 3-19a: FAR FIELD H-PLANE  $E_y$ -PATTERN FOR ANTENNA  
A-1. — 350 MHz, ..... 400 MHz, - - - 450 MHz,  
- - - 500 Mhz.



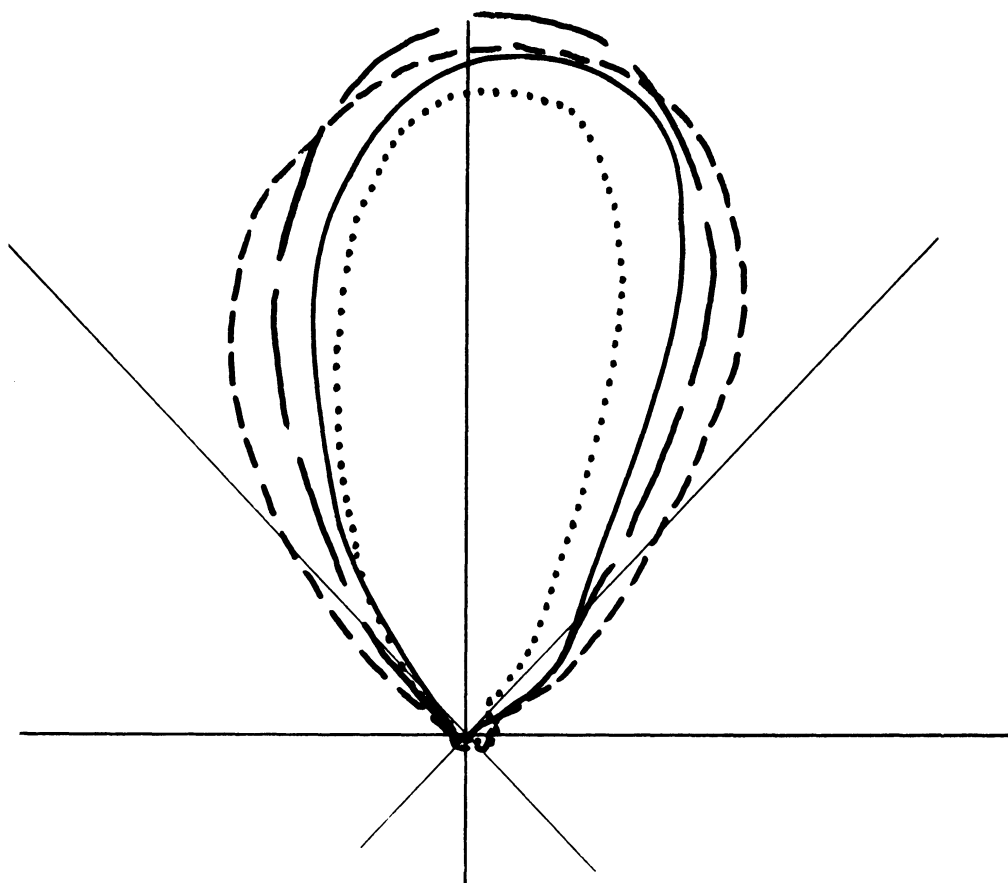


FIG. 3-19b: FAR FIELD H-PLANE  $E_y$ -PATTERN FOR ANTENNA A-1. — 550 MHz, ••• 600 MHz, - - - 650 MHz, — — — 700 MHz.

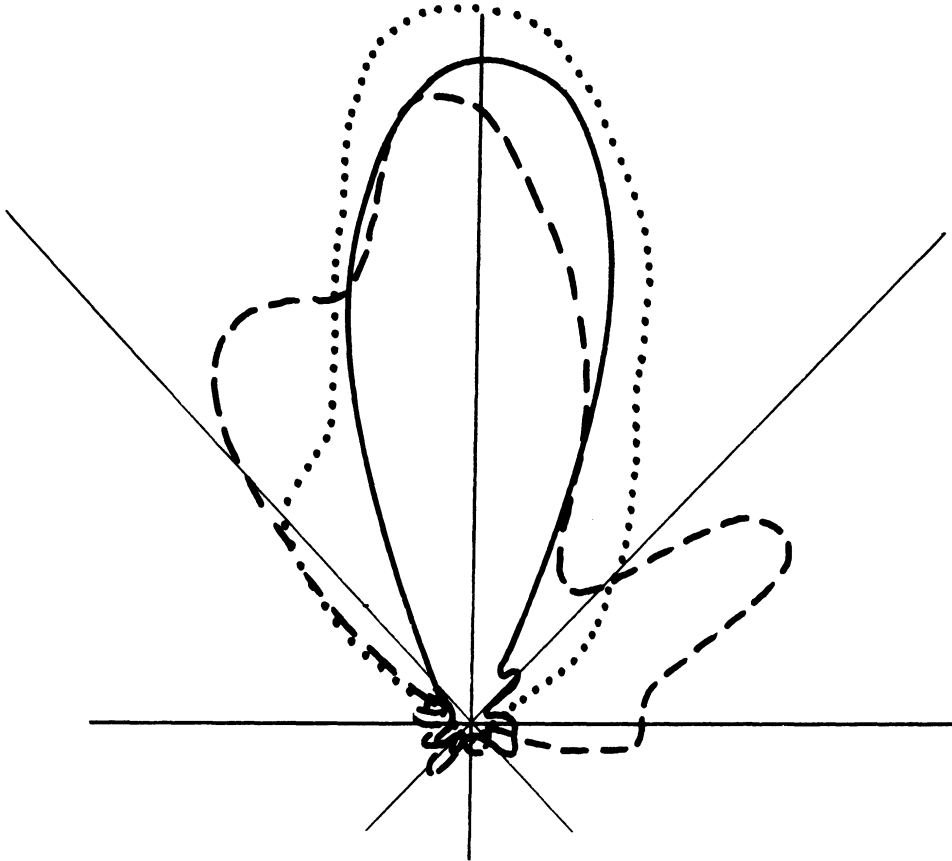


FIG. 3-19c: FAR FIELD H-PLANE  $E_y$ -PATTERN FOR ANTENNA  
A-1. — 750 MHz, •• 800 MHz, - - - 850 MHz.

THE UNIVERSITY OF MICHIGAN  
7848-1-F

Input impedance for the antenna of Fig. 3-13 is shown in Fig. 3-20. Note that a quarter wave line at 650 MHz could easily cancel out most of the reactive component over most of the band, resulting in a very good match to a 50  $\Omega$  transmission line. The interdigital spacing reduces the coupling enough between elements to maintain a high radiation resistance.

If the interdigital array is fed at either end, the patterns of Fig. 3-21 result. The array on which patterns were taken, antenna C-2, is similar to that shown in Fig. 3-13, except it is about a quarter again as long. At low frequencies (below about 650 MHz where  $kl = \pi/2$ ) the radiation is backfire. At higher frequencies, a change is made to the forward fire radiation typical of slow wave propagation. Interestingly enough, the impedance of this antenna is similar to that of the other antenna shown in Fig. 3-13.

### 3.4.2 Ferrite Loading

The ferrite powder EAF-2 was placed between the array surface and the ground plane for all models (A-1, A-2, A-3, B-1 and B-2) of the interdigital array (see Figs. 3-13 through 3-17). The specification of the models is repeated below in Table III for convenience.  $2N+1$  is the number of elements and  $2a, b, d$  and  $l$  are as defined in Fig. 3-12.

TABLE III: MODEL SPECIFICATIONS

Parameter	ANTENNA TYPE				
	A-1	A-2	A-3	B-1	B-2
$2N+1$	13	13	13	21	21
$(2a)^*$	0.15	0.15	0.15	0.15	0.15
$b$	1.2	1.8	2.4	1.2	1.8
$d$	1.0	1.0	1.0	1.0	1.0
$l$	8.0	8.0	8.0	8.0	8.0

\*Equivalent; all dimensions are in cm.

The far field patterns were taken and are shown in Figs. 3-22 through 3-26 along with the unloaded patterns at corresponding frequencies. Figure 3-22 shows the far field patterns of the antenna A-1. It is seen that the unloaded antenna has a fairly broad bandwidth above 350 MHz. This seems to indicate a shift in center

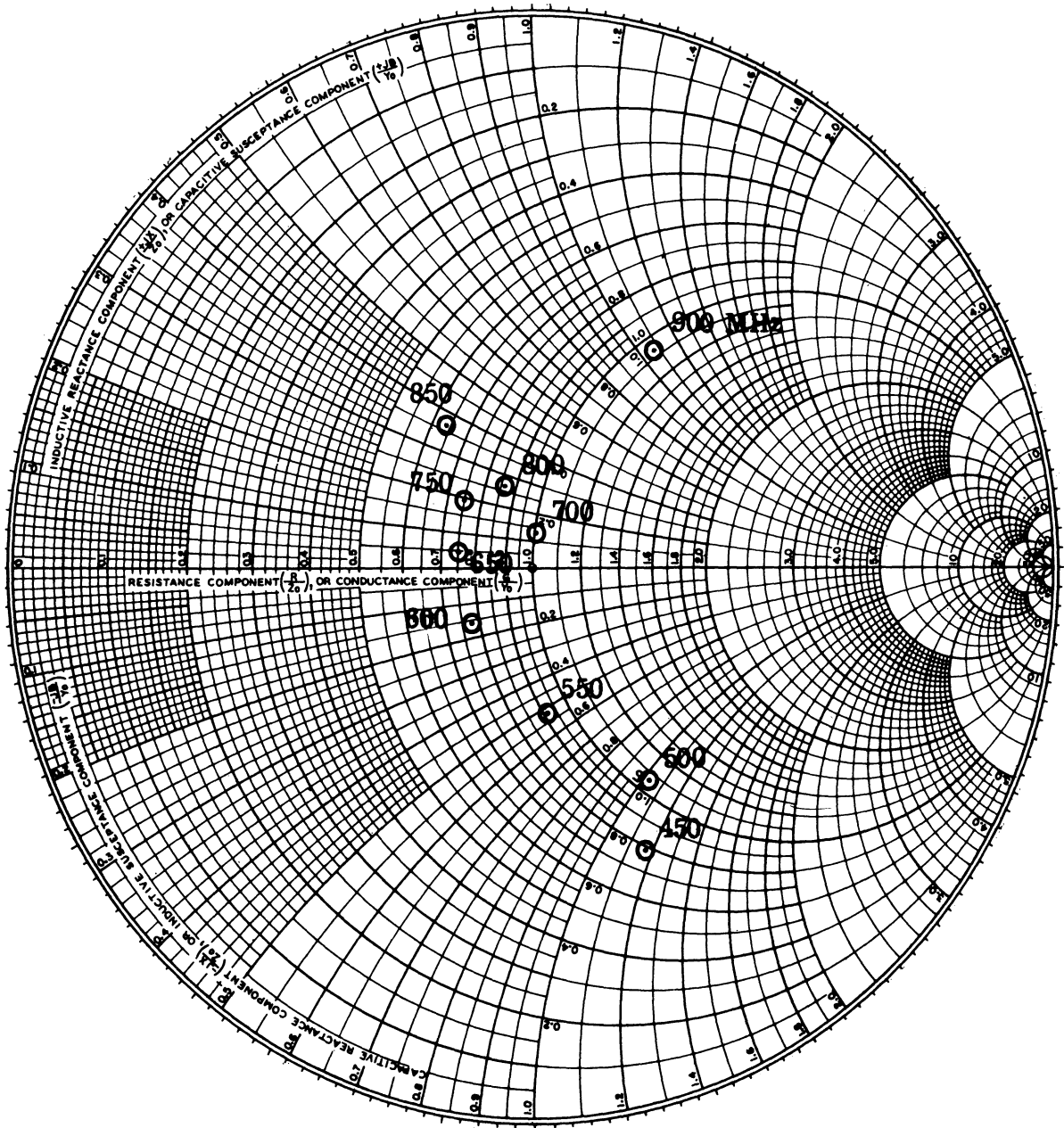
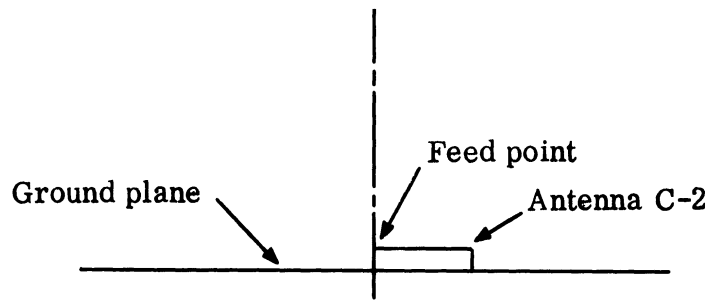
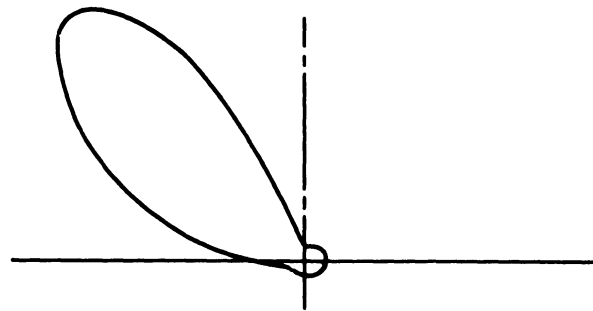


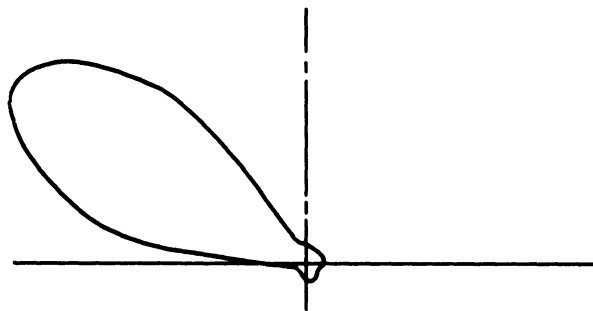
FIG. 3-20: INPUT IMPEDANCE FOR ANTENNA A-1.



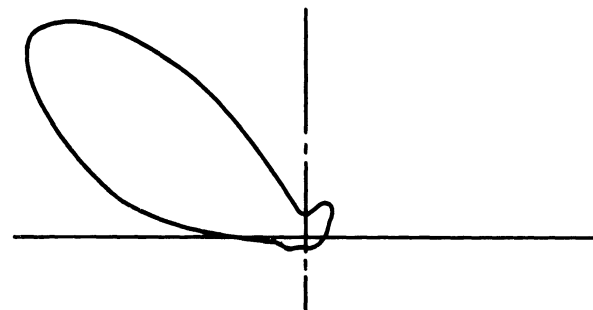
(a) Antenna C-2 Fed at Left End of the Array



(b) 450 MHz

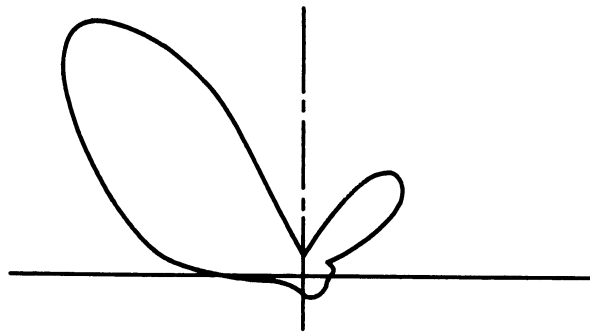


(c) 500 MHz

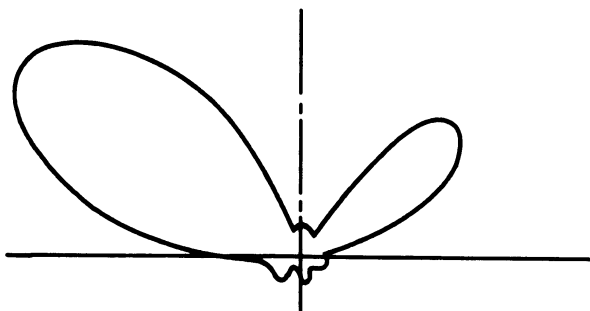


(d) 550 MHz

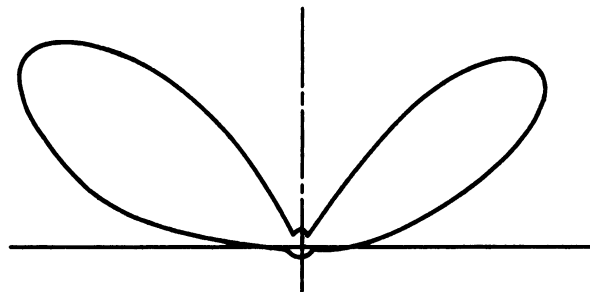
FIG. 3-21a: FAR FIELD H-PLANE POWER PATTERN FOR ANTENNA C-2 FED AT LEFT END OF THE ARRAY.



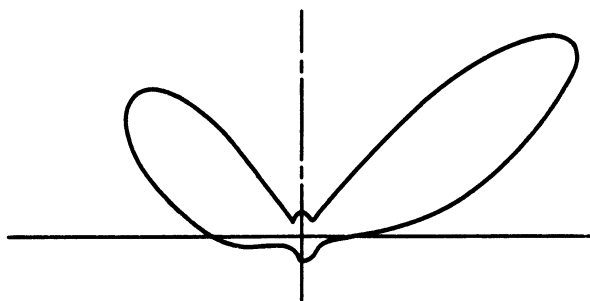
(e) 600 MHz



(f) 650 MHz

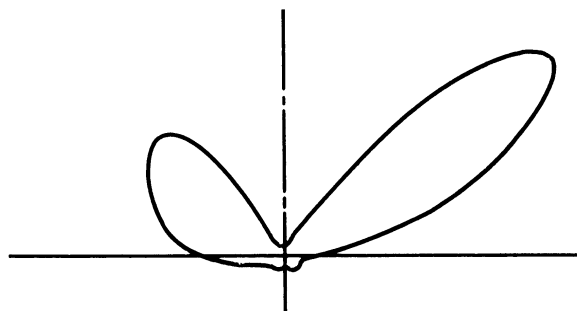


(g) 700 MHz

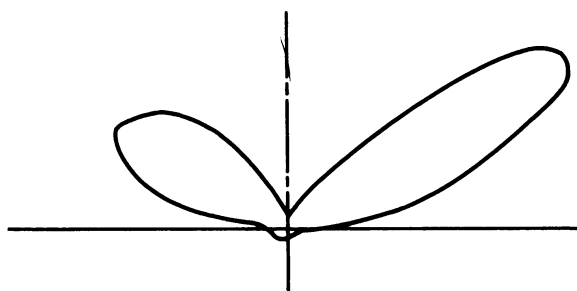


(h) 750 MHz

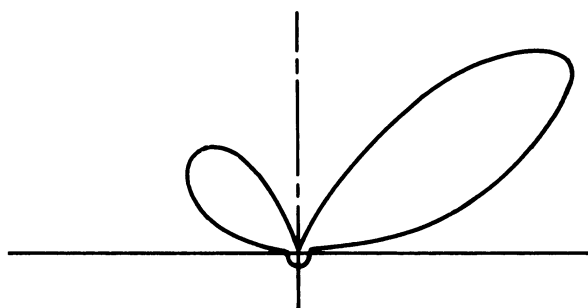
FIG. 3-21b: FAR FIELD H-PLANE POWER PATTERN FOR ANTENNA C-2 FED AT LEFT END OF THE ARRAY



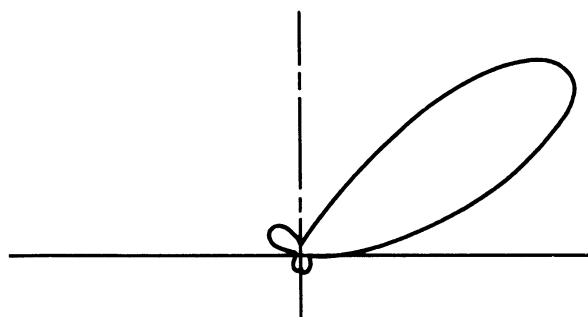
(i) 800 MHz



(j) 850 MHz

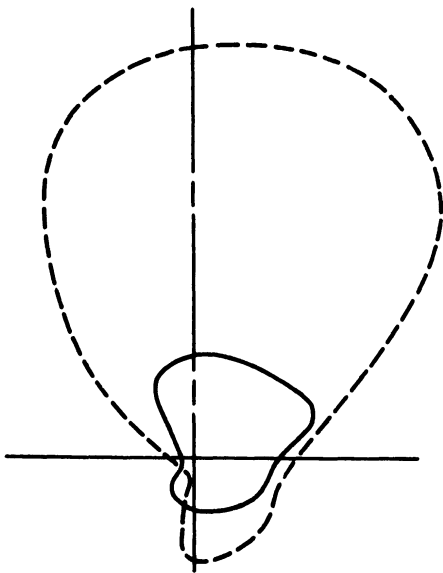


(k) 900 MHz

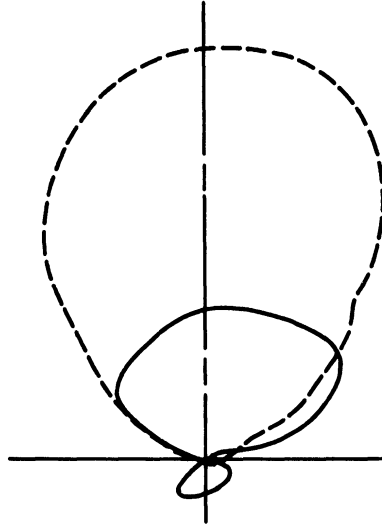


(l) 950 MHz

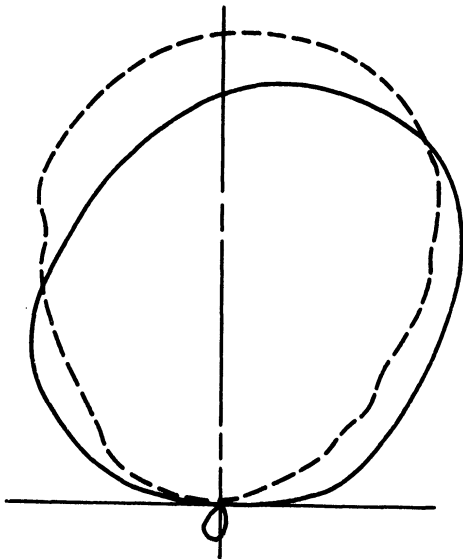
FIG. 3-21c: FAR FIELD H-PLANE POWER PATTERN FOR ANTENNA C-2 FED AT LEFT END OF THE ARRAY.



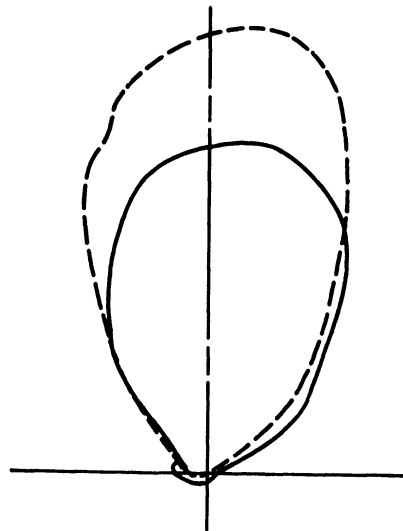
250 MHz



300 MHz



350 MHz



400 MHz

FIG. 3-22a: THE FAR FIELD PATTERNS OF THE INTERDIGITAL ARRAY ANTENNA A-1 LOADED AND UNLOADED WITH EAF-2 FERRITES. (—) Unloaded (---) Loaded.



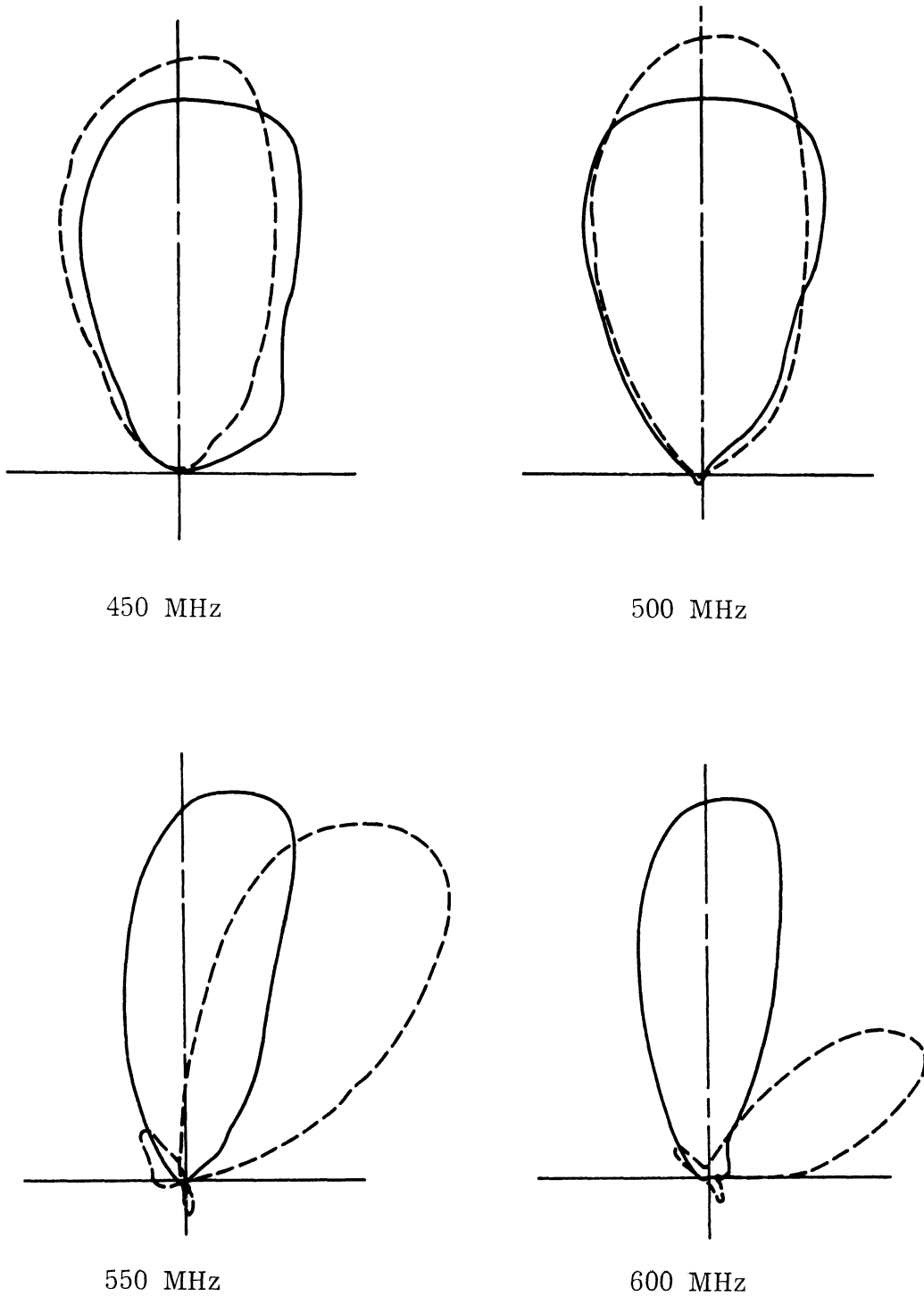


FIG. 3-22b: THE FAR FIELD PATTERNS OF THE INTERDIGITAL ARRAY ANTENNA A-1 LOADED AND UNLOADED WITH EAF-2 FERRITE. (—) Unloaded, (---) Loaded.

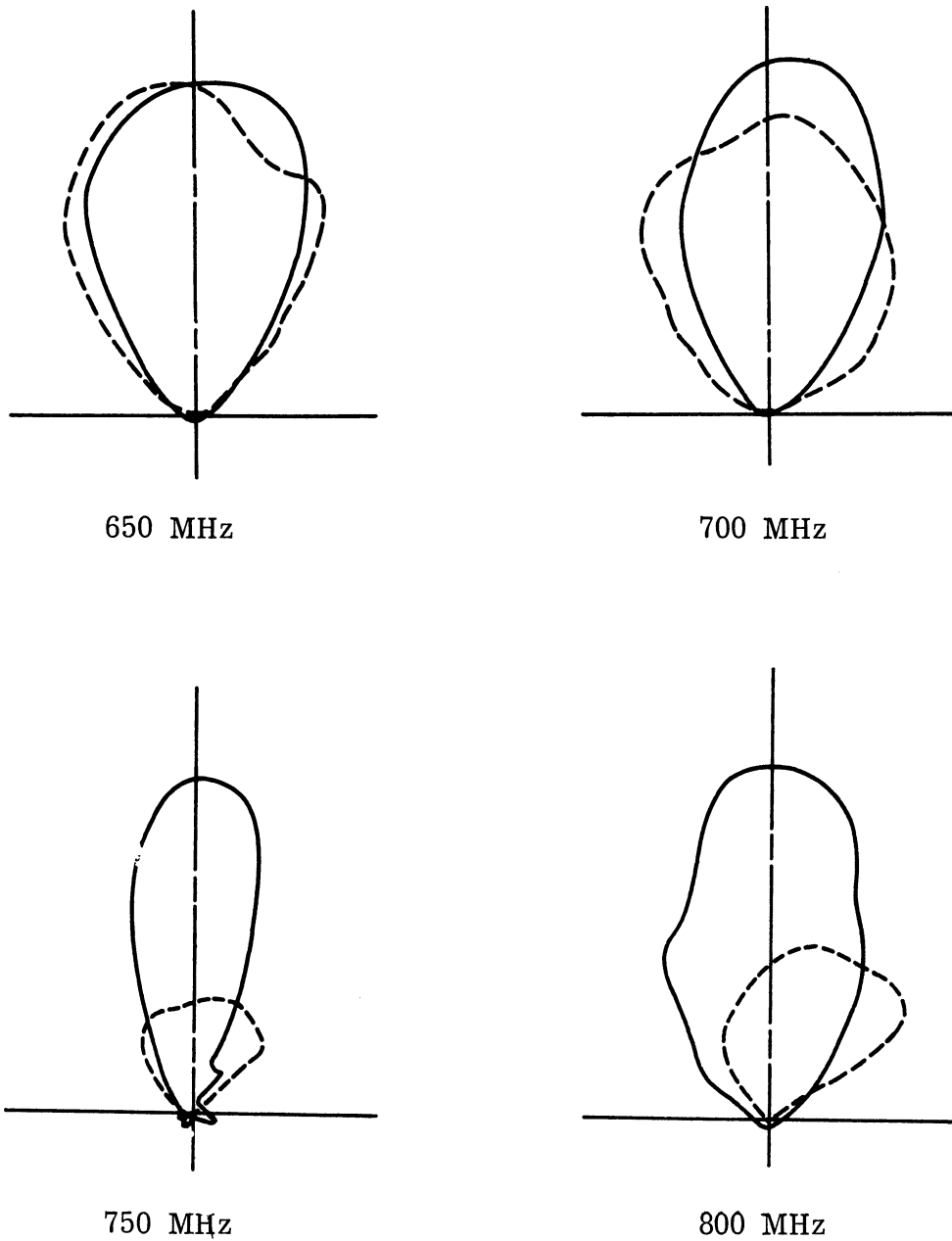
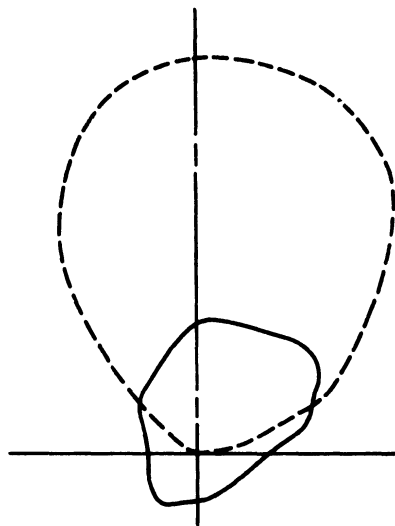
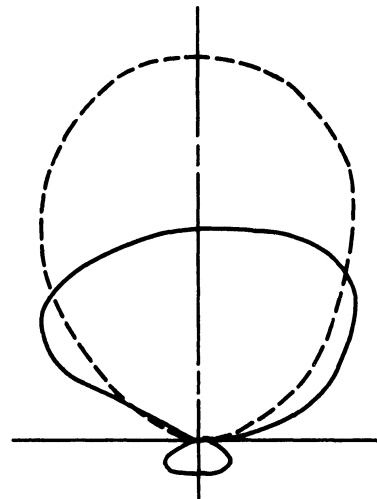


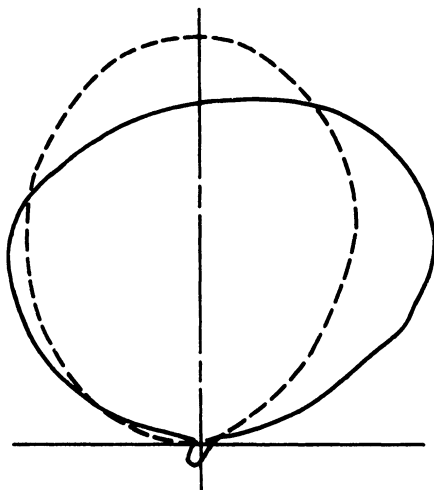
FIG. 3-22c: THE FAR FIELD PATTERNS OF THE INTERDIGITAL ARRAY ANTENNA A-1 LOADED AND UNLOADED WITH EAF-2 FERRITE. (—) Unloaded, (---) Loaded.



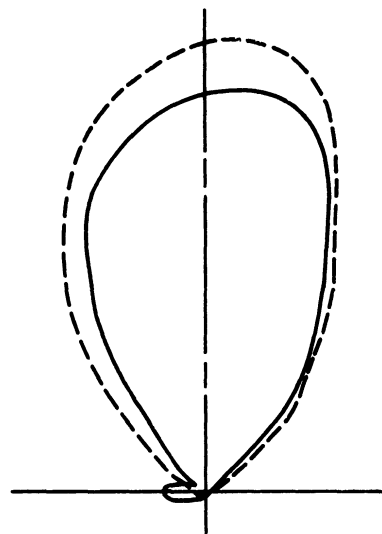
250 MHz



300 MHz



350 MHz



400 MHz

FIG. 3-23a: THE FAR FIELD PATTERNS OF THE INTERDIGITAL ARRAY ANTENNA A-2 LOADED AND UNLOADED WITH EAF-2 FERRITE. (—) Unloaded, (---) Loaded.

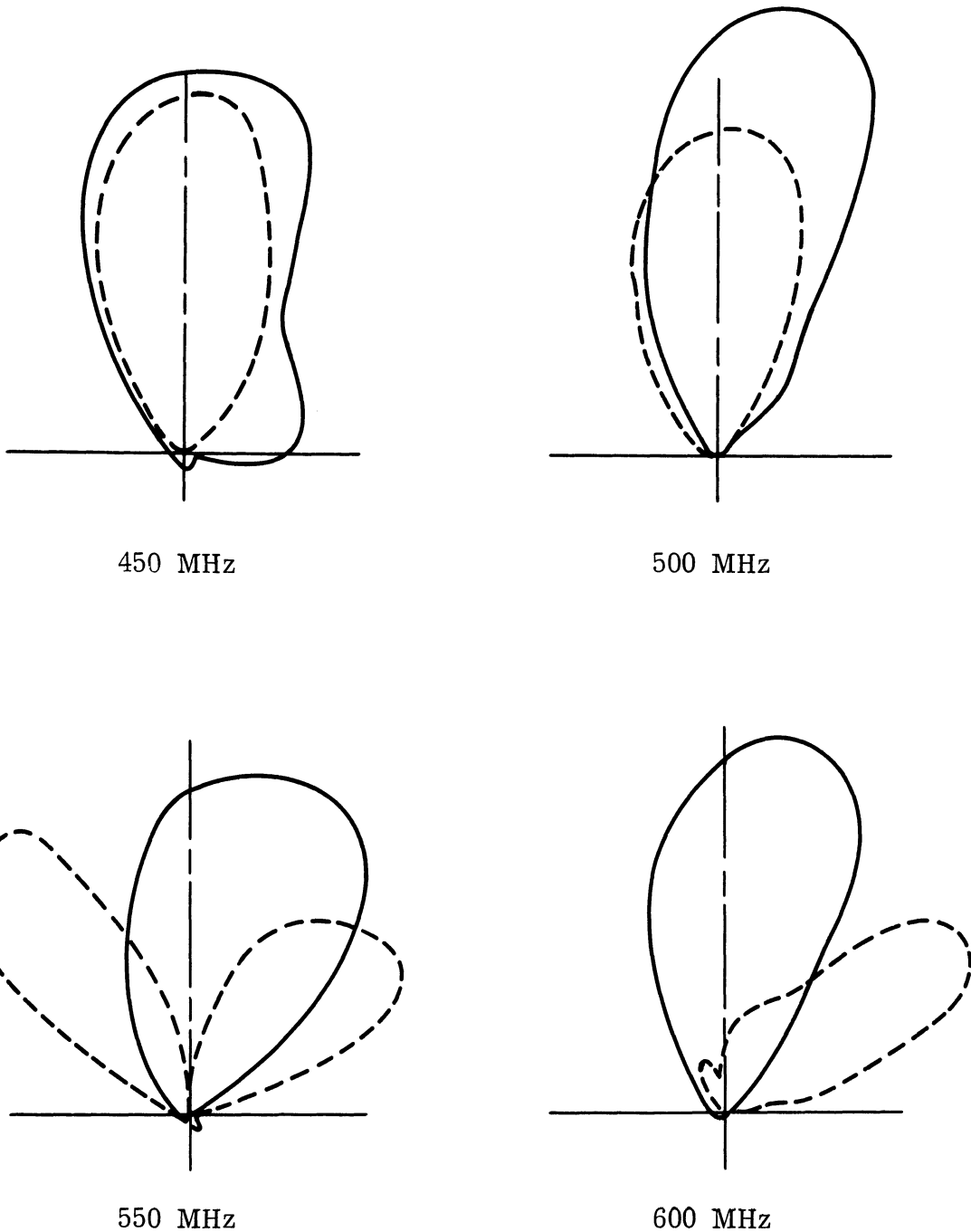
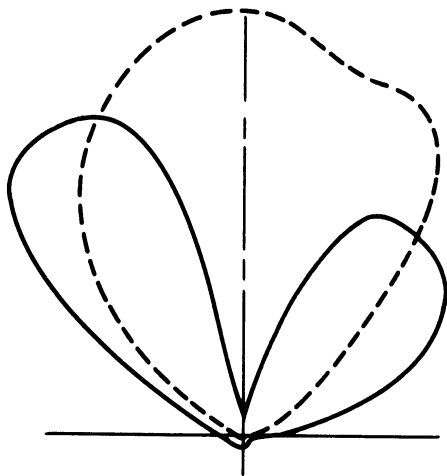
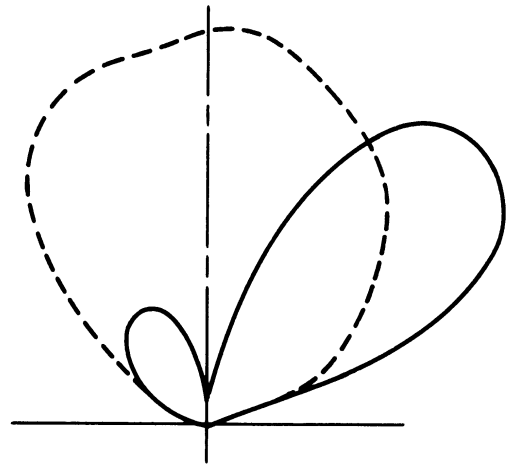


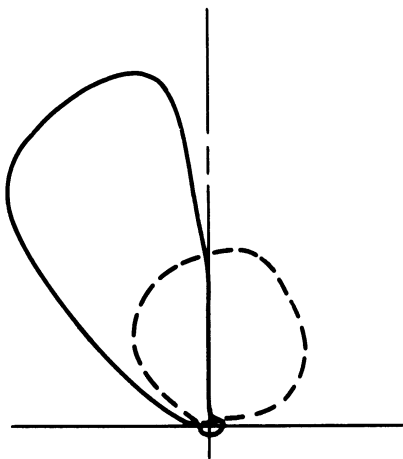
FIG. 3-23b: THE FAR FIELD PATTERNS OF THE INTERDIGITAL ARRAY ANTENNA A-2 LOADED AND UNLOADED WITH EAF-2 FERRITE. (—) Unloaded, (---) Loaded.



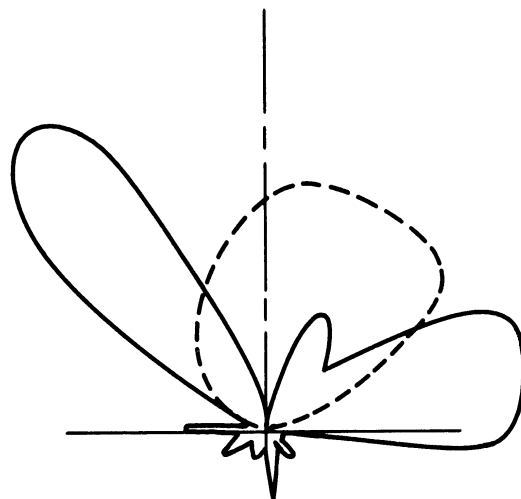
650 MHz



700 MHz



750 MHz



800 MHz

FIG. 3-23c: THE FAR FIELD PATTERNS OF THE INTERDIGITAL ARRAY ANTENNA A-2 LOADED AND UNLOADED WITH EAF-2 FERRITE. (—) Unloaded, (---) Loaded.

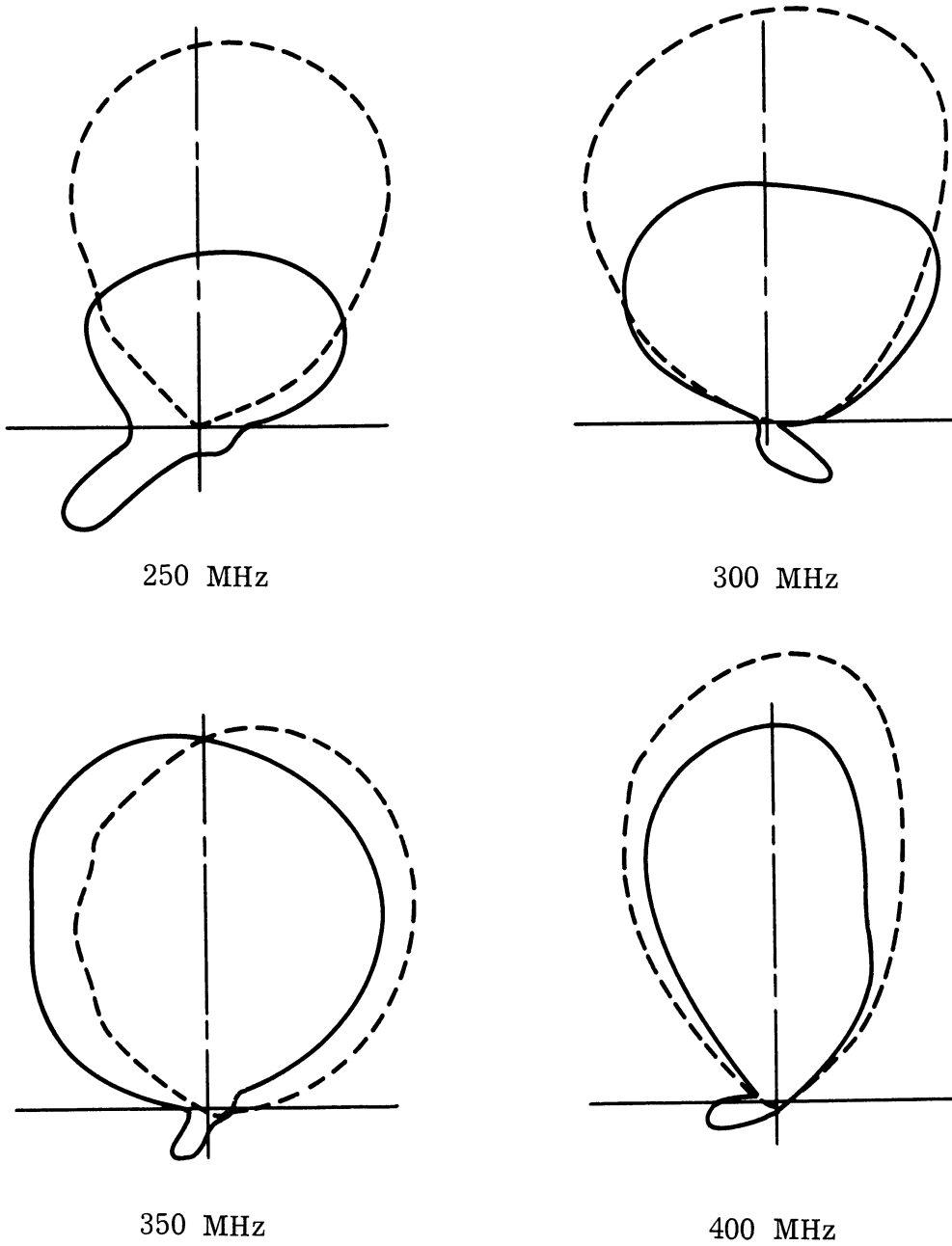
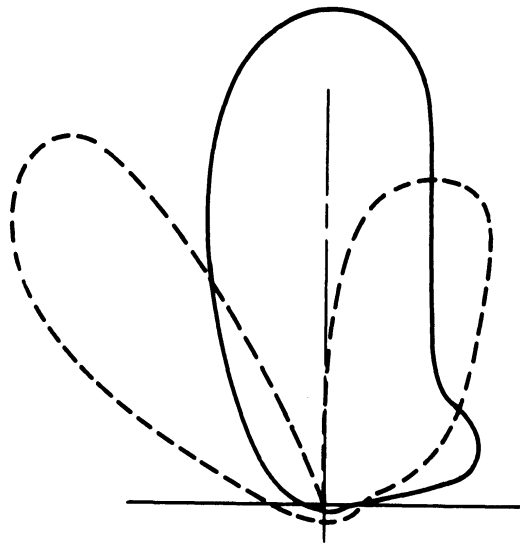
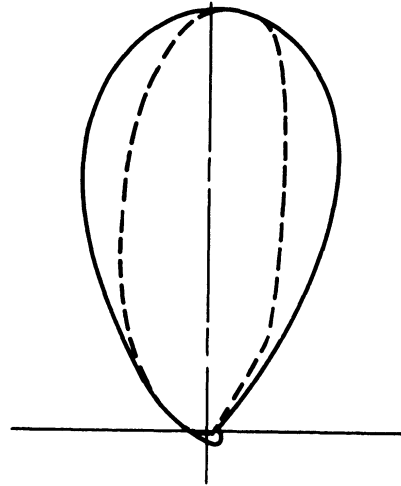


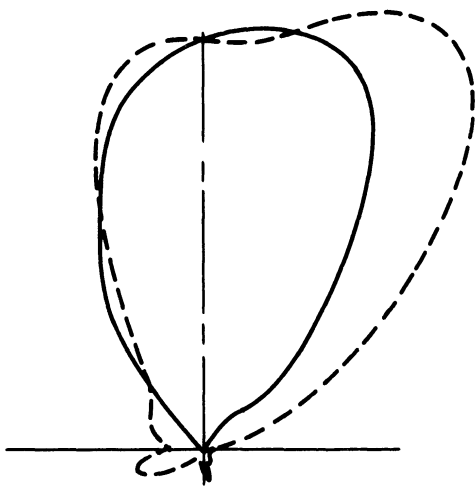
FIG. 3-24a: THE FAR FIELD PATTERNS OF ANTENNA A-3  
LOADED AND UNLOADED WITH EAF-2 FERRITE.  
(—) Unloaded, (---) Loaded.



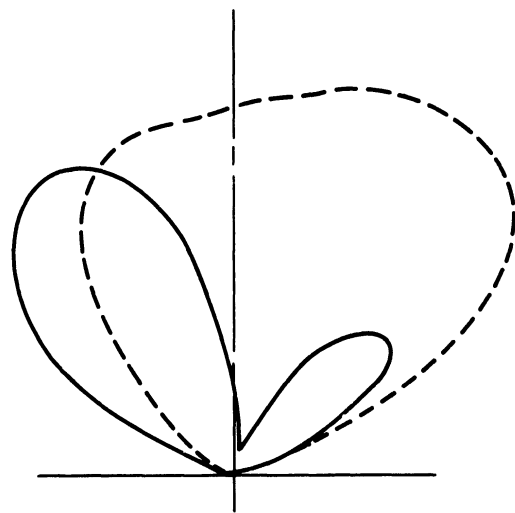
450 MHz



500 MHz



550 MHz



600 MHz

FIG. 3-24b: THE FAR FIELD PATTERNS OF ANTENNA A-3  
 LOADED AND UNLOADED WITH EAF-2 FERRITE.  
 (—) Unloaded, (---) Loaded.

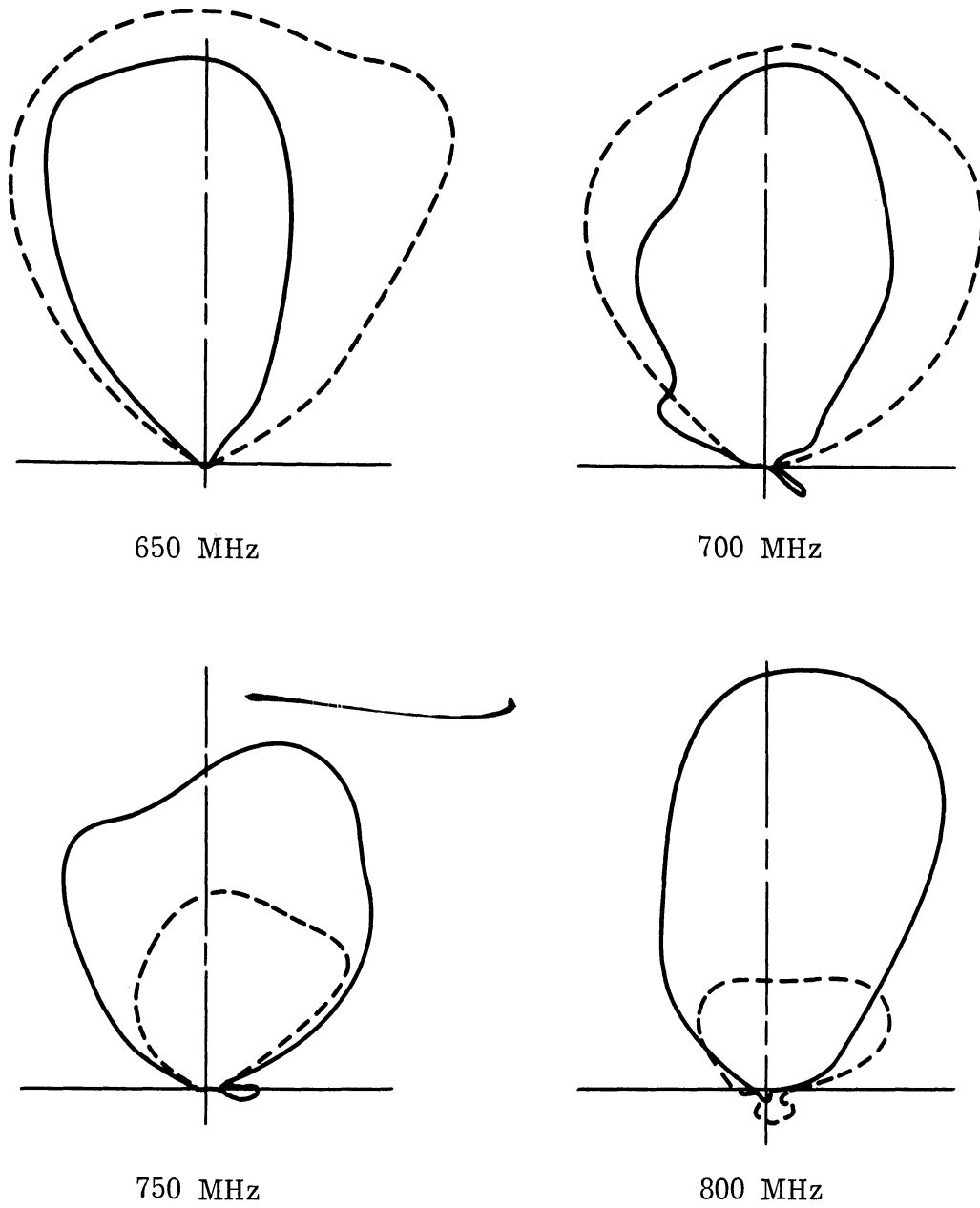


FIG. 3-24c: THE FAR FIELD PATTERNS OF ANTENNA A-3  
LOADED AND UNLOADED WITH EAF-2 FERRITE.  
(—) Unloaded, (---) Loaded.



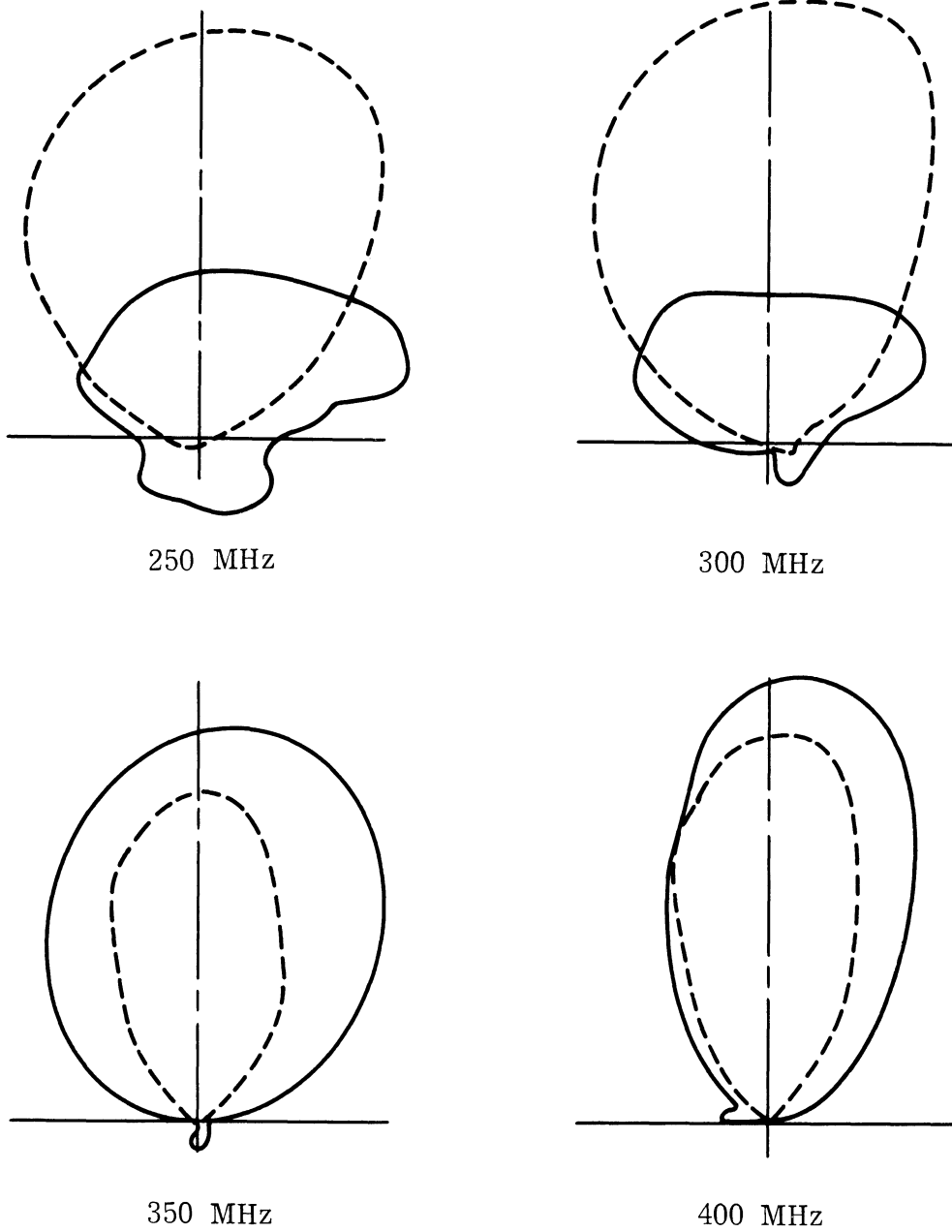
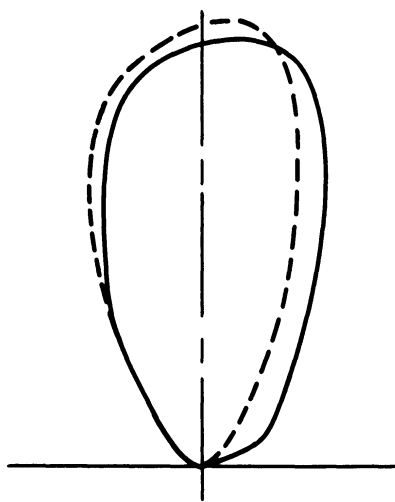
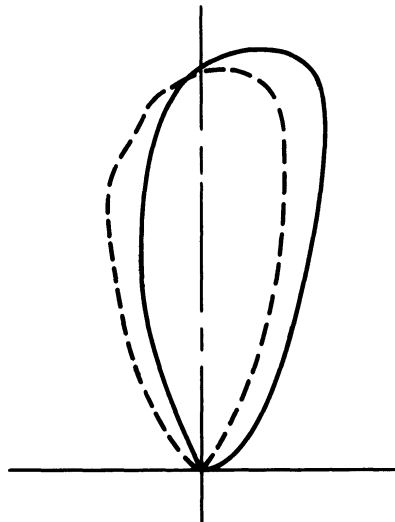


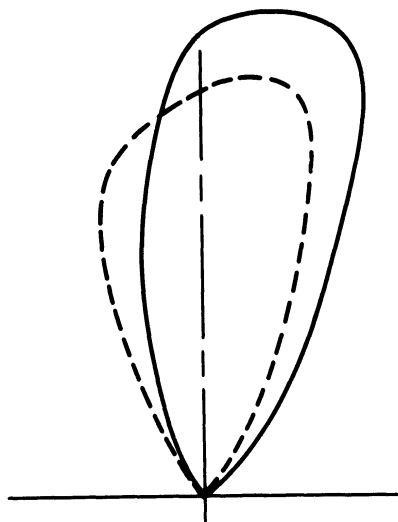
FIG. 3-25a: THE FAR FIELD PATTERNS OF ANTENNA B-1  
LOADED AND UNLOADED WITH EAF-2 FERRITE.  
(—) Unloaded, (---) Loaded.



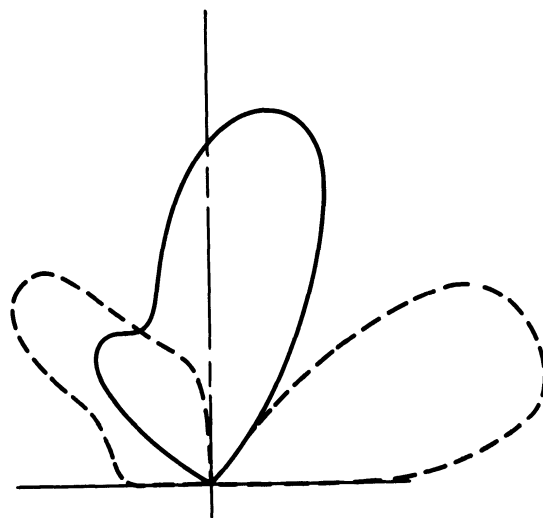
450 MHz



500 MHz



550 MHz



600 MHz

FIG. 3-25b: THE FAR FIELD PATTERNS OF ANTENNA B-1  
LOADED AND UNLOADED WITH EAF-2 FERRITE.  
(—) Unloaded, (---) Loaded.

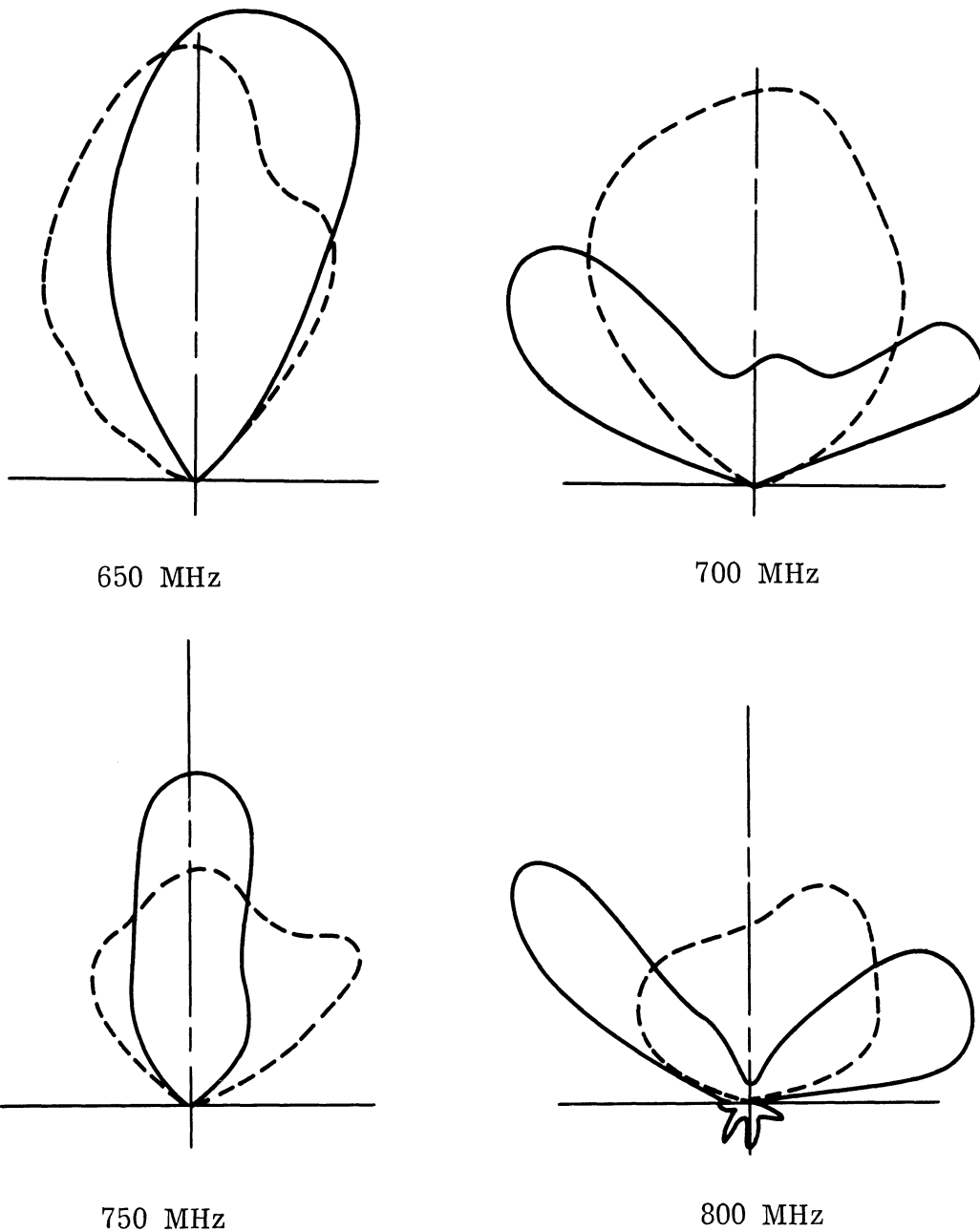


FIG. 3-25c: THE FAR FIELD PATTERNS OF ANTENNA B-1  
 LOADED AND UNLOADED WITH EAF-2 FERRITE.  
 (—) Unloaded, (---) Loaded.

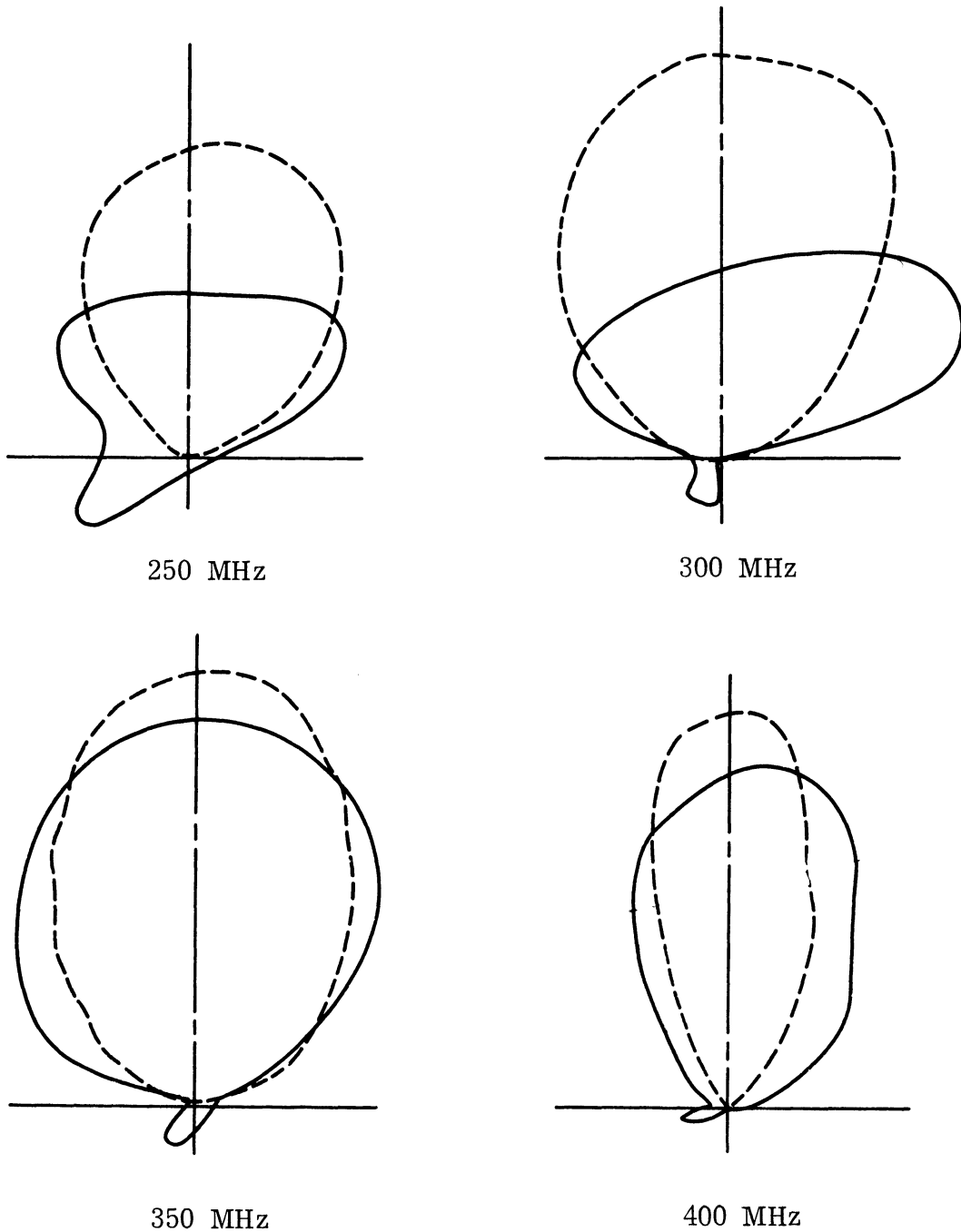


FIG. 3-26a: THE FAR FIELD PATTERNS OF ANTENNA B-2 LOADED AND UNLOADED WITH EAF-2 FERRITE. (—) Unloaded, (---) Loaded.

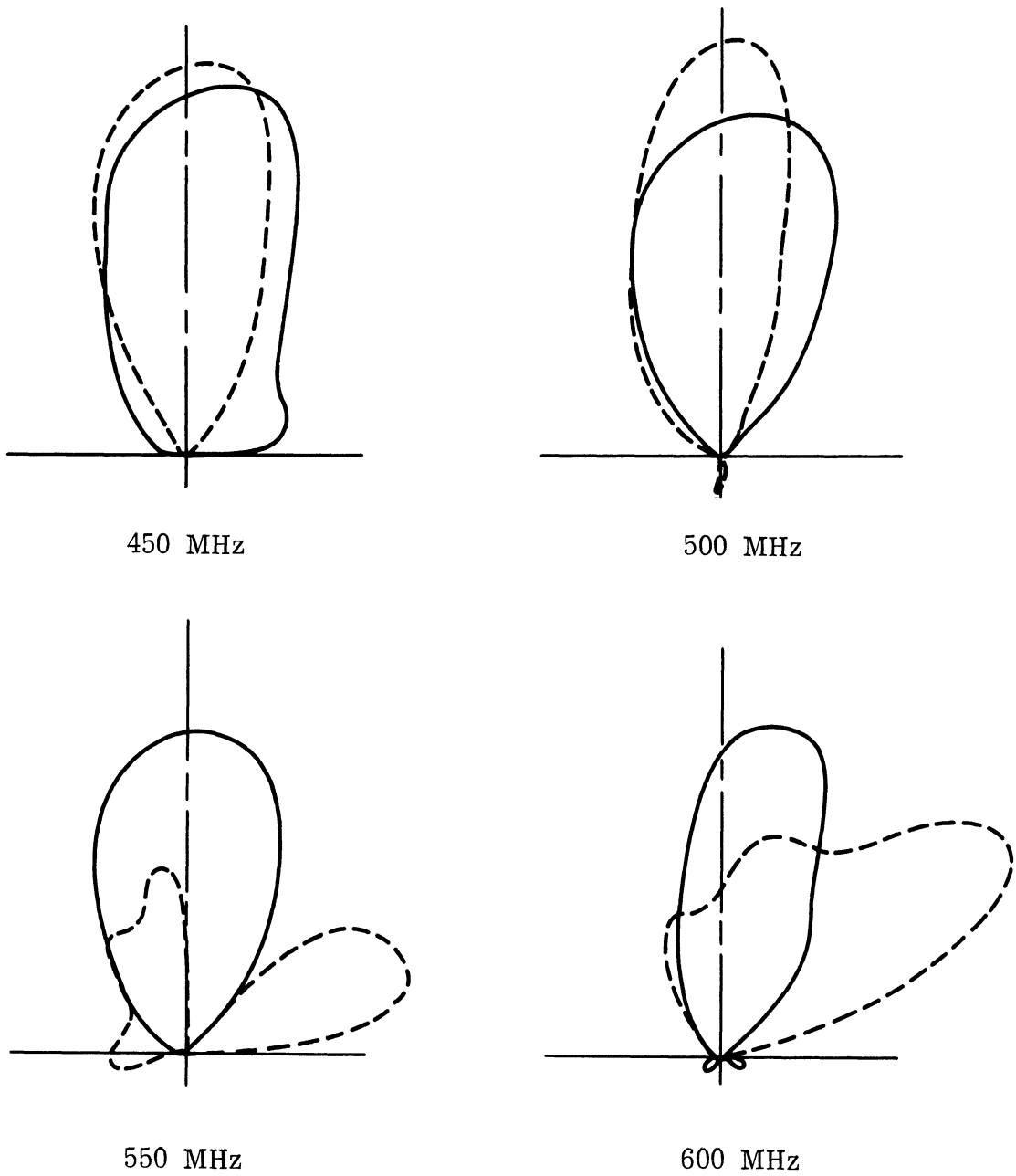
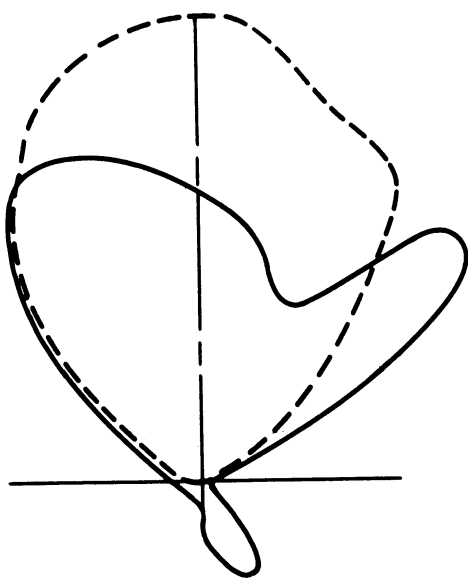
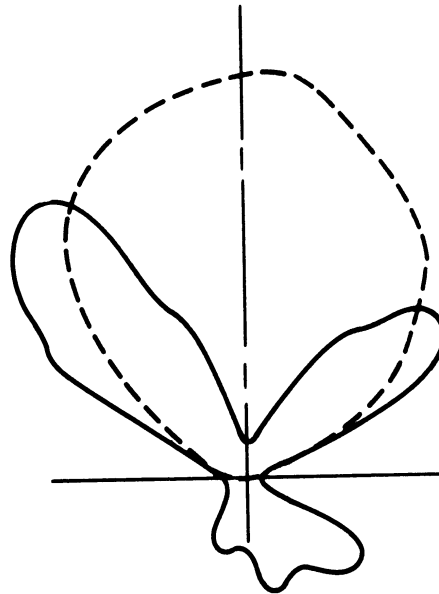


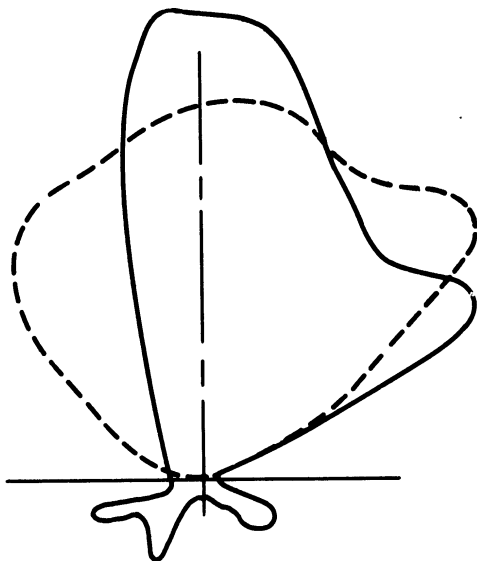
FIG. 3-26b: THE FAR FIELD PATTERNS OF ANTENNA B-2  
 LOADED AND UNLOADED WITH EAF-2 FERRITE.  
 (—) Unloaded, (---) Loaded.



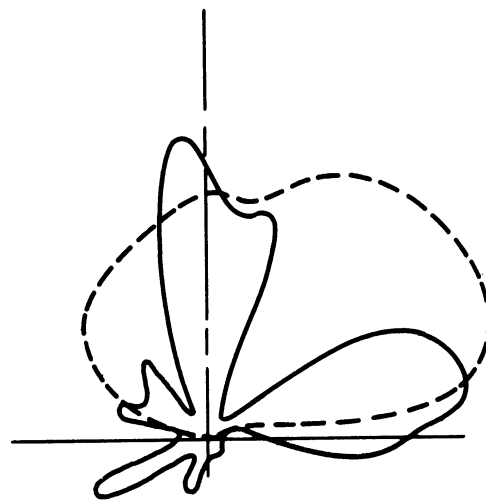
650 MHz



700 MHz



7500 MHz



800 MHz

FIG. 3-26c: THE FAR FIELD PATTERNS OF ANTENNA B-2 LOADED AND UNLOADED WITH EAF-2 FERRITE. (—) Unloaded, (---) Loaded.

frequency as well as a narrower bandwidth when the antenna is loaded with a ferrite material.

Similar effects are seen for antenna A-2 (Fig. 3-23). Antenna A-3 seems to have a lower center frequency and a lower upper frequency bound (450 MHz) than the other models (Fig. 3-24). Antenna B-1 (Fig. 3-25) is good up to 600 MHz, a little higher than antenna A-1, while B-2 (Fig. 3-26) is good up to only 550 MHz, a little lower than antenna A-2.

Although a conclusion cannot be drawn from the above observations, it can be said in general that the effect of loading an interdigital array with ferrite material is to lower the center frequency and to decrease the bandwidth of the structure. A shift of the lower frequency bound is seen to be from 350 MHz down to 250 MHz; this is quite significant if the decrease in bandwidth is not considered to be a serious disadvantage.

### 3.5 Power Capability of Ferrite Loaded Slot Antennas

Since it is anticipated that ferrite loaded transmitting antennas may be operated at high power input levels, an investigation was made of the limitations which may be imposed on allowable power levels due to excessive heating of the loading material and possible deterioration of its inherent magnetic and electrical properties. As a preliminary investigation, a cavity slot antenna filled with EAF-2A powdered ferrite was tested at 10, 50, 100 and 150 watt inputs. The temperature distribution was measured by means of a series of thermocouples placed along the broad center line of the cavity (Fig. 3-27).

The dimensions of the slot antenna tested are 12"x3" backed by a cavity 5" deep. The thermocouples are Copper-Constantan probes inserted 2.5" into the aperture face of the cavity. After a typical temperature vs thermocouple location curve was established (Fig. 3-27), only the thermocouple located at the point of maximum temperature rise (center of antenna) was retained. The rest were removed in order to eliminate the perturbations of the electromagnetic field. The data points for the curves of Fig. 3-27 were taken after thermal equilibrium was reached.

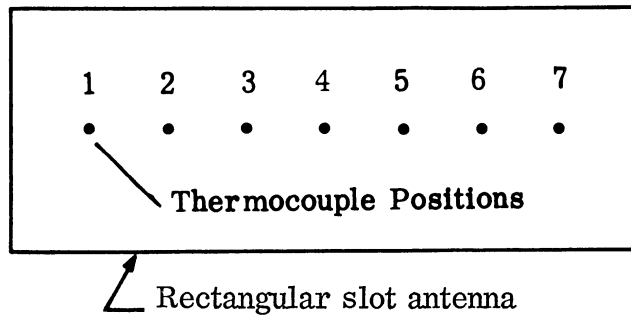
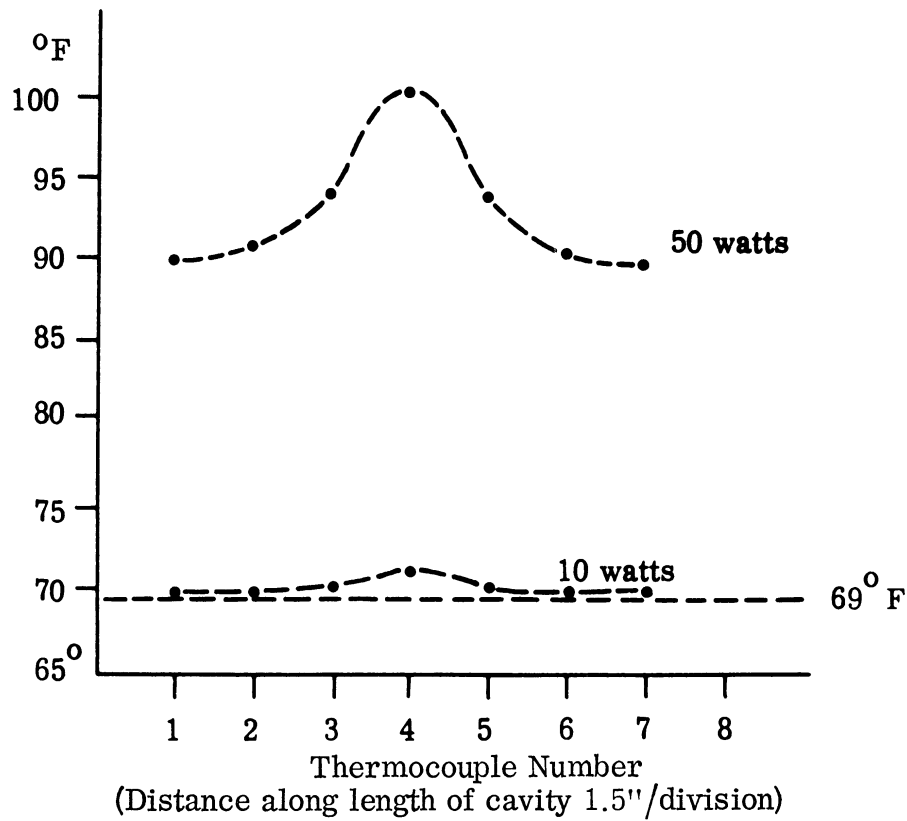


FIG. 3-27: TEMPERATURE VS POSITION IN CAVITY AT THERMAL EQUILIBRIUM.

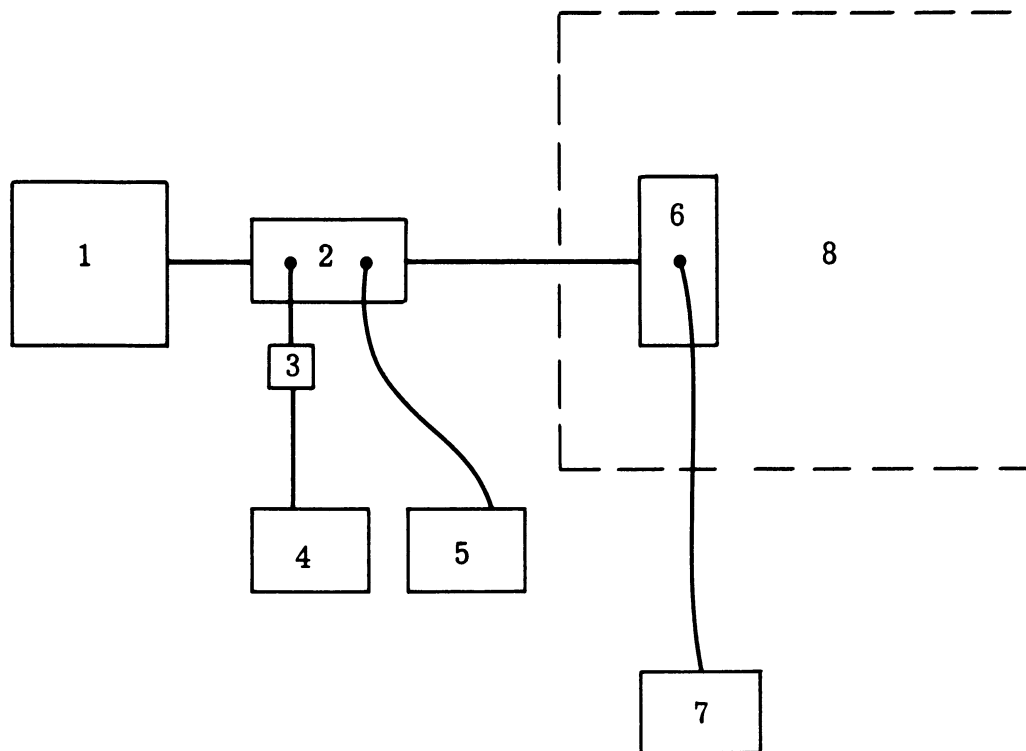


The block diagram of the experimental set-up is shown in Fig. 3-28. This arrangement was decided upon as the most appropriate, after several schemes were tried. The frequency of operation for the tests was 312.5 MHz where the VSWR was 1.16 and 1.47 respectively, with and without thermocouple No. 4 in position. Some of the results of the experiments are shown in Figs. 3-29 and 3-30. Of particular interest is the graph of temperature vs time which appears in Fig. 3-29. This graph corresponds to 150 watts input. The 150 watt curve covers an abrupt change of the characteristics of the ferrite at temperatures ranging between 120 and 150<sup>o</sup> F. If this change is attributed to the deterioration of  $\mu'$  and  $\mu''$  at these temperatures, then from Fig. 3-30 the power limitation of the ferrite loaded, slot antenna is about 50 watts. However, before any definite conclusions are reached one must determine the exact dependence of  $\mu'$  and  $\mu''$  on temperature for the EAF-2A powdered ferrite. For this investigation measurements can be taken using modified techniques as given in the references (Rado, 1953 and Lax, 1962). Also, measurements for the determination of the performance of ferrite loaded antennas, at elevated temperatures showing any deterioration of radiation pattern or efficiency should be made.

### 3.6 Waveguide Slot Arrays

Considerable effort was spent to fabricate a ferrite-loaded slot array to operate below 200 MHz. For the limited amount of ferrite material available in this Laboratory, a waveguide section (11.5cm x 1.0cm x 120 cm) designed to have a cutoff frequency at 126 MHz with Q-3 ferrite sticks filling the inside was tested as a transmission line before the slots were cut in the waveguide. A small current loop located approximately one-fourth of a guide wavelength from the adjustable shorting end was used to obtain an optimum impedance match. The VSWR characteristic as a function of frequency from 180 to 900 MHz is shown in Fig. 3-31. The cutoff frequency is much higher than the designed frequency due to the unavoidable air gaps between the small solid ferrite sticks and the imperfections of the material.

Measurements of the wave attenuation along the ferrite-loaded waveguide were made with a voltage probe of a Hewlett-Packard Vector Voltmeter moved



1. High Power transmitter
2. 40 db Directional coupler
3. 10 db Attenuator
4. Incident power meter
5. Reflected power meter
6. Antenna
7. Temperature bridge
8. Anechoic chamber

FIG. 3-28: EXPERIMENTAL SET-UP

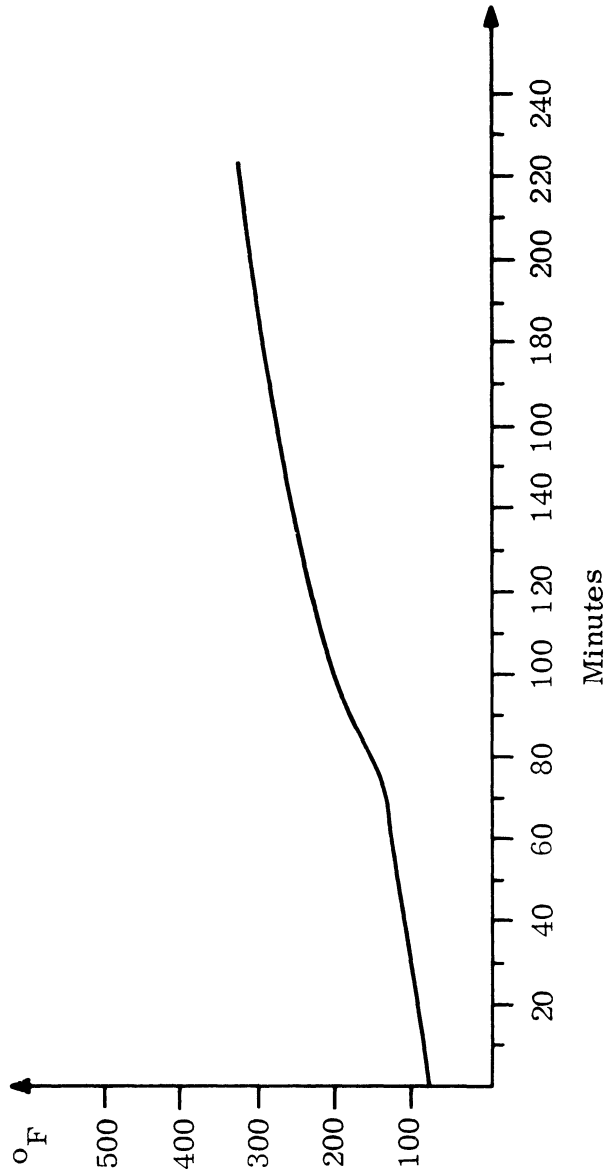


FIG. 3-29: INCREASE IN TEMPERATURE VS TIME (150 watts).

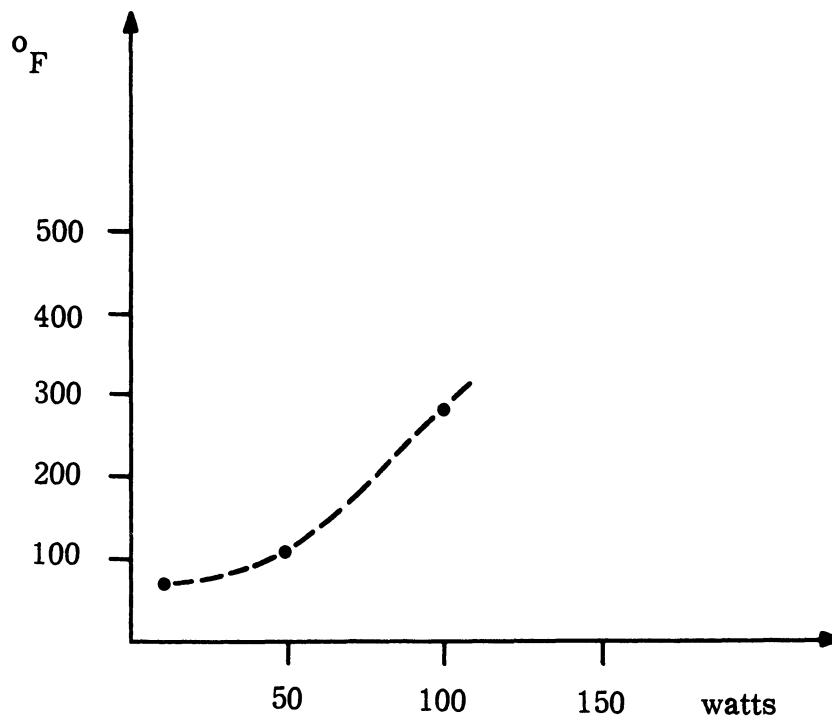


FIG. 3-30: °F VS WATTS.

THE UNIVERSITY OF MICHIGAN

7848-1-F

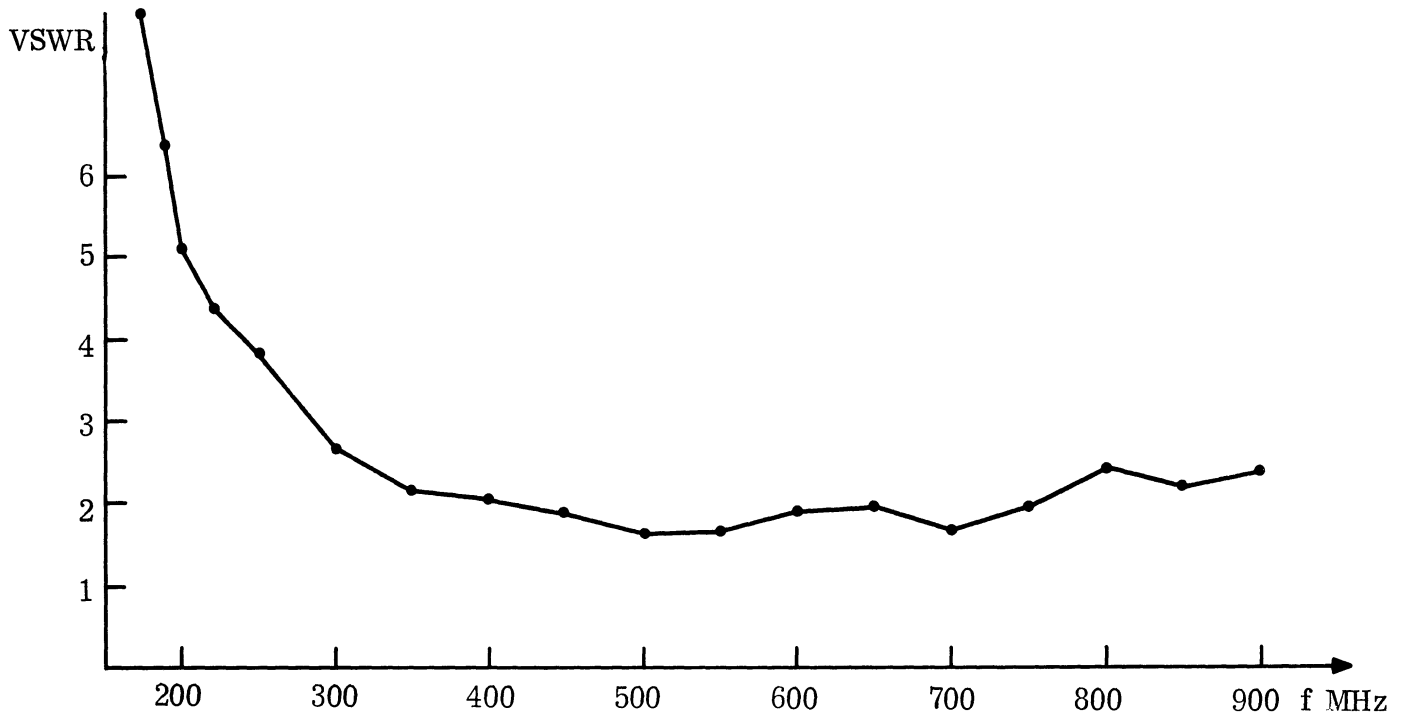


FIG. 3-31: VSWR OF THE 11.5 cm x 1.0 cm CROSS-SECTION Q-3 FERRITE FILLED WAVEGUIDE WITH A FEEDING LOOP LOCATED APPROXIMATELY 1/4 GUIDE WAVELENGTH FROM THE SHORTING END.

THE UNIVERSITY OF MICHIGAN  
7848-1-F

along a longitudinal slot located at the center of the waveguide. The results are shown in Fig. 3-32. An attenuation of -56 db per free space wavelength at 250 MHz was observed. The experimental study of the ferrite-loaded waveguide slot arrays was discontinued because of the impractically high ferrite loss in the waveguide.

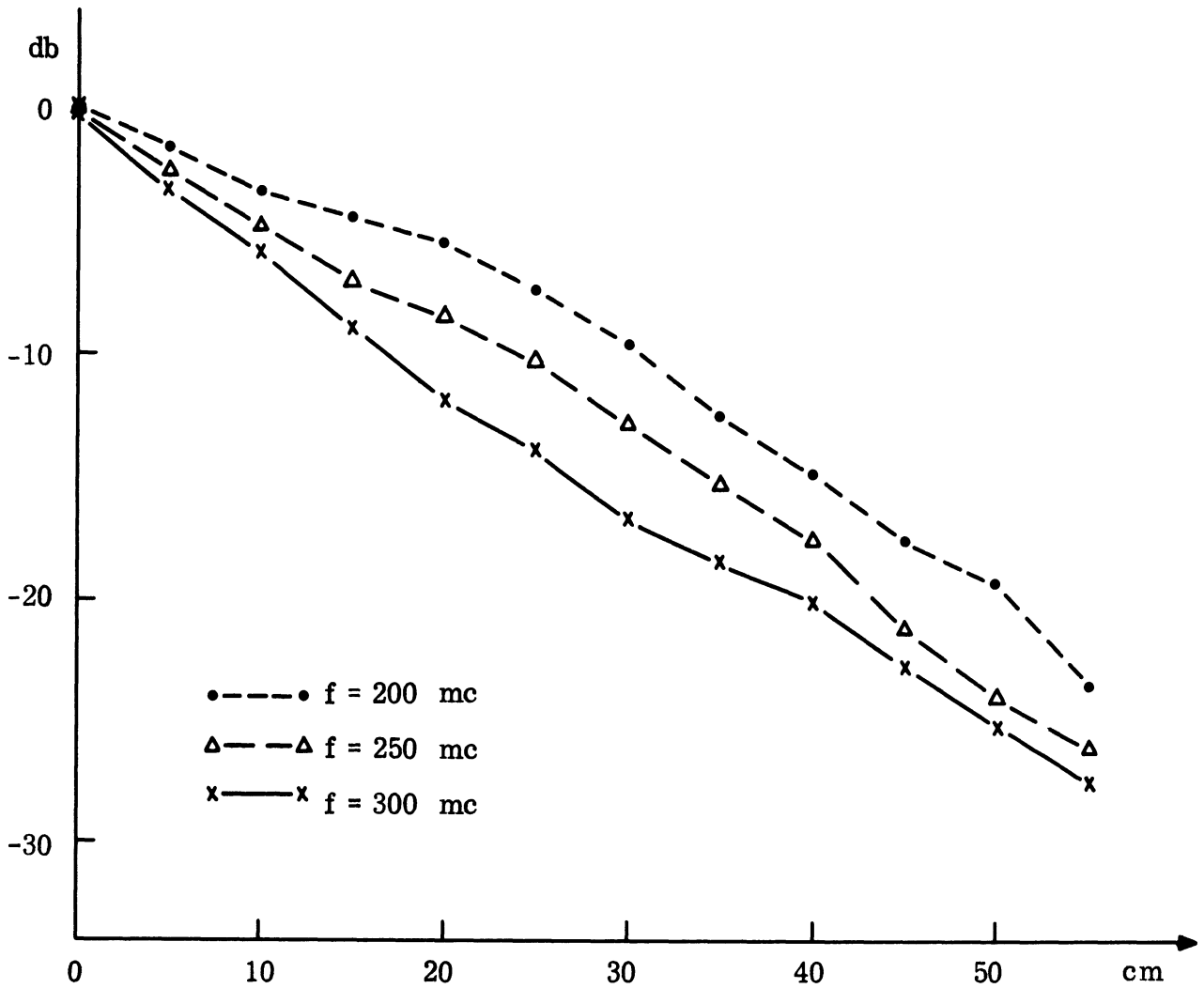


FIG. 3-32: WAVE ATTENUATION ALONG THE LONGITUDINAL DIRECTION OF THE 11.5 cm x 1.0 cm CROSS-SECTION Q-3FERRITE FILLED WAVEGUIDE.

IV

HE<sub>11</sub> MODE FERRITE ROD AND TUBE ANTENNAS\*

4.1 General Discussion

4.1.1 Introduction

A number of analyses on the dielectric rod antennas have been made in the past as listed in the references. Even so the dielectric rod antenna continues to be a challenging problem in electromagnetic theory because of not having an exact solution of the electromagnetic field distribution around the dielectric rod and its launching device.

Summaries of work on dielectric antennas appear in books (Kiely 1953), (Radwin 1961), (Wolff 1966). These books do not fully explore the radiation mechanism of these antennas nor explain some of the disagreements between those analyses and experiments. Therefore, no reliable design criteria exist for the dielectric rod antennas.

Arguments on the validity in the application of Schelkunoff's equivalence principle appear in a recent paper (James 1967). This article states that all treatments of a uniform cylindrical rod antenna radiating from the radial surface like a leaky guide are fallacious. Furthermore, the article states that radiation occurs only at discontinuities. These statements are examined in this report.

To extend the knowledge on this problem, the present analysis and experiments utilize a more general and effective guiding material — ferrite. For simplicity of the analysis throughout this work, the ferrite material will be assumed to be isotropic and lossless. Later, it will be shown that some losses in the ferrite material are tolerable without deteriorating the performance of the antenna as long as most of the surface wave energy is propagating external to the material. The present analysis shows that the radiation of the dielectric rod antenna is a superposition of the contributions from the primary current sources in the launching device and the induced

---

\* This section includes some of the results of the doctoral research of Mr. C-C Chen.



polarization and magnetization currents in the ferrite material. For a short rod antenna the radiated pattern is very close to the pattern from the open end of a circular waveguide supporting the  $TE_{11}$  mode. For a long rod antenna the induced currents becomes more important but in any case there is no null in the forward direction for a  $HE_{11}$  surface wave antenna. Before turning to the present work a brief review of the previous analyses will be given below for comparison.

4. 1. 2 Review of the Existing Approaches

1) Endfire Array Approach. Halliday and Kiely (1947), Mallach (1949), Beam (1950), Mueller (1952) and many others assumed the radial surface of the rod as an assemblage of a large number of isotropic radiators. By the Huygen's ray theory, these radiators result in the following pattern function:

$$F(\theta) = \frac{\sin U}{U} \tag{4. 1}$$

where

$$U = \frac{1}{2} kl \left( \frac{\lambda_o}{\lambda_g} - \cos \theta \right)$$

l = length of the dielectric rod

2) Equivalence Surface Approach. Watson and Horton (1948a, b), Kiely (1952), Chatterjee (1956), and Barnett (1963), assumed that the dielectric rod surface of the antenna has the same field components as those of the surface wave on an infinitely long undisturbed rod, and applied Schelkunoff's Equivalence Principle on the dielectric rod surface to calculate the radiation patterns. For the integration along the rod axis Z, the dominant pattern is

$$\int_0^l f(\phi, \theta) e^{jkz \left( \frac{\lambda_o}{\lambda_g} - \cos \theta \right)} dz \longrightarrow f(\phi, \theta) \frac{\sin U}{U} \tag{4. 2}$$

which is essentially the same as Eq. (4. 1).

3) Polarization Current Approach. Fradin (1961) assumed a  $HE_{11}$  wave propagating along the rod axis and that only the induced polarization current in the dielectric rod radiates. A volume integration of the polarization current again gives the same dominant pattern function of Eq. (4.2).

4) Two Aperture Array Approach. Brown and Spector (1957), and James (1967) gave a physical interpretation of the dielectric rod antenna as a two aperture array. Radiation only occurs at the discontinuities at the free end of the rod and at the feed of the dielectric rod. The field radiated from the feed is assumed to have a radiation pattern identical to the one estimated directly from the transverse wave - guide aperture as if the dielectric rod were absent.

#### 4.1.3 Discussion of the Problem

The dielectric rod antenna has functions similar to the Yagi antenna --- guiding the wave and modification of the phase front in the axial direction. The problem of radiation from the dielectric antenna may be seen to be more or less the same as the problem of scattering as shown in Fig. 4-1. The total field at a distant point in free space is the summation of the incident field produced by the open waveguide as an aperture and the scattered field produced by the induced polarization current in the dielectric material illuminated by the waveguide. The problem of the uniform dielectric rod also may be explained by the point of view of the transmission line analogy as shown in Fig. 4-2. A  $TE_{11}$  wave incident from the far end of the waveguide impinges on the discontinuity at the feed of the rod. It generates a  $HE_{11}$  surface wave traveling along the dielectric rod axis, a reflected wave returning in the waveguide, and a field corresponding to the direct radiation from the feed. For the endfire antenna it is desired to excite a  $HE_{11}$  wave on the rod and to have a continual flow of energy directly outward in the axial direction without reflection from the end. Because of symmetry the  $TM_{01}$  and  $TE_{01}$  modes radiate only in the broadside direction, and are therefore not considered.

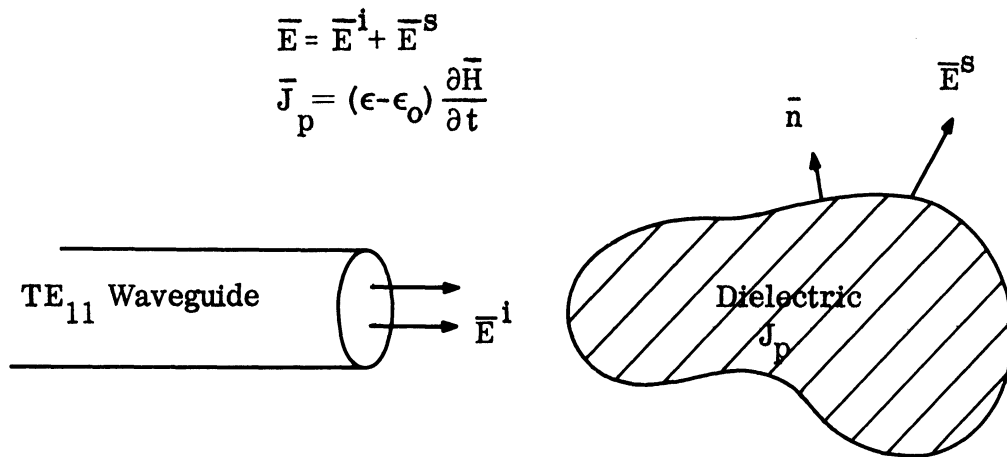


FIG. 4-1: SCATTERING FROM A DIELECTRIC MATERIAL

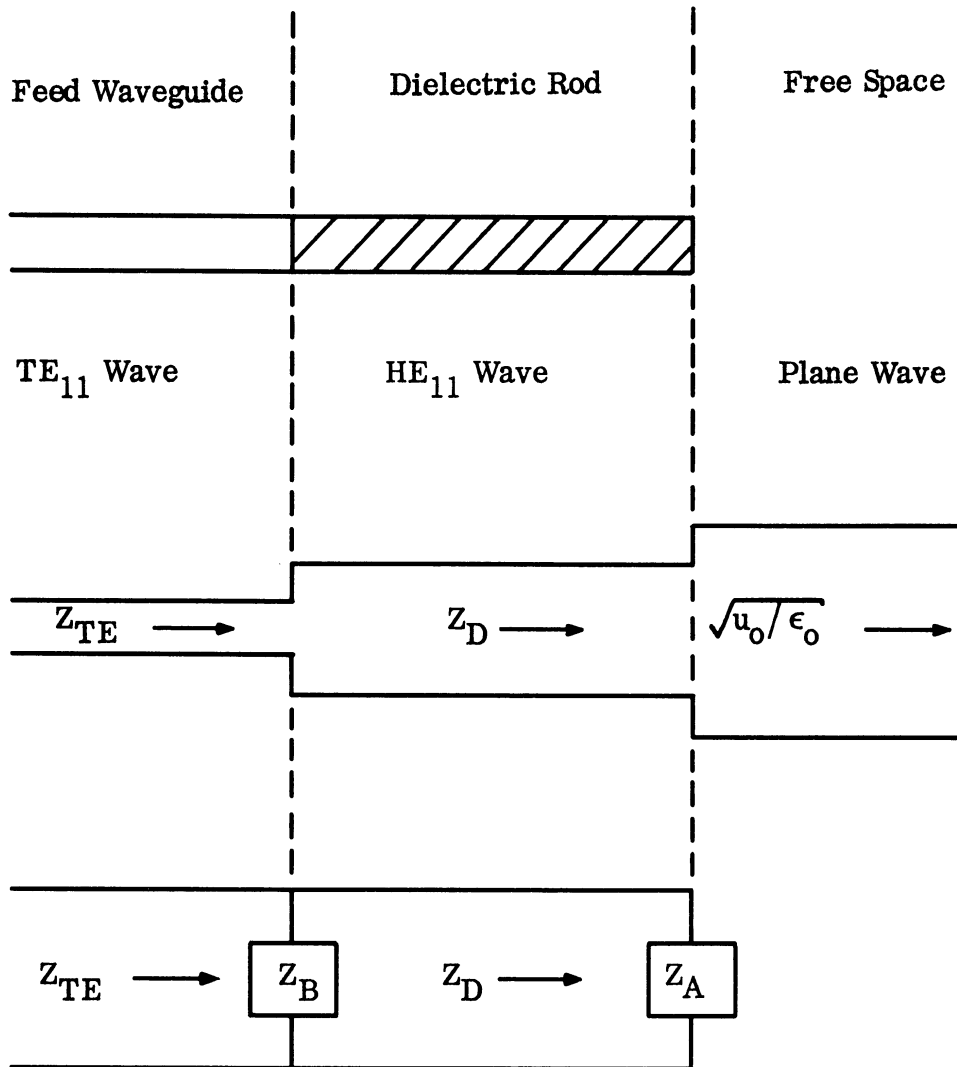


FIG. 4-2: TRANSMISSION LINE ANALOG OF THE DIELECTRIC ROD ANTENNA.

Since the boundary problem of this antenna could not be solved exactly, all the analyses attempts were based on various assumptions. The Huygen's principle is a scalar wave formulation, and it does not give the field direction. If the endfire array approach takes into consideration the polarization and the field distribution around the circumference of the rod, it yields the same result as the equivalence surface method. Both the equivalence surface method and the polarization current method are based on the vector Kirchhoff formula in spite of the difference in form. If all the currents and charges are excluded from a region which includes the field point, the volume integration of the vector Kirchhoff formula vanishes. The surface integral corresponds essentially to Schelkunoff's Equivalence Principle which represents the contributions of sources located outside the enclosing surface. On the other hand if all currents and charges are enclosed in an infinite surface including the field point, the surface integral vanishes. Only the volume integration of the vector Kirchhoff's formula contributes to the radiation.

#### 4. 1. 4 Some Comments on the Existing Analyses

In the equivalent surface method, the assumed field components on the radial rod surface are solutions of the homogeneous wave equation in the infinite rod. This equivalent surface used as an aperture and illuminated by the above field does not represent the contribution of the sources located outside nor the sources lying inside the surface. Furthermore, for the endfire antenna of interest most of the energy of the surface wave is carried outside the rod surface, otherwise the surface wave would be tightly bound to the rod and would not contribute to the endfire radiation. For these reasons, use of the assumed field components on the rod surface is a poor application of Schelkunoff's Equivalence Principle and can not wholly represent the behavior of the propagating surface wave.

In the polarization current method, Fradin failed to consider the contributions from the primary current sources in the feeding waveguide. As a result, radiation vanishes in his analysis when the relative permittivity  $\epsilon_r$  reduces to unity, or the length of the rod reduces to zero; whereas, experiment shows an open waveguide pattern.

Another example of the failure of both analyses stated above is they predicted a null in the axial direction when  $u = k\ell/2 (\lambda_o/\lambda_g - 1) = \pi$ ; whereas, experiment shows a well defined mainlobe in this direction.

Brown and Spector took a transverse aperture extended to infinity at the rod end, assumed all of the surface wave radiated from this end aperture, and made a correction of the radiation pattern by taking into account the direct radiation from the feed where some energy is not converted to the surface wave. This analysis gives better results than others but the direct radiation from the feed is still very difficult to evaluate precisely.

#### 4.1.5 Revised Method in this Report

The general vector Kirchhoff's formula will be applied to both types of antenna, rod and tube, with a more general and effective guiding material, ferrite. Rigorously the radiation can be considered to arise from the conducting current in the launching device, and both the electric polarization and magnetization currents throughout the ferrite material. However, the conducting current in the launching device is extremely difficult to estimate precisely. An alternative integration surface  $S_1$  as shown in Fig. 4-3 taken to exclude the launching device from the field point region  $V$ , takes into consideration the contribution from the launching device approximately by integrating the assumed aperture field over the transverse aperture  $S_1$  at the mouth of the feed waveguide. The whole integration procedure is presented in Section 4.2 to evaluate the far field expression of the solid rod antenna. The same procedure can be applied to the ferrite tube antenna. Due to the two layer boundaries of the tube the mathematical expressions are rather long and tedious. Therefore the two aperture array method is presented in Section 4.3 for the problem of the ferrite tube antenna. The experimental results of the ferrite tube are presented in Section 4.4. Finally a discussion of the results, features and design criteria of these antennas are discussed in Section 4.5.

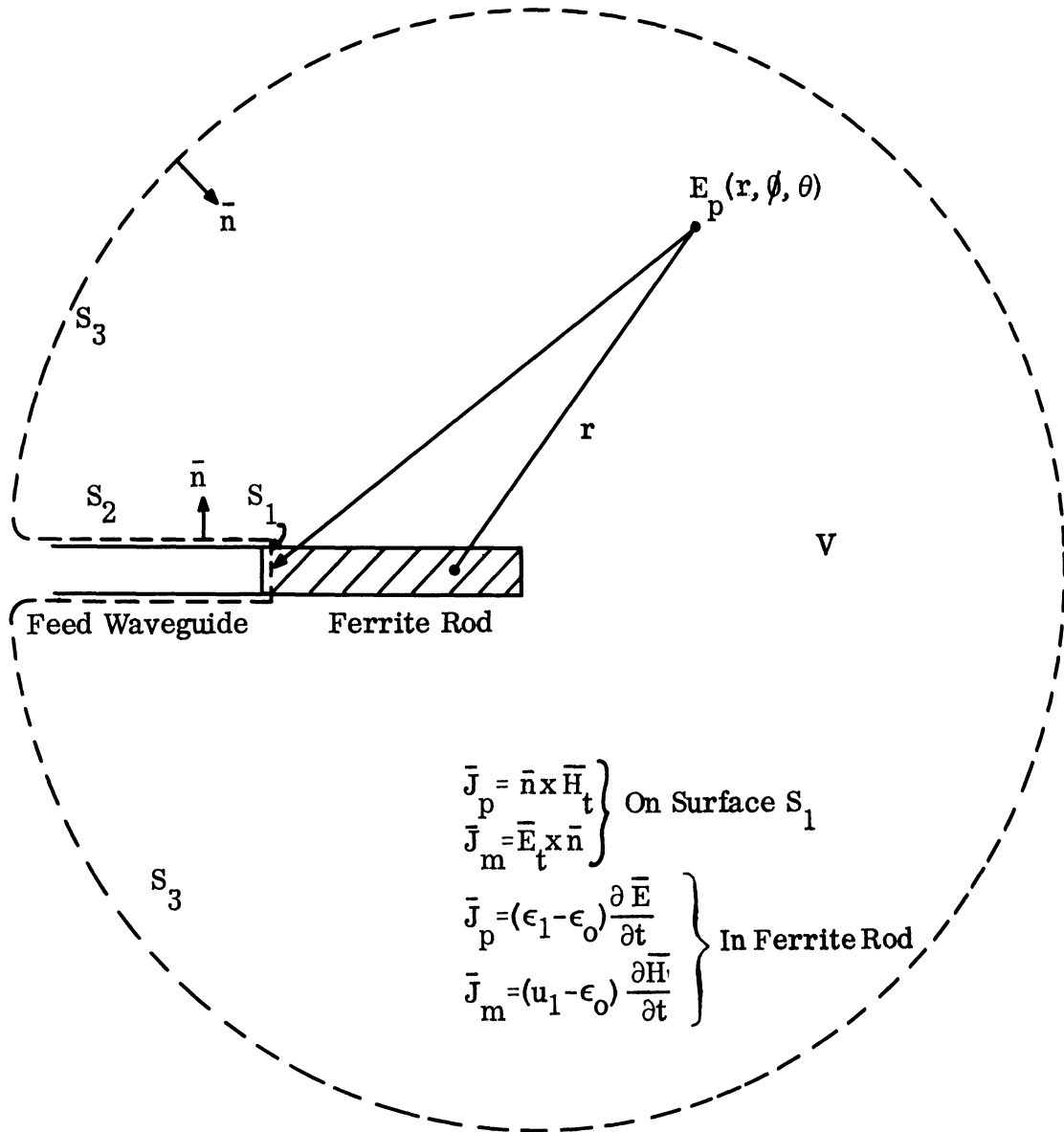


FIG. 4-3: VOLUME AND SURFACE SOURCES OF THE FERRITE ROD ANTENNA

4.2 Ferrite Rod Antennas

4.2.1 General Solution of the Field Equation in Terms of the Electric Polarization Current and the Magnetization Current

Maxwell's equation in a free space region except for small "islands" of homogeneous material media which contain the polarization current density  $\mathbf{J}_p$ , magnetization current density  $\mathbf{J}_m$  and possibly the conducting current density  $\mathbf{J}_c$  can be written as:

$$\left\{ \begin{array}{l} \nabla \times \bar{\mathbf{E}} = -\mu_o \frac{\partial \bar{\mathbf{H}}}{\partial t} - \bar{\mathbf{J}}_m \\ \nabla \times \bar{\mathbf{H}} = \epsilon_o \frac{\partial \bar{\mathbf{E}}}{\partial t} + \bar{\mathbf{J}} \\ \nabla \cdot \bar{\mathbf{E}} = \frac{\rho_p}{\epsilon_o} \\ \nabla \cdot \bar{\mathbf{H}} = \frac{\rho_m}{\mu_o} \end{array} \right. \quad (4.3)$$

where the effective currents in free space are:

$$\left\{ \begin{array}{ll} \bar{\mathbf{J}} = \mathbf{J}_c + \mathbf{J}_p & \\ \bar{\mathbf{J}}_p = (\epsilon - \epsilon_o) \frac{\partial \bar{\mathbf{E}}}{\partial t} & \text{polarization current density} \\ \bar{\mathbf{J}}_m = (\mu - \mu_o) \frac{\partial \bar{\mathbf{H}}}{\partial t} & \text{magnetization current density} \end{array} \right. \quad (4.4)$$

and the vector Helmholtz equations for a time harmonic field with  $e^{j\omega t}$  factor understood are:

$$\left\{ \begin{array}{l} \nabla \times \nabla \times \bar{\mathbf{E}} - k^2 \bar{\mathbf{E}} = -j\omega\mu_o \bar{\mathbf{J}} - \nabla \times \bar{\mathbf{J}}_m \\ \nabla \times \nabla \times \bar{\mathbf{H}} - k^2 \bar{\mathbf{H}} = -j\omega\epsilon_o \bar{\mathbf{J}}_m + \nabla \times \bar{\mathbf{J}} \end{array} \right. \quad (4.5)$$



The field solution of these Helmholtz equations at a point  $P$  in a volume  $V$  enclosed by a surface  $S$  can be derived to be:

$$\begin{aligned} \bar{E}_p = & -\frac{1}{4\pi} \int_V (j\omega\mu_o \bar{J} G + \bar{J}_m \times \nabla G - \frac{\rho}{\epsilon_o} \nabla G) dv \\ & + \frac{1}{4\pi} \int_S \left[ -j\omega\mu_o (\bar{n} \times \bar{H}) G + (\bar{n} \times \bar{E}) \times \nabla G + (\bar{n} \cdot \bar{E}) \nabla G \right] ds \end{aligned} \quad (4.6a)$$

$$\begin{aligned} \bar{H}_p = & -\frac{1}{4\pi} \int_V (j\omega\epsilon_o \bar{J}_m G - \bar{J}_m \times \nabla G - \frac{\rho_m}{\mu_o} \nabla G) dv \\ & + \frac{1}{4\pi} \int_S \left[ j\omega\epsilon_o (\bar{n} \times \bar{E}) G + (\bar{n} \times \bar{H}) \times \nabla G + (\bar{n} \cdot \bar{H}) \nabla G \right] ds \end{aligned} \quad (4.6b)$$

where  $G$  is the Green's function in the free space and  $\bar{n}$  is the unit vector normal to the bounding surface directed into the region  $V$ . The volume integration in the first term of Eq. (4.6) is the particular solution of the Helmholtz Eq. (4.5). Physically it represents the field distribution from the sources distributed through the region  $V$ . The surface integration in the second term of Eq.(4.6) is the complementary solution of the Helmholtz Eq. (4.5). Physically it represents the field contribution from the sources lying outside the region  $V$ . Equation (4.6) is essentially an integral equation since the unknown  $\bar{J}_p$  and  $\bar{J}_m$  appearing in the integrand are the unknown functions of  $\bar{E}$  and  $\bar{H}$ . However, if the material is small in the whole region  $V$  and if one can estimate  $\bar{E}$  and  $\bar{H}$  and also  $\bar{J}_p$  and  $\bar{J}_m$  in the material with a reasonable accuracy, Eq. (4.6) will give the approximate expressions of  $\bar{E}_p$  and  $\bar{H}_p$  elsewhere in the region  $V$ . Then the problem of radiation from a ferrite rod antenna is reduced to the problem of the electromagnetic field in the free space with the polarization and magnetization current densities  $\bar{J}_p$  and  $\bar{J}_m$  in the ferrite material and the conducting current density  $\bar{J}_c$  in the waveguide. When the surface  $S$  encloses the whole antenna and extends to infinity in the free space the surface integration in

Eq. (4.6) vanishes and the volume integral can be decomposed as:

$$\begin{aligned} \bar{\mathbf{E}}_p = & -\frac{1}{4\pi} \iiint_{\substack{\text{Ferrite} \\ \text{Rod}}} (j\omega\mu_o \bar{\mathbf{J}}_p G + \bar{\mathbf{J}}_m \times \nabla G) dv \\ & -\frac{1}{4\pi} \iiint_{\substack{\text{Launching} \\ \text{Waveguide}}} [j\omega\mu_o (\bar{\mathbf{J}}_p + \bar{\mathbf{J}}_c) G + \bar{\mathbf{J}}_m \times \nabla G] dv . \end{aligned} \quad (4.7)$$

The polarization and magnetization current densities  $\bar{\mathbf{J}}_p$  and  $\bar{\mathbf{J}}_m$  in the first term of Eq. (4.8) can be obtained from the relation of Eq. (4.4) by assuming that the field components in the rod are approximately the same as those of an infinitely long rod of the same material and cross section. The second term of Eq. (4.7) is the radiation from the loaded waveguide. The current distribution at the mouth of the feed waveguide is very difficult to determine precisely. However, the radiated field can be evaluated approximately from an assumed field distribution over the transverse aperture at the mouth of the feed waveguide.

$$\begin{aligned} \bar{\mathbf{E}}_p = & -\frac{1}{4\pi} \iiint_{\substack{\text{Ferrite} \\ \text{Rod}}} (j\omega\mu_o \bar{\mathbf{J}}_p G + \bar{\mathbf{J}}_m \times \nabla G) dv \\ & +\frac{1}{4\pi} \iint_{S_1 + S_2 + S_3} [-j\omega\mu_o (\bar{\mathbf{n}} \times \bar{\mathbf{H}}) G + (\bar{\mathbf{n}} \times \bar{\mathbf{E}}) \nabla \times G] ds . \end{aligned} \quad (4.8)$$

Equation (4.8) is the vector Kirchhoff's formula for which region  $V$  includes the ferrite rod but excludes the feed waveguide. The bounding surfaces are taken as the transverse aperture  $S_1$  at the mouth of the feed waveguide, the metal surface  $S_2$  of the feed waveguide and the surface  $S_3$  enclosing the region  $V$  at infinity as shown in Fig. 4-3. For

simplicity, assume the field contribution from  $S_2$  is negligible. The field at infinity satisfies the radiation condition. The approximate field expression reduces to the volume integration of the ferrite rod and the surface integration across the transverse aperture  $S_1$ .

#### 4.2.2 Ferrite Rod Waveguide

The field components of an isotropic infinite ferrite rod obtained by solving the homogeneous Helmholtz equation in cylindrical coordinates  $(\rho, \phi, \theta)$  subject to the boundary conditions on the cylindrical surface of the rod for the  $HE_{11}$  mode are as follows where the time dependence factor  $e^{j\omega t}$  is understood. The field inside the rod for  $(\rho < a)$ :

$$\begin{aligned}
 H_z &= A_1 J_1(k_1 \rho) \cos \phi e^{-j\gamma z} , \\
 H_\rho &= \left[ -A_1 \frac{j\gamma}{k_1} J_1'(k_1 \rho) + B_1 \frac{j\omega\epsilon_1}{k_1 \rho} J_1(k_1 \rho) \right] \cos \phi e^{-j\gamma z} , \\
 H_\phi &= \left[ A_1 \frac{j\gamma}{k_1 \rho} J_1(k_1 \rho) - B_1 \frac{j\omega\epsilon_1}{k_1} J_1'(k_1 \rho) \right] \sin \phi e^{-j\gamma z} , \\
 E_z &= B_1 J_1(k_1 \rho) \sin \phi e^{-j\gamma z} , \\
 E_\rho &= \left[ A_1 \frac{j\omega\mu_1}{k_1 \rho} J_1(k_1 \rho) - B_1 \frac{j\gamma}{k_1} J_1'(k_1 \rho) \right] \sin \phi e^{-j\gamma z} , \\
 E_\phi &= \left[ A_1 \frac{j\omega\mu_1}{k_1} J_1'(k_1 \rho) - B_1 \frac{j\gamma}{k_1 \rho} J_1(k_1 \rho) \right] \cos \phi e^{-j\gamma z} , \quad (4.9)
 \end{aligned}$$

The field surrounding the rod for ( $\rho > a$ ):

$$H_z = A_o H_n^{(1)}(k_o \rho) \cos \phi e^{-j\gamma z} ,$$

$$H_\rho = \left[ -A_o \frac{j\gamma}{k_o} H_1^{(1)}(k_o \rho) + B_o \frac{j\omega \epsilon_o}{k_o \rho} H_1^{(1)}(k_o \rho) \right] \cos \phi e^{-j\gamma z} ,$$

$$H_\phi = \left[ A_o \frac{j\gamma}{k_o \rho} H_1^{(1)}(k_o \rho) - B_o \frac{j\omega \epsilon_o}{k_o} H_1^{(1)}(k_o \rho) \right] \sin \phi e^{-j\gamma z} ,$$

$$E_z = B_o H_1^{(1)}(k_o \rho) \sin \phi e^{-j\gamma z} ,$$

$$E_\rho = \left[ A_o \frac{j\omega \mu_o}{k_o \rho} H_1^{(1)}(k_o \rho) - B_o \frac{j\gamma}{k_o} H_1^{(1)}(k_o \rho) \right] \sin \phi e^{-j\gamma z} ,$$

and

$$E_\phi = \left[ A_o \frac{j\omega \mu_o}{k_o} H_1^{(1)}(k_o \rho) - B_o \frac{j\gamma}{k_o \rho} H_1^{(1)}(k_o \rho) \right] \cos \phi e^{-j\gamma z} , \quad (4.10)$$

with

$$\begin{cases} k_1^2 = \omega^2 \mu_1 \epsilon_1 - \gamma^2 & \text{inside the rod} \\ k_o^2 = \omega^2 \mu_o \epsilon_o - \gamma^2 & \text{in surrounding free space.} \end{cases} \quad (4.11)$$

In the above "a" is the radius of the ferrite rod,  $J_1$  and  $H_1^{(1)}$  are Bessel and Hankel functions of the first kind and of order one respectively. The ferrite rod is assumed to have a permeability  $\mu_1 = \mu_o \mu_r$  and a permittivity  $\epsilon_1 = \epsilon_o \epsilon_r$ .

THE UNIVERSITY OF MICHIGAN

7848-1-F

All the tangential field components on the boundary surface  $\rho = a$  must be continuous. In matching these  $z$  and  $\phi$  components one obtains four equations for the four unknown constants  $A_1, A_0, B_1$  and  $B_0$ . In order to have a nontrivial solution the determinant of the coefficients of these constants must be zero. This results in the following determinantal equation and a relationship of the A's and B's.

$$\begin{aligned} & \left[ \frac{\epsilon_r}{k_1 a} \frac{J_1'(k_1 a)}{J_1(k_1 a)} - \frac{1}{k_0 a} \frac{H_1^{(1)}(k_0 a)}{H_1^{(1)}(k_0 a)} \right] \left[ \frac{\mu_0}{k_1 a} \frac{J_1'(k_1 a)}{J_1(k_1 a)} - \frac{1}{k_0 a} \frac{H_1^{(1)}(k_0 a)}{H_1^{(1)}(k_0 a)} \right] \\ & = \frac{(k_1 a)^2 - \mu_r \epsilon_r (k_0 a)^2}{(k_1 a)^2 - (k_0 a)^2} \left[ \frac{1}{(k_1 a)^2} - \frac{1}{(k_0 a)^2} \right]^2 \end{aligned} \quad (4.12)$$

$$\frac{A_1}{A_0} = \frac{B_1}{B_0} = \frac{H_1^{(1)}(k_0 a)}{J_1(k_0 a)} \quad (4.13)$$

$$\begin{aligned} \frac{B_1}{A_1} &= \frac{\gamma \left[ \frac{1}{(k_1 a)^2} - \frac{1}{(k_0 a)^2} \right]}{\omega \epsilon_0 \left[ \frac{\epsilon_r}{k_1 a} \frac{J_1'(k_1 a)}{J_1(k_1 a)} - \frac{1}{k_0 a} \frac{H_1^{(1)}(k_0 a)}{H_1^{(1)}(k_0 a)} \right]} = \frac{\omega \mu_0 \left[ \frac{\mu_r}{k_1 a} \frac{J_1'(k_1 a)}{J_1(k_1 a)} - \frac{1}{k_0 a} \frac{H_1^{(1)}(k_0 a)}{H_1^{(1)}(k_0 a)} \right]}{\gamma \left[ \frac{1}{(k_1 a)^2} - \frac{1}{(k_0 a)^2} \right]} \end{aligned} \quad (4.14)$$

The electric and magnetic surface charge densities on the rod surface are:

$$\begin{aligned} \sigma_e &= A_1 J_1(k_1 a) \frac{1}{j\omega a} \left[ \frac{1}{k_0^2} - \frac{\mu_r \epsilon_r}{k_1^2} \right] \left[ \frac{k_1^2 - k_0^2}{\mu_r \epsilon_r^{-1}} - \left( \frac{2\pi}{\lambda_0} \right)^2 \right] \sin \phi e^{-j\gamma z} \\ \sigma_m &= B_1 J_1(k_1 a) \frac{1}{j\omega a} \left[ \frac{1}{k_0^2} - \frac{\mu_r \epsilon_r}{k_1^2} \right] \left[ \frac{k_1^2 - k_0^2}{\mu_r \epsilon_r^{-1}} - \left( \frac{2\pi}{\lambda_0} \right)^2 \right] \cos \phi e^{-j\gamma z} \end{aligned} \quad (4.15)$$

THE UNIVERSITY OF MICHIGAN

7848-1-F

These oscillating surface charge densities on the rod surface produce the same field as the volume electric polarization current density and the magnetic polarization current density in the rod due to the subatomic displacement of charge centers and alignment of spin momenta. Magnetic charge as included in the density  $\sigma_m$  is fictional. The magnitude ratio of  $\sigma_e$  and  $\sigma_m$  is the same as the ratio of TE to TM components. In the limiting case with  $\mu_r = 1$ ,  $\epsilon_r = 1$  both electric and magnetic surface charges vanish.

Equation (4.12) is the determinantal equation which determines  $k_1 a$  and  $k_0 a$  and thus determines the propagation constant  $\gamma$  along the longitudinal axis of the rod. By eliminating  $\gamma$  in Eq. (4.11) and by rearranging the terms there results:

$$\left(\frac{2a}{\lambda_0}\right)^2 = \frac{(k_1 a)^2 - (k_0 a)^2}{\pi^2 (\mu_r \epsilon_r - 1)}, \quad (4.16)$$

and

$$\left(\frac{\lambda_g}{\lambda_0}\right)^2 = \frac{(k_1 a)^2 - (k_0 a)^2}{(k_1 a)^2 - \mu_r \epsilon_r (k_0 a)^2}. \quad (4.17)$$

The diameter of the rod is related to the axial phase velocity by Eqs. (4.16) and (4.17). By substituting the corresponding  $(k_1 a)$  and  $(k_0 a)$  values which satisfy the determinantal Eq. (4.12) into Eq. (4.17) the phase velocity of the surface wave along the rod axis is obtained. The cutoff frequency occurs at the frequency at which the argument of the Hankel function  $k_0 a$  approaches zero through imaginary values. The cutoff diameter of the ferrite rod can be found from Eq. (4.16) by substituting the values of  $k_1 a$  as  $k_0 a$  approaches zero.

$$\left. \frac{2a}{\lambda_0} \right|_{\text{cutoff}} = \frac{1}{\pi \sqrt{\mu_r \epsilon_r - 1}} \cdot (k_1 a) \Big|_{k_0 a \rightarrow 0} \quad (4.18)$$

The  $HE_{11}$  wave on the rod has no cutoff because  $k_1 a$  becomes zero as  $k_0 a$  approaches zero, and it is observed from Eq. (4.18) the surface wave cannot propagate along the rod without attenuation when the rod material has the value of  $\mu_r \epsilon_r$  equal to unity.

#### 4.2.3 Radiation Due to the Polarization Current and the Magnetization Current in the Rod

When a finite rod is used as an antenna the field present in the rod is not that of a simple  $HE_{11}$  mode; however, it is assumed that the  $HE_{11}$  mode component is the most important part of the field configuration. The analysis in the last section on the rod diameter and the axial phase velocity will serve for engineering purposes in the design of a rod antenna.

Once the polarization current and the magnetization current are taken to be in accordance with the assumed  $HE_{11}$  mode component in the finite rod, the volume integration of the rod can be performed with cylindrical coordinates  $(\rho, \phi, \theta)$  as shown in Fig. 4-4. If only the far field zone is considered, the components of the radiated electric field can be expressed as:

$$\begin{aligned} E_\theta &= - \frac{jke^{-jkr}}{4\pi r} \int_V \left[ \eta \bar{J} \cdot \hat{\theta} + \bar{J}_m \cdot \hat{\phi} \right] e^{jkr' \cos \xi} dv' \\ &= - \frac{jke^{-jkr}}{4\pi r} \left[ L_\phi + \eta N_\theta \right] \quad , \end{aligned} \quad (4.19)$$

and

$$E_\phi = \frac{jke^{-jkr}}{4\pi r} \left[ L_\theta - \eta N_\phi \right] \quad . \quad (4.20)$$

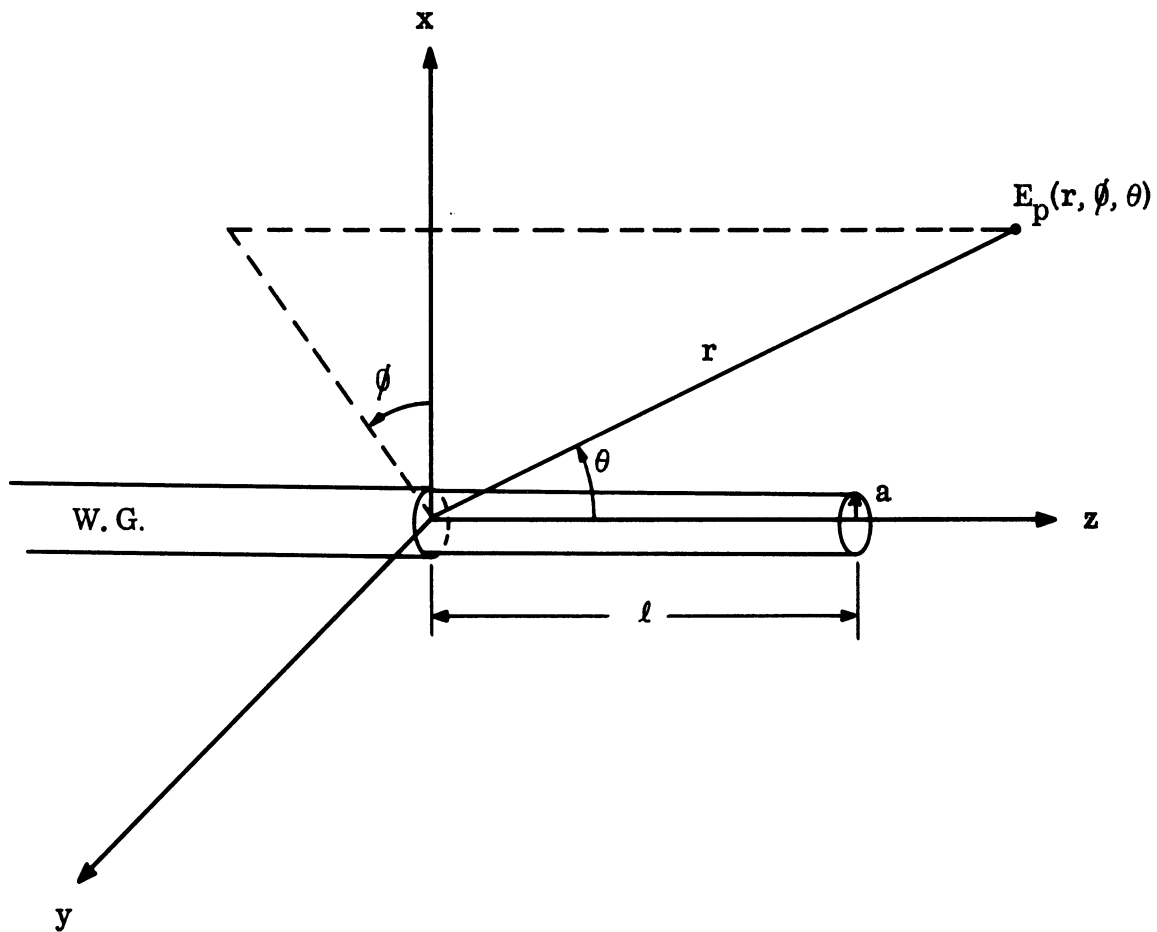


FIG. 4-4: COORDINATE SYSTEM ASSUMED FOR THE FERRITE ROD ANTENNA.



The components of the radiated magnetic field are:

$$H_{\theta} = \frac{-j e^{-jkr}}{2\lambda_0 r \eta} \left[ L_{\theta} - \eta N_{\phi} \right], \quad (4.21)$$

and

$$H_{\phi} = \frac{-j e^{-jkr}}{2\lambda_0 r \eta} \left[ L_{\phi} + \eta N_{\theta} \right]. \quad (4.22)$$

In the above

$$\eta = \sqrt{\frac{\mu_0}{\epsilon_0}},$$

$$r' \cos \xi = \rho' \sin \theta \cos(\phi - \phi') + z' \cos \theta, \quad (4.23)$$

$$\bar{N} = \int_V \bar{J}_p e^{jkr' \cos \xi} dv'$$

and

$$\bar{L} = \int_V \bar{J}_m e^{jkr' \cos \xi} dv'. \quad (4.24)$$

The rectangular components of the electric field can be obtained by the transformation of coordinates and the relationships of the Bessel functions:

$$\begin{cases} V_x = V_{\rho} \cos \phi - V_{\phi} \sin \phi \\ V_y = V_{\rho} \sin \phi + V_{\phi} \cos \phi \end{cases} \quad (4.25)$$

$$\begin{cases} J_0(k_1 \rho) = \frac{J_1(k_1 \rho)}{k_1 \rho} + J_1'(k_1 \rho) \\ J_2(k_1 \rho) = \frac{J_1(k_1 \rho)}{k_1 \rho} - J_1'(k_1 \rho) \end{cases} \quad (4.26)$$

Thus the assumed field components in rectangular coordinates along the ferrite rod from Eq. (4.9) are:

$$\begin{aligned}
 E_x &= \frac{j[A_i \omega \mu_1 + B_i \gamma]}{2k_1} J_2(k_1 \rho) \sin 2\phi e^{-j\gamma z} \\
 E_y &= \left\{ \frac{j[A_i \omega \mu_1 - B_i \gamma]}{2k_1} J_0(k_1 \rho) - \frac{j[A_i \omega \mu_1 + B_i \gamma]}{2k_1} J_2(k_1 \rho) \cos 2\phi \right\} e^{-j\gamma z} \\
 H_x &= \left\{ \frac{-j[A_i \gamma - B_i \omega \epsilon_1]}{2k_1} J_0(k_1 \rho) + \frac{j[A_i \gamma + B_i \omega \epsilon_1]}{2k_1} J_2(k_1 \rho) \cos 2\phi \right\} e^{-j\gamma z} \\
 H_y &= \frac{j[A_i \gamma + B_i \omega \epsilon_1]}{2k_1} J_2(k_1 \rho) \sin 2\phi e^{-j\gamma z} .
 \end{aligned} \tag{4.27}$$

Substitute Eq. (4.27) into Eqs. (4.4) and (4.24) and perform the integration by using Eq. (4.23) and the Bessel-Fourier series

$$\begin{aligned}
 e^{jk\rho' \sin \theta \cos(\phi - \phi')} &= J_0(k\rho' \sin \theta) \\
 &+ \sum_{m=1}^{\infty} 2j^m J_m(k\rho' \sin \theta) \cos m(\phi - \phi') .
 \end{aligned} \tag{4.28}$$

Thus the vector potential components of N and L in rectangular coordinate are:

$$N_x = \frac{-j\omega(\epsilon_1 - \epsilon_0)\pi}{k_1} [A_i \omega \mu_1 + B_i \gamma] L_2(k_1) \sin 2\phi f(\theta) ,$$

$$N_y = \frac{j\omega(\epsilon_1 - \epsilon_0)\pi}{k_1} \left\{ \left[ A_i \omega \mu_1 - B_i \gamma \right] L_0(k_1) + \left[ A_i \omega \mu_1 + B_i \gamma \right] L_2(k_1) \cos 2\theta \right\} f(\theta) ,$$

$$N_z = 2j\omega(\epsilon_1 - \epsilon_0)\pi B_i L_1(k_1) \sin \theta f(\theta) ,$$

$$L_x = \frac{-j\omega(\mu_1 - \mu_0)\pi}{k_1} \left\{ \left[ A_i \gamma - B_i \omega \epsilon_1 \right] L_0(k_1) + \left[ A_i \gamma + B_i \omega \epsilon_1 \right] L_2(k_1) \cos 2\theta \right\} f(\theta) ,$$

$$L_y = \frac{-j\omega(\mu_1 - \mu_0)\pi}{k_1} \left[ A_i \gamma + B_i \omega \epsilon_1 \right] L_2(k_1) \sin 2\theta f(\theta) ,$$

and

$$L_z = 2j\omega(\mu_1 - \mu_0)\pi A_i L_1(k_1) \cos \theta f(\theta) , \quad (4.29)$$

where

$$f(\theta) = \frac{\left[ e^{j(k \cos \theta - \gamma) \ell} - 1 \right]}{k \cos \theta - \gamma} ,$$

and the Lommel integral:

$$L_0(k_1) = \int_0^a \rho J_0(k_1 \rho) J_0(k \rho \sin \theta) d\rho ,$$

$$L_1(k_1) = \int_0^a \rho J_1(k_1 \rho) J_1(k \rho \sin \theta) d\rho ,$$

and

$$L_2(k_1) = \int_0^a \rho J_2(k_1 \rho) J_2(k \rho \sin \theta) d\rho .$$

The spherical components of the radiation vector can be obtained from the rectangular components using the relationships:

$$V_{\theta} = (V_x \cos \phi + V_y \sin \phi) \cos \theta - V_z \sin \theta \quad ,$$

and

$$V_{\phi} = -V_x \sin \phi + V_y \cos \phi \quad . \quad (4.30)$$

The spherical components of the radiation vector can be simplified to:

$$N_{\theta} = \frac{j\omega(\epsilon_1 - \epsilon_0)\pi}{k_1} f(\theta) \sin \phi \left\{ \left[ A_i \omega \mu_1 - B_i \gamma \right] L_0(k_1) \cos \theta \right. \\ \left. - 2k_1 B_i L_1(k_1) \sin \theta - \left[ A_i \omega \mu_1 + B_i \gamma \right] L_2(k_1) \cos \theta \right\} ,$$

$$N_{\phi} = \frac{j\omega(\epsilon_1 - \epsilon_0)\pi}{k_1} f(\theta) \cos \phi \left\{ \left[ A_i \omega \mu_1 - B_i \gamma \right] L_0(k_1) \right. \\ \left. + \left[ A_i \omega \mu_1 + B_i \gamma \right] L_2(k_1) \right\} ,$$

$$L_{\theta} = \frac{-j\omega(\mu_1 - \mu_0)\pi}{k_1} f(\theta) \cos \phi \left\{ \left[ A_i \gamma - B_i \omega \epsilon_1 \right] L_0(k_1) \cos \theta \right. \\ \left. + 2k_1 A_i L_1(k_1) \sin \theta + \left[ A_i \gamma + B_i \omega \epsilon_1 \right] L_2(k_1) \cos \theta \right\} ,$$

and

$$L_{\phi} = \frac{j\omega(\mu_1 - \mu_0)\pi}{k_1} f(\theta) \sin \phi \left\{ \left[ A_i \gamma - B_i \omega \epsilon_1 \right] L_0(k_1) \right. \\ \left. - \left[ A_i \gamma + B_i \omega \epsilon_1 \right] L_2(k_1) \right\} . \quad (4.31)$$

THE UNIVERSITY OF MICHIGAN

7848-1-F

Then the radiated field can be obtained by substituting Eq. (4.31) in (4.19) and (4.20).

$$E_{\theta} = f(r) f(\theta) \sin \theta \left\{ C_A \left[ (A_1 \omega \mu_1 - B_1 \gamma) L_0(k_1) \cos \theta - 2k_1 B_1 L_1(k_1) \sin \theta - (A_1 \omega \mu_1 + B_1 \gamma) L_2(k_1) \cos \theta \right] + C_F \left[ (A_1 \gamma - B_1 \omega \epsilon_1) L_0(k_1) - (A_1 \gamma + B_1 \omega \epsilon_1) L_2(k_1) \right] \right\}, \quad (4.32a)$$

and

$$E_{\phi} = f(r) f(\theta) \cos \theta \left\{ C_A \left[ (A_1 \omega \mu_1 - B_1 \gamma) L_0(k_1) + (A_1 \omega \mu_1 + B_1 \gamma) L_2(k_1) \right] + C_F \left[ (A_1 \gamma - B_1 \omega \epsilon_1) L_0(k_1) \cos \theta + 2k_1 A_1 L_1(k_1) \sin \theta + (A_1 \gamma + B_1 \omega \epsilon_1) L_2(k_1) \cos \theta \right] \right\} \quad (4.33a)$$

where

$$f(r) = \frac{e^{-jkr}}{r},$$

$$C_A = \frac{k^2(\epsilon_r - 1)}{4k_1}, \quad C_F = \frac{\eta k^2(\mu_r - 1)}{4k_1}, \quad \text{and} \quad \eta = \sqrt{\frac{\mu_0}{\epsilon_0}}.$$

Equations (4.32a) and (4.33a) can be rearranged as follows:

$$E_{\theta} = f(r) f(\theta) \sin \theta \left\{ C_A A_1 \omega \mu_1 \left[ L_0(k_1) - L_2(k_1) \right] \cos \theta - C_A B_1 \gamma \left[ L_0(k_1) + L_2(k_1) \right] \cos \theta - 2k_1 C_A B_1 L_1(k_1) \sin \theta + C_F A_1 \gamma \left[ L_0(k_1) - L_2(k_1) \right] - C_F B_1 \omega \epsilon_1 \left[ L_0(k_1) + L_2(k_1) \right] \right\}, \quad (4.32b)$$

and

$$E_{\theta} = f(r) f(\theta) \cos \theta \left\{ C_A A_i \omega \mu_1 [L_0(k_1) + L_2(k_1)] \right. \\ - C_A B_i \gamma [L_0(k_1) - L_2(k_1)] + C_F A_i \gamma [L_0(k_1) + L_2(k_1)] \cos \theta \\ \left. - C_F B_i \omega \epsilon_1 [L_0(k_1) - L_2(k_1)] \cos \theta + 2k_1 C_F A_i L_1(k_1) \sin \theta \right\} \quad (4.33b)$$

where

$$L_0(k_1) - L_2(k_1) = \frac{2J_1(k_1 a) J_1(k a \sin \theta)}{k_1 k \sin \theta} , \\ L_0(k_1) + L_2(k_1) = \frac{2a}{k_1^2 - (k \sin \theta)^2} \left[ k_1 J_1(k_1 a) J_1'(k a \sin \theta) \right. \\ \left. - k \sin \theta J_1'(k_1 a) J_1(k a \sin \theta) \right] ,$$

and

$$L_1(k_1) = \frac{-a}{k_1^2 - (k \sin \theta)^2} \left[ k_1 J_0(k_1 a) J_1(k a \sin \theta) \right. \\ \left. - k \sin \theta J_1(k_1 a) J_0(k a \sin \theta) \right] .$$

#### 4.2.4 Radiation Due to the Loaded Waveguide

The current distribution in the launching waveguide is very difficult to determine precisely. The far field contribution from the portion of the launching waveguide will be evaluated approximately by assuming  $TE_{11}$  mode aperture field components at the  $z = 0$  plane over the open circular guide. The surface integral of Eq. (4.8) over the waveguide aperture can be found in many antenna text books

(Silver 1965, p 337 or Wolff 1966, p 205). If the z component of the  $TE_{11}$  mode is assumed to be:

$$H_z = A_c J_1(k_c \rho) \cos \phi e^{-j\beta z} \quad (4.34)$$

then the resulting far field components can be derived.

$$E_\theta = \frac{-\mu_r k \eta A_c}{2k_c^2} f(r) \sin \phi \left[ 1 + \frac{\beta \cos \theta}{\mu_r k} + \Gamma \left( 1 - \frac{\beta \cos \theta}{\mu_r k} \right) \right] \cdot \frac{J_1(k_c a) J_1(k a \sin \theta)}{\sin \theta}, \quad (4.35)$$

$$E_\phi = \frac{-\mu_r k^2 \eta a A_c}{2} f(r) \cos \phi \left[ \frac{\beta}{\mu_r k} + \cos \theta - \Gamma \left( \frac{\beta}{\mu_r k} - \cos \theta \right) \right] \cdot \frac{J_1(k_c a) J_1'(k a \sin \theta)}{k_c^2 - (k \sin \theta)^2} \quad (4.36)$$

with

$$k_c = \frac{1.84}{a} \quad \text{and} \quad \beta = \sqrt{\omega^2 \mu_1 \epsilon_1 - k_c^2}. \quad (4.37)$$

For simplicity one may assume the reflection factor  $\Gamma$  is negligible.

The relationship among the constants  $A_c$ ,  $A_1$ , and  $B_1$  can be obtained from the principle of energy conservation. For the energy flow in the launching waveguide is equal to the sum of the directly radiated energy at the feed and the surface wave energy propagating along the rod axis. The resulting relationship is:

$$A_c^2 = \frac{\frac{W_i}{L_{\text{eff}}(W_i + W_o)}}{\frac{\omega\mu_1\beta}{k_c^2} \int_0^a \left[ \frac{J_1^2(k_c\rho)}{k_c^2\rho^2} + J_1'^2(k_c\rho) \right] d\rho} \cdot \left[ \int_0^a \left\{ \frac{\omega(\mu_1 A_i^2 + \epsilon_1 B_i^2)\gamma}{k_1^2} \left[ \frac{J_1^2(k_1\rho)}{k_1^2\rho^2} + J_1'^2(k_1\rho) \right] - 2A_i B_i \frac{\omega^2\mu_1\epsilon_1 + \gamma^2}{k_1^3\rho} J_1(k_1\rho) J_1'(k_1\rho) \right\} d\rho \right], \quad (4.38)$$

where  $L_{\text{eff}}$  is the launching efficiency of the launching waveguide,  $W_i$  the surface wave energy propagating inside the rod, and  $W_o$  the energy carried in the external space along the rod.

#### 4.2.5 Far Field Pattern of the Ferrite Rod Antenna and a Class of Degenerate Antennas

The total far field radiation due to  $\bar{J}_p$ ,  $\bar{J}_m$  and  $\bar{J}_c$  is the summation of Eqs. (4.32) to (4.36). The resulting electric field components are:

$$E_\theta = f(r)f(\theta) \sin\theta \left\{ C_A \left[ (A_i\omega\mu_1 - B_i\gamma) L_0(k_1) \cos\theta - 2k_1 B_i L_1(k_1) \sin\theta - (A_i\omega\mu_1 + B_i\gamma) L_2(k_1) \cos\theta \right] + C_F \left[ (A_i\gamma - B_i\omega\epsilon_1) L_0(k_1) - (A_i\gamma + B_i\omega\epsilon_1) L_2(k_1) \right] \right\} - f(r) \sin\theta \frac{A_c \eta}{2k_c^2} \left[ \mu_r k + \beta \cos\theta \right] \frac{J_1(k_c a) J_1(k a \sin\theta)}{\sin\theta}, \quad (4.39)$$



and

$$\begin{aligned}
 E_{\theta} = & f(r) f(\theta) \cos \theta \left\{ C_A \left[ (A_i \omega \mu_1 - B_i \gamma) L_0(k_1) + \right. \right. \\
 & + (A_i \omega \mu_1 + B_i \gamma) L_2(k_1) \left. \right] + C_F \left[ (A_i \gamma - B_i \omega \epsilon_1) L_0(k_1) \cos \theta \right. \\
 & \left. \left. + 2k_1 A_i L_1(k_1) \sin \theta + (A_i \gamma + B_i \omega \epsilon_1) L_2(k_1) \cos \theta \right] \right\} \\
 & - f(r) \cos \theta \frac{A_c \eta k a}{2} \left[ \beta + \mu_r k \cos \theta \right] \frac{J_1(k_c a) J_1'(k a \sin \theta)}{k_c^2 - (k \sin \theta)^2} \quad (4.40)
 \end{aligned}$$

In the case where  $\mu_r = 1$  then  $C_F = 0$  and the radiated field reduces to that of a dielectric rod antenna.

$$\begin{aligned}
 E_{\theta} = & f(r) \sin \theta \left\{ C_A f(\theta) \left[ (A_i \omega \mu_0 - B_i \gamma) L_0(k_1) \cos \theta \right. \right. \\
 & \left. \left. - 2k_1 B_i L_1(k_1) \sin \theta - (A_i \omega \mu_0 + B_i \gamma) L_2(k_1) \cos \theta \right] \right. \\
 & \left. - \frac{A_c \eta k}{2k_c^2} \left[ 1 + \frac{\beta \cos \theta}{k} \right] \frac{J_1(k_c a) J_1(k a \sin \theta)}{\sin \theta} \right\}, \quad (4.41)
 \end{aligned}$$

and

$$\begin{aligned}
 E_{\theta} = & f(r) \cos \theta \left\{ C_A f(\theta) \left[ (A_i \omega \mu_0 - B_i \gamma) L_0(k_1) \right. \right. \\
 & \left. \left. + (A_i \omega \mu_0 + B_i \gamma) L_2(k_1) \right] \right. \\
 & \left. - \frac{A_c k^2 \eta a}{2} \left[ \frac{\beta}{k} + \cos \theta \right] \frac{J_1(k_c a) J_1'(k a \sin \theta)}{k_c^2 - (k \sin \theta)^2} \right\}. \quad (4.42)
 \end{aligned}$$

When both  $\mu_r$  and  $\epsilon_r$  reduce to unity, the polarization current and the magnetization current vanish. The antenna becomes an open circular waveguide radiating directly into free space.

$$E_{\theta} = -\frac{\eta k}{2k_c^2} f(r) \sin \phi \left[ 1 + \frac{\beta \cos \theta}{k} \right] \frac{J_1(k_c a) J_1(k a \sin \theta)}{\sin \theta}, \quad (4.43)$$

and

$$E_{\phi} = -\frac{k^2 a \eta}{2} f(r) \cos \phi \left[ \frac{\beta}{k} + \cos \theta \right] \frac{J_1(k_c a) J_1'(k a \sin \theta)}{k_c^2 - (k \sin \theta)^2}. \quad (4.44)$$

The radiation pattern of a full core loaded circular waveguide can be expressed as:

$$E_{\theta} = \frac{-\mu_r k \eta}{2k_c^2} f(r) \sin \phi \left[ 1 + \frac{\beta \cos \theta}{\mu_r k} + \Gamma \left( 1 - \frac{\beta \cos \theta}{\mu_r k} \right) \right] \cdot \frac{J_1(k_c a) J_1(k a \sin \theta)}{\sin \theta}, \quad (4.35)$$

and

$$E_{\phi} = \frac{-\mu_r k^2 \eta a}{2} f(r) \cos \phi \left[ \frac{\beta}{\mu_r k} + \cos \theta - \Gamma \left( \frac{\beta}{\mu_r k} - \cos \theta \right) \right] \cdot \frac{J_1(k_c a) J_1'(k a \sin \theta)}{k_c^2 - (k \sin \theta)^2}. \quad (4.36)$$

#### 4.2.6 Operating Range of the Solid Rod Antennas

In order to be an efficient radiator and to be sure to radiate in the endfire direction, it is desirable to launch a  $HE_{11}$  mode on the finite rod antenna, and to

have a continual flow of energy directly outward along the axial direction into free space. The symmetric  $TM_{01}$  and  $TE_{01}$  modes would radiate in the broadside direction, and the reflection due to the discontinuity at the open end will divert the energy in the other direction. The solid rod antenna with a large rod diameter may propagate symmetric modes, and most of the surface wave energy will be bound to the rod, thus resulting in more losses in the rod and more reflection from the discontinuity at the open end. In practice most solid dielectric rod antennas with the relative dielectric permittivity  $\epsilon_r = 2.5$  operate in the diameter range  $0.4 \lambda_o \leq d \leq 0.6 \lambda_o$  with a guide wavelength  $\lambda_g$  somewhere around  $0.9 \lambda_o$ . In most cases about 40 to 60 percent of the surface wave energy is carried external to the rod. For a rod with higher permittivity and permeability, or larger diameter, tapering or loading along the axis is necessary. The lower operating frequency limit of the antenna is due to the cutoff of the launching device. The antenna directivity is proportional to the length of the rod, but in any case it should not exceed

$$l_{\max} = \frac{\lambda_o \lambda_g}{\lambda_o - \lambda_g}$$

For a rod longer than  $l_{\max}$  the sidelobes become very large.

### 4.3 Ferrite Tube Antennas

#### 4.3.1 Choice of the Mathematical Approaches

The polarization current and magnetization current method described in the preceding section also applies to the ferrite tube antennas. However it requires the solution of two waveguide problems before one can commence to evaluate the radiation of this antenna. First, it is necessary to solve an infinitely long ferrite tube waveguide to obtain the assumed polarization current and magnetization current in the ferrite. Second, it is necessary to solve the partially ferrite loaded metal waveguide to obtain the assumed transverse aperture field distribution at the feed of the antenna. The

procedure and the mathematical expression of the radiated field becomes very long and tedious. Therefore, the two aperture array method (Brown and Spector 1967) will be presented in this section. The field distribution over the open end aperture will be assumed to be approximately the same as that of the  $HE_{11}$  mode surface wave in a parallel transverse cross section in an infinite tube when the tube has a good matching to free space at the open end of the tube. The launching efficiency of a solid dielectric rod with a relative permittivity  $\epsilon_r = 2.5$  from a  $TE_{11}$  mode circular waveguide  $0.57\lambda_0$  in diameter is about 90 percent (Duncan and DuHamel 1957). The launching efficiency increases with the diameter of the feed waveguide. The launching efficiency of a ferrite tube is expected to be higher than the dielectric rod, because of the better guiding effect of the ferrite material and its two curved boundary surfaces. The reflection from the open end of the tube is small if the tube has a thin wall thickness at the open end. The approximate far field pattern can be predicted satisfactorily from the assumed field distribution at the open end of the tube and a small portion of the direct radiation from the feed.

#### 4.3.2 Ferrite Tube Waveguide.

The electromagnetic waves which exist in an infinite ferrite tube can be obtained by solving the Maxwell's equations in a cylindrical coordinate system for the boundaries as shown in Fig. 4-5. In region II, the ferrite material is assumed to have a permeability  $\mu = \mu_0 \mu_r$  and a permittivity  $\epsilon = \epsilon_0 \epsilon_r$ . Region I and III are free space. The most general type of waves which can exist in a ferrite tube are the hybrid modes which have both axial electric and magnetic components. They may be expressed as:

In region I:

$$\begin{cases} E_{z1} = A_1 I_n(Ws) e^{j(\omega t - \gamma_n z - n\phi)} \\ H_{z1} = B_1 I_n(Ws) e^{j(\omega t - \gamma_n z - n\phi)} \end{cases} \quad (4.45)$$

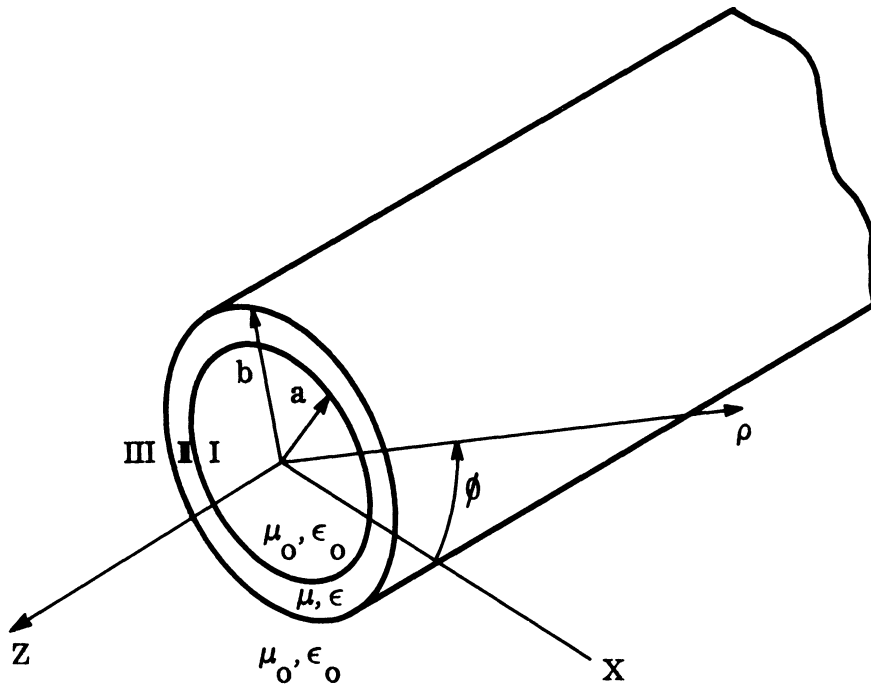


FIG. 4-5: COORDINATE SYSTEM ASSUMED FOR THE FERRITE TUBE WAVEGUIDE.

THE UNIVERSITY OF MICHIGAN

7848-1-F

In region II:

$$\begin{cases} E_{z2} = [A_2 J_n(Vs) + A_3 N_n(Vs)] e^{j(\omega t - \gamma_n z - n\phi)} \\ H_{z2} = [B_2 J_n(Vs) + B_3 N_n(Vs)] e^{j(\omega t - \gamma_n z - n\phi)} \end{cases} \quad (4.46)$$

In region III:

$$\begin{cases} E_{z3} = A_4 K_n(Ws) e^{j(\omega t - \gamma_n z - n\phi)} \\ H_{z3} = B_4 K_n(Ws) e^{j(\omega t - \gamma_n z - n\phi)} \end{cases} \quad (4.47)$$

with

$$s = \frac{\rho}{b}, \quad jW = k_{n1} b, \quad V = k_{n2} b \quad (4.48)$$

and

$$\begin{cases} k_{n1}^2 = \omega^2 \mu_o \epsilon_o - \gamma_n^2 \\ k_{n2}^2 = \omega^2 \mu \epsilon - \gamma_n^2 \end{cases} \quad (4.49)$$

$I_n$  and  $K_n$  are modified Bessel functions of the first and second kinds and of order  $n$  respectively.

The remaining  $\rho$  and  $\phi$  field components can be expressed in terms of  $E_z$  and  $H_z$  as follows:

$$E_{\phi} = k_i \left[ -\frac{j\gamma_n}{s} \frac{\partial E_z}{\partial \phi} + j\omega\mu \frac{\partial H_z}{\partial s} \right] ,$$

$$E_{\rho} = -k_i \left[ j\gamma_n \frac{\partial E_z}{\partial s} + \frac{j\omega\mu}{s} \frac{\partial H_z}{\partial \phi} \right] ,$$

$$H_{\phi} = -k_i \left[ j\omega\epsilon \frac{\partial E_z}{\partial s} + \frac{j\gamma_n}{s} \frac{\partial H_z}{\partial \phi} \right] ,$$

and

$$H_{\rho} = k_i \left[ \frac{j\omega\epsilon}{s} \frac{\partial E_z}{\partial \phi} - j\gamma_n \frac{\partial H_z}{\partial s} \right] \quad (4.50)$$

where

$$k_i = \frac{-b}{W} , \quad \epsilon = \epsilon_0 , \quad \mu = \mu_0 \quad \text{in region I and III}$$

$$k_i = \frac{b}{V} , \quad \epsilon = \epsilon_r \epsilon_0 , \quad \mu = \mu_r \mu_0 \quad \text{in region II.}$$

By substituting Eqs. (4.45), (4.46) and (4.47) into Eq. (4.50) to obtain the  $r$  - and  $\phi$  - components results in the following set of field equations:

$$\begin{aligned} E_{\phi 1} &= j \frac{2\pi}{W} \left\{ \frac{n}{Ws} \frac{b}{\lambda_g} I_n(Ws) A_1 - \eta \frac{b}{\lambda_0} I_n'(Ws) B_1 \right\} \sin n\phi , \\ H_{\phi 1} &= j \frac{2\pi}{W} \left\{ \frac{1}{\eta} \frac{b}{\lambda_0} I_n'(Ws) A_1 + \frac{n}{Ws} \frac{b}{\lambda_g} I_n(Ws) B_1 \right\} \cos n\phi , \\ E_{\rho 1} &= j \frac{2\pi}{W} \left\{ \frac{b}{\lambda_g} I_n'(Ws) A_1 + \frac{n}{Ws} \eta \frac{b}{\lambda_0} I_n(Ws) B_1 \right\} \cos n\phi , \\ H_{\rho 1} &= j \frac{2\pi}{W} \left\{ \frac{n}{Ws} \frac{1}{\eta} \frac{b}{\lambda_0} I_n(Ws) A_1 + \frac{b}{\lambda_g} I_n'(Ws) B_1 \right\} \sin n\phi , \end{aligned} \quad (4.51)$$

$$\begin{aligned}
 E_{\phi 2} &= j \frac{2\pi}{V} \left\{ \frac{n}{Vs} \frac{b}{\lambda_g} \left[ J_n(Vs) A_2 + N_n(Vs) A_3 \right] \right. \\
 &\quad \left. + \mu_r \eta \frac{b}{\lambda_o} \left[ J'_n(Vs) B_2 + N'_n(Vs) B_3 \right] \right\} \sin n\phi , \\
 H_{\phi 2} &= -j \frac{2\pi}{V} \left\{ \frac{\epsilon_r}{\eta} \frac{b}{\lambda_o} \left[ J'_n(Vs) A_2 + N'_n(Vs) A_3 \right] \right. \\
 &\quad \left. + \frac{n}{Vs} \frac{b}{\lambda_g} \left[ J_n(Vs) B_2 + N_n(Vs) B_3 \right] \right\} \cos n\phi , \\
 E_{\rho 2} &= -j \frac{2\pi}{V} \left\{ \frac{b}{\lambda_g} \left[ J'_n(Vs) A_2 + N'_n(Vs) A_3 \right] \right. \\
 &\quad \left. + \frac{n\mu_r}{Vs} \eta \frac{b}{\lambda_o} \left[ J_n(Vs) B_2 + N_n(Vs) B_3 \right] \right\} \cos n\phi , \\
 H_{\rho 2} &= -j \frac{2\pi}{V} \left\{ \frac{n\epsilon_r}{Vs} \frac{1}{\eta} \frac{b}{\lambda_o} \left[ J_n(Vs) A_2 + N_n(Vs) A_3 \right] \right. \\
 &\quad \left. + \frac{b}{\lambda_g} \left[ J'_n(Vs) B_2 + N'_n(Vs) B_3 \right] \right\} \sin n\phi , \quad (4-52)
 \end{aligned}$$

$$\begin{aligned}
 E_{\phi 3} &= -j \frac{2\pi}{W} \left\{ \frac{n}{Ws} \frac{b}{\lambda_g} K_n(Ws) A_4 + \eta \frac{b}{\lambda_o} K'_n(Ws) B_4 \right\} \sin n\phi , \\
 H_{\phi 3} &= j \frac{2\pi}{W} \left\{ \frac{1}{\eta} \frac{b}{\lambda_o} K'_n(Ws) A_4 + \frac{n}{Ws} \frac{b}{\lambda_g} K_n(Ws) B_4 \right\} \cos n\phi , \\
 E_{\rho 3} &= j \frac{2\pi}{W} \left\{ \frac{b}{\lambda_g} K'_n(Ws) A_4 + \frac{n}{Ws} \eta \frac{b}{\lambda_o} K_n(Ws) B_4 \right\} \cos n\phi , \\
 H_{\rho 3} &= j \frac{2\pi}{W} \left\{ \frac{n}{Ws} \frac{1}{\eta} \frac{b}{\lambda_o} K_n(Ws) A_4 + \frac{b}{\lambda_g} K'_n(Ws) B_4 \right\} \sin n\phi . \quad (4.53)
 \end{aligned}$$



All the tangential field components on the boundary surfaces at  $\rho = a$  and  $\rho = b$  must be continuous. In matching these boundary conditions one obtains eight equations for the eight A's and B's which are coefficients. In order to have a non-trivial solution, the determinant of the coefficient of these eight equations must be zero. The complete derivation is given in the Appendix B where it is shown that the determinantal equation is:

$$\begin{aligned}
 & -n^4 T^4 (\Delta_3 - \Delta_4)^2 - C^4 Q^2 \left[ \Delta_3 (\epsilon_r \Delta_1 - \Delta_8)(\epsilon_r \Delta_7 - \Delta_5) \right. \\
 & \left. - \Delta_4 (\epsilon_r \Delta_6 - \Delta_8)(\epsilon_r \Delta_2 - \Delta_5) \right] \cdot \left[ \Delta_3 (\mu_r \Delta_1 - \Delta_8)(\mu_r \Delta_7 - \Delta_5) \right. \\
 & \left. - \Delta_4 (\mu_r \Delta_6 - \Delta_8)(\mu_r \Delta_2 - \Delta_5) \right] - 2n^2 T^2 \mu_r \epsilon_r Q C^2 \Delta_3 \Delta_4 \cdot \\
 & \cdot (\Delta_1 - \Delta_6)(\Delta_2 - \Delta_7) + n^2 T^2 Q \left[ \Delta_3^2 (\epsilon_r \Delta_7 - \Delta_5)(\mu_r \Delta_7 - \Delta_5) \right. \\
 & \left. - \Delta_3 \Delta_4 (\epsilon_r \Delta_7 - \Delta_5)(\mu_r \Delta_2 - \Delta_5) - \Delta_3 \Delta_4 (\epsilon_r \Delta_2 - \Delta_5)(\mu_r \Delta_7 - \Delta_5) \right. \\
 & \left. + \Delta_4^2 (\epsilon_r \Delta_2 - \Delta_5)(\mu_r \Delta_2 - \Delta_5) \right] + n^2 T^2 Q C^4 \left[ \Delta_3^2 (\epsilon_r \Delta_1 - \Delta_8)(\mu_r \Delta_1 - \Delta_8) \right. \\
 & \left. - \Delta_3 \Delta_4 (\epsilon_r \Delta_1 - \Delta_8)(\mu_r \Delta_6 - \Delta_8) - \Delta_3 \Delta_4 (\epsilon_r \Delta_6 - \Delta_8)(\mu_r \Delta_1 - \Delta_8) \right. \\
 & \left. + \Delta_4^2 (\epsilon_r \Delta_6 - \Delta_8)(\mu_r \Delta_6 - \Delta_8) \right] = 0 \tag{4.54}
 \end{aligned}$$

where

$$C = \frac{a}{b}$$

$$\Delta_1 = \frac{J'_n(CV)}{CVJ'_n(CV)}$$

$$\Delta_2 = \frac{J'_n(V)}{VJ'_n(V)}$$

$$\Delta_3 = \frac{J_n(CV)}{N_n(CV)}$$

$$\Delta_4 = \frac{J_n(V)}{N_n(V)}$$

THE UNIVERSITY OF MICHIGAN  
7848-1-F

$$\begin{aligned}
 \Delta_5 &= \frac{K'_n(W)}{WK'_n(W)} & \Delta_6 &= \frac{N'_n(CV)}{CVN'_n(CV)} \\
 \Delta_7 &= \frac{N'_n(V)}{VN'_n(V)} & \Delta_8 &= \frac{I'_n(CW)}{CWI'_n(CW)} \\
 T &= \frac{1}{V^2} + \frac{1}{W^2} & Q &= \left(\frac{\lambda_g}{\lambda_o}\right)^2 = \frac{V^2 + W^2}{V^2 + \mu_r \epsilon_r W^2}
 \end{aligned}
 \tag{4.55}$$

When the dimension "a" reduces to zero, then  $C = 0$  and the determinantal Eq. (4.55) reduces to

$$(\epsilon_r \Delta_2 - \Delta_5)(\mu_r \Delta_2 - \Delta_5) = \frac{T}{Q}
 \tag{4.56}$$

which is essentially the same as the determinantal equation of a solid rod. By eliminating  $\gamma_n$  in Eq. (4.58) with Eq. (4.59) gives:

$$\left(\frac{2b}{\lambda_o}\right)^2 = \frac{V^2 + W^2}{\pi^2(\mu_r \epsilon_r - 1)}
 \tag{4.57}$$

$$\left(\frac{\lambda_g}{\lambda_o}\right)^2 = \frac{V^2 + W^2}{V^2 + \mu_r \epsilon_r W^2}
 \tag{4.58}$$

For a wave propagating along the ferrite tube, the parameters  $W$  and  $V$  must satisfy the determinantal Eq. (4.55). By substituting the corresponding values of  $W$  and  $V$  into Eqs. (4.57) and (4.58), the relation between the tube diameter and phase velocity can be obtained. For  $V \gg W$ ,  $\lambda_g/\lambda_o$  tends to unity. For  $W \gg V$ ,

$\lambda_g/\lambda$  tends to  $1/\sqrt{\mu_r \epsilon_r}$ . Therefore the guide wavelength has the range:

$$\frac{\lambda_0}{\sqrt{\mu_r \epsilon_r}} < \lambda_g < \lambda_0 \quad (4.59)$$

The cutoff properties of the waves can be found from Eq. (4.57) by substituting the values of  $V$  when  $W$  approaches zero.

$$\left. \frac{2b}{\lambda_0} \right|_{\text{cutoff}} = \frac{1}{\pi \sqrt{\mu_r \epsilon_r - 1}} \cdot V \Big|_{W \rightarrow 0} \quad (4.60)$$

The above equation shows that the surface waves cannot propagate along the tube without attenuation in the absence of a material with  $\mu_r \epsilon_r$  unity.

#### 4.3.3 Radiation from the Open End of the Ferrite Tube

The far field radiation formula from the open end of the tube oriented in the  $z = 0$  plane can be expressed as:

$$E_\theta = \frac{-jke^{-jkr}}{4\pi r} [L_\theta + \eta N_\theta] \quad (4.19)$$

$$E_\phi = \frac{jke^{-jkr}}{4\pi r} [L_\phi - \eta N_\phi] \quad (4.20)$$

with the magnetic radiation vector  $N$  and the electric radiation vector  $L$  defined:

$$\begin{aligned} \bar{N} &= \int_S \bar{n} \times \bar{H} e^{jkr' \cos \xi} ds \\ &= \int_0^\infty \int_0^{2\pi} (\hat{y}H_x - \hat{x}H_y) e^{jkr' \cos \xi} \rho d\phi d\rho, \end{aligned} \quad (4.61)$$

$$\begin{aligned}\bar{L} &= \int_S \bar{E} \times \bar{n} e^{jkr' \cos \xi} ds \\ &= \int_0^\infty \int_0^{2\pi} (\hat{x} E_y - \hat{y} E_x) e^{jkr' \cos \xi} \rho d\phi d\rho\end{aligned}\quad (4.62)$$

and with

$$kr' \cos \xi = k\rho' \sin \theta \cos(\phi - \phi') \quad \text{for } z = 0 \quad . \quad (4.63)$$

The rectangular field components of the assumed  $HE_{11}$  mode in the transverse plane  $z = 0$  can be obtained by using Eq. (4.25), for the transformation of coordinates, and Eq. (4.26), the recurrence relations of the Bessel functions.

$$\begin{aligned}E_{x1} &= j \frac{\pi b}{W\lambda_g} A_1 \left[ I_0(Ws) + I_2(Ws) \cos 2\phi \right] \\ &\quad + j \frac{\pi b}{W\lambda_o} \eta B_1 \left[ I_0(Ws) - I_2(Ws) \cos 2\phi \right] \\ E_{y1} &= \left[ j \frac{\pi b}{W\lambda_g} A_1 - j \frac{\pi b}{W\lambda_o} \eta B_1 \right] I_2(Ws) \sin 2\phi \\ H_{x1} &= - \left[ j \frac{\pi b}{W\lambda_o} \frac{A_1}{\eta} - j \frac{\pi b}{W\lambda_g} B_1 \right] I_2(Ws) \sin 2\phi \\ H_{y1} &= j \frac{\pi b}{W\lambda_o} \frac{A_1}{\eta} \left[ I_0(Ws) + I_2(Ws) \cos 2\phi \right] \\ &\quad + j \frac{\pi b}{W\lambda_g} B_1 \left[ I_0(Ws) - I_2(Ws) \cos 2\phi \right] .\end{aligned}\quad (4.64)$$

Substitute Eq. (4.64) into Eqs. (4.61) and (4.62) and perform the integration using Eq. (4.63) and the Bessel-Fourier series expansion:

$$e^{jk\rho' \sin\theta \cos(\phi - \phi')} = J_0(k\rho' \sin\theta) + \sum_{m=1}^{\infty} 2j^m J_m(k\rho' \sin\theta) \cos m(\phi - \phi') .$$

Thus the vector potential components of N and L in rectangular coordinate are:

$$\begin{aligned} N_{x1} &= -j \frac{2\pi^2 b}{W\lambda_o} \frac{A_1}{\eta} \left[ L_{I0} - L_{I2} \cos 2\phi \right] \\ &\quad - j \frac{2\pi^2 b}{W\lambda_g} B_1 \left[ L_{I0} + L_{I2} \cos 2\phi \right] , \\ N_{y1} &= \left[ j \frac{2\pi^2 b}{W\lambda_o} \frac{A_1}{\eta} - j \frac{2\pi^2 b}{W\lambda_g} B_1 \right] L_{I2} \sin 2\phi , \\ L_{x1} &= - \left[ j \frac{2\pi^2 b}{W\lambda_g} A_1 - j \frac{2\pi^2 b}{W\lambda_o} \eta B_1 \right] L_{I2} \sin 2\phi , \\ L_{y1} &= -j \frac{2\pi^2 b}{W\lambda_g} A_1 \left[ L_{I0} - L_{I2} \cos 2\phi \right] \\ &\quad - j \frac{2\pi^2 b}{W\lambda_o} \eta B_1 \left[ L_{I0} + L_{I2} \cos 2\phi \right] , \end{aligned} \tag{4.65}$$

where Lommel integral are:

$$\begin{aligned} L_{I0} &= \int_0^a \rho I_0(Ws) J_0(k\rho \sin\theta) d\rho \\ L_{I2} &= \int_0^a \rho I_2(Ws) J_2(k\rho \sin\theta) d\rho \end{aligned} \tag{4.66}$$

and

$$s = \frac{\rho}{b}$$

By using Eq. (4.30). The spherical components of the radiation vector  $\bar{N}$  and  $\bar{L}$  can be simplified to:

$$N_{\theta 1} = 2\pi \cos \phi \cos \theta \left[ -L_{I0} \left( j \frac{\pi b}{W\lambda_o} \frac{A_1}{\eta} + j \frac{\pi b}{W\lambda_g} B_1 \right) + L_{I2} \left( j \frac{\pi b}{W\lambda_o} \frac{A_1}{\eta} - j \frac{\pi b}{W\lambda_g} B_1 \right) \right],$$

$$N_{\phi 1} = 2\pi \sin \phi \left[ L_{I0} \left( j \frac{\pi b}{W\lambda_o} \frac{A_1}{\eta} + j \frac{\pi b}{W\lambda_g} B_1 \right) + L_{I2} \left( j \frac{\pi b}{W\lambda_o} \frac{A_1}{\eta} - j \frac{\pi b}{W\lambda_g} B_1 \right) \right],$$

$$L_{\theta 1} = 2\pi \sin \phi \cos \theta \left[ -L_{I0} \left( j \frac{\pi b}{W\lambda_g} A_1 + j \frac{\pi b}{W\lambda_o} \eta B_1 \right) - L_{I2} \left( j \frac{\pi b}{W\lambda_g} A_1 - j \frac{\pi b}{W\lambda_o} \eta B_1 \right) \right],$$

and

$$L_{\phi 1} = 2\pi \cos \phi \left[ -L_{I0} \left( j \frac{\pi b}{W\lambda_g} A_1 + j \frac{\pi b}{W\lambda_o} \eta B_1 \right) + L_{I2} \left( j \frac{\pi b}{W\lambda_g} A_1 - j \frac{\pi b}{W\lambda_o} \eta B_1 \right) \right]. \quad (4.67)$$

Substitute Eq. (4.67) into Eqs. (4.19) and (4.20). The resulting radiation from the inner aperture at the open end is:

$$E_{\theta 1} = \frac{-ke^{-jkr}}{2r} \cos \phi \left[ (L_{I_0} - L_{I_2}) \frac{\pi b}{W\lambda_g} A_1 \left( 1 + \frac{\lambda_g}{\lambda_o} \cos \theta \right) + (L_{I_0} + L_{I_2}) \frac{\pi b}{W\lambda_o} \eta B_1 \left( 1 + \frac{\lambda_o}{\lambda_g} \cos \theta \right) \right], \quad (4.68)$$

and

$$E_{\phi 1} = \frac{ke^{-jkr}}{2r} \sin \phi \left[ (L_{I_0} + L_{I_2}) \frac{\pi b}{W\lambda_o} A_1 \left( 1 + \frac{\lambda_o}{\lambda_g} \cos \theta \right) + (L_{I_0} - L_{I_2}) \frac{\pi b}{W\lambda_g} \eta B_1 \left( 1 + \frac{\lambda_g}{\lambda_o} \cos \theta \right) \right]. \quad (4.69)$$

Using the same procedure, the radiation from the outer aperture around the end of the rod can be found to be:

$$E_{\theta 3} = \frac{ke^{-jkr}}{2r} \cos \phi \left[ (L_{k_0} - L_{k_2}) \frac{\pi b}{W\lambda_g} A_4 \left( 1 + \frac{\lambda_g}{\lambda} \cos \theta \right) + (L_{k_0} + L_{k_2}) \frac{\pi b}{W\lambda_o} \eta B_4 \left( 1 + \frac{\lambda_o}{\lambda_g} \cos \theta \right) \right], \quad (4.70)$$

$$E_{\phi 3} = \frac{-ke^{-jkr}}{2r} \sin \phi \left[ (L_{k_0} + L_{k_2}) \frac{\pi b}{W\lambda_o} A_4 \left( 1 + \frac{\lambda_o}{\lambda_g} \cos \theta \right) + (L_{k_0} - L_{k_2}) \frac{\pi b}{W\lambda_g} \eta B_4 \left( 1 + \frac{\lambda_g}{\lambda_o} \cos \theta \right) \right], \quad (4.71)$$

where the Lommel integrals are,

$$L_{k_0} = \int_b^{\infty} \rho k_o (W s) J_o(k\rho \sin \theta) d\rho, \quad ,$$

and

$$L_{k_2} = \int_b^{\infty} \rho k_2 (W s) J_2(k\rho \sin \theta) d\rho. \quad (4.72)$$

4.3.4 The Far Field Pattern of the Ferrite Tube Antenna

Since one has little knowledge of the field distribution at the feed, it is extremely difficult to evaluate the direct radiation from the metal waveguide because of the presence of the tube. Therefore the following expression of the far field pattern of the ferrite tube antenna is based on the following assumptions:

- 1) Reflections from both the feed of the metal waveguide and from the open end of the tube will be neglected.
- 2) The direct radiation is small in magnitude and approximately the same as the radiation from the open  $TE_{11}$  waveguide without the presence of the tube.
- 3) All symmetric and higher order modes are comparatively small and negligible.
- 4) The ferrite tube has a thin wall thickness, and most of the energy is carried external to the ferrite material.

Based on the above assumptions the far field expression of the ferrite tube antenna is the summation of Eqs. (4.43), (4.44) and (4.68) to (4.71).

The far field expressions are:

$$\begin{aligned}
 E_{\theta} = & - \cos \theta \left\{ \frac{-\eta}{k_c} \left( 1 + \frac{\beta \cos \theta}{k} \right) \frac{J_1(k_c b) J_1(k b \sin \theta)}{\sin \theta} \right. \\
 & + \frac{\pi b}{W \lambda_g} \left( 1 + \frac{\lambda_g}{\lambda_o} \cos \theta \right) \left[ A_1(L_{I_o} - L_{I_2}) - A_4(L_{k_o} - L_{k_2}) \right] e^{jk \ell \left( \cos \theta - \frac{\lambda_o}{\lambda_g} \right)} \\
 & + \frac{\pi b}{W \lambda_o} \eta \left( 1 + \frac{\lambda_o}{\lambda_g} \cos \theta \right) \left[ B_1(L_{I_o} + L_{I_2}) - B_4(L_{k_o} + L_{k_2}) \right] \\
 & \left. \cdot e^{jk \ell \left( \cos \theta - \frac{\lambda_o}{\lambda_g} \right)} \right\} , \tag{4.73}
 \end{aligned}$$



$$\begin{aligned}
 E_{\theta} = \sin \theta \left\{ & b \eta (\beta + k \cos \theta) \frac{J_1(k_c b) J_1'(k b \sin \theta)}{k_c^2 - (k \sin \theta)^2} \right. \\
 & + \frac{\pi b}{W \lambda_o} \left(1 + \frac{\lambda_o}{\lambda_g} \cos \theta\right) \left[ A_1 (L_{I_o} + L_{I_2}) - A_4 (L_{k_o} + L_{k_2}) \right] e^{j k l \left(\cos \theta - \frac{\lambda_o}{\lambda_g}\right)} \\
 & + \frac{\pi b}{W \lambda_g} \eta \left(1 + \frac{\lambda_g}{\lambda_o} \cos \theta\right) \left[ B_1 (L_{I_o} - L_{I_2}) - B_4 (L_{k_o} - L_{k_2}) \right] e^{j k l \left(\cos \theta - \frac{\lambda_o}{\lambda_g}\right)} \left. \right\}.
 \end{aligned}
 \tag{4.74}$$

#### 4.3.5 Advantages of the Tube Antenna over the Solid Rod Antenna

In order to be an efficient antenna, the surface wave propagating in the axial direction should not be tightly bound to the rod, otherwise the surface wave energy pulsates back and forth in the ferrite and nearby space. This would result in more losses in the ferrite and more reflection from the open end of the rod. For this reason the solid rod can only operate in a certain frequency band in a small range of diameter in wavelengths. Material with high permeability and permittivity is not applicable to the uniform rod antenna. When the solid rod is replaced by a hollow tube, these deficiencies of the solid rod are removed. Use of a hollow tube offers certain advantages over the solid rod:

- 1) Because of the two boundary layers of the tube, the tube antenna has a higher launching efficiency.
- 2) The tube shape offers a better guiding effect of the electromagnetic wave.
- 3) The open end of the tube antenna offers a better matching to free space.
- 4) The wall thickness of the tube can be selected so as to permit use of all kinds of material with high permeability and permittivity.

In a summary of the comparison, a tube antenna has higher directivity, lower sidelobe level and a wider frequency band in addition to its lightness.

#### 4.4 Experimental Results

In the analysis of the ferrite rod waveguide it is seen that an increase in the permeability  $\mu$  or the permittivity  $\epsilon$  of the ferrite rod has the effect of increasing the propagation constant along the axis. This may be the cause of increasing the number of sidelobes and the level of sidelobes. In order to obtain endfire narrow beam patterns it is preferable to have an axial propagation constant nearly equal to free space propagation constant. As shown in Fig. 4-6 a cylindrical ferrite tube was used instead of a solid rod; it appears that the hollow tube has better guiding properties than the solid rod. During this investigation several ferrite tube antennas excited by a quadrifilar helix, a quadrupole and a dipole have been built and tested. More than 200 far field patterns were taken for various tube lengths and thicknesses for the study of the beamwidth, sidelobe level and position. All patterns were taken on an outdoor range with the test antenna rotated through 360 degrees and receiving from a linearly polarized zig-zag transmitting antenna operated in the 200 to 1400 MHz frequency range. All ferrite tubes used in this experiment were formed by placing EAF-2 ferrite powder with  $\mu_r = 3.8$ ,  $\epsilon_r = 2.2$  between a fiber glass shell and a balsa wood core. Fig. 4-6 shows the coordinate system assumed and the radiation plane defined for the ferrite tube antenna. In order to check the guiding effect of the ferrite material, a 15 cm diameter phenolic shell and a 13.5 cm balsa wood core both 100 cm in length including the feeding cylindrical cavity were tested before the ferrite powder was inserted between the phenolic shell and balsa wood core. Radiation patterns shown in Fig. 4-7 are essentially the  $TE_{11}$  mode cavity patterns. The effects of the fiber glass and the balsa wood have been found to be very small.

##### 4.4.1 Ferrite Tube Excited by a Quadrifilar Helix

A uniform ferrite tube with 12.5 cm outside diameter, 10 cm inside diameter and 35 cm in length was fed from one end by a quadrifilar helix with a 10 cm diameter, a 32 degrees pitch angle and 27 cm in length excited in  $0^\circ - 90^\circ - 180^\circ - 270^\circ$  phase

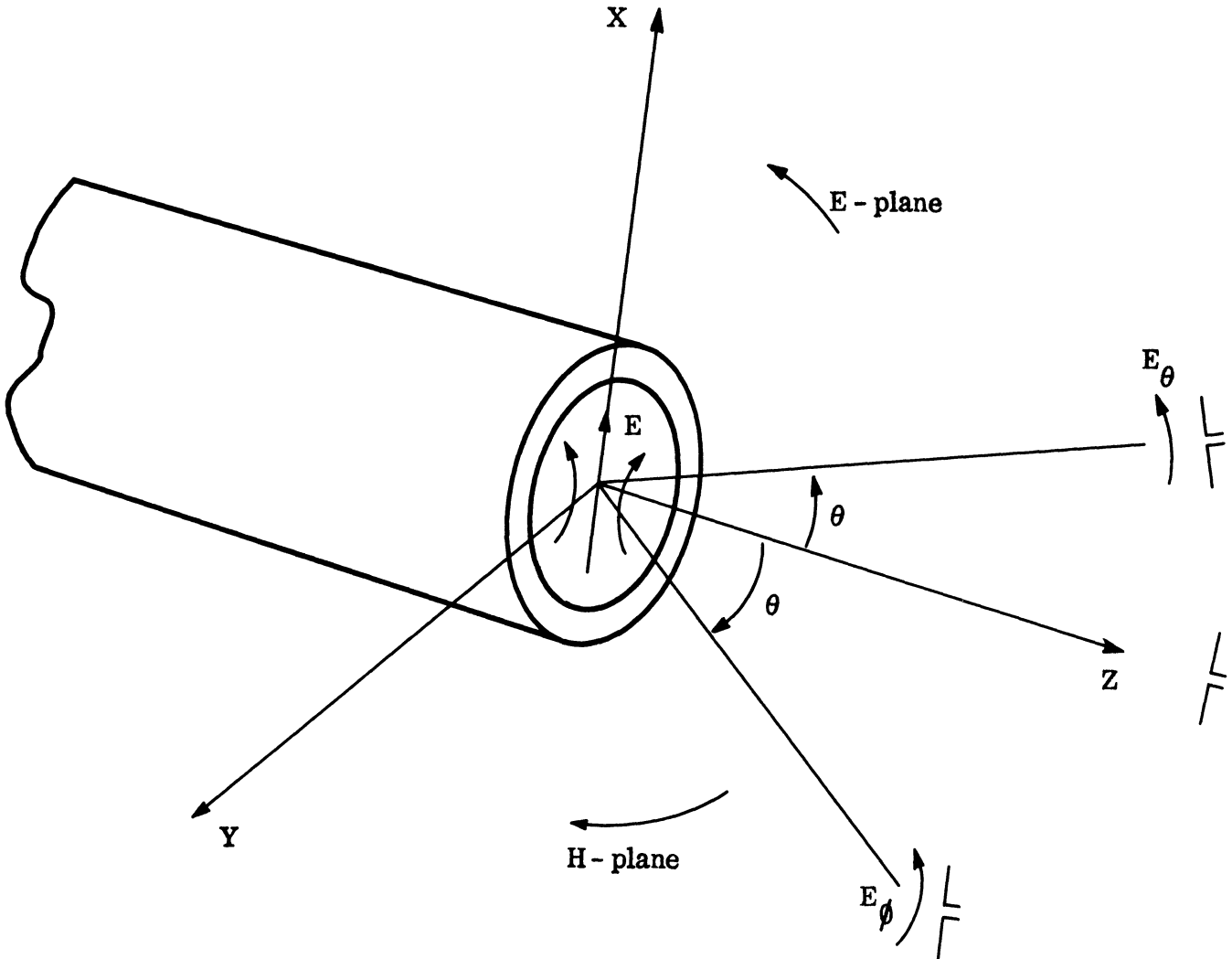


FIG. 4-6: COORDINATE SYSTEM ASSUMED FOR THE FERRITE TUBE ANTENNA AND THE RADIATION PLANE DEFINED.

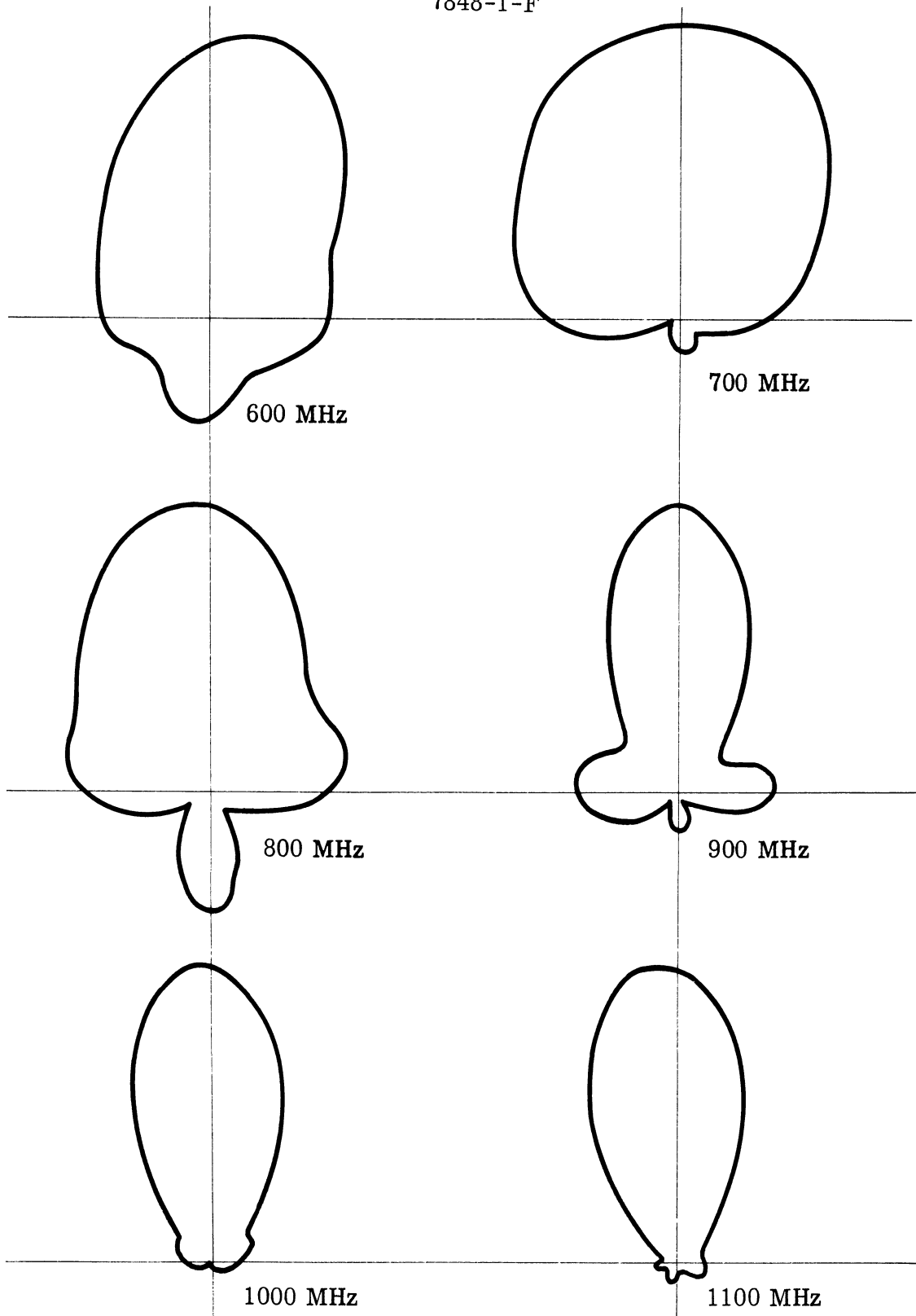


FIG. 4-7a: LINEAR POWER PATTERNS FROM THE DIPOLE EXCITED METAL CUP WITH THE BALSA WOOD CORE AND THE PHENOLIC SHELL WITHOUT EAF-2 FERRITE POWDER.

(a)  $|E_{\theta}|^2$  Plot in E - plane.

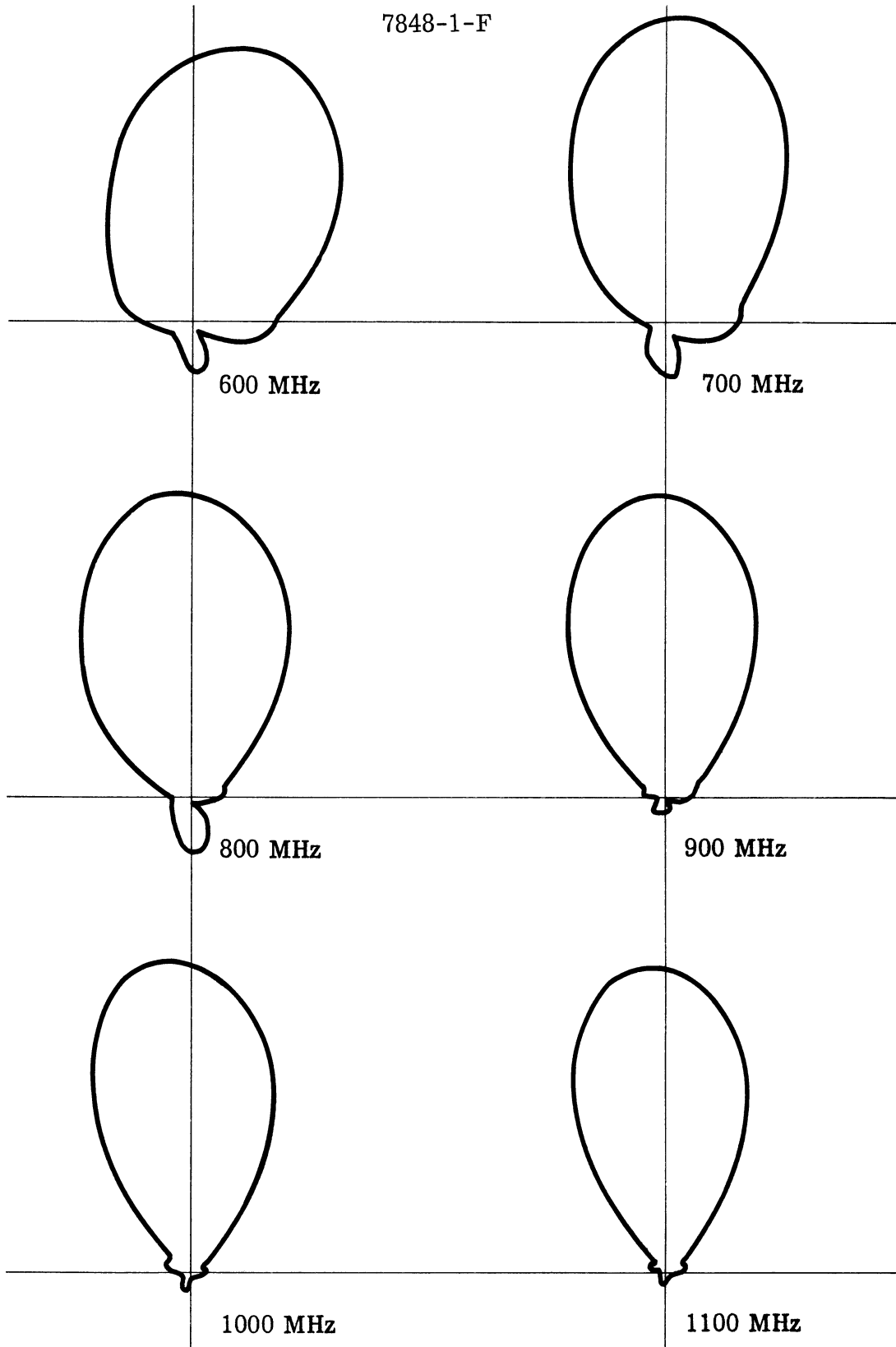


FIG. 4-7b: LINEAR POWER PATTERNS FROM THE DIPOLE EXCITED METAL CUP WITH THE BALSA WOOD CORE AND THE PHENOLIC SHELL WITHOUT EAF-2 FERRITE POWDER.

(b)  $|E_{\theta}|^2$  Plot in H-plane.

sequence. It was planned in order to launch a surface wave along the axis of the tube like the  $HE_{11}$  mode to radiate in the endfire direction. The radiation patterns are shown in Fig. 4-8 from 750 MHz to 1000 MHz. At 750 MHz it corresponds to having a tube  $0.313\lambda_0$  in outside diameter and  $2.1\lambda_0$  in length. At 1000 MHz, it corresponds to having  $0.42\lambda_0$  in diameter and  $2.83\lambda_0$  in length. Below 1000 MHz the antenna is well below the cutoff frequency of the symmetric  $TM_{0m}$  or  $TE_{0m}$  modes. Above 1000 MHz the sidelobe level increases and the tube antenna tends to radiate in the broadside direction. It may be due to the unwanted symmetric modes becoming more important.

#### 4.4.2 Ferrite Tube Excited by Quadrupole

The same ferrite tube as described in Section 4.4.1 was used in this experiment except the quadrifilar helix was replaced by the 13 cm quadrupole placed parallel to the axis of the tube. Again the quadrupole was excited in a  $0^\circ - 90^\circ - 180^\circ - 270^\circ$  phase sequence. Figure 4-9a shows the radiation patterns of this antenna when the quadrupole was placed at the inside circumference of the tube. The mainlobe of the pattern is very close to that of the quadrifilar helix excited antenna except the sidelobes are slightly lower at high frequency.

When the excitation quadrupole was moved to the outside circumference of the tube, this antenna radiated in the broadside direction as shown in Fig. 4-9b. The guiding effect of the ferrite material is very obvious. When it was excited from the outside instead, most of the energy radiated directly to the surrounding space and little remained in the tube.

#### 4.4.3 Ferrite Tube with a Conical Tapered End Excited by a Cylindrical Cavity

The structure of the tested antenna is shown in Fig. 4-10. One end of the tube was fitted tightly into a metal circular cylindrical cavity 6 inches in depth. Excitation was by a symmetrical dipole inserted from the base of the cavity and mounted diametrically. In this way the ferrite radiator has a 1/2 inch shell layer, 6 inches outer

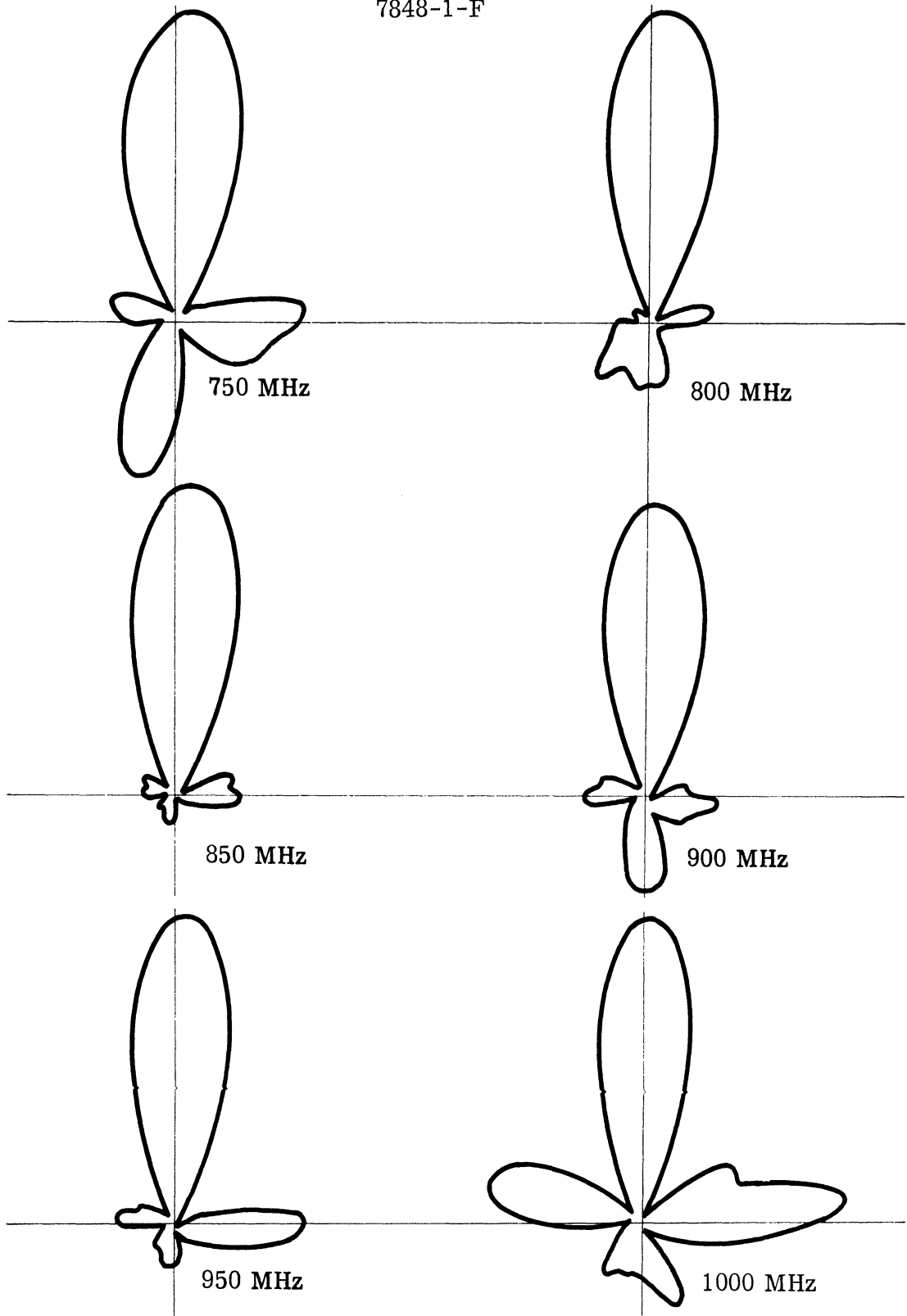


FIG. 4-8: LINEAR POWER PATTERNS FROM A QUADRIFILAR HELIX EXCITED FERRITE TUBE ANTENNA.

Ferrite Tube =	{	O.D. = 12.5 cm	Feeding	{	Diameter = 10 cm
		I.D. = 10 cm			Quadrifilar =
		Length = 85 cm	Helix		Length = 27 cm

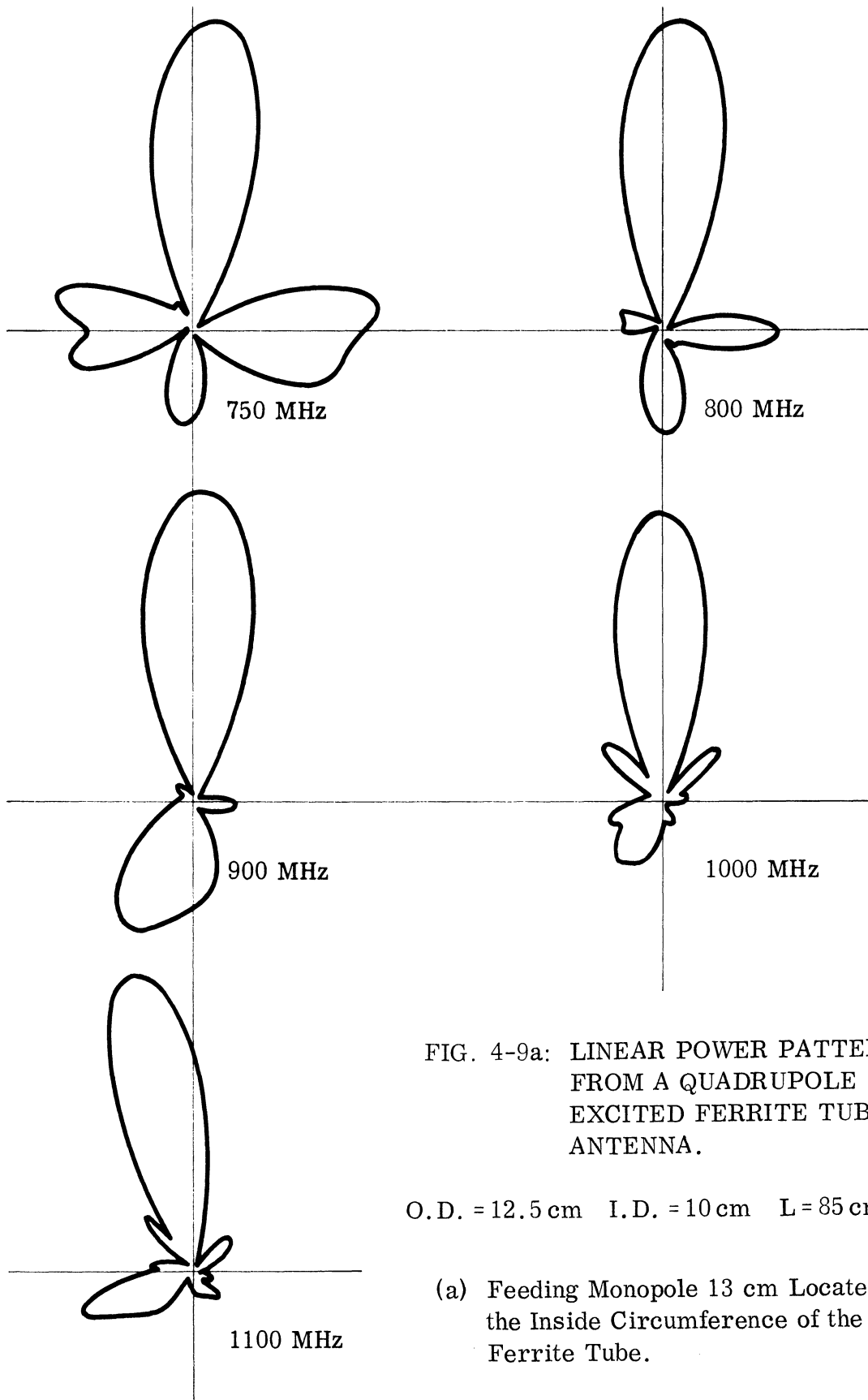


FIG. 4-9a: LINEAR POWER PATTERNS FROM A QUADRUPOLE EXCITED FERRITE TUBE ANTENNA.

O.D. = 12.5 cm I.D. = 10 cm L = 85 cm

(a) Feeding Monopole 13 cm Located at the Inside Circumference of the Ferrite Tube.



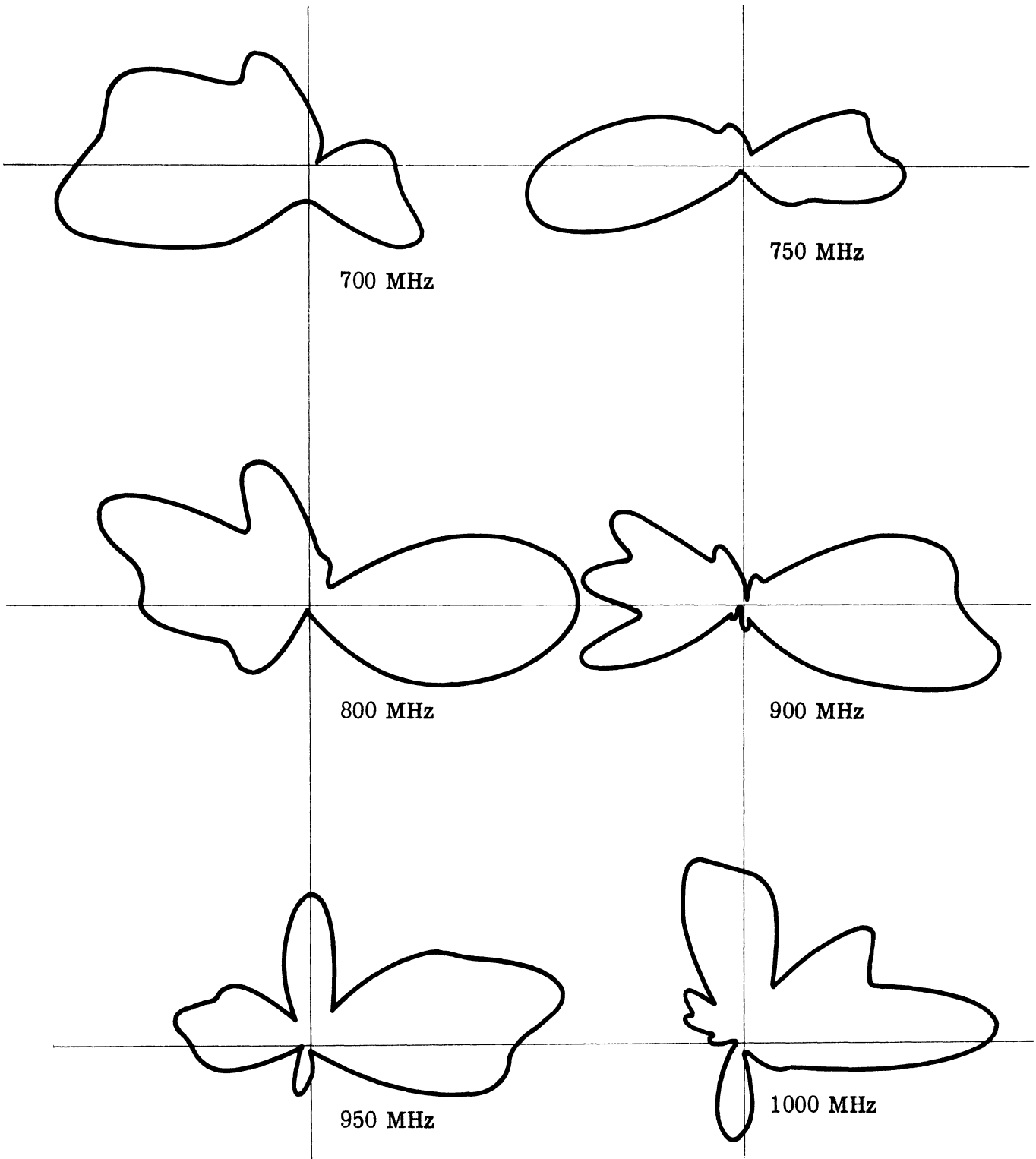


FIG. 4-9b: LINEAR POWER PATTERNS FROM A QUADRUPOLE EXCITED FERRITE TUBE ANTENNA.

(b) Feeding Monopole 13 cm Located at the Outside Circumference of the Ferrite Tube.

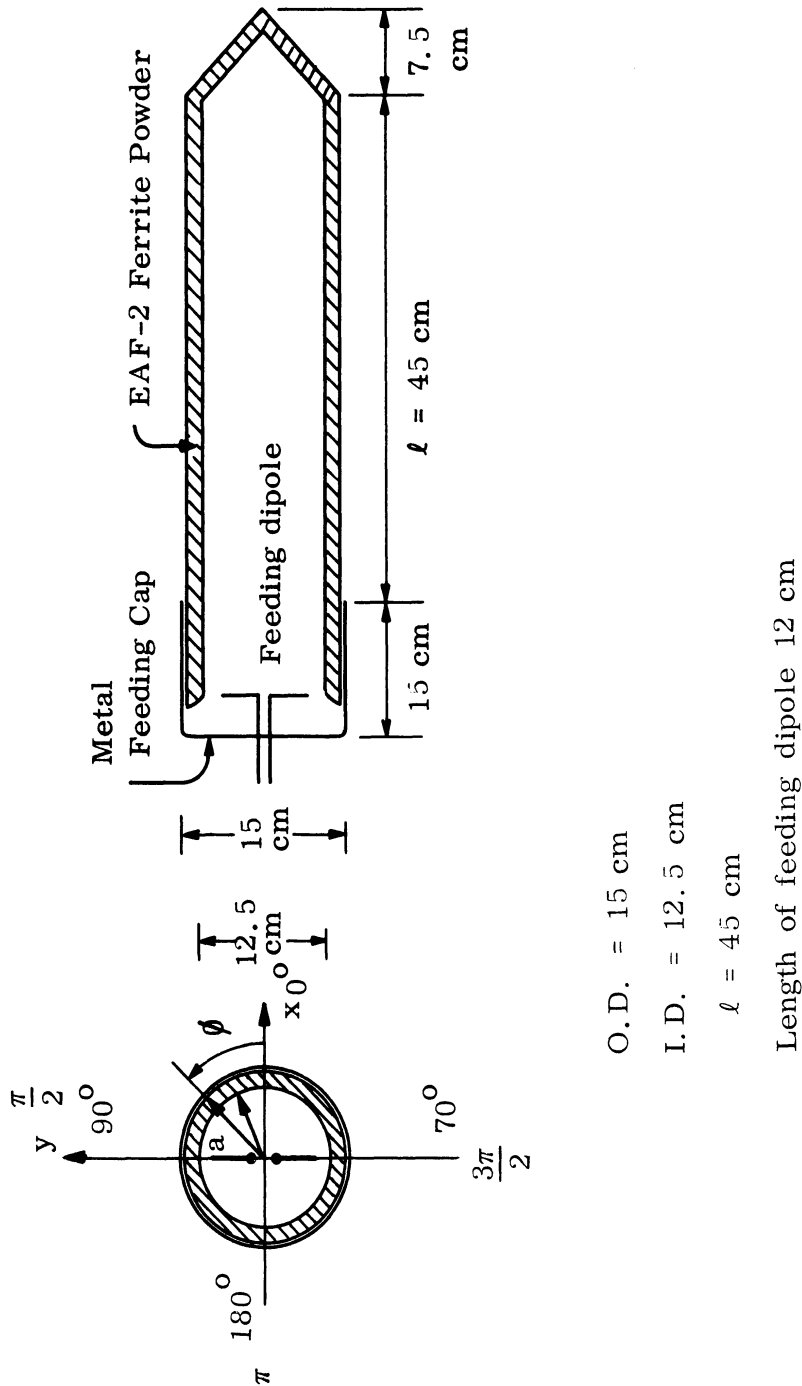


FIG. 4-10: GEOMETRY OF THE FERRITE TUBE ANTENNA WITH A CONICAL END.

diameter, 18 inches length and a 45 degree conical shape tapered end. The radiation patterns in the E-plane and in the H-plane are presented in Figs. 4-11.

The near field distribution along the outer surface of the ferrite tube has been measured by using a probe moving axially and along the circumference. Figure 4-12 shows the  $E_{\rho}$  - distribution against the coordinate  $\phi$  taken at 2 inches from the feed end and 2 inches from the free end respectively. The  $E_{\rho}$  field is observed to be sinusoidal around the circumference and the sudden change of phase at  $\phi = \pi/2$  and  $\phi = 3\pi/2$  is to be expected. Figure 4-13 show the  $E_{\rho}$  - distribution along the tube axis at 600 MHz and 900 MHz. The observed pattern using a voltage probe appears to be for standing waves rather than traveling waves, probably because the conical cap free end and the short length ferrite tube form a resonance cavity.

#### 4.4.4 Ferrite Tube with an Open End Excited by a Cylindrical Cavity

The radiation patterns of the conical end ferrite tube antenna were satisfactory except the average VSWR found to be 3.5 was rather high because of the reflection from the conical free end. When the conical free end was removed as shown in Fig. 4-14, the average VSWR is reduced to less than 2 due to the improved matching from the open tube end to free space. Obviously, this also indicates that the open end aperture provides the main radiation of this antenna, if the surface wave propagating along the tube axis is bounded. A series of radiation patterns were taken for this kind of antenna with various tube lengths and thicknesses as shown in Table IV.

TABLE IV

Dimension Antenna Number	O. D. 2b (cm)	I. D. 2a (cm)	Thickness C = a/b	Length l (cm)
1	15	11.2	0.75	38
2	15	12	0.8	41
3	15	12	0.8	51
4	15	12.8	0.85	33
5	15	12.8	0.85	68.5
6	15	13.5	0.9	36
7	15	13.5	0.9	71.5

THE UNIVERSITY OF MICHIGAN

7848-1-F

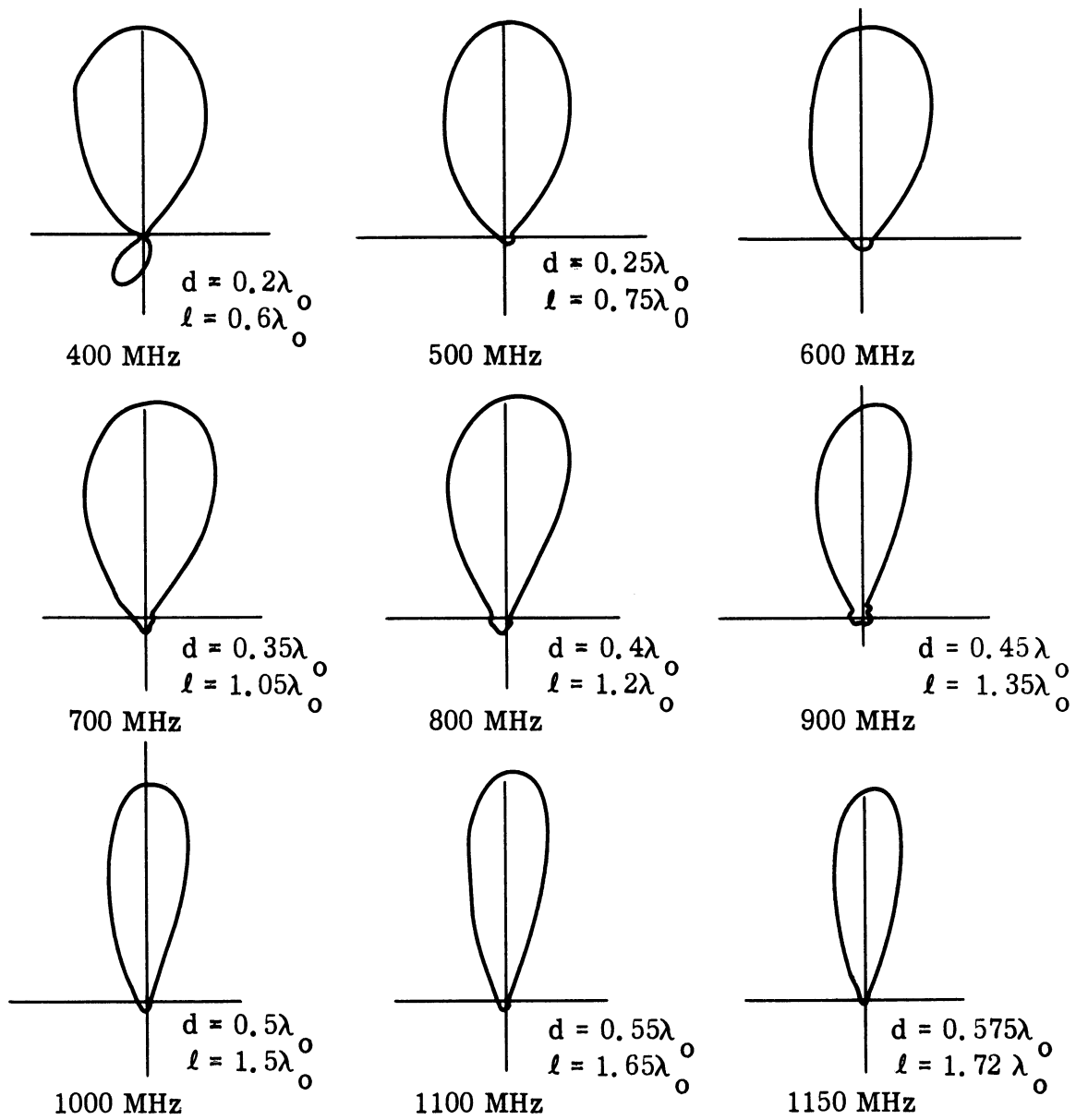


FIG. 4-11a: LINEAR POWER PATTERNS OF THE FERRITE TUBE ANTENNA WITH A CONICAL END.

(a)  $|E_\phi|^2$  Plot in H-plane.

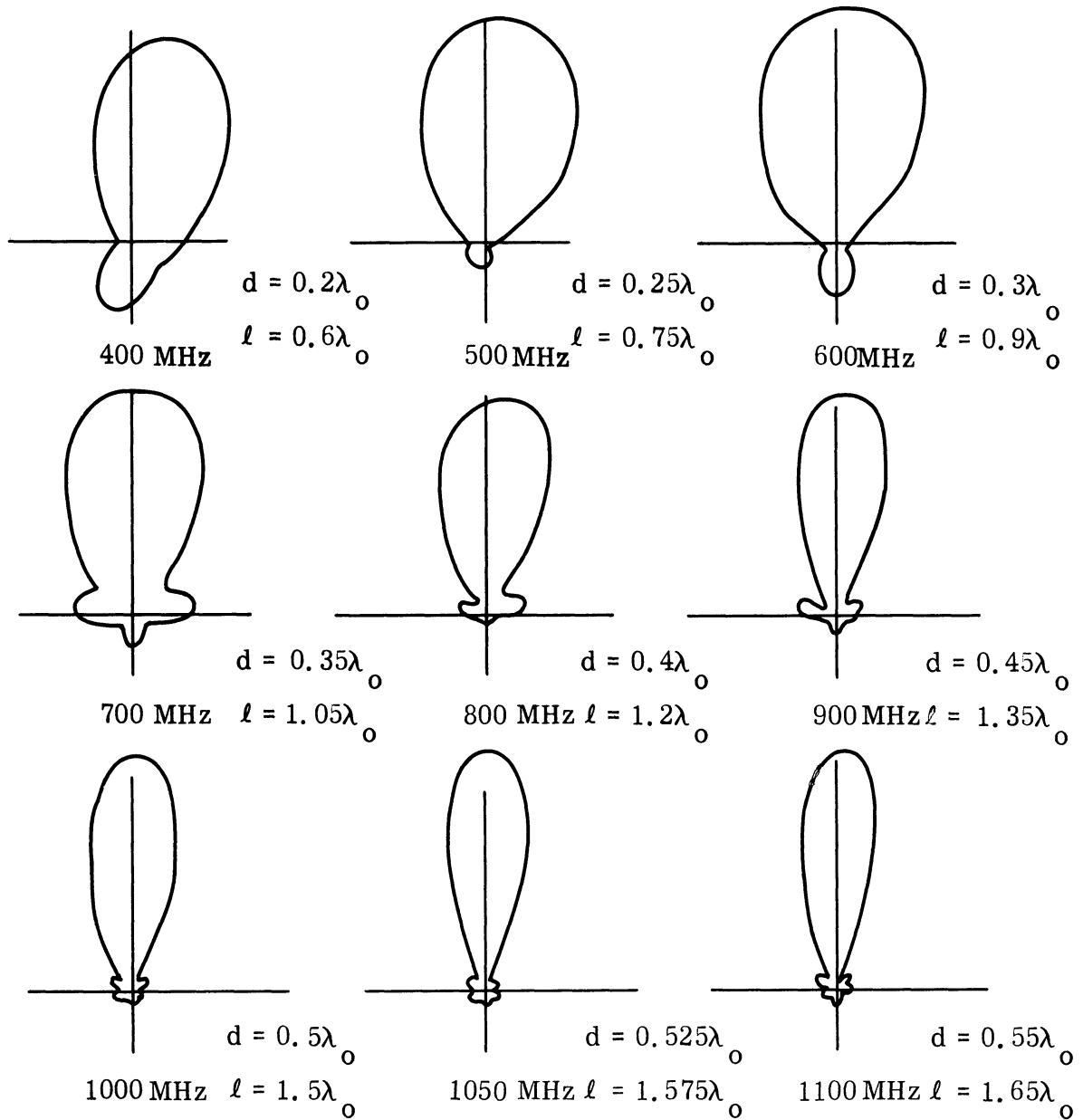


FIG. 4-11b: LINEAR POWER PATTERNS OF THE FERRITE TUBE ANTENNA WITH A CONICAL END.

(b)  $|E_\theta|^2$  Plot in E-plane.

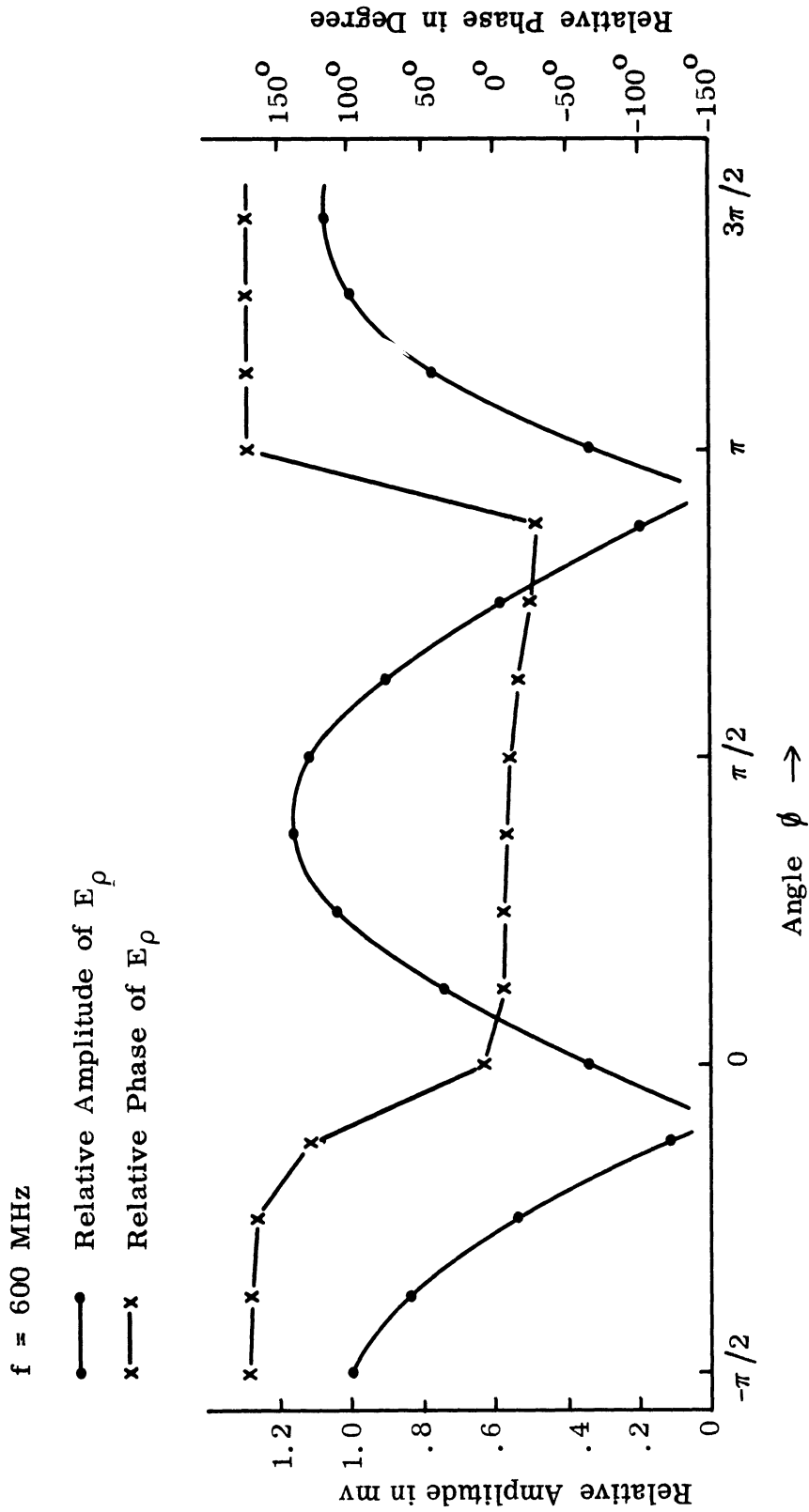


FIG. 4-12a: NEAR FIELD MEASUREMENT, THE RELATIVE AMPLITUDE AND THE PHASE OF  $E_\rho$  AGAINST THE COORDINATE ANGLE  $\phi$ .

(a) Taken at 5 cm from the Feed End of the Ferrite Tube Antenna with a Conical End.

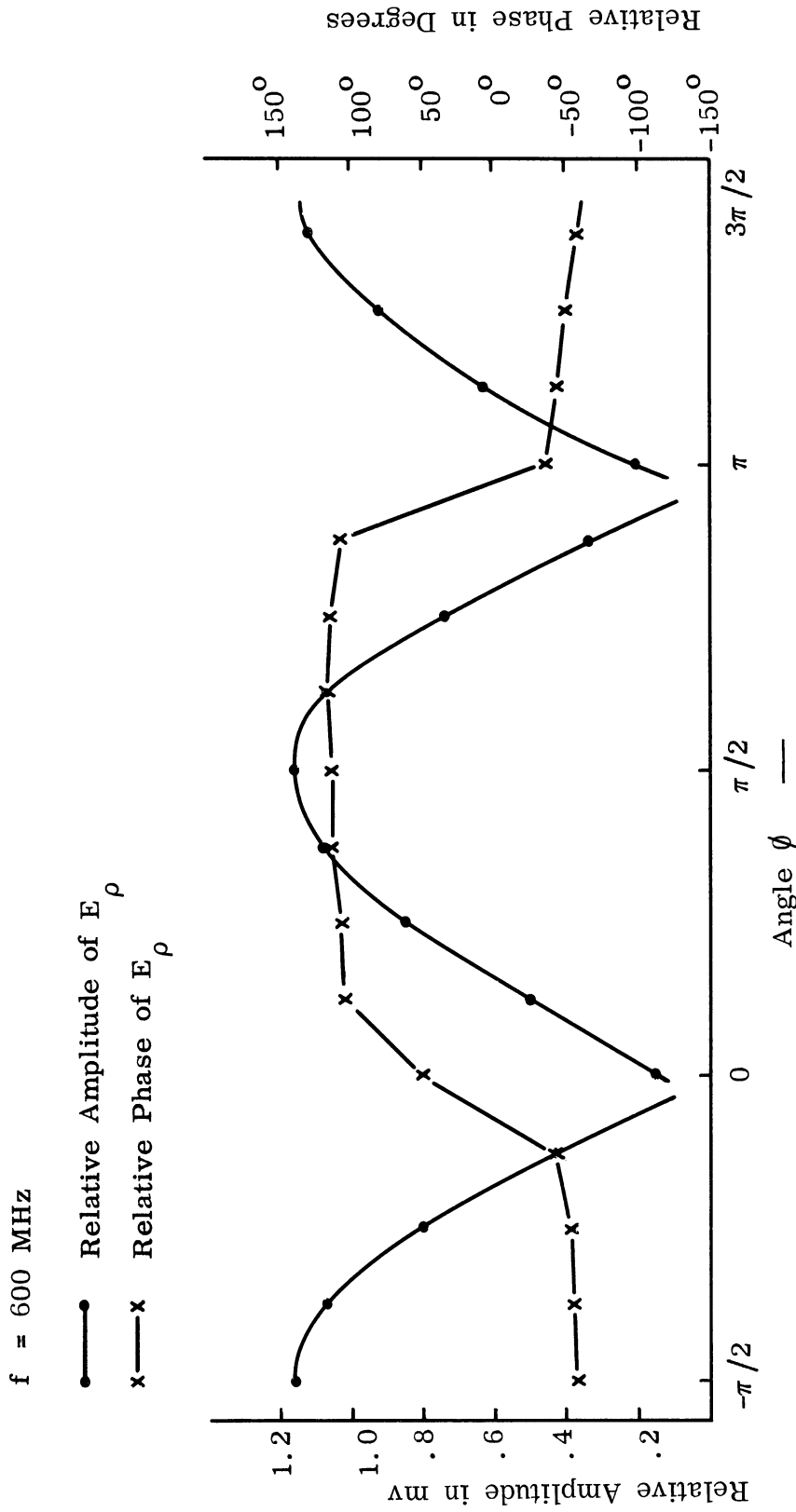


FIG. 4-12b: NEAR FIELD MEASUREMENT, THE RELATIVE AMPLITUDE AND THE PHASE OF  $E_\rho$  AGAINST THE COORDINATE ANGLE  $\phi$ .

(b) Taken at 5 cm from the Free End of the Ferrite Tube Antenna with a Conical End.

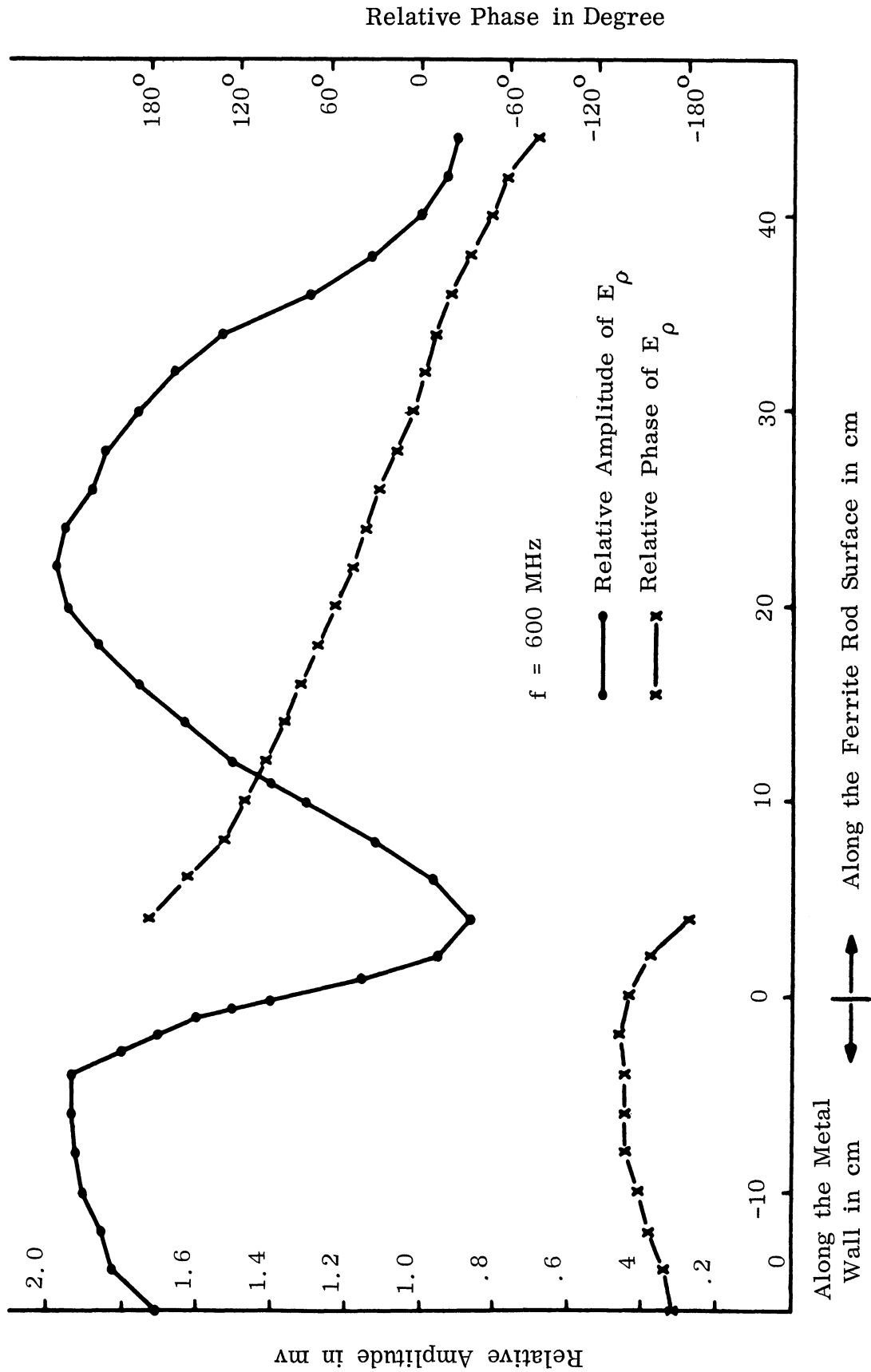


FIG. 4-13a: NEAR FIELD MEASUREMENT, THE RELATIVE AMPLITUDE AND THE PHASE OF THE  $E_\rho$  AGAINST THE FERRITE TUBE AXIS AT 600 MHz IN  $\phi = \pi/2$  PLANE.



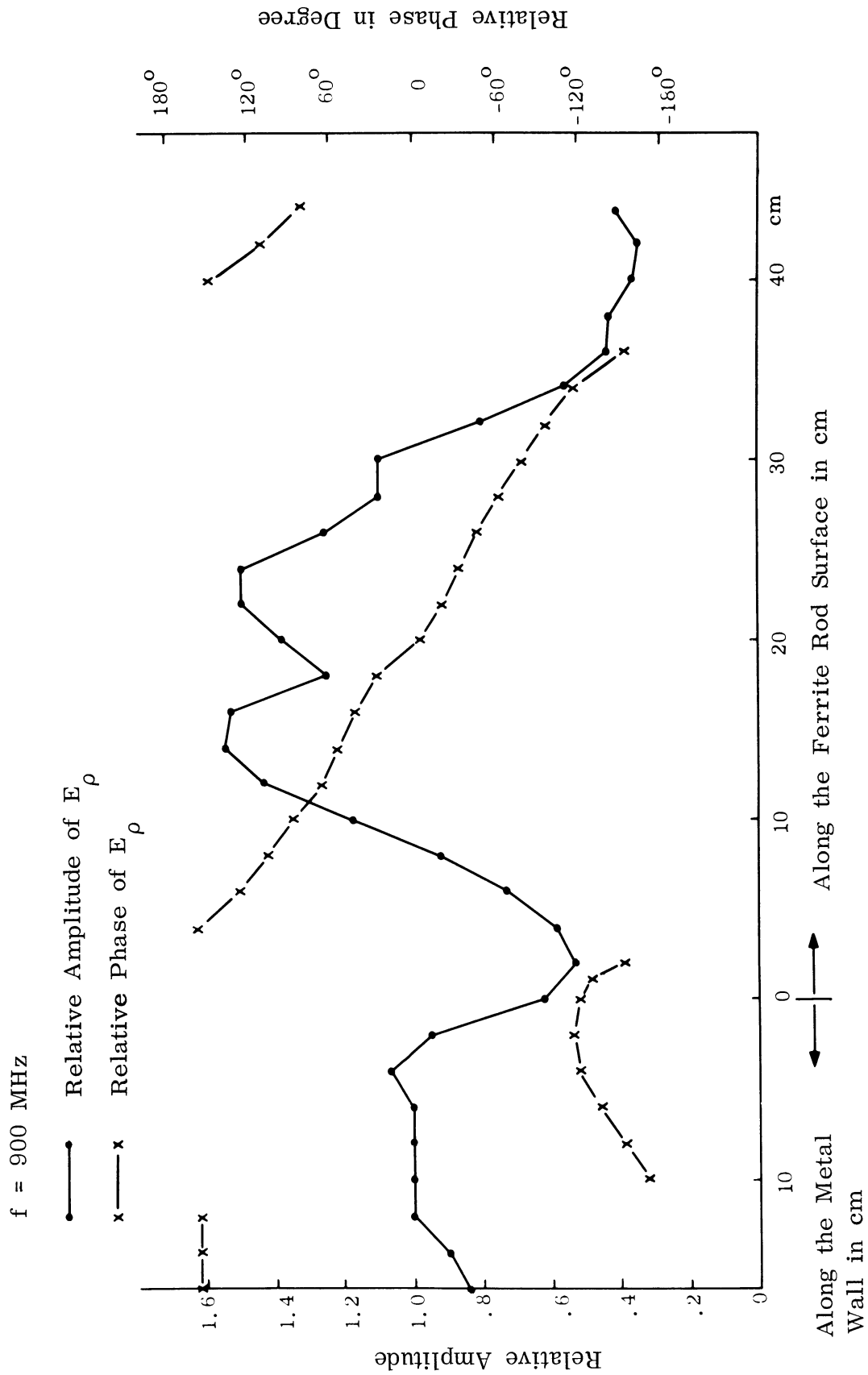


FIG. 4-13b: NEAR FIELD MEASUREMENT, THE RELATIVE AMPLITUDE AND THE PHASE OF  $E_\rho$  AGAINST THE FERRITE TUBE AXIS AT 900 MHz IN  $\phi = \pi/2$  PLANE.

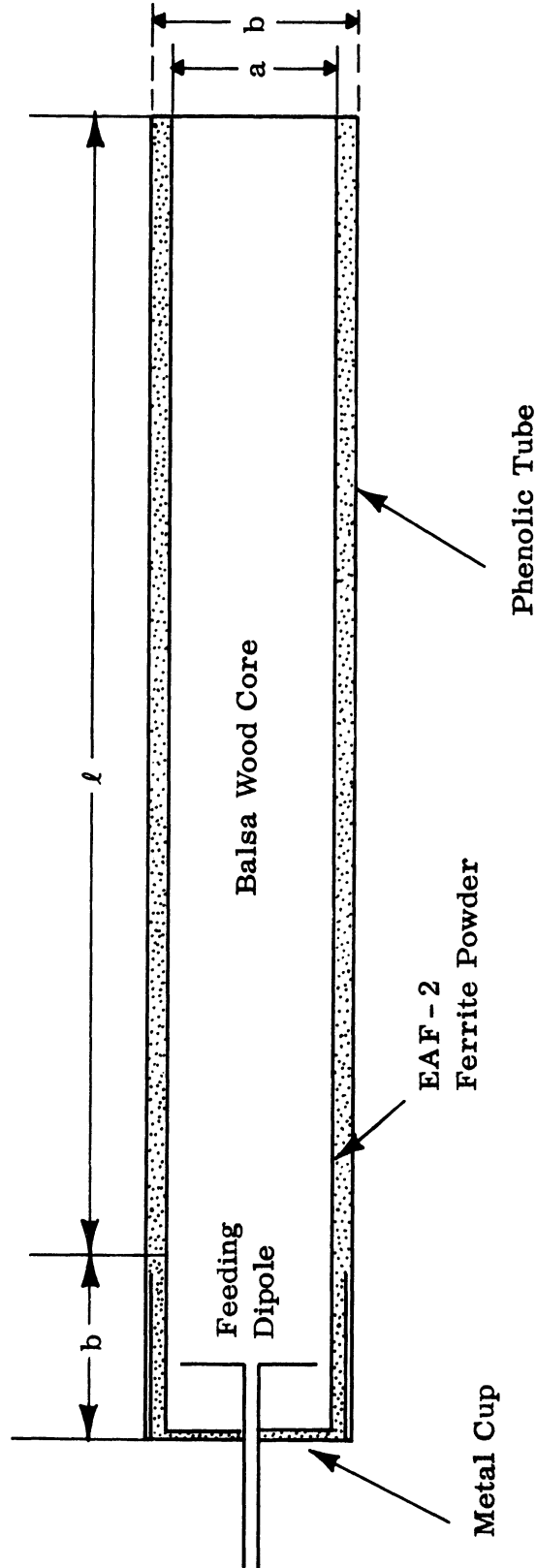


FIG. 4-14: GEOMETRY OF THE FERRITE TUBE ANTENNA.

# THE UNIVERSITY OF MICHIGAN

7848-1-F

Most experiments were done with the outside tube diameter having  $2b = 0.3\lambda_0$  to  $0.6\lambda_0$  and tube length from  $l = 0.7\lambda_0$  to  $3\lambda_0$ .

As the tube becomes thinner and longer, both directivity and sidelobe level are slightly improved. This might be due to the better matching at the open end and to the continuous coupling to free space while the wave propagates along the tube axis towards the open end. Figure 4-15 presents the radiation patterns of a thin tube indicated as No. 7 in Table IV. At 1200 MHz, the tube has a diameter  $2b = 0.6\lambda_0$  and length  $l = 2.8\lambda_0$ . The measured 3 db, 6 db and 12db beamwidths vary with frequency for the thin tube antenna No. 7 and are presented in Fig. 4-16. The positions of the first sidelobe are plotted in Fig. 4-17 and the maximum sidelobe or backlobe level is plotted in Fig. 4-18. It is noted that the mainlobe and sidelobe positions in both E and H-plane have no significant difference. The sidelobe levels in E-plane are more prominent which is to be expected, partly due to the asymmetric field distribution of the  $HE_{11}$  mode in the ferrite tube and partly due to the symmetric  $TM_{01}$  mode excited at higher frequency and which makes no contribution to  $E_\theta$  patterns in H-plane. The input impedance of the thin tube antennas Nos. 6 and 7 are shown in Fig. 4-19. These values were measured with the Hewlett Parkard Model 8405A Vector Voltmeter referenced to a  $50\Omega$  line. Since there is good matching from the open end to free space the average VSWR is less than 2 and the input impedances are almost the same even though the tube length is changed. However, when the open end is replaced by a conical closed end the average VSWR will increase to 3.5 and about 30 percent of the incident input power is reflected.

## 4.5 Conclusions

A ferrite tube antenna can be made of any kind of low loss material with permeability  $\mu$  and permittivity  $\epsilon$ . The far field pattern of the antenna is due to the primary current sources in the launching device and both the induced polarization and magnetization currents in the ferrite. From another point of view the uniform tube antenna may be explained as the diffraction of the  $HE_{11}$  surface wave from the open

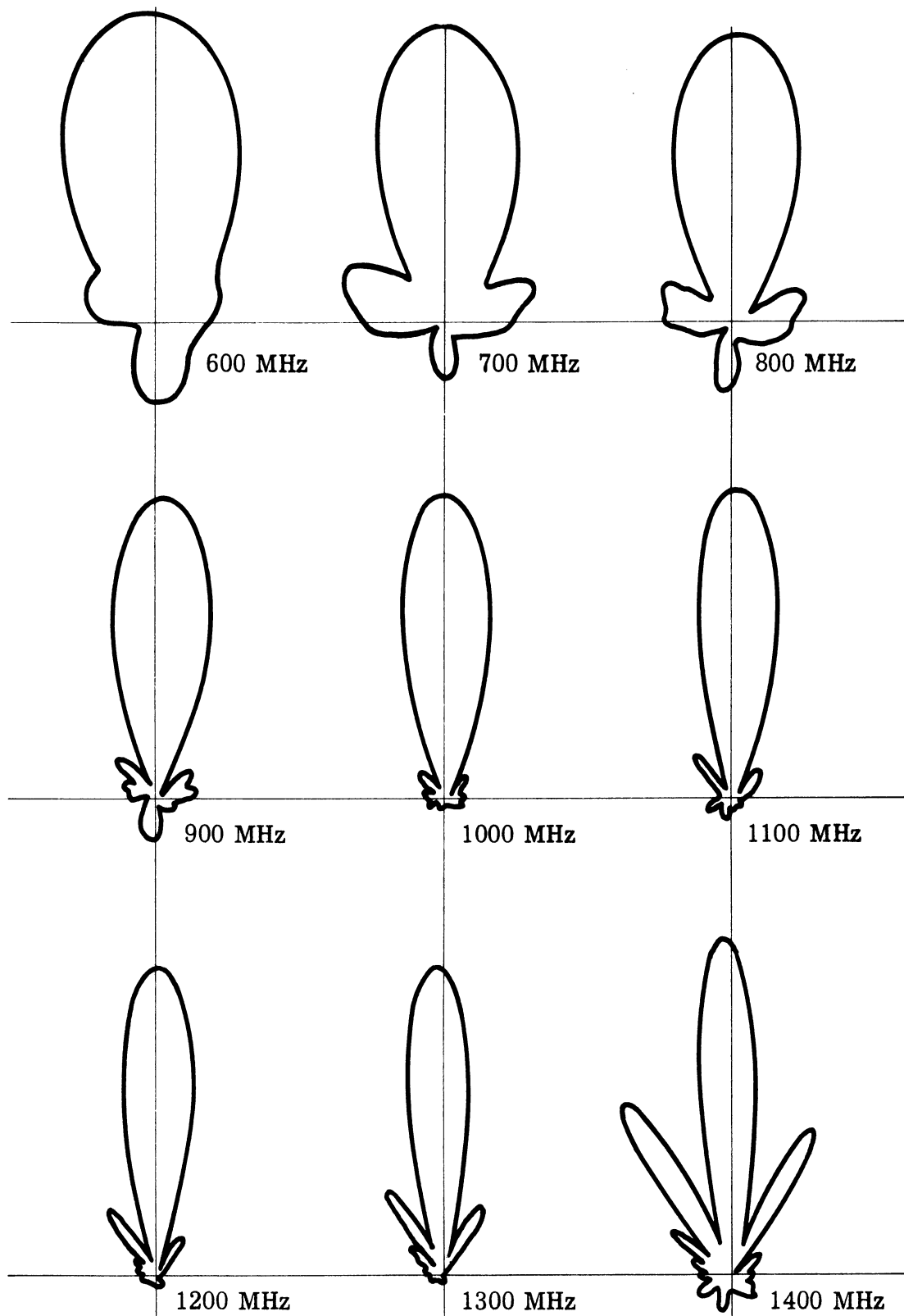


FIG. 4-15a: LINEAR POWER PATTERNS FROM A DIPOLE EXCITED FERRITE TUBE.

O.D. = 15 cm I.D. = 13.5 cm Length = 71.5 cm

(a)  $|E_{\theta}|^2$  Plot in E-plane.

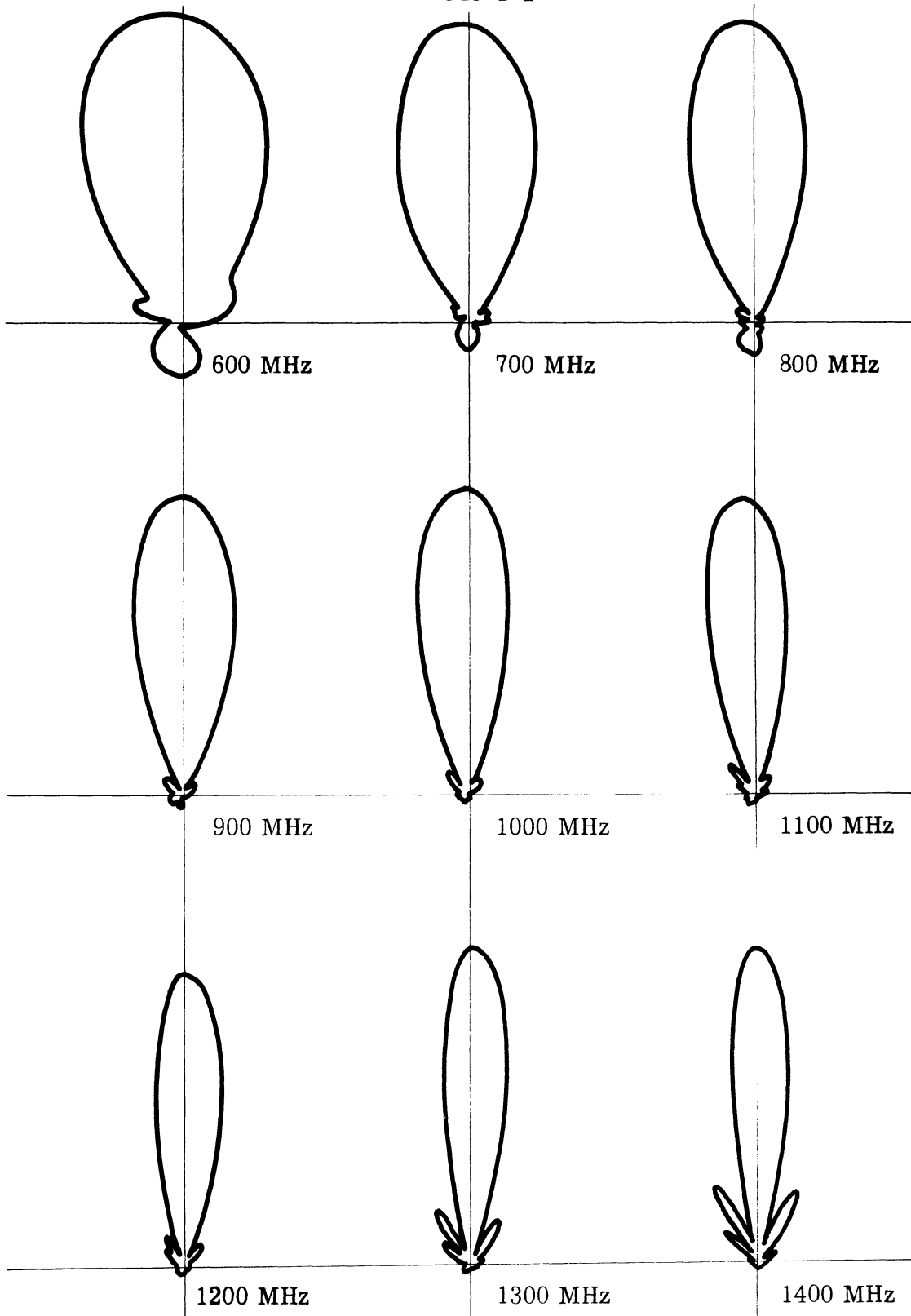
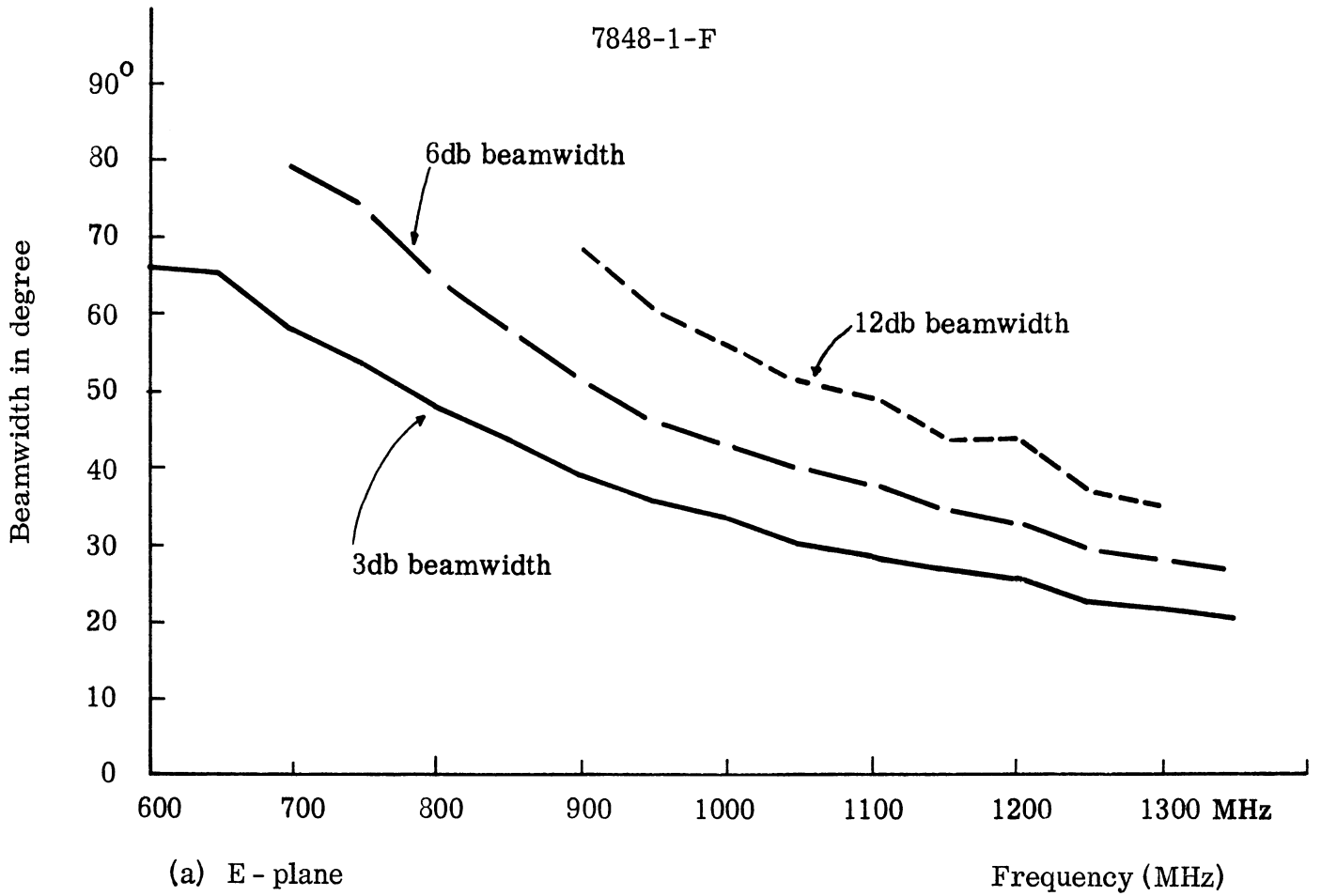


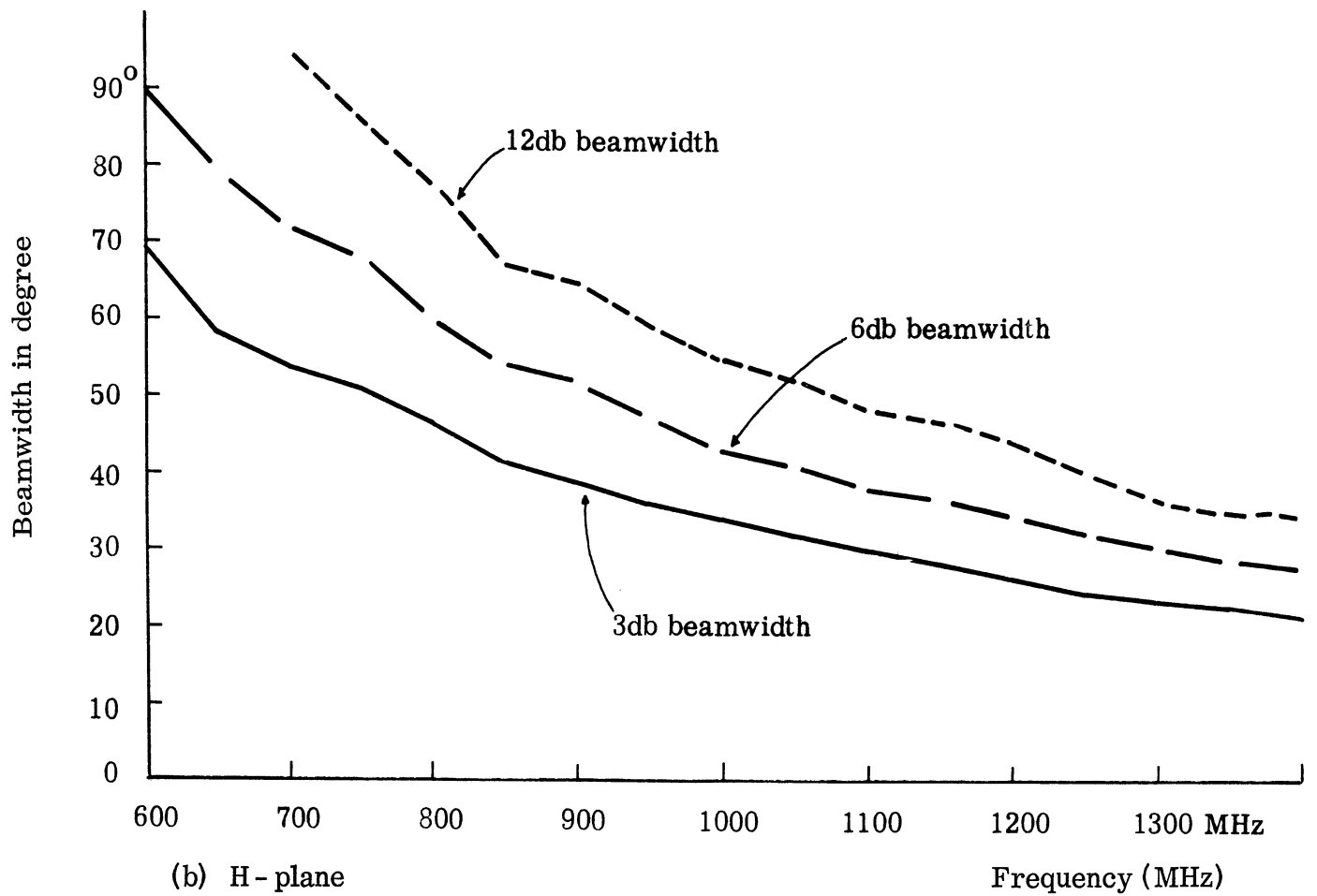
FIG. 4-15b: LINEAR POWER PATTERNS FROM A DIPOLE EXCITED FERRITE TUBE.

(b)  $|E_\phi|^2$  Plot in H-plane.

7848-1-F



(a) E - plane

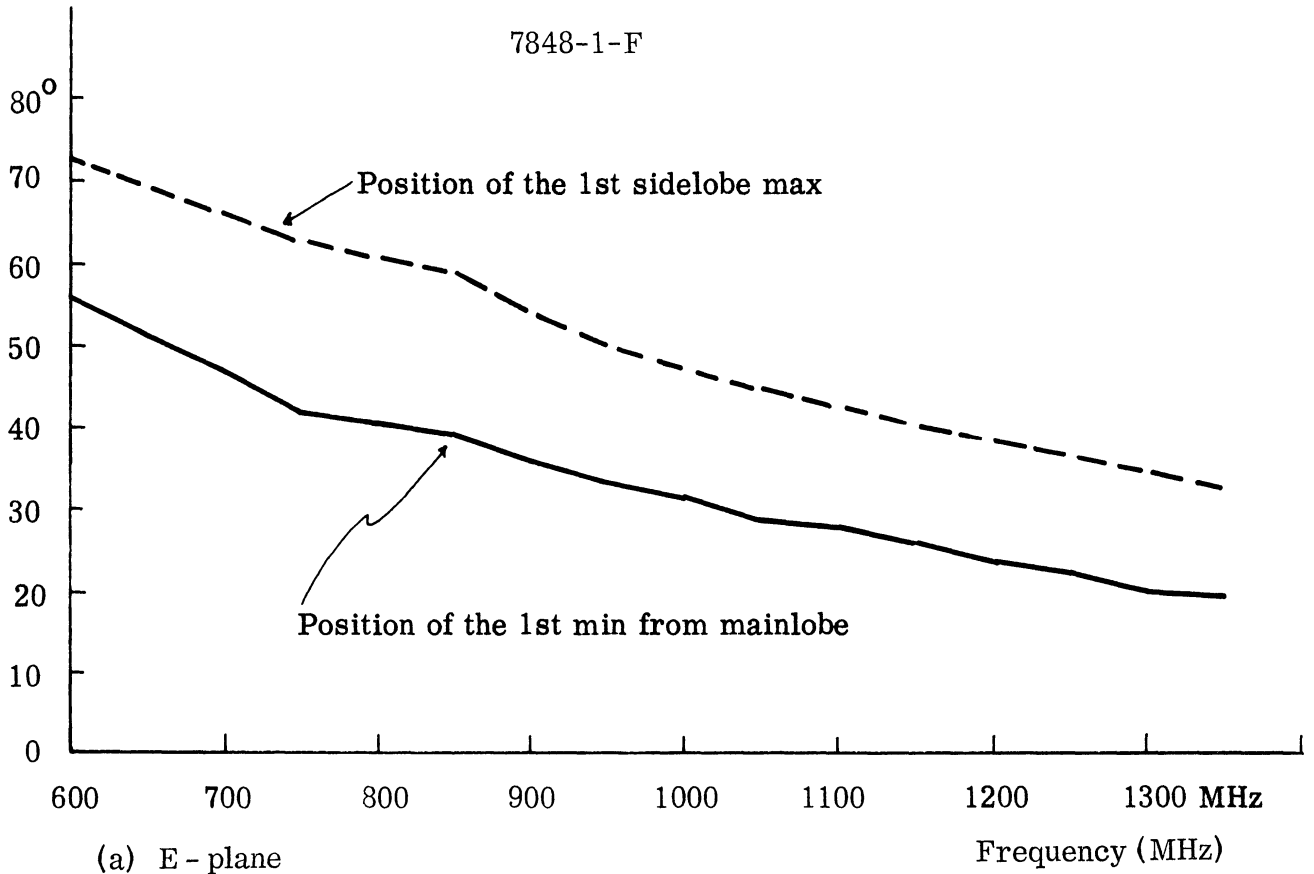


(b) H - plane

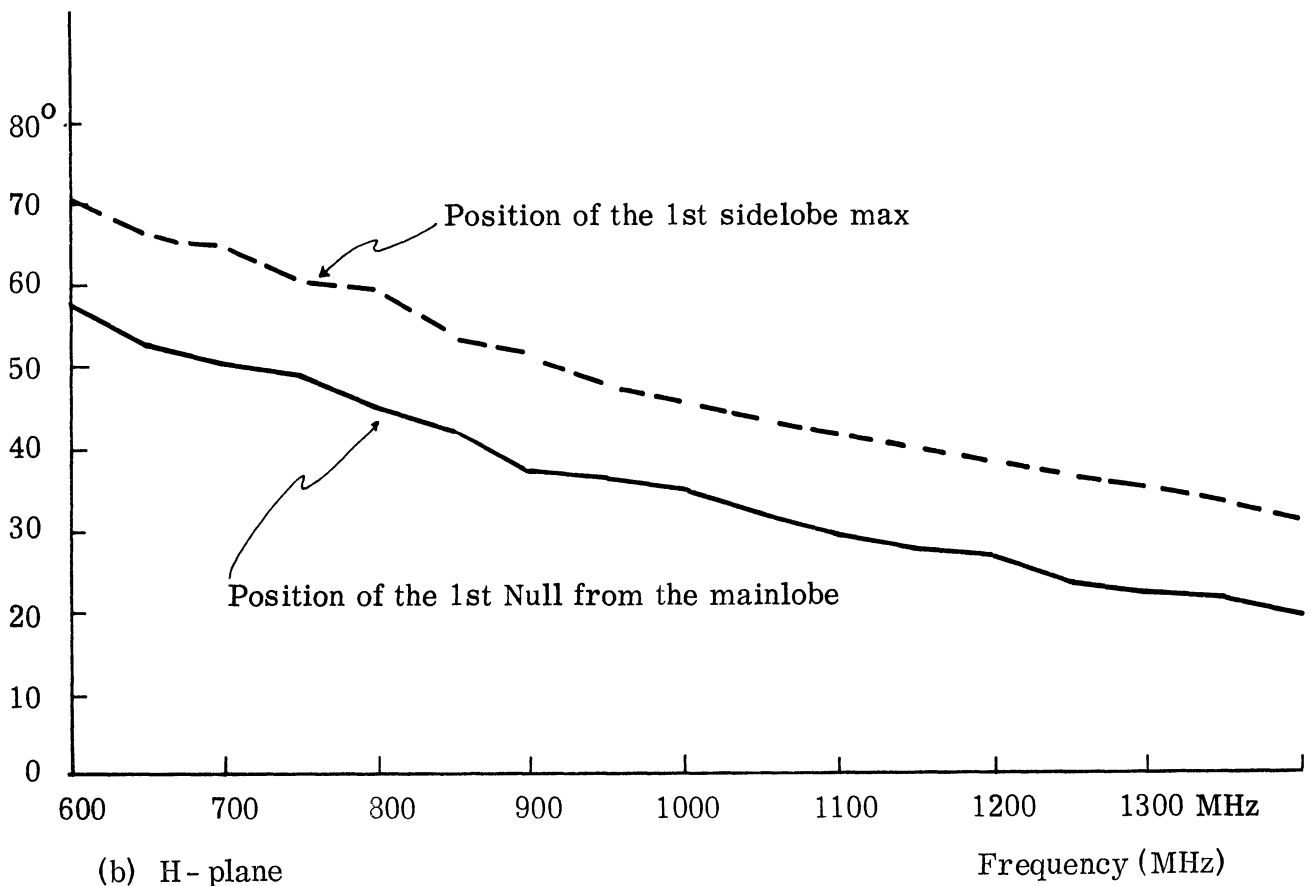
FIG. 4-16a,b: VARIATION OF BEAMWIDTH WITH FREQUENCY.

THE UNIVERSITY OF MICHIGAN

7848-1-F



(a) E - plane



(b) H - plane

FIG. 4-17 a,b: POSITION OF FIRST SIDELobe VARYING WITH FREQUENCY.

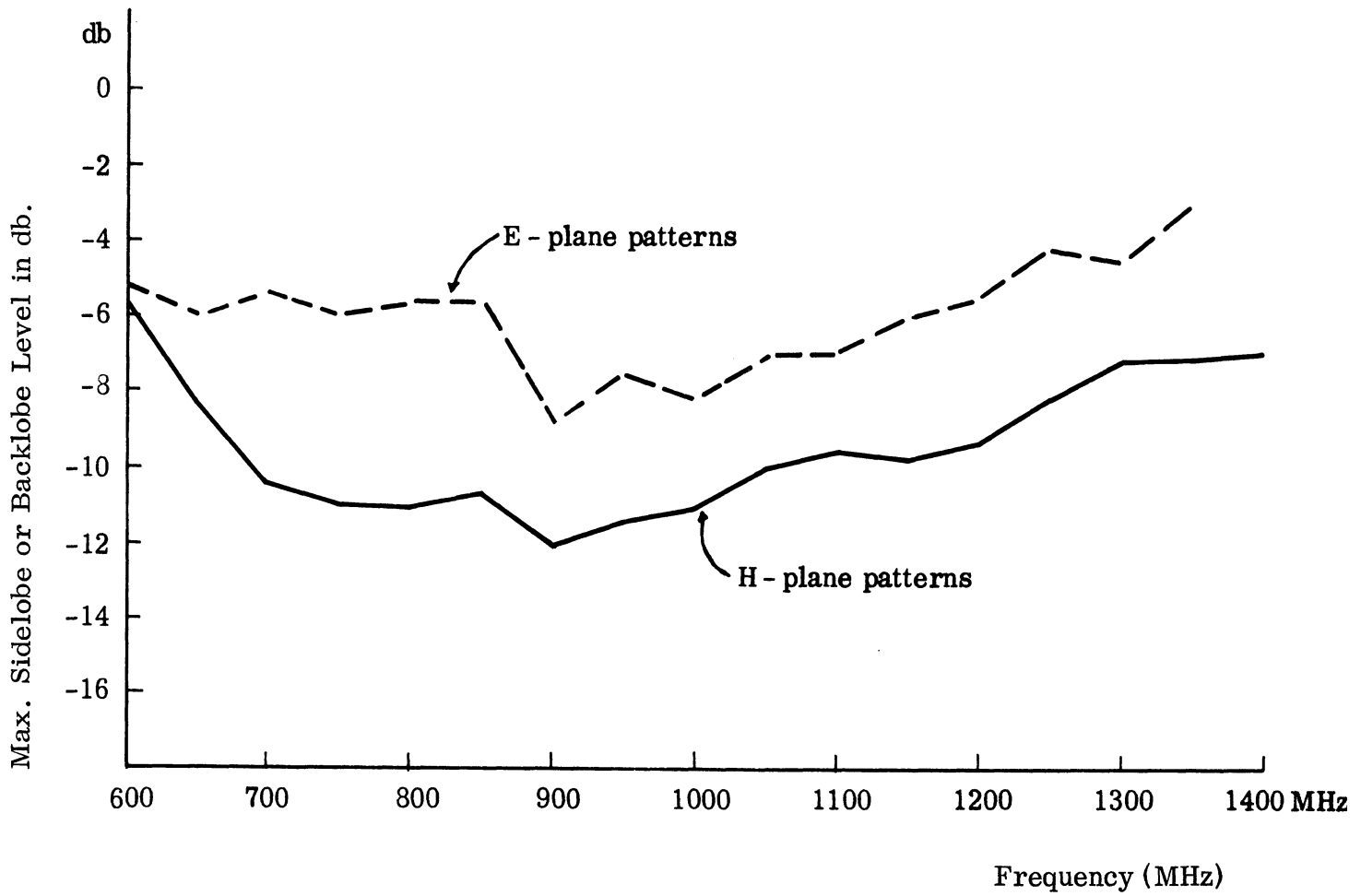


FIG. 4-18: MAXIMUM SIDELobe OR BACKLOBE LEVEL VS FREQUENCY.



# THE UNIVERSITY OF MICHIGAN

7848-1-F

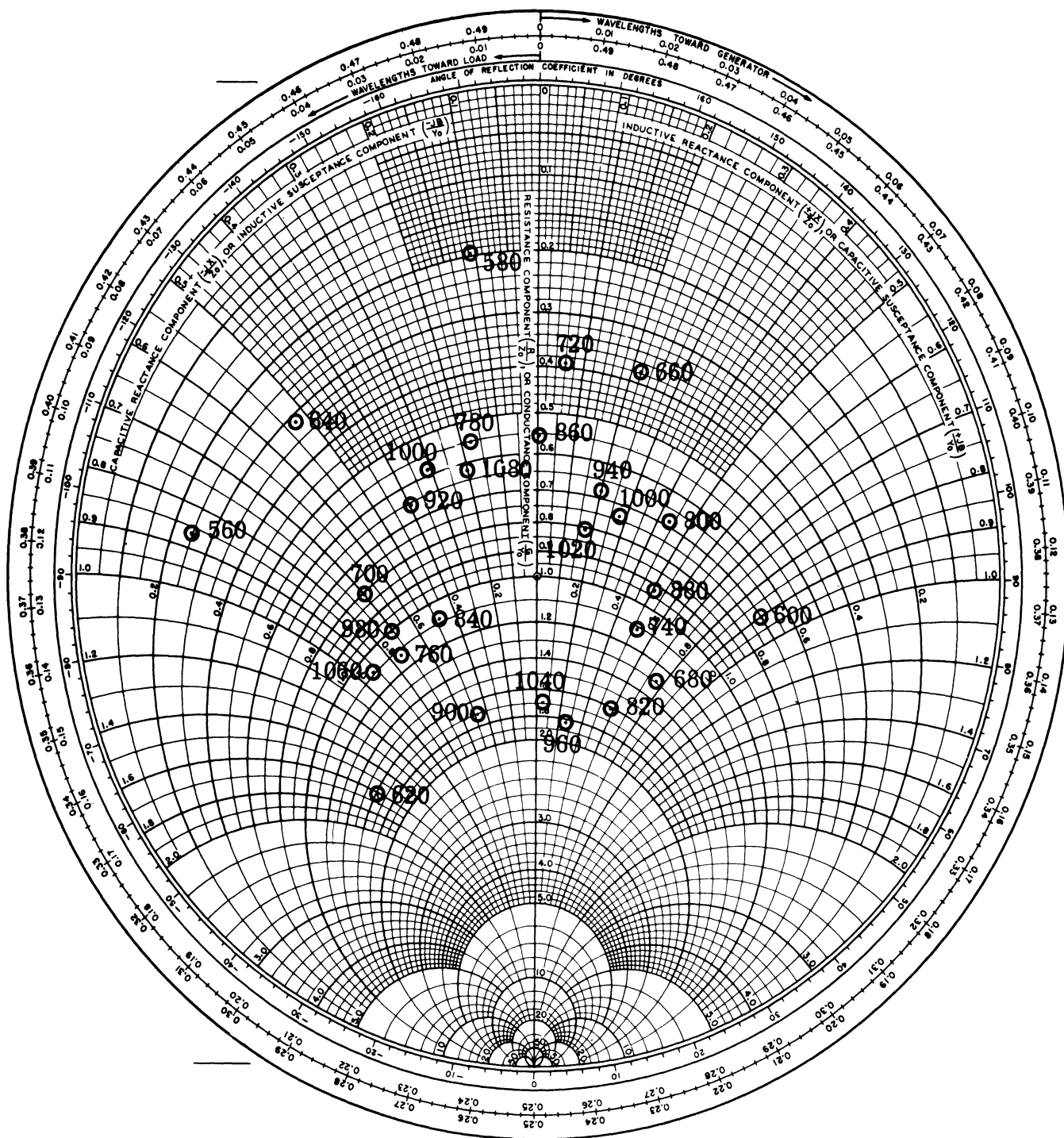


FIG. 4-19a: INPUT IMPEDANCE OF THE DIPOLE EXCITED FERRITE TUBE ANTENNA.

O. D. = 15 cm    I. D. = 13.5 cm    Length = 36 cm

(Referenced to 50 ohms)

# THE UNIVERSITY OF MICHIGAN

7848-1-F

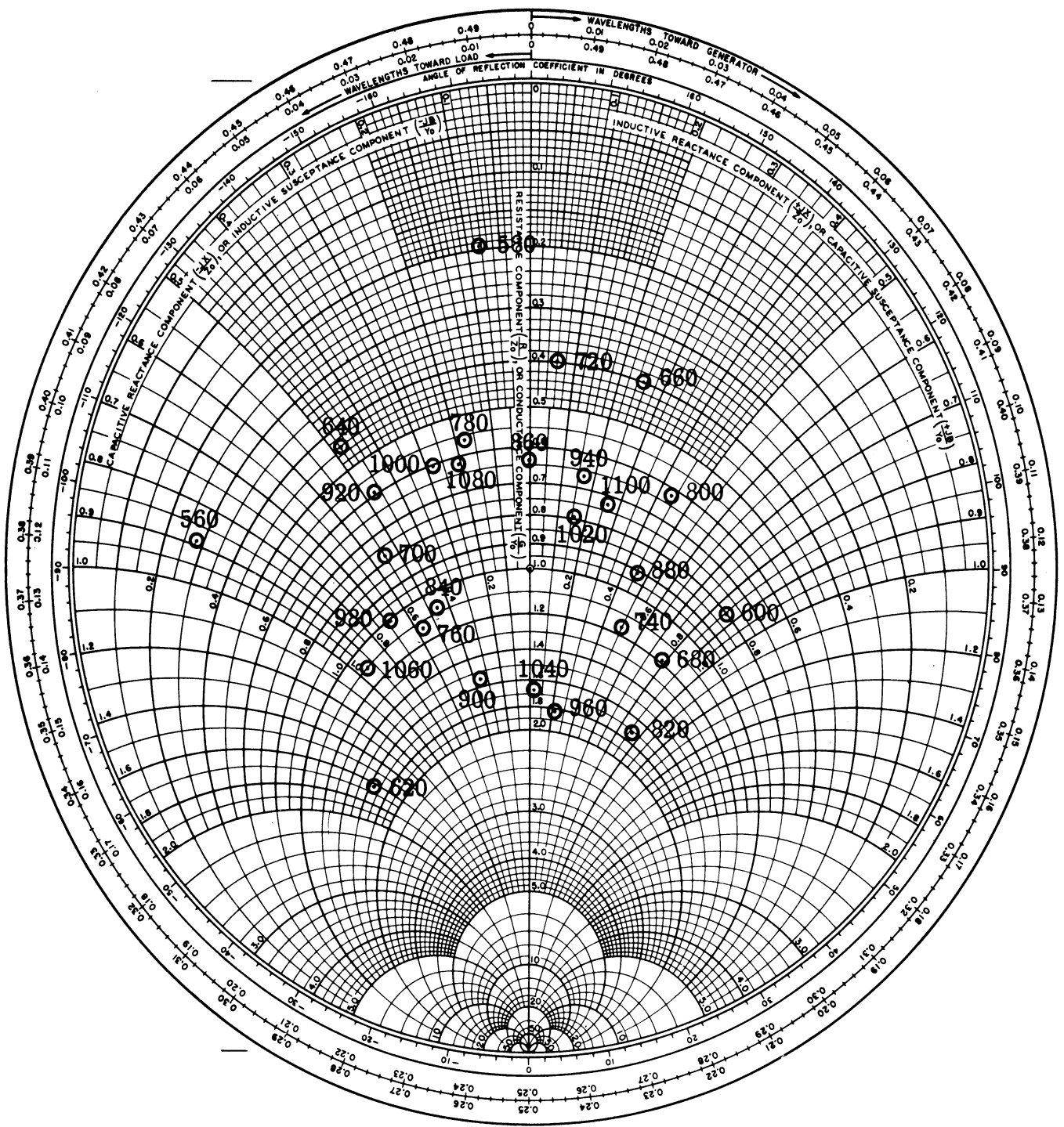


FIG. 4-19b: INPUT IMPEDANCE OF THE DIPOLE EXCITED FERRITE TUBE ANTENNA.

O.D. = 15 cm    I.D. = 13.5 cm    Length = 71.5 cm

(Referenced to 50 ohms)

# THE UNIVERSITY OF MICHIGAN

7848-1-F

end, and the direct radiation from the mouth of the launching device. The general far field expression of the ferrite tube antenna will reduce in limiting cases to the field of the solid ferrite rod, dielectric rod, dielectric tube and loaded waveguide antennas. All of them are particular cases of the ferrite tube antennas. In order to be an efficient radiator and to be sure to radiate in the endfire direction:

1) A  $HE_{11}$  mode is required to propagate along the tube axis, for the symmetric  $TM_{01}$  and  $TE_{01}$  modes radiate in the broadside direction.

2) The  $HE_{11}$  mode launching device is desired to have a high launching efficiency.

3) The  $HE_{11}$  surface wave propagating along the tube axis should not be tightly bound to the tube, otherwise the surface wave energy pulsates back and forth in the tube and nearby space. It results in more losses in the material and more reflection from the discontinuities at the end.

4) At the open end of the tube, it is desired to have a continual flow of energy directly outward in the axial direction.

Tube antenna design must consider various possible choices of parameters. For most applications with a given material it is required to design for maximum directivity with a moderate sidelobe level over a given frequency band. The following will furnish a basis for the design considerations:

1) The ferrite tube antenna can be designed to have a linear, circular or elliptical polarization. Polarization depends upon the excitation of the launching device.

2) The lower operating frequency limit of the antenna is the cutoff of the launching device. The upper frequency limit depends on the mode of the propagating waves in the tube and the losses in the material at that frequency.

3) The launching efficiency and the directivity of the antenna are proportional to the diameter of the tube, but the diameter should not be too large to propagate the symmetric modes.

# THE UNIVERSITY OF MICHIGAN

7848-1-F

4) The wall thickness of the tube should be designed to have a surface wave phase velocity nearly equal to 0.9 the free space phase velocity. For a thinner tube, it loses its waveguiding properties.

5) The directivity of the antenna is also proportional to the length of the tube but in any case the length should not exceed

$$l_{\max} = \frac{\lambda_o \lambda_g}{\lambda_o - \lambda_g} .$$

For a tube longer than  $l_{\max}$ , sidelobes become very large, and the radiation patterns begin to deteriorate.

6) The solid rod antenna should use only low  $\mu$  and low  $\epsilon$  material in a small range of diameters, and the phase velocity along the rod axis is nearly 0.9 the free space phase velocity.

7) For a large diameter rod or thick tube, the surface wave phase velocity is less than 0.8 the free space phase velocity, tapering or loading along the axis is necessary.

Since most of the surface wave energy is propagating externally to the material some loss in the material is tolerable so long as the guiding property of the electromagnetic waves is maintained.

The tube antenna can be compared to the conical horn and Yagi antennas— each guides the wave and modifies the phase front in the axial direction. The tube antenna has great mechanical simplicity and ruggedness. It can be slimmer in shape. It can provide a wide range of beamwidths over a frequency band with comparatively low sidelobe level. It is suitable for array use because of the low mutual coupling between such elements.

## LOW FREQUENCY FERRITE ANTENNAS

### 5.1 Introduction

The objective of this task is to investigate the design feasibility of new types of ferrite antennas that are usable at frequencies as low as 30 MHz. An effort has been made to identify realistic applications of ferrite loading to linear radiating elements. Accordingly, the investigation has focused upon applications which improve the performance of antennas that are relatively small. The range of sizes considered is  $0.1\lambda < 2h < 0.5\lambda$ , where  $\lambda$  = free space wavelength and  $h$  = element half length. The low end was chosen so as to avoid severe supergain limitations in element performance, while the high end was considered to be a practical size limit for a loaded 30 MHz element. Moreover, the detailed discussion is limited to center fed (or ground plane imaged) elements which support standing wave current distributions. Although such elements are highly resonant and hence quite frequency sensitive, they can be used as constituent parts in the broadband structures, such as the log-periodic dipole array. The motivation for restricting the study to linear elements which support standing waves arises from the desirability of using relatively small quantities of material, since useful materials are characteristically rather heavy. Familiar concepts which entail matching the wave impedance within the antenna structure to free space impedance by encapsulation techniques are impractical at 30 MHz since they usually require the use of too large a volume of material. The most effective use of small quantities of material is in the control of phase velocities arising from conduction currents. For this reason relatively short lengths of linear slow wave structures form an effective "building block" from which more elaborate structures may be fashioned. The general properties of this basic slow wave structure are discussed in Section 5.2, before proceeding to describe various useful combinations of such structures in following sections.

The primary advantages inherent in radiating structures composed of several elements (hereafter designated as multiple linear element structures) are the properties of impedance matching and impedance broadbanding. These advantages become apparent in the transition from one element to two elements. Examples are given which illustrate the mechanism by which each of these properties can be achieved. In discussing distributed material loadings, the point is emphasized that the presence of ferrite or dielectric material affects the symmetric and asymmetric current modes in a dissimilar fashion. Hence, an additional degree of freedom is available for controlling the impedance characteristics of such structures. Another advantage of material loading which has been exploited is the possibility of applying static biasing fields to the materials, and thereby altering the RF properties. This technique allows an element to be electrically tuned to resonance without the need of either mechanically moving components, or active circuit components which characteristically tend to be limited in use to low power applications. In principle, both static electric and magnetic fields may be used to advantage; a static electric field to control the incremental permittivity, and a static magnetic field to control the incremental permeability. This latter technique has been initially tested on two small diameter helical structures having ferrite cores; the experimental details are described in Section 5.3. In this case the tuning results from an ability to control the axial phase velocity of the helical structure. Due to a fundamental limitation on the percentage change in phase velocity, effort has been directed toward obtaining an optimum utilization of this phase velocity control. Accordingly, a detailed analysis of the multiple resonance behavior of composite slow wave structures (cascaded sections of dissimilar structures) has been undertaken.

The interesting features of a composite slow wave structure are: (a) the ability of the structure to generate multiple resonances, and (b) the sensitivity of the locations of resonance upon the structure's controllable phase velocity. An approximate theoretical model is presented in Section 5.4.2 which describes the

dominant reactance behavior for the special case of two dissimilar slow wave structures. An improved formulation based on the EMF method is presented in Section 5.4.3 which describes the input impedance for the general case of an arbitrary number of dissimilar structures. The EMF formulation has two advantages: (1) the reactance variations are described more accurately, thereby allowing a better determination of the resonant frequencies, and (2) the method furnishes information about the input resistance. Having a reliable formulation for the input impedance should allow a precise assessment of the tuning capabilities resulting from continuous phase velocity control.

## 5.2 General Properties of Loaded Linear Elements

Parameters which are considered most important in describing element performance are: (a) radiation pattern, (b) radiation efficiency, and (c) impedance bandwidth. The applicability of ferrite loading is assessed by its influence upon these parameters. As the relative importance of these parameters varies according to the intended antenna application, so does the relative applicability of ferrite loading. The remainder of this section discusses the relationship between ferrite loading and the parameters, and points out the manner in which the parameters may be enhanced by the use of ferrite.

### 5.2.1 Radiation Patterns

The E-field radiation pattern of a uniformly loaded linear element having a standing wave current distribution for which  $2h < .5\lambda$ , is always a single lobe. The lobe has its maximum in the plane normal to the dipole axis, and possesses E-plane symmetry. E-plane beamwidth depends: 1) upon element length, and 2) upon phase velocity (Stephenson and Mayes, 1966). The radiation pattern for a small element is proportional to  $|\sin\theta|$ . The pattern becomes somewhat more directive as either  $h$  (element half-length) is increased, or  $v_p$  (phase velocity along the element) is decreased. The directivity increase is rather insignificant for practical values of  $h$  and  $v_p$ . Consequently, the addition of uniformly distributed ferrite loading to

linear elements, with its inherent effect upon  $v_p$ , will not appreciably affect the radiation pattern. This result allows the use of ferrite materials to enhance other element parameters, for instance impedance bandwidth, without fear of causing pattern deterioration.

### 5.2.2 Radiation Efficiency

While the radiation pattern is fairly insensitivity to  $h$ ,  $v_p$ , and the standing wave current distribution, the radiation efficiency is quite dependent upon these factors. Radiation efficiency is determined from the ratio of radiation resistance to ohmic resistance, the efficiency being greatest when the ratio is large. Since a certain amount of ohmic resistance is unavoidable, it is important to maintain high radiation resistance. Attainment of this objective becomes increasingly difficult for very short radiation elements. As an example, for an unloaded short linear element, radiation resistance is proportional to  $h^2$ , whereas the conductive ohmic resistance is proportional to  $h$ .

It is well known that the maximum radiation resistance for a given element of length  $2h < .5\lambda$ , assuming the value of current at the feed is at least as great as the value anywhere else on the element, occurs when the current distribution is uniform; this corresponds to  $I(z)=I_0$  (constant amplitude) over the entire element length. However, to a fair approximation, the current distribution for an unloaded thin element is:  $I(z)=I_m \sin \beta_0(h-|z|)$ . For a short element, this distribution is essentially triangular. A conventional technique for optimizing the current distribution on a short element is to end load the element. This tends to create the desired uniform current distribution, and hence increase the radiation resistance for a given length,  $h$ . Another effective technique is to uniformly load the element so as to decrease the phase velocity of the current. This results in a current distribution approximated by  $I(z)=I_m \sin \beta(h-|z|)$ , where  $\beta = \omega/v_p > \beta_0 = \omega/c$ . This distribution has a larger current moment, and hence a larger radiation resistance, than that of a short unloaded element of the same length.



In employing these techniques, the ohmic resistance is also increased somewhat. Hence, a trade-off is usually reached in obtaining the maximum ratio of radiation resistance to ohmic resistance. Similar trade-offs exist whether lumped or distributed loadings are incorporated in the techniques described above. Depending upon the quantity, quality and placement of ferrite loading, the radiation efficiency parameter can vary appreciably.

### 5.2.3 Impedance Bandwidth

The input impedance of a linear element can be represented for small frequency deviations about any frequency, except for anti-resonance, by a series resistance and reactance. Moreover, the derivative with respect to frequency of this reactance will always be positive, unless some impedance compensation network is acting upon the element terminals. When a linear element is operated at a frequency away from self-resonance, a pure reactance is sometimes placed in series with the terminals of the element to make the total impedance series resonant. Since the frequency derivative of any passive purely reactive single element impedance is positive, the frequency sensitivity of the resulting series resonant circuit will be increased. For this situation it may be said that any element loading which has the effect of adding series reactance will increase the frequency sensitivity, and hence decrease the impedance bandwidth of the element.

An alternative approach which tends to increase the impedance bandwidth is the insertion of a parallel resonant circuit across the terminals of the element. In this case, the susceptances of the element and the parallel resonant circuit tend to cancel over some frequency band. An optimum configuration using a parallel resonant circuit has been treated by Shnitkin and Levy(1962). This approach works well at VHF-UHF frequencies where stubby dipoles having low  $Q$  may conveniently be constructed. For applications at lower frequencies, its usefulness decreases since elements are generally of higher  $Q$ .

In summary, a single linear element of fixed length can have its impedance bandwidth increased by external compensating techniques. The simplest of these compensating techniques is a parallel resonant circuit across the terminals of the element. At the expense of added complexity in the external compensating circuit, one can obtain only successively smaller incremental improvements in impedance bandwidth.

Multiple linear elements which are tightly coupled may be interconnected so as to serve a dual purpose. That is, in addition to serving as a linear radiator, the elements can function as transmission line impedance compensators. The sections of transmission line essentially function as the elements in the compensating circuit discussed above. A familiar example of such a configuration is the conventional  $\lambda/2$  folded dipole. Details on this method of compensation will be described in Section 5.3.

As indicated under the discussion of radiation efficiency, the application of ferrite loading can alter the element current distribution, and hence the element input impedance. In particular, ferrite may be used to advantage in raising the radiation resistance. Experience has indicated that any increase in radiation resistance of a single linear element due to ferrite loading can be accompanied by a corresponding increase in reactance at certain frequencies. Consequently there may be no net increase in impedance bandwidth. A net decrease in bandwidth may sometimes occur (Taylor, 1955). Similar dependencies may apply for multiple linear elements, in consideration of overall frequency sensitivity. However, one may trade improved impedance bandwidth over some frequency interval for accentuated frequency sensitivity elsewhere. In view of the built-in impedance compensation ability of multiple linear elements, it is theoretically possible to improve impedance bandwidth over some finite frequency interval. It is expected that this impedance compensating capability may be enhanced by an appropriate application of ferrite loading. Potentially promising configurations are discussed in Section 5.3.

#### 5.2.4 Helical Slow Structure

Some inherent advantages of applying static biasing fields to material loaded multiple linear elements are discussed in Section 5.3. Section 5.3.2 describes some magnetic biasing experiments which used small diameter material loaded helices as the linear slow wave structure. The interesting results of these experiments, combined with promising theoretical implications, has motivated a rather thorough study of this particular slow wave structure. To this end, extensive design curves for small diameter core loaded helices have been prepared, and appear in Appendix C along with the details of the mathematical origin. An underlying assumption of isotropic core material is implied by the mathematics, so that strictly speaking the results are rigorous only for the unbiased structure. However, since saturation of the ferrite core material represents a limit on the tuning range of magnetic biasing, the theory discussed in Chapter II was applied to obtain approximate results for this limit.

As an approximation, a helix filled with a ferrite material biased into saturation by a unidirectional magnetic field can be assumed equivalent to one filled with only a dielectric material of the same dielectric constant as the ferrite. This approximation is deduced by noting that the magnetic properties of a ferrite biased into saturation do not affect the wave number of the wave equation for electromagnetic waves inside such a material. By assuming that there is no variation of the field in the  $\phi$  direction for the helix (which is not the case for anisotropic loading), the characteristic equation becomes identical to the isotropically loaded case with the relative permeability of the material identically unity. This approach yields a rough idea of the phase velocity reduction for a biased loading.

To establish the reduction in phase velocity obtainable with ferrites that are available in the project laboratory, the computer program described in Appendix C was used to obtain graphical solutions of the characteristic equation. Plots were made for the following core loadings: 1) air, 2) EAF-2 ferrite powder, 3) Indiana General Q-3 ferrite at 100, 150 and 200 MHz, and 4) Eccosorb CR at 300 MHz.

Eccosorb CR is an Emerson and Cuming microwave absorber having fairly low electric and magnetic loss properties at the frequency of interest. In certain instances two plots were made for each loading so that the results could be read with greater resolution. The solution of the characteristic equation for an air core is given in Fig. C-1 for purposes of comparison with the loaded results. Figures C-2 through C-4 depict the approximate results when the indicated ferrite loadings are biased into saturation. The results for a saturated core and an air core are seen to be nearly identical. Figures C-5 through C-9 depict rigorous results for the same ferrite loading without magnetic bias. A substantial reduction in phase velocity is seen to occur for a given helix pitch angle. Intermediate values of bias field should produce phase velocity reductions between the no-bias and saturation-bias cases. For small helix pitch angles, the sheath helix is an excellent approximation to the physical problem, and close agreement between theoretical and experimental phase velocity reduction factors can be expected. At the larger helix pitch angles, the theoretical model would be more closely approximated by using multifilar windings connected in parallel at the feed. To date, good agreement between theory and experiment has been obtained for the unbiased loadings. Since fields of sufficient intensity to saturate the ferrite have not yet been generated in the project laboratory, the accuracy of the graphs for the saturated core awaits experimental verification.

### 5.3 Advantages of Using Multiple Linear Elements

Multiple linear elements which are tightly coupled can be interconnected to serve a dual purpose. In addition to performing as linear radiators, the elements also serve as sections of transmission line. This latter function can be utilized to provide both impedance matching and impedance broadbanding inherent within the antenna structure. Moreover, the applications of material loading can be used to accentuate this matching and broadbanding capability. The following sub-sections discuss the specific manner in which these capabilities may be enhanced.

### 5.3.1 Analysis of Two Parallel Elements

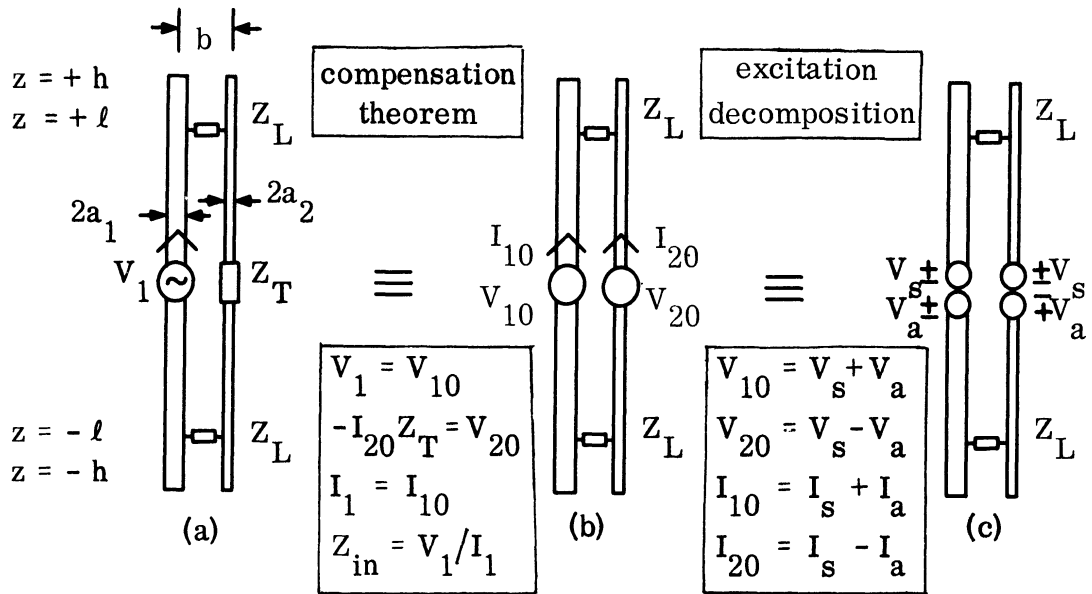
The essential features of multiple linear elements are manifested in the transition from one single element to two coupled elements. For this reason the study was focused upon the two-element case, although the same principles apply to three or more elements. In the following paragraphs is outlined the analysis of two parallel linear elements, and the appropriate equations for the case of tight coupling are given. Tight coupling is essential in order to apply transmission line theory to advantage. It will be shown that the antenna excitation can be decomposed into a symmetric (radiating) mode, and asymmetric (transmission line) mode. Since radiation from asymmetric current is negligible (due to the close element spacing), this mode may be altered to advantage in controlling the impedance variations without experiencing detrimental effects upon the radiation pattern. Various geometrical arrangements exist for altering the asymmetric mode without affecting the symmetric (radiation) mode. Additional freedom is obtained by applying material loading techniques, since the material has dissimilar electrical effects upon the two modes. In particular the current phase velocity differs for the two modes. This is a result of the interaction between the fixed material and dissimilar field distributions of the two modes.

General Formulation: Consider two parallel linear elements of half-length  $h$  and separation distance  $b$  as shown in Fig. 5-1a. Element 1 is center driven with a voltage source  $V_1$ , while Element 2 is center loaded with an arbitrary terminating impedance  $Z_T$ . In addition, arbitrary impedances  $Z_L$  are placed between the two elements a distance  $l$  either side of center. This problem may be analyzed by: 1) applying the compensation theorem to replace  $Z_T$  by an equivalent generator; and 2) decomposing the excitation into symmetric and asymmetric excitation components. These steps are shown in Fig. 5-1b and c, respectively. By applying the principle of superposition, one may solve for the current due to the symmetric and asymmetric excitation as two separate problems and add the results to obtain the desired solution. Strictly speaking, the current distribution resulting

from each mode of excitation should be determined as a boundary value problem. Under certain limiting conditions, results having acceptable accuracy may be obtained by using a simpler analysis. In any event, the distribution of currents is uniquely determined by the geometrical structure of the element, which is independent of the excitation magnitude. The sum of the resulting two current distributions is then the solution to the original problem. The current on each element is given by Eq. (5.1), which appears with Fig. 5-1. A symmetric impedance  $Z_s$  and an asymmetric impedance  $Z_a$  may be identified with each mode of excitation (Eq. 5.2). These mode impedances along with  $Z_T$  determine the input impedance  $Z_{in}$  (Eq. 5.3). Moreover, the actual magnitude of mode excitation is determined by the impedances and the voltage source  $V_1$  (Eq. 5.4).

A mathematical simplification results if the linear elements are thin ( $h^2 \gg b^2 \gg a^2$ ), identical ( $a_1 = a_2 = a$ ), and closely spaced ( $b/h \ll \lambda$ ). Although not strictly necessary for some statements, this situation is assumed in all that follows. In such cases the solutions simplify to those of two tightly coupled antennas, for the symmetric excitation, and a substantially non-radiating transmission line for the asymmetric excitation. The effect of  $Z_L$  upon the symmetric excitation is negligible since its ends are at equipotential points. The effect of  $Z_L$  upon the asymmetric excitation depends upon its value and position on the structure. The solutions to the two parts of the formulated problem are now outlined.

The problem of coupled equal length linear elements not incorporating material loading, but with an arbitrary terminating impedance  $Z_T$ , has been thoroughly treated, among others, by Tai (1948). Tai has an integral equation formulation which yields accurate results on the impedance and the current distribution. Analytic results are also presented in graphical form for selected element lengths and thicknesses, as a function of element spacing. While Tai's formulation may be used where precision is warranted, its immediate usefulness is in establishing the appropriateness of invoking less exact but simpler formulations. In particular, the results indicate that the EMF method, which assumes a sinusoidal current distribution, yields acceptably accurate impedance information for symmetric excitation over the range of element lengths of present interest. Furthermore, for close



$$I_1(z) = I_s(z) + I_a(z) \tag{5.1}$$

$$I_2(z) = I_s(z) - I_a(z)$$

$$Z_s \equiv \frac{V_s}{I_s(o)} \quad Z_a \equiv \frac{V_a}{I_a(o)} \tag{5.2}$$

$$Z_{in} = \frac{2Z_s Z_a + (Z_s + Z_a) Z_T}{Z_s + Z_a + 2Z_T} \tag{5.3}$$

element spacing the exact analysis for asymmetric excitation coincides with the solution derived from transmission line theory. With the foregoing as justification, the viewpoint is taken that sufficient accuracy is obtained by using the EMF method, and transmission line results, for the symmetric and asymmetric excitation portions of the problem, respectively.

Symmetric Excitation Mode: Uniform material loading exerts certain influences. The first order effect of the material is to alter the phase velocity of the symmetric currents flowing on the structure. While certain second order aspects of this alteration may in some instances be difficult to evaluate in an analytical fashion, they are amenable to experimental determination, as is the justification of assumptions involved. Accordingly, the symmetric excitation current distribution for each element is approximated by:

$$I_s(z) = \frac{V_s}{Z_s} \frac{\sin \beta_s (h - z)}, \quad 0 \leq |z| \leq h \quad (5.5)$$

where

$$\beta_s = \omega/v_{ps} > \beta_0, \text{ symmetric excitation wave number.}$$

The symmetric excitation impedance is given by:

$$Z_s = 2Z_{11}(a_e) \quad (5.6)$$

where

$$Z_{11}(a_e) = \text{input impedance of a single linear element of length } 2h \text{ with effective radius } a_e = \sqrt{ab}.$$

Numerical values of  $Z_{11}$  are obtainable from the EMF method. An outline of the analytical development and complete graphical results are presented in Appendix D of this report, for the case of dipole elements constructed of a small diameter helical slow wave structure.

Asymmetric Excitation Mode: The solution for asymmetric excitation is obtainable directly from transmission line theory. A general formulation is used which takes into account ohmic losses, since in certain instances relatively high transmission line currents may exist. The results are presented below, where many of the symbols have been previously defined. The asymmetric excitation current distribution is given by:



$$I_a(z) = \left\{ \begin{array}{ll} I_o \left[ e^{\gamma(\ell-|z|)} - \Gamma_o e^{-\gamma(\ell-|z|)} \right], & 0 \leq |z| \leq \ell \\ I_o \frac{1+\Gamma_o}{\cosh \gamma(h-\ell)} \sinh \gamma(h-|z|), & \ell < |z| \leq h \end{array} \right\} \quad (5.7)$$

where

$$I_o \equiv \frac{V_a}{Z_o} \frac{1}{\left[ e^{\gamma \ell} + \Gamma_o e^{-\gamma \ell} \right]},$$

$Z_o$  = characteristic impedance of the transmission line,

$\gamma = \alpha + j\beta_a$  complex propagation constant, and

$$\Gamma_o = \frac{Z(\ell) - Z_o}{Z(\ell) + Z_o} \text{ complex reflection coefficient.}$$

The asymmetric impedance is given by

$$Z_a = Z_o \frac{Z(\ell) + Z_o \tanh \gamma \ell}{Z_o + Z(\ell) \tanh \gamma \ell} \quad (5.8)$$

where

$$Z(\ell) = \frac{Z_{oc}(\ell) Z_L}{Z_{oc}(\ell) + Z_L}, \text{ and}$$

$$Z_{oc}(\ell) = Z_o \coth \gamma (h-\ell) .$$

Knowing Eqs. (5.6) and (5.8) allow the determination of  $Z_{in}$ , (5.3). Moreover, since  $V_s$  and  $V_a$  are now known by (5.4), the element currents have been determined through (5.1) with (5.5) and (5.7)

**Internal Impedance Matching:** To illustrate the use of multiple linear elements for impedance matching, consider first a structure corresponding to the familiar  $\lambda/2$  folded dipole. This is a special case of the previous formulation corresponding to:

$$Z_L = Z_T = 0, \beta_s = \beta_a = \beta_o, h = \ell = \lambda/4.$$

Neglecting losses, the pertinent relations from Eqs. (5.3), (5.6) and (5.8) are:

$$Z_{in} = \frac{2Z_s Z_a}{Z_s + Z_a} \quad , \quad Z_s = 2Z_{11}(a_e), \quad Z_a = j Z_0 \tan \beta_0 h = j \omega \quad .$$

The above yield the familiar result of  $Z_{in} = 4Z_{11}(a_e)$ , where  $Z_{11}(a_e) \approx 73 \Omega$ . The factor of 4 in  $Z_{in}$  (which for  $N$  linear elements is equal to  $N^2$ ) is also a consequence of the two elements having equal radii ( $a_1 = a_2 = a$ ), and may be varied by making  $a_1/a_2 \neq 1$ . Of more importance is the fact that this factor is unchanged if  $h \neq \ell \neq \lambda/4$ , provided only that  $|Z_a| = \infty$ . This can be accomplished in either of two ways: 1) by use of distributed material loading so that  $\pi/2 = \beta_0 h = \beta_a \ell$ ; or 2) by adding a parallel capacitor across the antenna terminals which will resonate with  $Z_a = 2jZ_0 \tan \beta_0 \ell$ . The factor 2 arises since there are two transmission line segments of length  $\beta_0 \ell$  connected in series across the antenna terminals. Since the factor of 4 can be maintained independent of  $h$ , one can foreshorten the antenna to any extent and still have  $Z_{in}$  equal 4 times the impedance of a single foreshortened element. This technique is an efficient way of raising the inherently low impedance of foreshortened elements.

As a second example consider the slightly more general case where  $h = \lambda/4$ , but  $\ell$  is allowed to vary ( $0 \leq \ell \leq h$ ). The input impedance  $Z_{in}$  is seen to be twice the parallel combination of  $Z_s \approx 146 \Omega$  and  $Z_a = jZ_0 \tan \beta_0 \ell$ . Since  $0 \leq |Z_a| \leq \infty$  as  $0 \leq \ell \leq h$ ,  $|Z_{in}|$  may be adjusted continuously from 0 to  $292 \Omega$ . Moreover,  $\text{Re}\{Z_{in}\}$  may be set at any desired level from 0 to  $292 \Omega$  by proper adjustment of  $\ell$ , and the  $\text{Im}\{Z_{in}\}$  may be made zero by a slight readjustment of  $h$ , or by adding a lumped series reactance at the antenna terminals. This versatility allows a wide range of input impedances with a minimum of external matching. A number of curves illustrating the effect have been calculated by Chang (King, 1956, p. 345). A popular version of this fundamental principle is the so-called "T" match. Similar results are obtained when material loading is incorporated.

While it was indicated in the first example that the material loading was a practical way of maintaining  $|Z_a| = \infty$  (via adjusting  $\beta_a \ell$  to equal  $\pi/2$ ), a unique advantage of material loading is that it can enhance frequency compensation, as described in the next subsection.

Internal Impedance Broadbanding: The impedance broadbanding capability of multiple linear elements can best be illustrated by again considering first the familiar  $\lambda/2$  folded dipole, described earlier in this section and then its generalization. Two distinct mechanisms tend to increase the impedance bandwidth of this structure. First, the impedance associated with the symmetric excitation mode,  $Z_s = 2Z_{11}(a_e)$ , corresponds to twice that of a single linear element having an effective radius  $a_e = \sqrt{ab}$ . Since this effective radius is substantially larger than the radius of an individual element, the reactance variation with respect to frequency about the resonant point is reduced from what it would be for either element operating alone. The second mechanism is that of susceptance cancellation between the parallel impedances of the symmetric mode and the asymmetric (transmission line) mode. Take, for example, the situation when the structure is operated slightly below the normal  $\lambda/2$  resonant frequency.  $Z_s$  is capacitive since the elements are electrically shorter than  $\lambda/2$  resonance, while  $Z_a$  is inductive since the elements function as a transmission line of electrical length  $< \pi/2$  terminated in a short circuit. Slightly above resonance the reverse situation occurs.

While the susceptances of the two modes oppose each other, the cancellation is not complete. This is because the susceptance of  $Z_a$  which is given by

$$\left( \frac{1}{jZ_o} \cot \frac{\pi f}{2f_o} \right)$$

is much smaller near resonance than that of  $Z_s$ . However, for appreciable frequency excursions from resonance (perhaps 25 percent) the susceptances will cancel, thus forming two additional resonant frequencies. The impedance characteristics about these resonant frequencies are described in Beam and Andris (1952) and King (1956). It can be observed that the impedance variation with frequency change is high at the lower resonant point, whereas the impedance variation is more attractive at the higher resonant frequency. In particular, at this higher resonant frequency the input resistance is only moderately higher than at normal  $\lambda/2$  resonance. Moreover, the reactance change with frequency is broad and negative, which offers the possibility of easy compensation.

The foregoing discussion has been on the ordinary  $\lambda/2$  folded dipole for which  $\beta_s = \beta_a = \beta_0$ . The application of material loading will improve the utility of the folded dipole. For instance, applying coatings of ferrite and dielectric material to the elements results in  $\beta_a = \omega/v_{pa} > \beta_0$ . The appropriate formula for describing the phase velocity reduction was presented in Section 2.6 in connection with the helix discussion. While the material coatings will also increase  $\beta_s$ , the quantitative effects of the increase will be dissimilar, since the near zone field distributions resulting from the symmetric and asymmetric current modes are unlike. Hence, this affords an independent control of the resonant frequencies for  $Z_s$  and  $Z_a$ . In addition, the coatings affect the frequency sensitivity of  $Z_a$ , and also the value of  $Z_0$ . The interplay between these various parameters is being investigated, with the expectation that the increased versatility can be put to advantage in improving the impedance bandwidth.

### 5.3.2 Input Impedance for a Generalized Folded Dipole

The analysis developed in Section 5.3.1 has been incorporated into a computer program which calculates the input impedance  $Z_{in}$  from Eq. (5.3). Computer results for the particular case corresponding to a folded dipole formed of two small diameter helical slow wave elements are presented in Figs. 5-2 through 5-7. Numerical results which appear in Appendix D for helical elements were used in the computations. The slow wave elements have symmetric and asymmetric mode phase velocity reduction factors of  $p_s$  and  $p_a$ , respectively, a length to thickness ratio of 55, and an asymmetric mode characteristic impedance of 250 ohms. As the figures clearly show, some interesting variations in impedance behavior result from different combinations of  $p_s$  and  $p_a$ . Figure 5-2 illustrates the input impedance for an ordinary open wire folded dipole since  $p_s = p_a = 1.0$ . Figure 5-4 illustrates an interesting negative reactance slope behavior near  $\beta_0 h = \pi/2$  when  $p_s = 1.0$ , and  $p_a = 0.6$ . This structure may be realized by placing dielectric material between two linear conducting elements, thereby affecting only the asymmetric phase velocity reduction factor as is the case for TV "twin lead" cable.

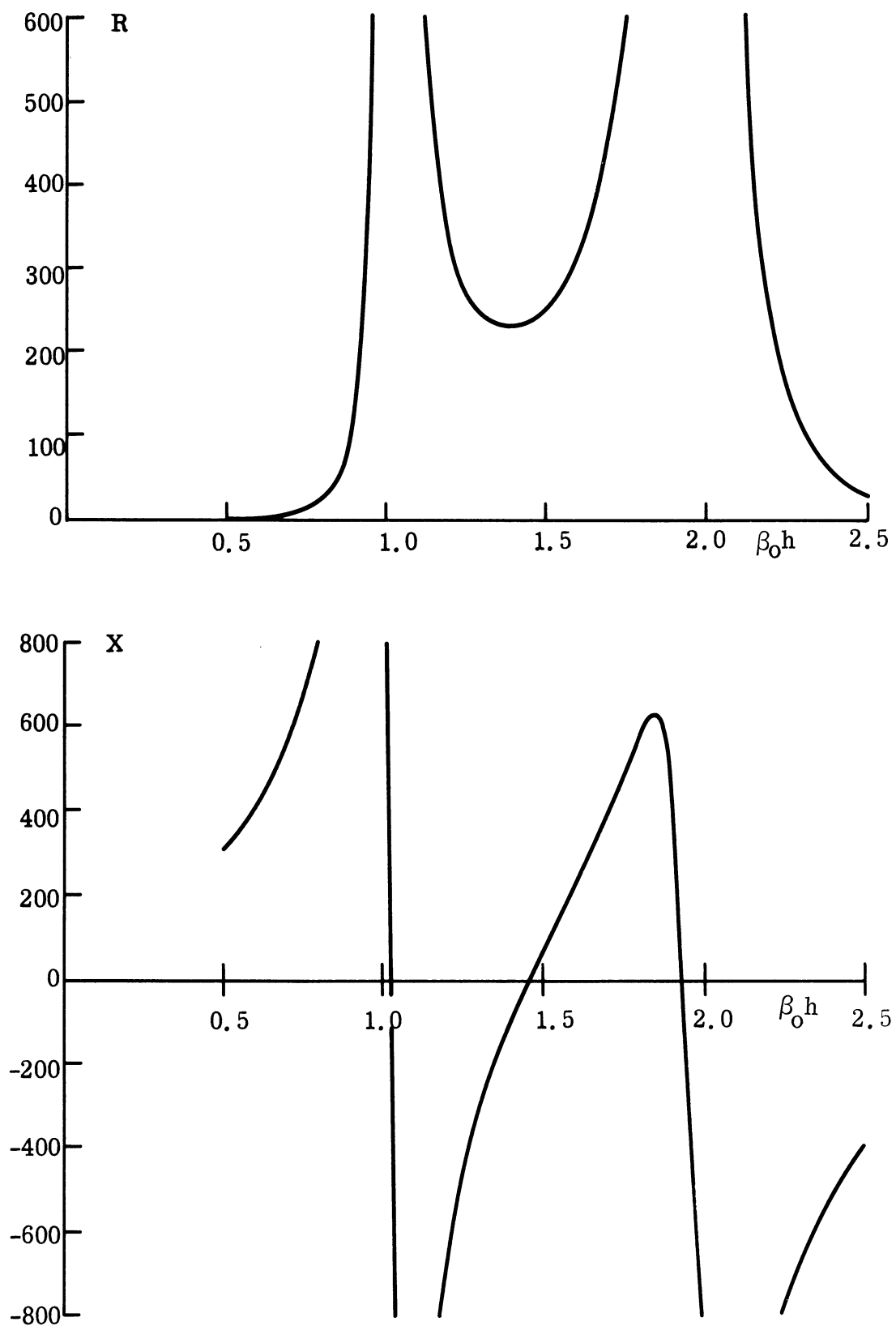


FIG. 5-2: INPUT RESISTANCE  $R$  AND REACTANCE  $X$  FOR FOLDED DIPOLE STRUCTURE WHERE  $p_s = 1.0$ ,  $p_a = 1.0$ .

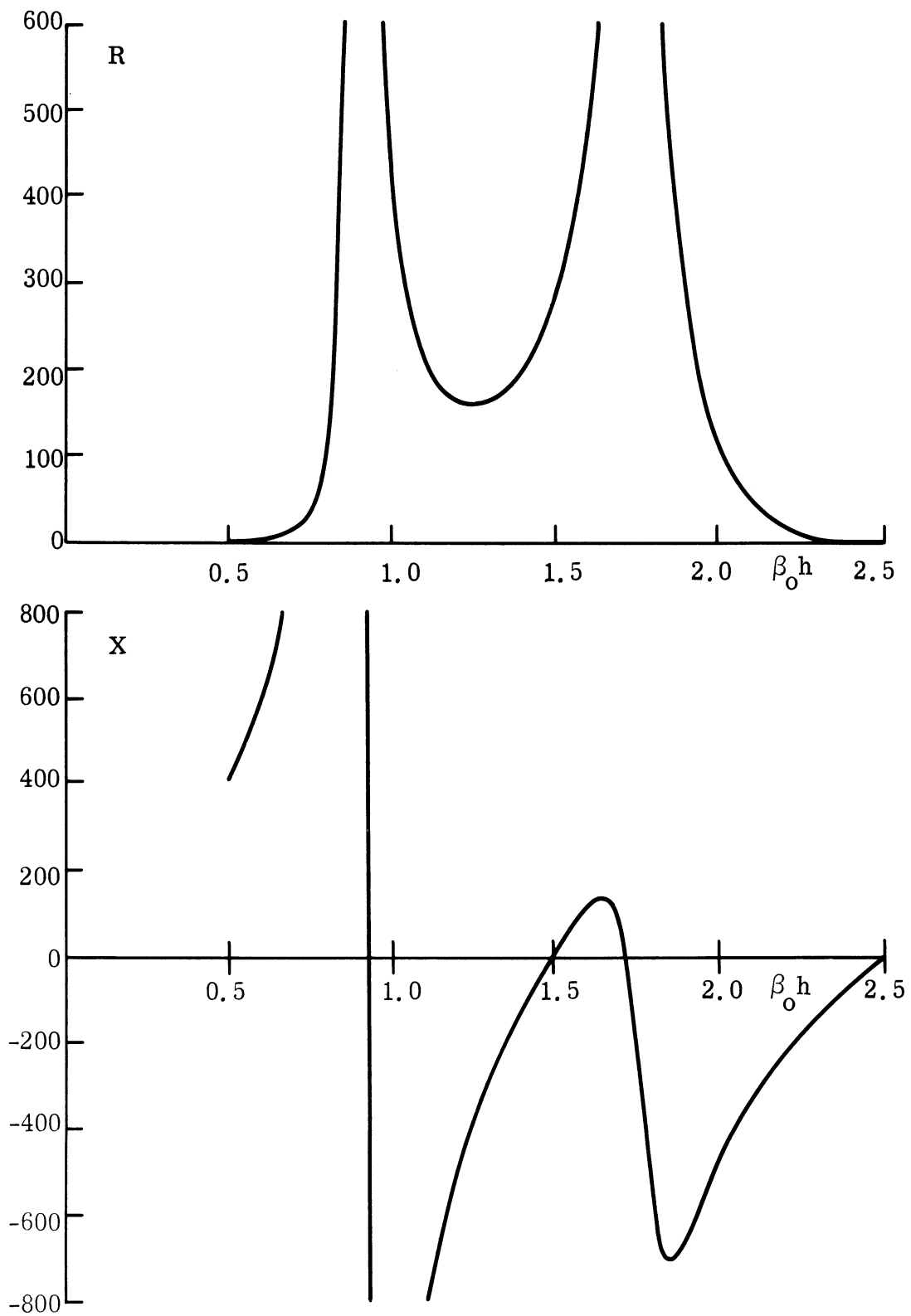


FIG. 5-3: INPUT RESISTANCE  $R$  AND REACTANCE  $X$  FOR FOLDED DIPOLE STRUCTURE WHERE  $p_s = 1.0$ ,  $p_a = 0.8$ .

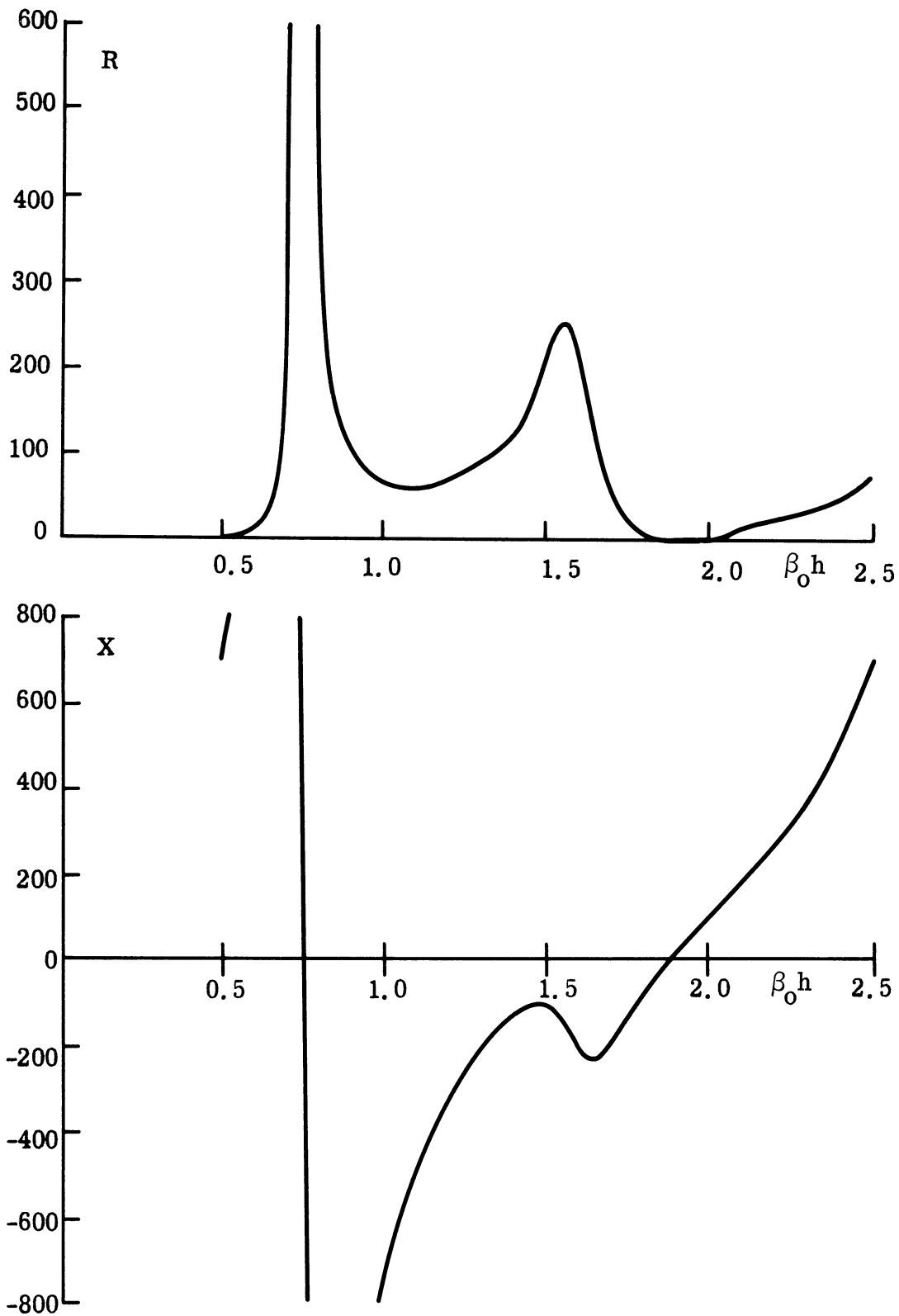


FIG. 5-4: INPUT RESISTANCE  $R$  AND REACTANCE  $X$  FOR FOLDED DIPOLE STRUCTURE WHERE  $p_s = 1.0$ ,  $p_a = 0.6$ .

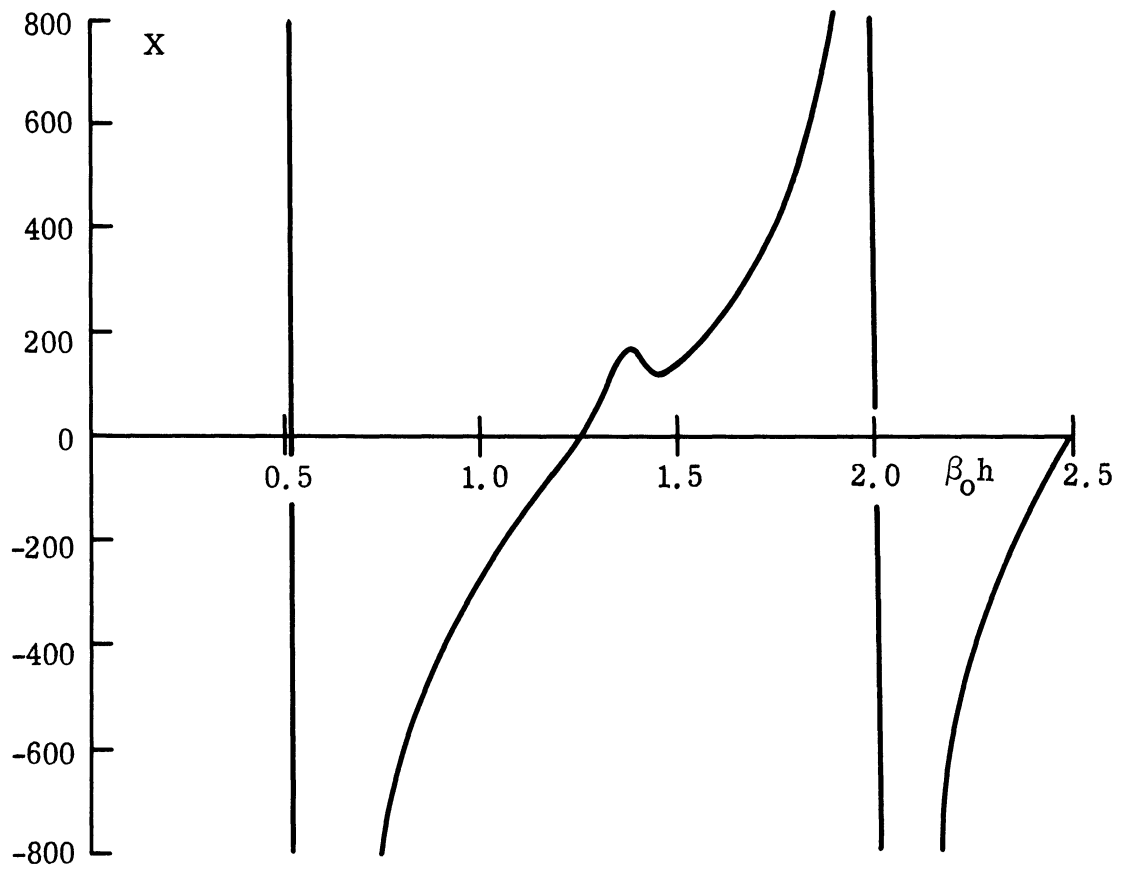
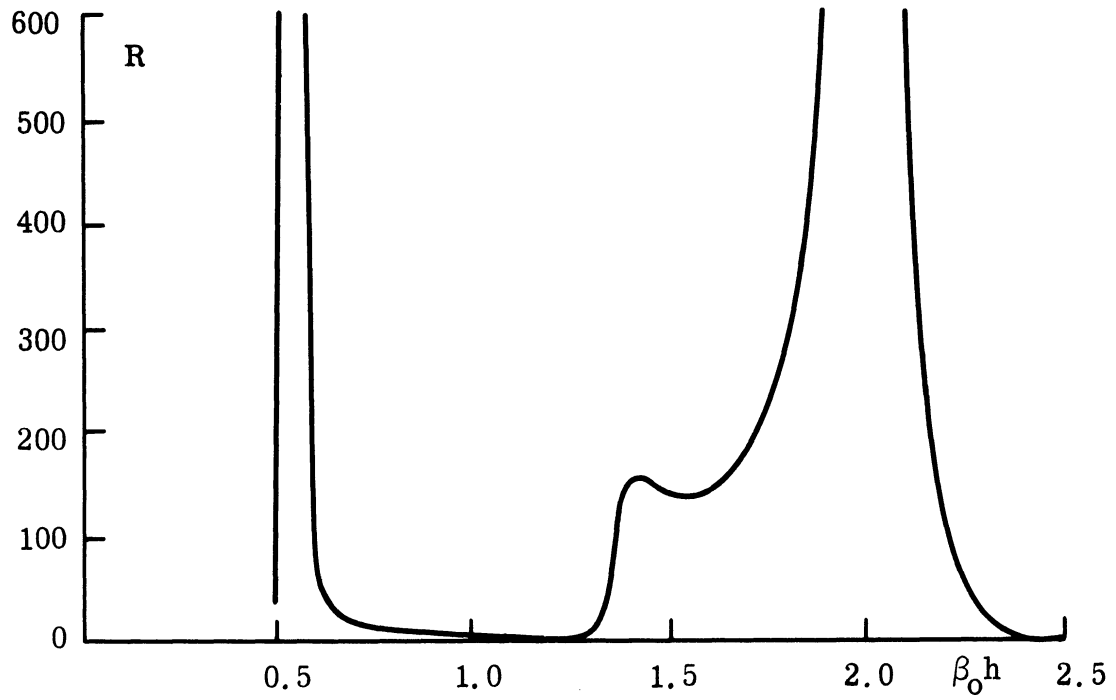


FIG. 5-5: INPUT RESISTANCE  $R$  AND REACTANCE  $X$  FOR FOLDED DIPOLE STRUCTURE WHERE  $p_s = 1.0$ ,  $p_a = 0.4$ .



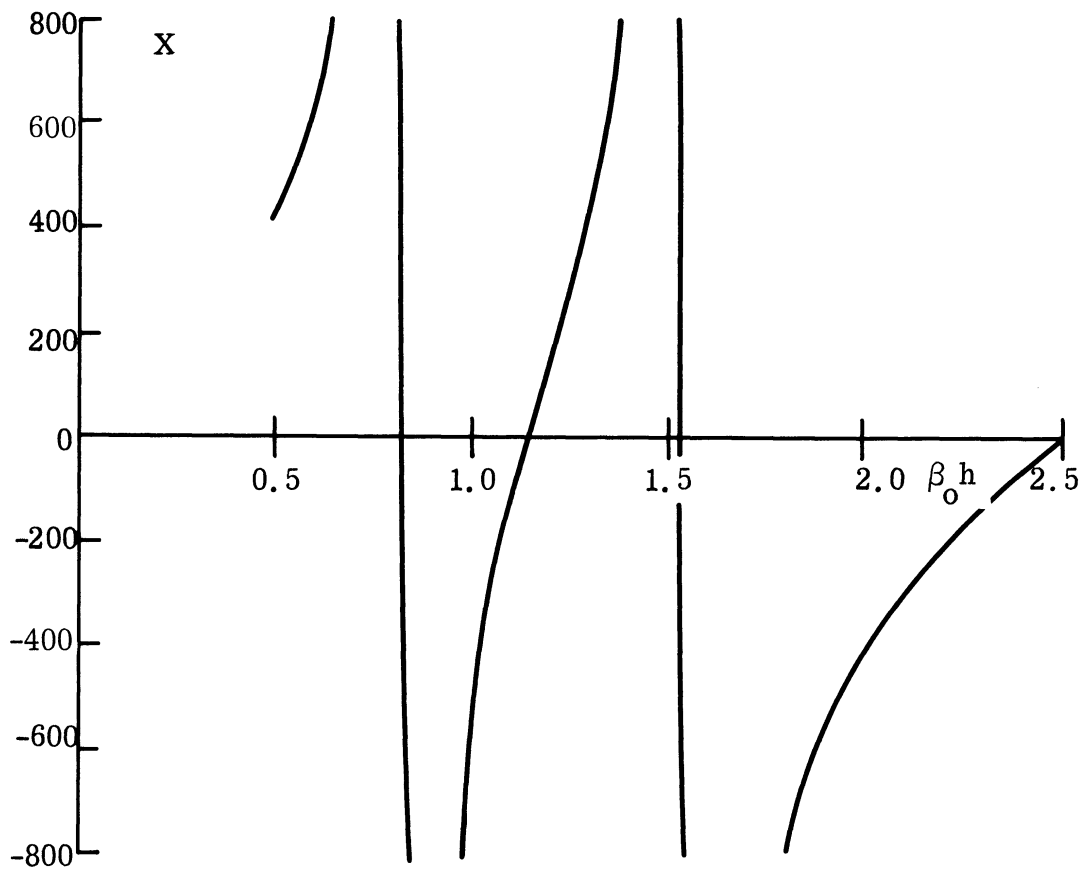
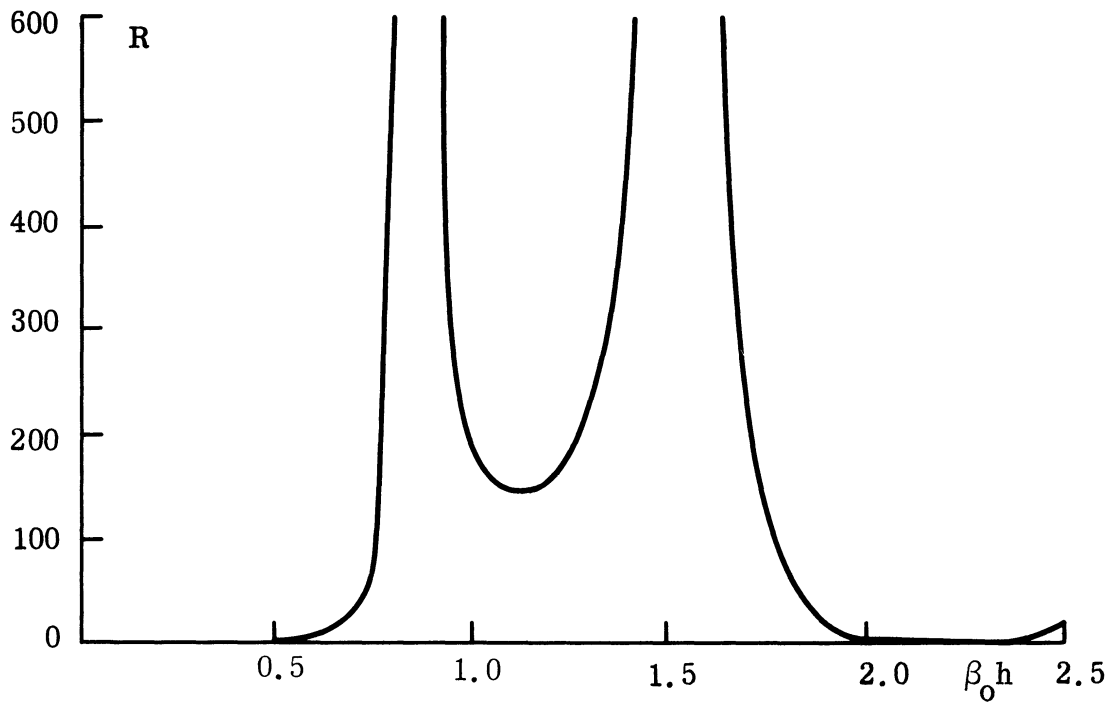


FIG. 5-6: INPUT RESISTANCE  $R$  AND REACTANCE  $X$  FOR FOLDED DIPOLE STRUCTURE WHERE  $p_s = 0.8$ ,  $p_a = 0.8$ .

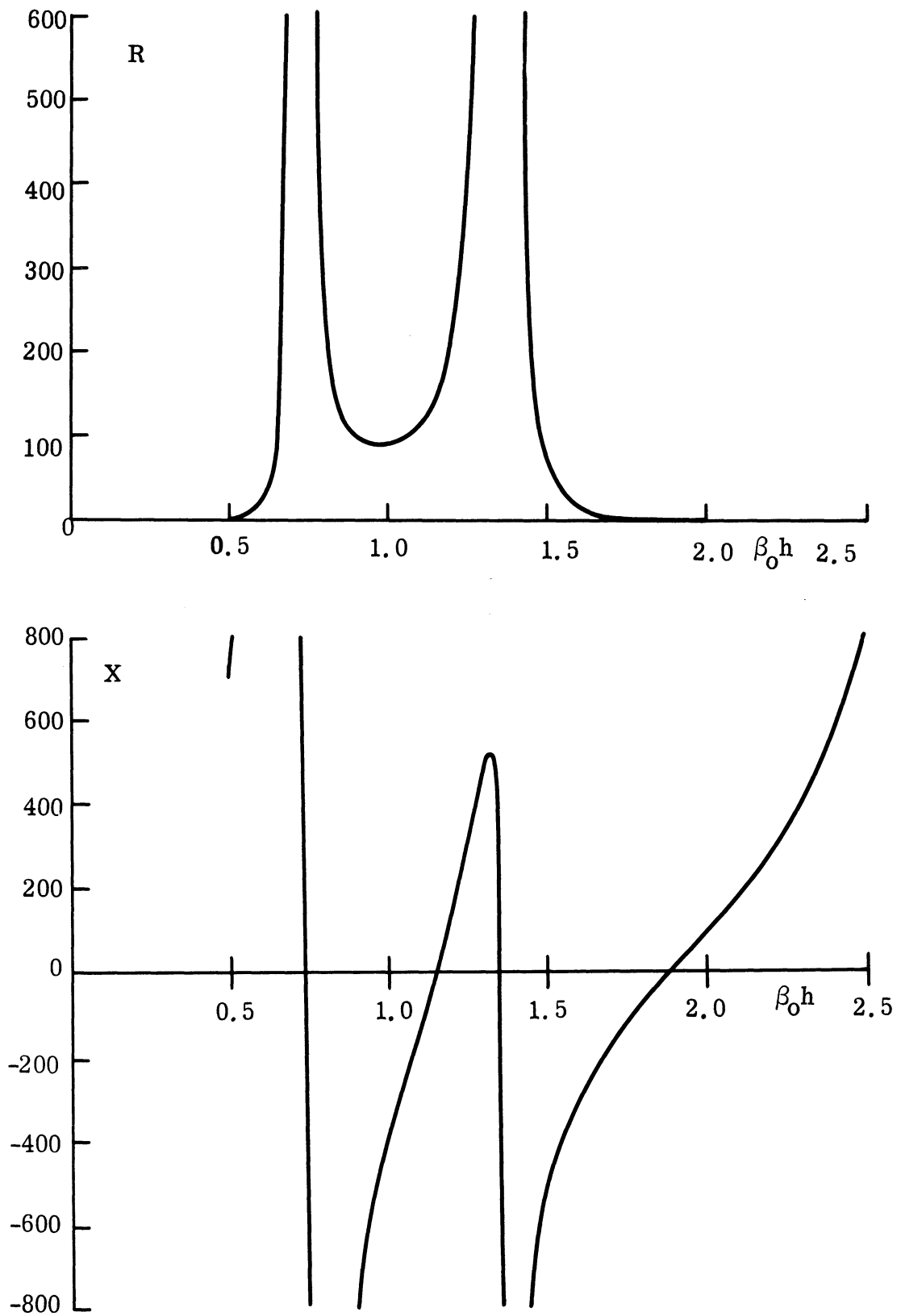


FIG. 5-7: INPUT RESISTANCE  $R$  AND REACTANCE  $X$  FOR FOLDED DIPOLE STRUCTURE WHERE  $p_s = 0.8$ ,  $p_a = 0.6$ .

### 5.3.3 Experimental Results

To verify several of the concepts developed through theoretical reasoning, a number of experiments have been performed on small diameter helical slow wave structures. These helices were tested with both hollow and ferrite cores, and excited in several different geometrical configurations. The experiments consisted of measuring the magnitude of the reflection coefficient versus swept frequency, and the resonant input resistance at several discrete frequencies. Results obtained were in reasonable agreement with those anticipated by the theoretical development. The details of the experiments, along with a correlation to theory, are presented below.

All measurements of reflection coefficients and impedance for the small diameter helix configurations were made with the elements fed against a large aluminum ground plane inserted in the end of an anechoic chamber. Three different geometrical configurations were tested; a single helical monopole, a double helical monopole and a folded helical monopole. Each of these configurations were tested with the helix having a hollow core, and a partially filled ferrite core. The helix construction is depicted in Fig. 5-8 for the folded helical monopole configuration having a partial core of ferrite. Measurements were made on the magnitude of the reflection coefficient versus swept frequency. These are presented in Fig. 5-9 for the three element configurations and two core conditions. All reflection coefficients are with respect to 50 ohms; the lower trace in each photograph is a reference value of 0.5. In each photograph the second division from the left represents zero frequency, and the top horizontal line corresponds approximately to a 1.0 reflection coefficient. Due to the rapid changes in reflection coefficient near resonance, the limited detector response occasionally prevents the dip from reaching its true null. Also, since the ordinate is not precisely linear in magnitude of reflection coefficient, particular values of interest near the resonance conditions were measured independently.

Photograph (a) of Fig. 5-9 indicates that the single helical monopole with hollow core has a resonance near 90 MHz. A separate impedance measurement indicated a resonant input resistance of 14 ohms at 88.9 MHz. In photograph (c), two identical

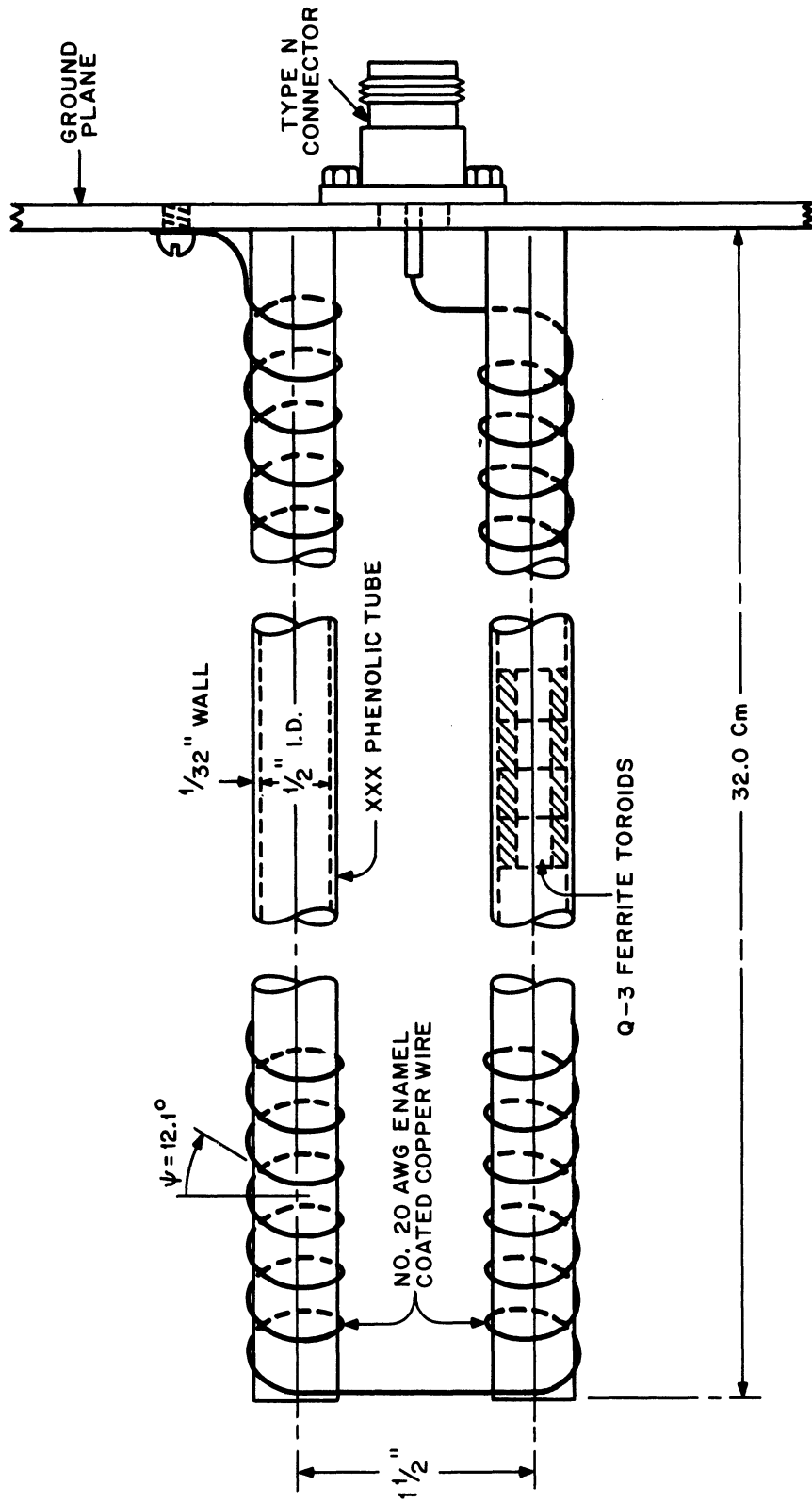
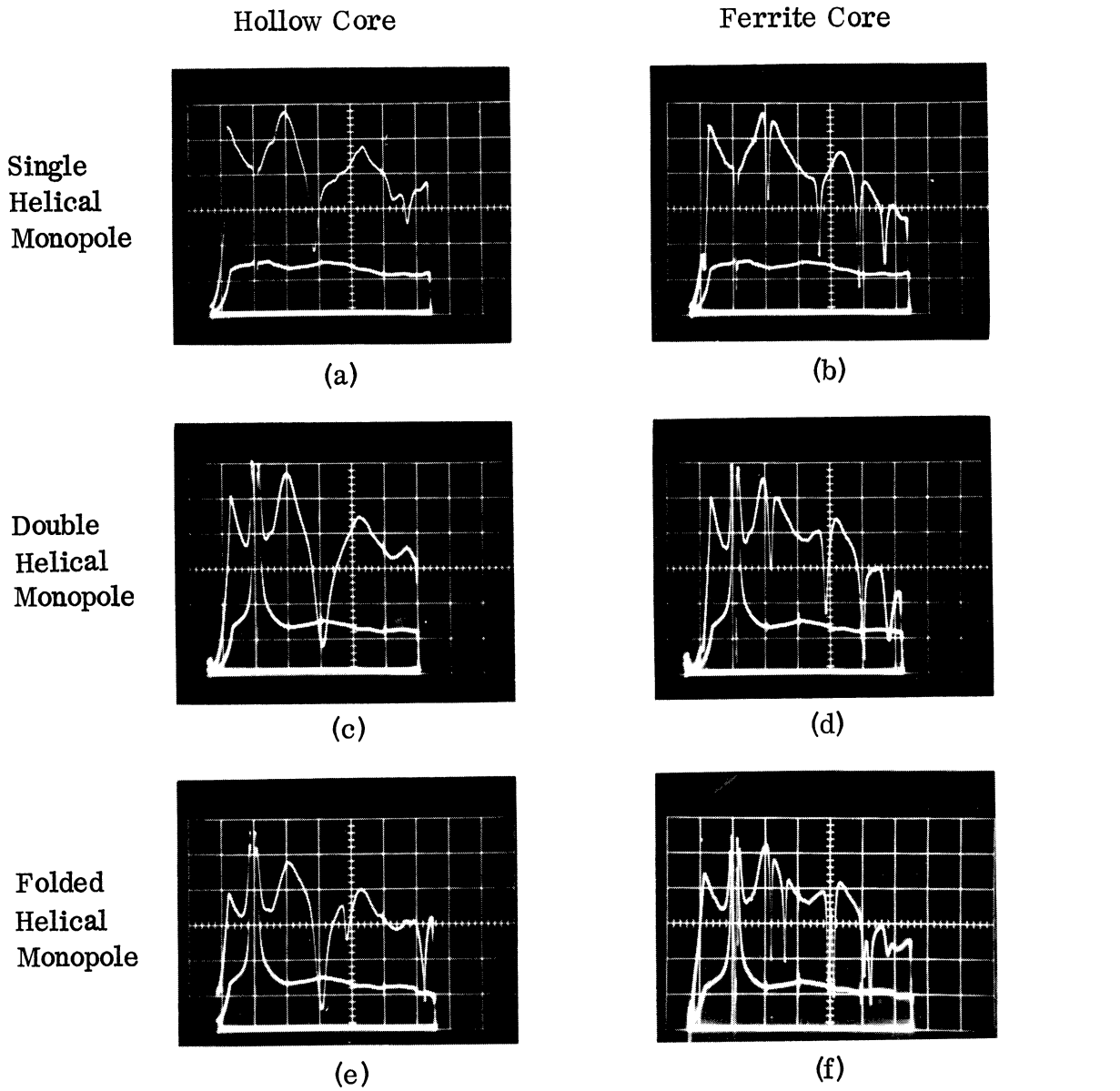


FIG. 5-8: CONSTRUCTION OF FOLDED HELICAL MONOPOLE WITH FERRITE CORE.



VERTICAL - Top Curve  $|\rho|$  for Element; Bottom Curve  $|\rho| = 0.5$  Reference  
HORIZONTAL - 50 MHz/Square, Center = 150 MHz

FIG. 5-9: MAGNITUDE OF REFLECTION COEFFICIENT VERSUS FREQUENCY FOR VARIOUS HOLLOW CORE AND FERRITE CORE HELICAL ELEMENT CONFIGURATIONS.

helices, except for having opposite pitch angles, were fed in parallel. For this configuration, the resonant resistance was 26 ohms at 102.9 MHz. By comparison with photograph (a) it can be seen that some interaction exists between the helices which results in effectively less phase velocity reduction. For photograph (e) the two helical elements were connected in a folded monopole configuration. The new resonant resistance is 93 ohms at 103.6 MHz. Hence, the folding operation has increased the resonant resistance by a factor of 3.6. The theoretical factor corresponding to the symmetric mode current dividing evenly between the two helical elements would be 4.0. Apparently the slight asymmetry of the feed configuration altered somewhat the division of current. Another theoretically predicted result is the highly mismatched resonance near 142 MHz. The generation of additional resonances slightly above and below the primary resonant frequency is characteristic of the folded configuration, as illustrated in Section 5.3.2. Both additional resonances typically have a large resistive mismatch, the mismatch being more pronounced at the lowest frequency resonance. The configurations corresponding to photographs (a), (c) and (e) but which have ferrite toroids placed in the helix core are presented in photographs (b), (d) and (f), respectively of Fig. 5-9. Photograph (b) indicates that the application of ferrite loading to the single helical monopole significantly lowered the first resonant frequency. The new resonant resistance was 5.3 ohms at 49.6 MHz. Additional resonances due to higher order current excitation modes are also in evidence. Photographs (d) and (f) indicate that each loaded element configuration has characteristics corresponding to those of the unloaded element. In particular there is a slight increase in resonant frequency due to an interaction effect, and the appearance of an additional resonance for the folded configuration. The first resonance in photograph (d) increased to 57.3 MHz and had an input resistance of 4.3 ohms. The corresponding first resonance at 57.3 MHz of photograph (f) had input resistance of 15 ohms. This represents an increase by a factor of 3.5, which compares well with the factor of 3.6 obtained for the corresponding unloaded configuration.

THE UNIVERSITY OF MICHIGAN  
7848-1-F

The conclusions to be drawn from the experimental data may be summarized as follows.

- 1) Only a slight interaction occurs between two closely spaced small diameter helices, allowing each to function effectively as a linear slow wave structure.
- 2) The folded helical monopole is an effective configuration for transforming low resonant resistances to higher values.
- 3) The insertion of ferrite into the core of a small diameter helix substantially reduces the phase velocity.
- 4) A decrease in phase velocity is accompanied by a proportionately lower value of input resistance at the lowest resonant frequency.

The concept of varying the resonant frequency of a linear element configuration utilizing material loading by means of applying a static electric or magnetic field has been previously described. While these ideas are quite sound in principle, certain quantitative aspects may be investigated most expediently through the use of experiments. Accordingly, initial experiments have been made on two separate geometrical configurations in order to ascertain the quantitative effect of static magnetic field biasing. The primary motivation was to establish the feasibility of such concepts. Hence, the experiments represent in no way an optimum design configuration. The results of these initial experiments are encouraging and indicate that the resonant frequency can be shifted several percent. The details of the experiments are described below.

One experiment on static magnetic field biasing was performed using the configuration described in Fig. 5-8. This folded helical monopole having a ferrite toroidal core has a d-c closed circuit path between the center conductor and ground of the input connector. A direct current was applied to this closed path which produced essentially an axial static magnetic field in each of the two loaded helical elements. Due to the opposite pitch angle of the two elements, the axial components

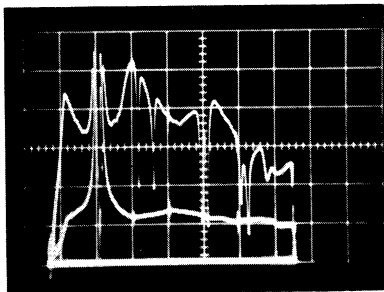
of the static magnetic fields were applied to the same vector direction. The change in resonant frequency due to applying magnetic bias was determined through observation of the swept frequency reflection coefficient information, as depicted in Fig. 5-10, first column. Photograph (a) represents the unbiased configuration, and is identical to that of Fig. 5-9, photograph (f). Photograph (b) illustrates with an expanded frequency scale the effect of biasing near the 80 MHz resonance. Two superimposed curves are shown; the right-hand curve is the normal unbiased resonance, the left-hand curve illustrates the downward shift in resonant frequency with the application of 7.6 amps of bias current. Photograph (c) is a similar presentation of the double resonance near 150 MHz. The left-hand curve again represents the downward shift in resonant frequency resulting from the application of a 7.6 amp bias current. The d-c power required to achieve this shift was less than 9 watts.

While these changes in resonant frequency are significant, a more pronounced variation would be desirable. This could be achieved simply by applying a larger bias current, but with the disadvantage of increased d-c power dissipation. Alternatively, a structure having a closed path magnetic circuit could be used to intensify the magnetization effect of the bias current. Realizing that the principal effect of the static magnetic field is an alteration of the incremental permeability, effort has been directed toward obtaining an element configuration whose resonant frequency has an accentuated sensitivity to incremental permeability. Since the observed resonances result from an interaction between radiation and transmission line modes, alteration of the transmission line frequency behavior can significantly affect the behavior of the resonance.

A particular technique of transmission line mode alteration under present investigation involves achieving a significantly greater phase velocity reduction for the transmission line mode in relation to the radiation mode. This results in the asymmetric mode impedance being substantially more sensitive to a change in electrical length than the symmetric impedance. While large phase velocity reductions in the symmetric mode are undesirable due to the accompanying severe decrease in resonant

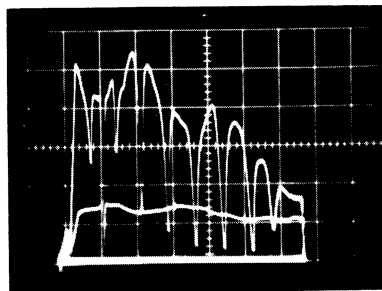


Folded Helical Monopole  
With Ferrite Core

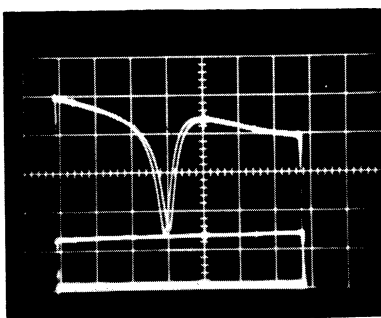


(a)

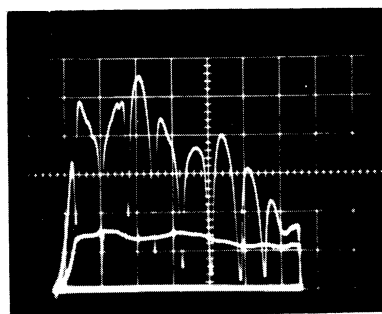
Helical Monopole With  
Ferrite and Copper Core



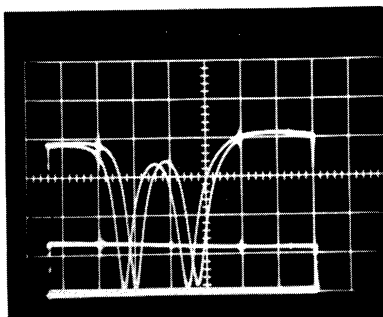
(d)



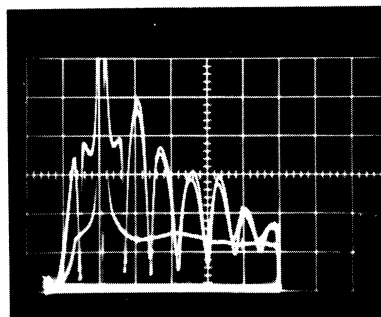
(b)



(e)



(c)



(f)

VERTICAL - Top Curves,  $|\rho|$  for Element; Bottom Curve,  $|\rho| = 0.5$  Reference  
HORIZONTAL - 50 MHz /Square, Center = 150 MHz, Except as Follows:  
(b) Center = 85 MHz; (c) Center = 155 MHz; Both 5 MHz/Square

FIG. 5-10: EFFECT OF MAGNETIC BIASING ON MAGNITUDE OF REFLECTION COEFFICIENT VERSUS FREQUENCY FOR TWO DIFFERENT ELEMENT FERRITE CORE CONFIGURATIONS.

radiation resistance, such a phase velocity reduction in the asymmetric mode appears quite desirable. With this line of thinking as motivation, the configuration described in Fig. 5-11 was constructed and tested. The new configuration has several distinctive features. In particular, the concept of symmetric and asymmetric excitation is slightly more difficult to envision. Essentially, symmetric excitation corresponds to feeding a helical slow wave structure having a metal core surrounded by ferrite. Asymmetric excitation corresponds to feeding a type of helical transmission line. Owing to the dissimilar field distributions for the two modes, the phase velocity reduction appears to be substantially greater for the asymmetric mode than for the symmetric mode. The experimental results for this configuration are described below.

Swept frequency reflection coefficient measurements are presented in the second column of Fig. 5-10. Photographs (d) and (e) correspond to the connection between the outer ends of the helix and metal core being open circuited, and short circuited, respectively. The multiple resonances which occur at approximately 40 MHz intervals are seen to shift about 20 MHz corresponding to this change in configuration. Apparently the asymmetric mode impedance repeats itself with a period of 40 MHz. The highly frequency sensitive reactance from this transmission line mode is seen to periodically cancel the radiation mode reactance, thereby causing the multiple resonances. Such a characteristic may in itself be desirable, aside from enhancing the resonant frequency sensitivity to magnetic biasing. For this configuration the unidirectional bias creates a static magnetic field in both the axial and tangential directions. The effect of applying a direct current is illustrated in photograph (f). The trace shifted farthest to the left and having the smallest peak-to-peak variation represents a momentary application of approximately 10 amps of current. The second curve represents the effect of residual magnetization after the biasing current was removed. A comparison between photographs (e) and (f) indicates that the bias current has lowered the resonant frequency by approximately 7 percent. This represents a substantial improvement over the previous folded helical monopole configuration.

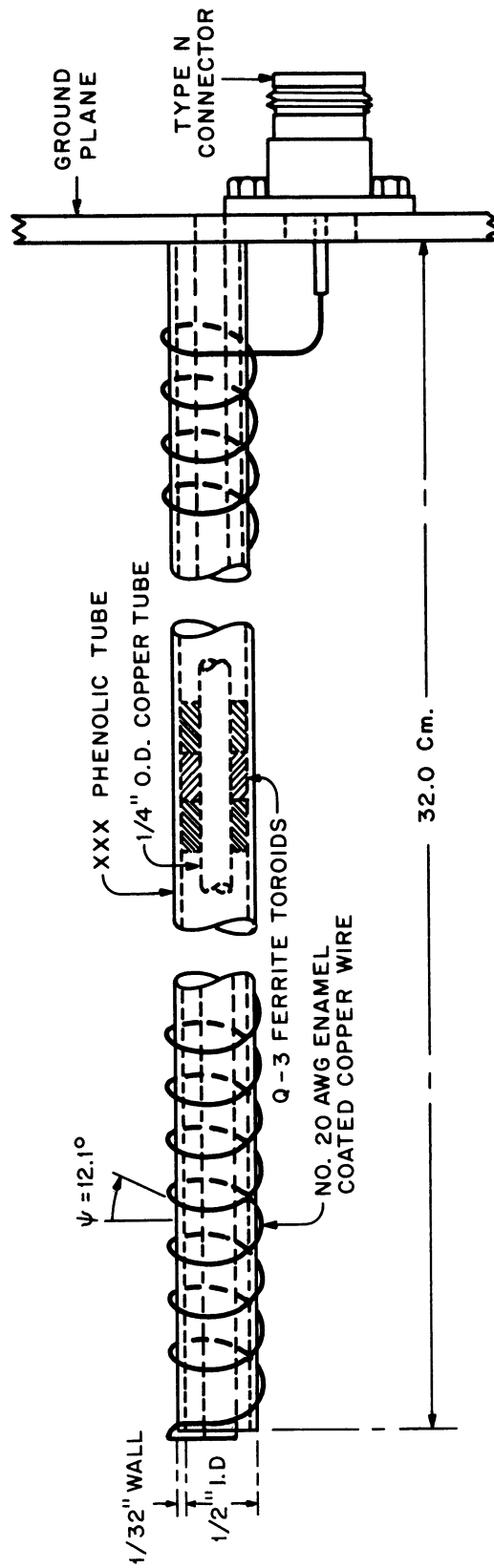


FIG. 5-11: CONSTRUCTION OF HELICAL MONOPOLE WITH FERRITE AND COPPER CORE.

The residual effect suggests the possibility of tuning the elements by means of using pulses of current to establish a specified residual condition. This would remove the necessity of having to continuously apply d-c power to maintain a particular resonance. Such an application would require the ability to demagnetize, and then reapply a different residual condition, when a change in operating frequency is desired. With the presence of a large number of multiple resonant frequencies, the percentage change in frequency required to establish continuous tuning is substantially decreased. It is clear, however, that further modifications will be necessary in order to obtain a capability for continuous tuning. Future effort directed at optimization should yield substantial progress toward achieving this goal. Nevertheless, it is felt that these present experiments do demonstrate the feasibility of such operation.

#### 5.4 Multiple Resonance Behavior of Composite Structures

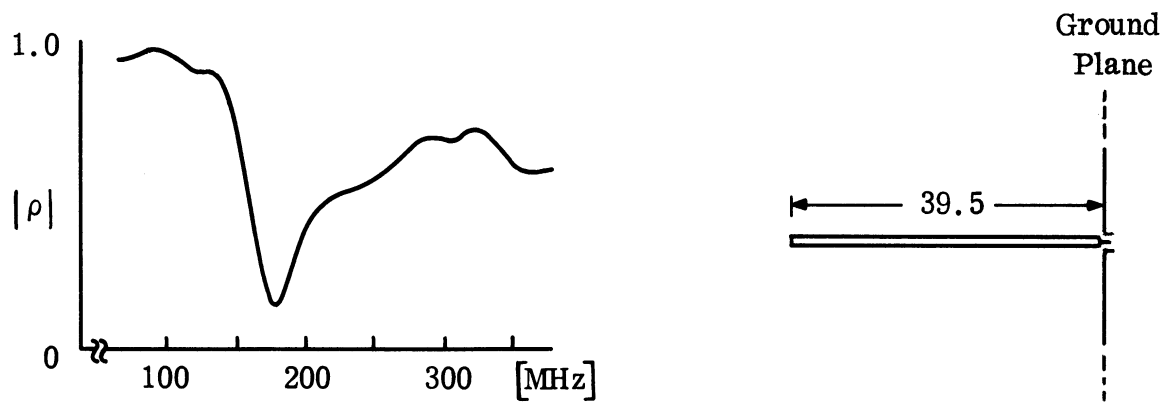
Subsection 5.3.3 discussed how multiple resonances could result from the interaction between transmission line and radiation type modes of excitation. There is now presented a means of generating multiple resonant frequencies through utilization of only the symmetric mode of excitation. The purpose of this discussion is two-fold. First, from the standpoint of desiring a continuously tunable radiating element, the larger the number of multiple resonances which exist before applying magnetic biasing techniques, the less stringent the requirements of the biasing technique to shift the resonant frequency. For example, the number of resonances appearing in Fig. 5-10 (photograph e) might be doubled by doubling the number of resonances associated with the symmetric excitation mode. Secondly, it is sometimes desirable to optimally foreshorten elements which are normally excited only in a symmetric mode, as for example in a log periodic dipole array, where the occurrence of multiple resonant frequencies may be detrimental to overall array operation. In this situation it is necessary to foreshorten the element in such a way as to control certain prescribed resonances to an advantage if possible without introducing additional

extraneous resonances. The following subsections first describe the mechanism by which multiple resonances occur on structures having only symmetric mode excitation, then develop a simplified theory for predicting the resonance behavior, and finally, describe certain improvements in the analysis. The results obtained are useful in the design of composite structures for either of the aforementioned applications.

#### 5.4.1 Experimental Evidence

It is known that to achieve a specified amount of linear element foreshortening, while at the same time minimizing the degradation in impedance bandwidth, a form of "end loading" is needed so as to enhance the current moment of the radiating element. Helical slow wave structures placed at the outer ends of normal linear dipole arms tend to accomplish this goal. In addition to the helices and the normal dipole segments having dissimilar phase velocities, they also have in general different characteristic impedances. These two properties give rise to a reflection of the electromagnetic field at the interface between the two structures, in addition to the normal reflections at the outer tips of the composite structure. The result is that this composite element experiences resonance at generally twice as many frequencies.

To illustrate the effectiveness of a composite element structure in generating multiple resonances, the results of a simple experiment are presented in Fig. 5-12. The left column shows a plot of reflection coefficient versus frequency corresponding to the element configurations shown in the right columns. The lengths of the two dissimilar structures are indicated in the figure. The structure nearest the ground plane is 5/32" O. D. brass tube. A helix wound with No. 20 AWG copper wire forming a 10.3° pitch angle constitutes the second structure. This helix is supported by a 1/4" O. D. paper phenolic tube which telescopes over the 5/32" O. D. brass structure. A good electrical contact exists between the brass tube and the right hand end of the helix. The first curve shows a single resonance at approximately



ALL DIMENSIONS IN cm

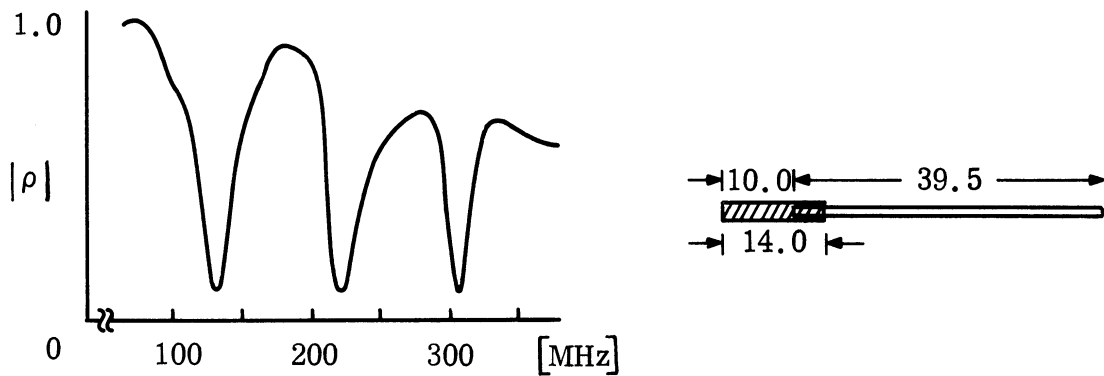
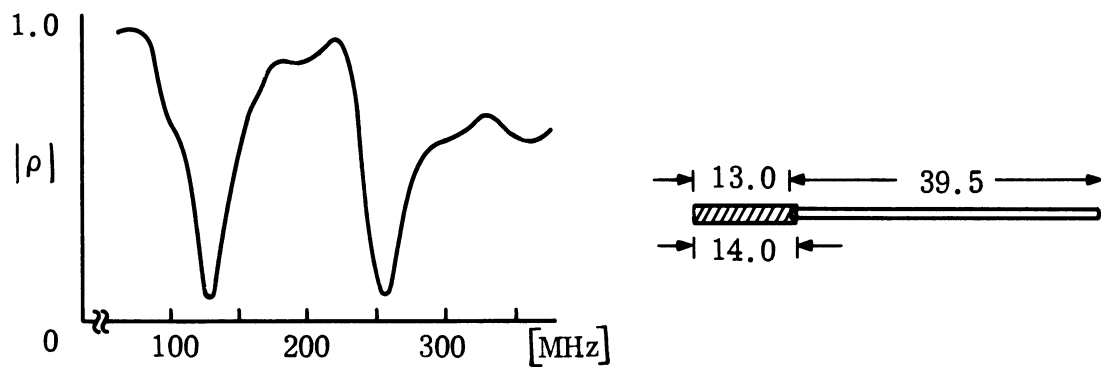


FIG. 5-12: MULTIPLE RESONANCE BEHAVIOR OF VARIOUS COMPOSITE ELEMENT STRUCTURES.

180 MHz for the brass tube structure alone fed against the ground plane. The addition of a relatively short length of helical slow wave structure introduces a double resonance as indicated in the second curve. Along with the expected lower resonance at 130 MHz, an additional resonance occurs at 260 MHz. By telescoping 4.0 cm of the helical structure back over the brass tube, effectively, a third type of slow wave structure is introduced. The interaction of reflections from the two interfaces between the dissimilar slow wave structures, along with the reflection from the outermost tip, all combine to generate three resonant frequencies as shown in the corresponding curve. It is especially significant to note the rather drastic change in resonance behavior between the middle and bottom configuration which resulted from the introduction of only a 3.0 cm segment of a third slow wave structure. Moreover, the electrical length of this third structure had a pronounced influence upon the location of the center resonance. Application of ferrite loading and a variable magnetic bias to control this electrical length might permit positioning this resonance over an appreciable bandwidth. This behavior infers that magnetic biasing may be capable of a substantial alteration in resonant frequency provided that the point of application is judiciously chosen. The theory to describe the behavior of three dissimilar structures follows straightforwardly from the approach used below for two structures.

#### 5.4.2 Approximate Mathematical Analysis

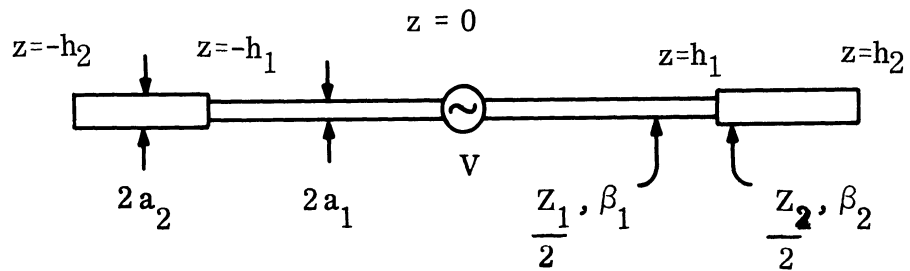
One can now develop a rather simple theoretical model to describe the multiple resonance behavior of a composite element composed of two dissimilar slow wave structures. To account for the discontinuity in thickness between the two structures, a technique is adopted which has been used successfully in analyzing cylindrical antennas. The zeroth order integral equation formulation for the discontinuous cylindrical antenna yields a solution for input reactance which is identical to that obtained by using a transmission line analogy. Moreover, this solution is known to describe the dominant reactive behavior. Appendix D contains a detailed presentation of the input impedance of a small diameter helical slow wave structure based

upon the induced EMF method. The EMF formulation verifies that the dominant behavior of the input reactance for the helix may also be described by a mathematical expression which formally represents that of an equal length of open circuited lossless transmission line. Thus, since the transmission line analogy is applicable to the separate situations of discontinuous thickness, and of a helix having arbitrary axial phase velocity, it should also be reasonably applicable to the combined situation. With this motivation, an approximate analysis of a composite slow wave structure was developed based upon the transmission line analogy. This method allows the determination of the dominant input reactance behavior, and hence specification of the approximate multiple resonant frequencies. This approach of using a transmission line analog to approximate the reactance behavior of an element configuration excited by a symmetric mode is to be sharply contrasted with the rigorously developed transmission line mode discussed in Section 5.3.1. For the types of element configurations discussed in that section, the asymmetric or transmission line excitation was seen to result from a rigorous mathematical decomposition of the source excitation. It should be emphasized that the decomposition into two separate problems was entirely rigorous, even though approximations were invoked to solve the two resulting simpler problems. This present development is strictly an analog which is known to give useful approximate results.

Although the experiment presented in Fig. 5-12 contained a segment of normal linear monopole near the ground plane, the following development is generalized to include the possibility of arbitrary phase velocity in this central portion. Realization of such an element is possible using various small diameter helices. The geometry of the corresponding dipole configuration, along with its analogous transmission line is shown in Fig. 5-13. The characteristic impedances  $Z_1$  and  $Z_2$  of the transmission line represent "average" values of the antenna characteristic impedance and will be discussed in greater detail shortly.



Dipole Geometry:



Analogous Transmission Line:

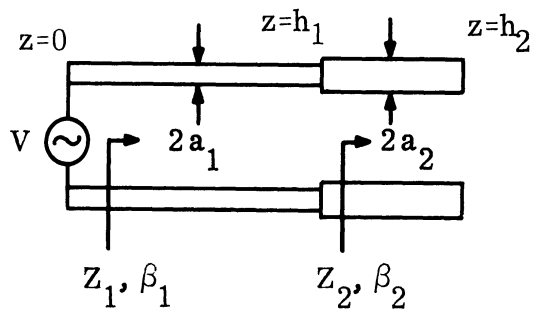


FIG. 5-13: GEOMETRY OF CORRESPONDING DIPOLE CONFIGURATION WITH ANALOGOUS TRANSMISSION LINE.

The solution to the analogous transmission line problem is straightforward. First, the general form of the current and voltage distribution is written for each region:

$$\begin{aligned}
 & \left. \begin{aligned} I(z) &= A \sin \beta_2 (h_2 - |z|) \\ V(z) &= -jZ_2 A \cos \beta_2 (h_2 - |z|) \end{aligned} \right\} h_1 \leq |z| \leq h_2 \\
 \text{and} \\
 & \left. \begin{aligned} I(z) &= B \sin \beta_1 (h_1 - |z|) + C \cos \beta_1 (h_1 - |z|) \\ V(z) &= -jZ_1 B \cos \beta_1 (h_1 - |z|) + jZ_1 C \sin \beta_1 (h_1 - |z|) \end{aligned} \right\} 0 \leq |z| \leq h_1 .
 \end{aligned} \tag{5.9}$$

Next, the boundary conditions at  $z=h_1$  are applied;

$$I(h_1^-) = I(h_1^+) ; \quad V(h_1^-) = V(h_1^+) . \tag{5.10}$$

It is here that a basic approximation enters. Since voltage may be defined uniquely only for the TEM type waves which exist on a uniform transmission line, the voltage boundary condition precludes from consideration the known existence of higher order modes generated by the discontinuity. Such higher order modes are precisely the terms which contribute to the input resistance and a corrective reactance term. However, since the TEM mode accounts for the dominant reactance term, it is justifiable to exclude the higher order modes from consideration. From the boundary conditions all but one of the unknown constants are determined, and after minor trigonometric manipulation one obtains for the region  $0 \leq |z| \leq h_1$  :

$$I(z) = A \left\{ \sin \left[ \beta_2 (h_2 - h_1) + \beta_1 (h_1 - |z|) \right] - \frac{Z_1 - Z_2}{Z_1} \cos \beta_2 (h_2 - h_1) \sin \beta_1 (h_1 - |z|) \right\} . \tag{5.11}$$

For the special case of  $\beta_2 = \beta_1$ , this expression reduces to a result given by Schelkunoff and Friis (1952). Figure 5-14 is a sketch of the current distribution for the general result when  $Z_2 < Z_1$ . The voltage distribution is found similarly, and the input reactance evaluated as

$$X_{in} = \frac{V(o)}{I(o)} = jZ_1 \frac{Z_1 \sin \beta_2 (h_2 - h_1) \sin \beta_1 h_1 - Z_2 \cos \beta_2 (h_2 - h_1) \cos \beta_1 h_1}{Z_1 \sin \beta_2 (h_2 - h_1) \cos \beta_1 h_1 + Z_2 \cos \beta_2 (h_2 - h_1) \sin \beta_1 h_1} . \tag{5.12}$$

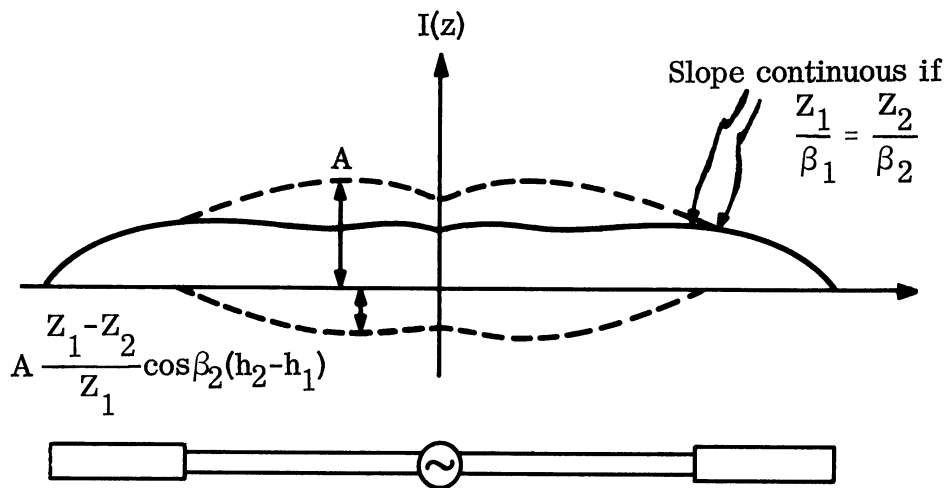


FIG. 5-14: CURRENT DISTRIBUTION FOR GENERAL RESULT  
WHEN  $Z_2 < Z_1$ .

This expression reduces as a special case to the zeroth order integral equation solution for a cylindrical antenna with discontinuous thickness as given in Wolff (1966) . Wolff's result can be obtained from the above expression by setting :

$$\beta_1 = \beta_2 = \beta_0 ; \quad Z_1 = 60 \Omega_1 , \quad \text{and} \quad Z_2 = 60 \Omega_2 ,$$

where the thickness parameter is

$$\Omega_i = 2 \ln \frac{2h_2}{a_i} , \quad i = 1, 2 . \quad (\ln \text{ is the symbol for logarithm to the base "e"}) .$$

Thus, the equivalent transmission line characteristic impedances using the thickness parameter concept are given by

$$Z_i = 120 \ln \frac{2h_2}{a_i} . \quad (5.13)$$

The resonance condition for the generalized dipole requires that the input reactance equal zero. Since the numerator and denominator are both real functions, and the denominator is bounded, the resonance condition requires that the numerator equals zero. Hence,

$$Z_1 \sin \beta_2 (h_2 - h_1) \sin \beta_1 h_1 - Z_2 \cos \beta_2 (h_2 - h_1) \cos \beta_1 h_1 \equiv 0$$

which can be expressed in the more compact form

$$\tan \beta_2 (h_2 - h_1) \tan \beta_1 h_1 = \frac{Z_2}{Z_1} . \quad (5.14)$$

While this transcendental equation is somewhat awkward to handle in hand computations, it is readily solvable by computer techniques. Recalling that

$$\beta_i = \frac{\omega}{v_i} = \frac{2\pi f}{p_i c} , \quad i=1, 2 ,$$

the parameters which need to be controlled for design purposes are the phase velocity reduction factors  $p_i$  , and the characteristic impedances  $Z_i$ . Appendix C presents design data useful for controlling the  $p_i$ , and the characteristic impedance for a single small diameter helix is given by Sichak (1954). An equivalent transmission line characteristic impedance is given by twice that of a single element as

$$Z_i = 120 \frac{\beta_i}{\beta_0} \ln \left( \frac{1.123}{\beta_i^2 - \beta_0^2 a_i} \right) . \quad (5.15)$$

If a normal linear element is used in place of the center helical structure, an appropriate expression for  $Z_1$  would be given by (5.13).

#### 5.4.3 Generalization and Improved Analysis

An approximate theoretical model was presented in Section 5.4.2 which described the dominant reactance behavior for the special case of two dissimilar slow wave structures. An improved formulation based upon the EMF method is presented below which describes the input impedance for the general case of an arbitrary number of dissimilar structures. The EMF formulation has two advantages: 1) the reactance variations are described more accurately, thereby allowing a better determination of the resonant frequencies, and 2) the method furnishes information about the input resistance.

The accuracy of the EMF method depends heavily upon the extent to which an assumed current distribution is realistic, and the usefulness of the method depends on the ease with which the resulting integrals may be evaluated. Following the long established approach used for the familiar linear dipole, the approximate current distribution for the composite slow wave structure is obtained from the solution of an analogous uniform transmission line problem. From the resulting current distribution, the magnetic vector potential is obtained, thereby leading to a determination of the electric field. The electric field expression contains integrals which must in turn be integrated against the assumed current distribution in order to obtain the input impedance. Such an evaluation is possible for relatively thin structures. The evaluation depends upon forming a rapidly convergent series expansion for the integrand of one integral and retaining after integration the leading terms. This method also permits an extension of the single structure result (Appendix D) to cover element half-lengths greater than  $\beta_s h = \pi$ , which was a prior restriction.

The current distribution for the composite structure composed of  $N$  segments, each having dissimilar phase velocities and characteristic impedances, is obtained

by a procedure identical to that discussed in Section 5.4.2 for the particular case of  $N = 2$ . Proceeding as before, the general form of the current and voltage for each of the  $N$  segments is given by:

$$\begin{aligned} I_i(z) &= K_{\mathbf{I}, i} \sin \beta_i (h_i - |z|) + K_{\mathbf{II}, i} \cos \beta_i (h_i - |z|) \\ V_i(z) &= -jZ_i K_{\mathbf{I}, i} \cos \beta_i (h_i - |z|) + jZ_i K_{\mathbf{II}, i} \sin \beta_i (h_i - |z|) \\ h_{i-1} \leq z \leq h_i, \quad h_0 &\equiv 0, \quad 1 \leq i \leq N. \end{aligned} \quad (5.16)$$

Upon applying the boundary conditions that the current vanishes at the structures tips,  $|z| = h_N$ , and that the voltage and current be continuous at the transitions between the segments,  $|z| = h_i$ , where  $1 \leq i \leq N-1$ , one obtains:

$$K_{\mathbf{I}, N} = I_m \text{ (a constant)}, \quad K_{\mathbf{II}, N} = 0, \quad i = N \quad (5.17a)$$

and the following recursion relations for the remaining constants of lower index:

$$K_{\mathbf{I}, i} = \frac{Z_{i+1}}{Z_i} K_{\mathbf{I}, i+1} \cos \beta_{i+1} (h_{i+1} - h_i) - \frac{Z_{i+1}}{Z_i} K_{\mathbf{II}, i+1} \sin \beta_{i+1} (h_{i+1} - h_i) \quad (5.17b)$$

$$K_{\mathbf{II}, i} = K_{\mathbf{I}, i+1} \sin \beta_{i+1} (h_{i+1} - h_i) + K_{\mathbf{II}, i+1} \cos \beta_{i+1} (h_{i+1} - h_i), \quad 1 \leq i \leq N-1.$$

The average characteristic impedances  $Z_i$  may be determined from (5.15) in the case of helical segments, or from (5.13) for the tubular segments. Thus, Eqs. (5.16) and (5.17) completely specify the current distribution on each segment of the composite structure, and form the required generalization of (5.11) which pertained to the particular case of  $N = 2$ .

Having an expression for the current distribution, the axial component of the electric field may be obtained from the magnetic vector potential as:

$$E_z(z) = \frac{-j\omega}{\beta_0^2} \left[ \beta_0^2 + \frac{\partial^2}{\partial z^2} \right] A_z(z),$$

where the vector potential is given by:

$$A_z(z) = \frac{\mu_0}{4\pi} \int_{-h_N}^{h_N} \frac{I(z') e^{-j\beta_0 R}}{R} dz' = \frac{\mu_0}{4\pi} \sum_{i=1}^N \int_{h_{i-1}}^{h_i} I_i(z') [g_+ + g_-] dz'$$

with

$$R = \sqrt{\rho^2 + (z-z')^2}, \quad g_+ = \frac{e^{-j\beta_0 \sqrt{\rho^2 + (z+z')^2}}}{\sqrt{\rho^2 + (z+z')^2}}, \quad g_- = \frac{e^{-j\beta_0 \sqrt{\rho^2 + (z-z')^2}}}{\sqrt{\rho^2 + (z-z')^2}}.$$

Interchanging the order of integration and differentiation, the axial electric field becomes:

$$E_z(\rho, z) = \frac{-j\omega\mu_0}{4\pi\beta_0^2} \sum_{i=1}^N \int_{h_{i-1}}^{h_i} I_i(z') \left[ \beta_0^2 + \frac{\partial^2}{\partial z^2} \right] [g_+ + g_-] dz'.$$

Considerable simplification results by noting that

$$\frac{\partial^2}{\partial z^2} [g_+ + g_-] = \frac{\partial^2}{\partial z'^2} [g_+ + g_-]$$

and

$$\frac{d^2 I_i(z')}{dz'^2} = -\beta_i^2 I_i(z'),$$

thereby allowing one to integrate twice by parts to obtain

$$E_z(\rho, z) = \frac{-j\omega\mu_0}{4\pi\beta_0^2} \sum_{i=1}^N \left\{ I_i(z') \frac{\partial}{\partial z'} [g_+ + g_-] \Big|_{h_{i-1}}^{h_i} - \frac{dI_i(z')}{dz'} [g_+ + g_-] \Big|_{h_{i-1}}^{h_i} + (\beta_0^2 - \beta_i^2) \int_{h_{i-1}}^{h_i} I_i(z') [g_+ + g_-] dz' \right\}.$$

This expression reduces for  $N \geq 2$  to:

$$\begin{aligned}
 E_z(\rho, z) = & \frac{-j\omega\mu_0}{4\pi\beta_0^2} \left\{ 2K_1 \frac{e^{-j\beta_0 R_0}}{R_0} + \beta_N I_m \left( \frac{e^{-j\beta_0 R_{N+}}}{R_{N+}} + \frac{e^{-j\beta_0 R_{N-}}}{R_{N-}} \right) \right. \\
 & \left. + (\beta_0^2 - \beta_1^2) \int_0^{h_1} I_1(z') [g_+ + g_-] dz' \right. \\
 & \left. + \sum_{i=2}^N \left[ K_i \left( \frac{e^{-j\beta_0 R_{(i-1)+}}}{R_{(i-1)+}} + \frac{e^{-j\beta_0 R_{(i-1)-}}}{R_{(i-1)-}} \right) + (\beta_0^2 - \beta_i^2) \int_{h_{i-1}}^{h_i} I_1(z') [g_+ + g_-] dz' \right] \right\}
 \end{aligned}
 \tag{5.18}$$

where

$$\begin{aligned}
 K_1 &= \frac{dI_1(0)}{dz'} = \beta_1 [K_{\mathbf{I}, 1} \sin \beta_1 h_1 - K_{\mathbf{I}, 1} \cos \beta_1 h_1] \quad , \quad i = 1 \\
 K_i &= \frac{d}{dz'} [I_i(h_{i-1}) - I_{i-1}(h_{i-1})] \quad , \quad 2 \leq i \leq N \\
 &= \beta_i [K_{\mathbf{I}, i} \sin \beta_i (h_i - h_{i-1}) - K_{\mathbf{I}, i} \cos \beta_i (h_i - h_{i-1})] + \beta_{i-1} K_{\mathbf{I}, i-1}
 \end{aligned}$$

and

$$R_{i+} = \sqrt{\rho^2 + (z+h_i)^2} \quad , \quad R_{i-} = \sqrt{\rho^2 + (z-h_i)^2} \quad .$$

Equation (5.18) furnishes the required generalization of Eq. (D-2) in Appendix D. The last terms involving the summation in (5.18) account for all additional segments beyond the first ( $i \geq 2$ ), and hence must be omitted if only one segment is present ( $i = 1$ ). Moreover, when several segments are present but none are slow wave structures (i. e.,  $\beta_i = \beta_0$ ,  $1 \leq i \leq N$ ), then the integral terms vanish because of their coefficients but a contribution from the summation term may still result since the  $K_i$  are not zero unless all  $Z_i$  happen to be identical.



The foregoing has established the axial component of the electric field,  $E_z(\rho, z)$ . A transverse component,  $E_\phi(z)$ , is contributed by those slow wave segments formed by a small diameter helix. Using a sheath model for the helix, each  $E_\phi(a_i, z)$  term (evaluated at the sheath surface) can be closely approximated by an equation similar to (D. 3) in Appendix D, where a slight modification accounts for the more general current distribution. According to the EMF method for determining the input impedance, both of the above components are used to form the total tangential electric field, which is then integrated against the assumed current distribution over the total length of the composite structure, thereby obtaining the complex power contributed to the electromagnetic field. It turns out that the contribution to the complex power from each  $E_\phi(a_i, z)$  term is entirely reactive, and is almost identically cancelled by a contribution from the portions of  $E_z(a_i, z)$  arising from the real part of the corresponding integral terms in (5. 18). By corresponding integral terms in (5. 18) is meant those which have an interval of integration with respect to  $z'$  within which is included the range of  $z$  under consideration in each  $E_\phi(a_i, z)$ . Hence, over regions of the composite structure composed of a small diameter helix, the tangential electric field is accounted for by (5. 18), where only the imaginary parts of the integral terms are used. Moreover, over those regions of the composite structure which are not composed of a small diameter helix, the contribution to the total electric field from each corresponding integral term in (5. 18) vanishes completely because of its coefficient vanishing, while the contributions from the integral terms for remaining segments are negligible. Thus, over either slow wave or normal regions of the composite structure, the total tangential electric field  $E_t(z)$  is accounted for by Eq. (5. 18), where only the imaginary parts of the integral terms are used.

In view of the foregoing discussion, the expression for the input impedance to the composite structure is:

$$Z_{in} = \frac{2P}{I^2(0)} = \frac{-1}{I^2(0)} \int_{-h_N}^{h_N} E_t(z) I(z) dz = \frac{-2}{I_1^2(0)} \sum_{\alpha=1}^N \int_{h_{\alpha-1}}^{h_\alpha} E_t(a_\alpha, z) I_\alpha(z) dz .$$

Substituting for the tangential electric field, this expression becomes:

$$Z_{in} = \frac{j\omega\mu_0}{2\pi\beta_0^2 I_1^2(0)} \sum_{\alpha=1}^N (I_{\alpha} + II_{\alpha} + III_{\alpha}) , \quad (5.19)$$

where the following terms must yet be evaluated.

$$I_{\alpha} = I_m \beta_N \int_{h_{\alpha-1}}^{h_{\alpha}} \left( \frac{e^{-j\beta_0 R_{N+}}}{R_{N+}} + \frac{e^{-j\beta_0 R_{N-}}}{R_{N-}} \right) I_{\alpha}(z) dz \quad (5.20 a)$$

$$II_{\alpha} = \sum_{i=1}^N K_i \int_{h_{\alpha-1}}^{h_{\alpha}} \left( \frac{e^{-j\beta_0 R_{(i-1)+}}}{R_{(i-1)+}} + \frac{e^{-j\beta_0 R_{(i-1)-}}}{R_{(i-1)-}} \right) I_{\alpha}(z) dz \quad (5.21 a)$$

$$III_{\alpha} = j \sum_{i=1}^N (\beta_0^2 - \beta_i^2) \int_{h_{\alpha-1}}^{h_{\alpha}} \left\{ \int_{h_{i-1}}^{h_i} I_1(z') [g_+ + g_-] dz' \right\} I_{\alpha}(z) dz . \quad (5.22 a)$$

Consider first the evaluation of the last terms (5.22 a). Since  $I_1(z')$  is an even function of  $z'$ , the following manipulation is allowable.

$$\begin{aligned} \int_{h_{i-1}}^{h_i} I_1(z') [g_+ + g_-] dz' &= \int_{-h_i}^{h_i} I_1(z') \frac{\sin \beta_0 \sqrt{a_{\alpha}^2 + (z-z')^2}}{\sqrt{a_{\alpha}^2 + (z-z')^2}} dz' \\ &- \int_{-h_{i-1}}^{h_{i-1}} I_1(z') \frac{\sin \beta_0 \sqrt{a_{\alpha}^2 + (z-z')^2}}{\sqrt{a_{\alpha}^2 + (z-z')^2}} dz' . \end{aligned} \quad (5.23)$$

The second factor in the integrands may be expanded into a rapidly convergent Fourier cosine series,

$$\frac{\sin \beta_o \sqrt{a_\alpha^2 + (z-z')^2}}{\sqrt{a_\alpha^2 + (z-z')^2}} = \frac{b_o}{2} + \sum_{n=1}^{\infty} b_n \cos [nc(z-z')] ,$$

where  $c = 2\beta_o/m$ ,  $m$  being the lowest odd integer for which  $\beta_o h_N \leq \frac{m\pi}{2}$ . This choice for  $c$  yields coefficients  $b_n$  which diminish rapidly for increasing  $n$ , thereby permitting a convenient partial sum approximation to the infinite series. For the relatively small element radii under consideration, the resulting Fourier coefficients are closely approximated by:

$$b_n = \frac{2\beta_o}{m\pi} \left\{ S_i(n + \frac{m}{2})\pi - S_i(n - \frac{m}{2})\pi \right\}$$

$$\equiv \frac{2\beta_o}{m\pi} C_{mn} \quad ; \quad m \text{ odd, } n=0, 1, 2, \dots$$

Table V indicates that two or three terms in the partial sum represents a useful approximation:

TABLE V: VALUES OF  $C_{mn}$  FOR  $m=3, 5$  AND  $n=0, 1, \dots, 5$ .

$C_{mn}$	$n = 0$	1	2	3	4	5
$m=3$	3.217	2.927	0.208	-0.042	0.018	-0.010
$m=5$	3.112	3.187	2.937	0.203	-0.040	0.017

Expanding the cosine series as:

$$\cos [nc(z-z')] = \cos ncz \cos ncz' + \sin ncz \sin ncz' ,$$

and noting that the odd part integrates to zero over symmetric limits, there is obtained for Eq. (5.23):

$$\sum_{n=0}^{\infty} e_n b_n \cos ncz \left\{ \int_0^{h_1} I_1(z') \cos ncz' dz' - \int_0^{h_{i-1}} I_1(z') \cos ncz' dz' \right\}$$

$$= \sum_{n=0}^{\infty} e_n b_n (K_{\mathbf{I},i} B_{\mathbf{I},n,i} + K_{\mathbf{II},i} B_{\mathbf{II},n,i}) \cos ncz,$$

where

$$e_n = \begin{cases} 1, & n=0 \\ 2, & n \geq 1 \end{cases},$$

$$B_{\mathbf{I},n,i} = \left\{ \frac{\sin[\beta_1(h_1+h_{i-1})+nch_{i-1}] - \sin[2\beta_1 h_1 + nch_1]}{2(\beta_1+nc)} + \frac{\sin[\beta_1(h_1+h_{i-1})-nch_{i-1}] - \sin[2\beta_1 h_1 - nch_1]}{2(\beta_1-nc)} \right\},$$

and

$$B_{\mathbf{II},n,i} = \left\{ \frac{\cos[\beta_1(h_1+h_{i-1})+nch_{i-1}] - \cos[2\beta_1 h_1 + nch_1]}{2(\beta_1+nc)} + \frac{\cos[\beta_1(h_1+h_{i-1})-nch_{i-1}] - \cos[2\beta_1 h_1 - nch_1]}{2(\beta_1-nc)} \right\}.$$

The integration of this last expression against  $I_\alpha(z)$  proceeds similarly, so there is obtained finally for Eq. (5-22 a):

$$\mathbb{III}_\alpha = j \sum_{i=1}^N (\beta_0^2 - \beta_i^2) \sum_{n=0}^{\infty} 2e_n b_n (K_{\mathbf{I},i} B_{\mathbf{I},n,i} + K_{\mathbf{II},i} B_{\mathbf{II},n,i}) \cdot$$

$$\cdot (K_{\mathbf{I},\alpha} B_{\mathbf{I},n,\alpha} + K_{\mathbf{II},\alpha} B_{\mathbf{II},n,\alpha}) \quad (5.22 b)$$

Equation (5. 21 a) is evaluated by first expressing the current  $I_\alpha(z)$  in its exponential form, and then considering the evaluation of four simpler integrals. One obtains:

$$\begin{aligned} \Pi_\alpha &= \sum_{i=1}^N K_i \int_{h_{\alpha-1}}^{h_\alpha} \left( \frac{e^{-j\beta_o R_{(i-1)+}}}{R_{(i-1)+}} + \frac{e^{-j\beta_o R_{(i-1)-}}}{R_{(i-1)-}} \right) \cdot \\ &\cdot \left( K_{\mathbf{I},\alpha} \frac{e^{-j\beta_\alpha(h_\alpha-z)} - e^{-j\beta_\alpha(h_\alpha-z)}}{2j} + K_{\mathbf{II},\alpha} \frac{e^{j\beta_\alpha(h_\alpha-z)} + e^{-j\beta_\alpha(h_\alpha-z)}}{2} \right) dz \\ &= \sum_{i=1}^N \frac{K_i}{2} \left[ jK_{\mathbf{I},\alpha} (\textcircled{1} + \textcircled{2} - \textcircled{3} - \textcircled{4}) + K_{\mathbf{II},\alpha} (\textcircled{1} + \textcircled{2} + \textcircled{3} + \textcircled{4}) \right] \end{aligned} \quad (5. 21 b)$$

where the resulting integrals are given by

$$\begin{aligned} \textcircled{1} &= e^{-j\beta_\alpha h_\alpha} \int_{h_{\alpha-1}}^{h_\alpha} \frac{e^{-j[\beta_o R_{(i-1)+} - \beta_\alpha z]}}{R_{(i-1)+}} dz, \\ \textcircled{2} &= e^{-j\beta_\alpha h_\alpha} \int_{h_{\alpha-1}}^{h_\alpha} \frac{e^{-j[\beta_o R_{(i-1)-} - \beta_\alpha z]}}{R_{(i-1)-}} dz, \\ \textcircled{3} &= e^{j\beta_\alpha h_\alpha} \int_{h_{\alpha-1}}^{h_\alpha} \frac{e^{-j[\beta_o R_{(i-1)+} + \beta_\alpha z]}}{R_{(i-1)+}} dz, \\ \textcircled{4} &= e^{j\beta_\alpha h_\alpha} \int_{h_{\alpha-1}}^{h_\alpha} \frac{e^{-j[\beta_o R_{(i-1)-} + \beta_\alpha z]}}{R_{(i-1)-}} dz. \end{aligned}$$

THE UNIVERSITY OF MICHIGAN  
7848-1-F

By making suitable changes of variable, each integral is reduced to the form

$$\int_{x_{\alpha-1}}^{x_{\alpha}} \frac{e^{-jx} dx}{\sqrt{x^2 + (\beta_{\alpha}^2 - \beta_0^2) a_{\alpha}^2}},$$

which can be evaluated in terms of sine and cosine integrals using various standard approximation techniques. In integral (1), change variables by letting

$$t = \beta_0 R_{(i-1)+} - \beta_{\alpha} (z + h_{i-1}).$$

Then,

$$dt = \frac{\beta_0 (z + h_{i-1}) - \beta_{\alpha} R_{(i-1)+}}{R_{(i-1)+}} dz$$

and

$$\frac{dz}{R_{(i-1)+}} = \frac{dt}{\beta_0 (z + h_{i-1}) - \beta_{\alpha} R_{(i-1)+}} = \frac{-dt}{\sqrt{t^2 + (\beta_{\alpha}^2 - \beta_0^2) a_{\alpha}^2}}.$$

New limits of integration  $t_{\alpha}$  and  $t_{\alpha-1}$  are obtained by letting  $z = h_{\alpha}$  and  $z = h_{\alpha-1}$ , respectively, in the change of variable equation:

$$t_{\alpha} = \beta_0 \sqrt{a_{\alpha}^2 + (h_{\alpha} + h_{i-1})^2} - \beta_{\alpha} (h_{\alpha} + h_{i-1})$$

$$t_{\alpha-1} = \beta_0 \sqrt{a_{\alpha}^2 + (h_{\alpha-1} + h_{i-1})^2} - \beta_{\alpha} (h_{\alpha-1} + h_{i-1}).$$

Thus, integral (1) becomes:

$$(1) = -e^{-j\beta_{\alpha} (h_{\alpha} + h_{i-1})} \int_{t_{\alpha-1}}^{t_{\alpha}} \frac{e^{-jt} dt}{\sqrt{t^2 + (\beta_{\alpha}^2 - \beta_0^2) a_{\alpha}^2}}.$$

The remaining three integrals are transformed in similar fashion. Changes of

variable are made as follows:

$$u = \beta_0 R_{(i-1)-} - \beta_\alpha (z - h_{i-1}),$$

$$v = \beta_0 R_{(i-1)+} + \beta_\alpha (z + h_{i-1}),$$

$$w = \beta_0 R_{(i-1)-} + \beta_\alpha (z - h_{i-1}).$$

The corresponding limits of integration are

$$u_\alpha = \beta_0 \sqrt{a_\alpha^2 + (h_\alpha - h_{i-1})^2} - \beta_\alpha (h_\alpha - h_{i-1}),$$

$$u_{\alpha-1} = \beta_0 \sqrt{a_\alpha^2 + (h_{\alpha-1} - h_{i-1})^2} - \beta_\alpha (h_{\alpha-1} - h_{i-1}),$$

$$v_\alpha = \beta_0 \sqrt{a_\alpha^2 + (h_\alpha + h_{i-1})^2} + \beta_\alpha (h_\alpha + h_{i-1}),$$

$$v_{\alpha-1} = \beta_0 \sqrt{a_\alpha^2 + (h_{\alpha-1} + h_{i-1})^2} + \beta_\alpha (h_{\alpha-1} + h_{i-1}),$$

$$w_\alpha = \beta_0 \sqrt{a_\alpha^2 + (h_\alpha - h_{i-1})^2} + \beta_\alpha (h_\alpha - h_{i-1}),$$

$$w_{\alpha-1} = \beta_0 \sqrt{a_\alpha^2 + (h_{\alpha-1} - h_{i-1})^2} + \beta_\alpha (h_{\alpha-1} - h_{i-1}).$$

Thus, after undergoing the transformations indicated, the remaining integrals become:

$$\textcircled{2} = -e^{-j\beta_\alpha (h_\alpha - h_{i-1})} \int_{u_{\alpha-1}}^{u_\alpha} \frac{e^{-ju} du}{\sqrt{u^2 + (\beta_\alpha^2 - \beta_0^2) a_\alpha^2}},$$

$$\textcircled{3} = e^{j\beta_\alpha(h_\alpha + h_{i-1})} \int_{v_{\alpha-1}}^{v_\alpha} \frac{e^{-jv} dv}{\sqrt{v^2 + (\beta_\alpha^2 - \beta_0^2) a_\alpha^2}},$$

$$\textcircled{4} = e^{j\beta_\alpha(h_\alpha - h_{i-1})} \int_{w_{\alpha-1}}^{w_\alpha} \frac{e^{-jw} dw}{\sqrt{w^2 + (\beta_\alpha^2 - \beta_0^2) a_\alpha^2}}.$$

The integrals involved in Eq. (5-20 a) are evaluated as a special case of those in (5-21 a), where one simply replaces  $h_{i-1}$  by  $h_N$ . Thus (5-20 a) becomes:

$$I_\alpha = \frac{I_m \beta_N}{2} \left[ jK_{\mathbf{I}, \alpha} (\textcircled{1} + \textcircled{2} - \textcircled{3} - \textcircled{4}) + K_{\mathbf{II}, \alpha} (\textcircled{1} + \textcircled{2} + \textcircled{3} + \textcircled{4}) \right].$$

(5.20 b)



VI  
FERRITE MATERIALS

6.1 Introduction

Properties of ferrite and related materials are necessarily of interest in the study of ferrite loading of materials. Included in this chapter is a survey of absorbing materials that have magnetic properties and which could have sufficiently low loss to be useful in the UHF-VHF spectrum. The survey finds that only the MF series of materials of Emerson and Cuming is potentially useful.

Another technique for measuring the dielectric constant of ferrites in the upper VHF range was also explored during the contract period. Indiana General Q-4, an experimental ferrite not yet in production, was tested using this technique and was found to have a dielectric constant of about 4.2.

A technique was also devised, but not tested, for accurately measuring the magnetic Q-factor using a transmission line technique.

6.2 Loading Materials

One of the difficulties in using ferrite materials in antennas is that most ferrites become exceedingly lossy in the UHF range. Some powdered ferrites, such as the EAF-2, can be used up to 600 MHz (Lyon et al, 1966). However, the relative permeability is low. This is a common characteristic of all ferrites: to get low loss at higher UHF, the relative permeability must be small (Lyon et al, 1965).

As was reported earlier (Lyon et al, 1966), Emerson and Cuming Eccosorb CR (a microwave casting resin absorber) turns out to be a fairly good magnetic material in the UHF range. To determine if other microwave absorbing materials would be good magnetic materials in the UHF range, a survey was conducted of all producers listed under "Absorbers, Microwave" on page 11 of the EEM for 1966-67 (Electronic Engineers Master, 1966). Several companies replied to the questionnaire and some of these organizations do produce absorbers that are good magnetic materials in the UHF range.

### 6.2.1 Useful Materials

Emerson and Cuming appears to produce the largest selection of materials that can be used in the UHF range. Their Eccosorb MF series includes six materials that have a "Q" of about 20 and a relative permeability ranging from 1 to 5. The relative dielectric constant ranges from about 2 to 27. These materials have a specific gravity of about 4.0 and are quite strong physically, although brittle.

Stock sizes of these materials are 1, 2 and 3" dia rods that are 12" long and 12"x12" sheets that are 1/2", 1" and 2" thick. The Eccosorb CR mentioned earlier is a casting resin identical to one member of this family, except it can be cast into any desired shape.

### 6.2.2 Possible Useful Materials

Four companies supplied information about microwave absorbers. There is some indication that these products may be good over part of the UHF band, although the useful upper frequency would be near 300 - 500 MHz. However, the data supplied are not sufficient to determine precisely what the upper limit would be.

Custom Components, Inc., produces a type MP2312 Polyiron that has an attenuation of 160 db per inch at 3.3 GHz. More than likely, this material would be too lossy even at the lower UHF band, although there is not enough information to determine this precisely.

Co-Ax Devices Inc., produces a microwave absorber that is recommended for use between 500 - 2000 MHz as an absorber. So possibly, below 500 MHz, this would be a low loss material. Again, however, insufficient information was supplied.

Core-Tronics, Inc., produces several microwave absorbers that, unfortunately, appear to be good absorbers throughout most of the UHF band. These materials would probably be useful only in the VHF band. One company, Magnetic Core Corporation, supplied information on torroid core materials that are useful up to about 250 MHz. However, no information was supplied on materials sold expressly as absorbers.

Three companies, Raytheon Company, Sperry Microwave Electronics Company and Countis Industries, sell microwave ferrite material, but their data

do not include relative permeability or magnetic loss tangent. These materials are intended primarily for use in circulators, phase shifters, isolators, and other microwave ferrite components. Possibly, these materials could be of use as low loss materials at UHF. However, insufficient information is available at this time. These materials may be no better than existing ferrites.

One company, B. F. Goodrich Sponge Products Division, has delayed in forwarding information. Hence the acceptability of their materials cannot be determined.

#### 6.2.3 Non-useful Materials

The following companies replied to the survey, but offered no information on suitable materials: Silk City Industrial Ceramics, Inc., Waveline Inc., Microtech Division of Ovitron Corp., Custom Materials, Inc., and Conductron Corp. The latter company does make UHF ferrites and they were helpful in discussing general characteristics of ferrite materials.

#### 6.2.4 Summary

At the present time, only the Eccosorb MF series produced by Emerson and Cuming is useful over a sizable portion of the UHF spectrum. To cover the higher end of the range, however, very low relative permeabilities would have to be accepted to obtain a "Q" greater than 10. In a conversation at Dayton Ohio in August 1966 with one of the authors, Dr. E. F. Buckley of Emerson and Cuming pointed out that the properties of the MF series of materials could be expected to be within 10 percent of the published values. Consequently, the Eccosorb MF series appears to be a promising line of materials.

### 6.3 Measurement of Dielectric Constant

Two samples of Indiana General Q-4 ferrite were made available for measurement of the dielectric constant of the material. Because of the small size of the material, it was impossible to fit it into the sample holder made for the transmission line technique used for previous ferrite measurements by the Radiation Laboratory.

Until a strip line holder can be made and the material precisely tested, rough checks of the dielectric constant of the material were made by the dielectric sample holder technique described below. This techniques indicates that the relative dielectric constant of Q-4 is about 4.2.

The manufacturer of Q-4 ferrite has indicated (that the average value of the relative permeability in the 200 - 500 MHz range is 4.5, and that the Q is 140 at 200 MHz, 100 at 300 MHz and 80 at 400 MHz. (Venerus, 1967)

### 6.3.1 Measurement Technique

The dielectric constant of Indiana General Q-4 ferrite was measured in a General Radio Type 1690A, Dielectric Sample Holder using the test circuit indicated in Fig. 6-1. The reflection from the dielectric sample holder was noted with the ferrite in place. Then the ferrite was removed and the sample holder adjusted until the same reflection was produced, and both the first and second settings of the micrometer screw of the sample holder were recorded.

Once the micrometer setting is known, the capacitance can be readily determined from the data supplied with the sample holder by General Radio. The difference in the capacitance calculated in this manner is related to the dielectric constant of the material by the formula

$$\Delta C = 0.225 \epsilon_r A/t \quad (6.1)$$

where  $\Delta C$  is the difference in capacitance, in picofarads, for the two micrometer settings,  $\epsilon_r$  is the relative dielectric constant, A is the area of the surface of the dielectric sample in square inches, and t is the thickness of the sample expressed in inches. The possibility of the material under test having a relative permeability other than one does not affect the result. A derivation of the formula is given in Section 6.3.4.

### 6.3.2 Results

The dielectric constant was measured for several frequencies. The results are summarized in Table VI below.

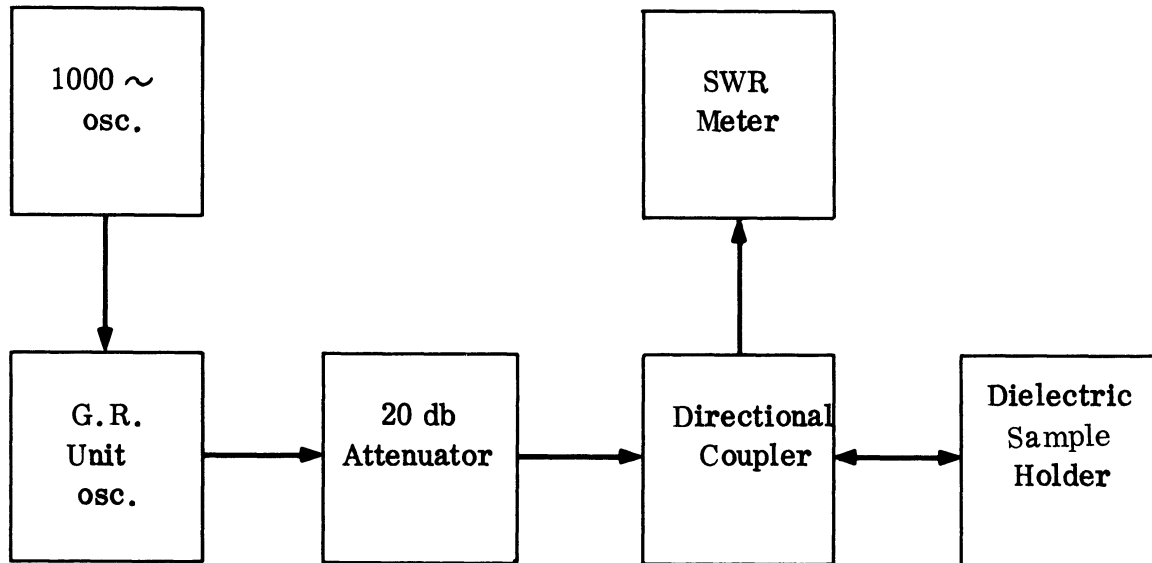


FIG. 6-1: TEST ARRANGEMENT FOR MEASURING THE DIELECTRIC CONSTANT OF INDIANA GENERAL Q-4 FERRITE.

THE UNIVERSITY OF MICHIGAN  
7848-1-F

TABLE VI: VALUES OF RELATIVE DIELECTRIC CONSTANT OF  
INDIANA GENERAL Q-4 FERRITE VS FREQUENCY.

<u>Frequency (MHz)</u>	<u>Dielectric Constant</u>
100	4.18
125	5.03
150	3.07
175	5.91
200	2.94

The use of the dielectric sample holder is not recommended above 100 MHz. The reason is that stray coupling becomes significant and environmental influences (such as the breathing of the person doing the measurements) become intolerable.

Another difficulty encountered with the measurements was that the amount of power reflected was an insensitive function of the micrometer adjustment on the sample holder. Consequently, determining the micrometer setting for the second trial was not precise. This hampered accuracy considerably. An attempt to use a tuner to produce a resonant circuit near resonance was a failure because of the inability to desensitize the circuit to mechanical vibrations in the work area.

One additional attempt at improving accuracy was made, but was unsuccessful. More line was inserted between the direction coupler and the sample holder. However, this just made the insensitivity greater.

### 6.3.3 Conclusions

Since the ferrite should not be very lossy to an electric field in the UHF-VHF range, and since the effect of stray capacitance became more pronounced at higher frequencies, the value of the relative dielectric constant measured at 100 MHz is probably closest to being correct. Thus the dielectric constant of Indiana General Q-4 ferrite material is about 4.2.

### 6.3.4 Theory of Measurement

The measurement procedure is based on the fact that two pure capacitances give the same reflection in a transmission line at the same frequency. Thus, assuming that the material to be measured is lossless and that the power being fed by the

generator is constant, the capacitance of the holder with the sample can be determined by removing the sample and re-adjusting the holder until the same reflection is produced. The second micrometer reading determines the capacitance of the sample holder with the test material inserted. Now the first micrometer reading gives the capacitance of the sample holder if the sample were not in place. Thus, the difference in the capacitance is the capacitance associated with the presence of the material.

This capacitance can be readily calculated since the sample holder is nothing more than a shielded parallel plate capacitance. The formula relating the geometry of a parallel plate capacitance to its capacitance is well known:

$$C = 0.255 \epsilon_r A/t \quad (6.2)$$

where A and t are expressed in inches and C in picofarads. If the sample placed in the holder is a right cylinder, and if the plates of the sample holder are brought in contact with the faces of the sample in the first trial, then the change in capacitance calculated earlier can be related to the dielectric constant by Eq. (6.1).

#### 6.4 Q of Lossy Ferrites

The loss tangent and magnetic Q factor of lossy ferrite materials can be accurately measured by employing a short-circuited coaxial transmission line technique. The short-circuited impedance of a coaxial line is given by

$$Z_{sc} = Z_0 \tan \gamma \ell . \quad (6.3)$$

If the line is loaded by ferrite material in a length  $\ell_f$  (as shown in Fig. 6-2), then Eq. (6.3) is modified to:

$$Z_{sc} = Z_f \tanh \gamma_f \ell_f , \quad (6.4)$$

where

$$Z_f = \sqrt{\frac{\mu}{\epsilon}} Z_0, \quad \gamma_f = \alpha_f + j\beta_f,$$

$\alpha_f$  = attenuation constant in the ferrite,

$\beta_f$  = phase constant in the ferrite.

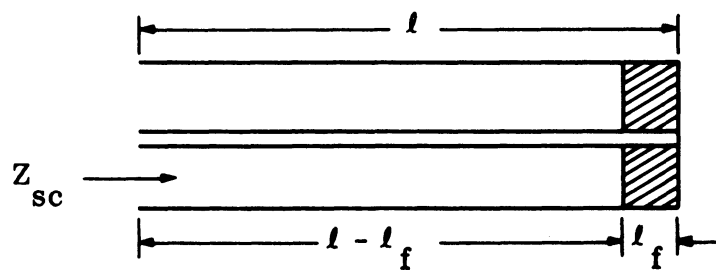


FIG. 6-2: COAXIAL LINE WITH SPECIMEN IN POSITION



Using an impedance bridge, a reference for the shorted air-loaded line is established by employing (6.3) and a Z- $\theta$  chart. When the ferrite specimen is placed in the line, the readings taken by the use of the bridge are transformed through an  $l-l_f$  rotation in the Z- $\theta$  chart, in degrees. This then gives the correct  $Z_{sc}$  for the ferrite material. If the length of the ferrite sample is very small relative to the wavelength ( $l \leq \lambda/70$ ) one can approximate the relation (6.4) by:

$$Z_{sc} \approx \sqrt{\frac{\mu}{\epsilon}} Z_0 \gamma_f l_f \quad (6.5)$$

Also, for ferrites assuming the lossy component of the permittivity constant negligible and writing  $Z_{sc} = R + jX$ , one obtains

$$R + jX = \sqrt{\frac{\mu' - j\mu''}{\epsilon}} Z_0 \gamma_f l_f \quad (6.6)$$

From the above relation by squaring both sides, rearranging terms and then separating real and imaginary components one obtains:

$$\mu' (\alpha_f^2 - \beta_f^2) + \mu'' (2\alpha_f \beta_f) = (r^2 - x^2) \frac{\epsilon}{2} l_f \quad (6.7)$$

and

$$\mu' (2\alpha_f \beta_f) - \mu'' (\alpha_f^2 - \beta_f^2) = (2rx) \frac{\epsilon}{2} l_f \quad (6.8)$$

with  $r = R/Z_0$ , and  $x = X/Z_0$ .

Solving (6.7) and (6.8) for  $\mu'$  and  $\mu''$ , and taking the ratio  $\mu''/\mu'$ , there results:

$$\tan \delta_m = \frac{\mu''}{\mu'} = \frac{\frac{r^2 - x^2}{2rx} - \frac{\alpha_f^2 - \beta_f^2}{2\alpha_f \beta_f}}{1 + \left( \frac{r^2 - x^2}{2rx} \right) \left( \frac{\alpha_f^2 - \beta_f^2}{2\alpha_f \beta_f} \right)} \quad (6.9)$$

Thus the magnetic Q is:

$$Q_m = \frac{1 + \left( \frac{r^2 - x^2}{2rx} \right) \left( \frac{\alpha_f^2 - \beta_f^2}{2\alpha_f \beta_f} \right)}{\frac{r^2 - x^2}{2rx} - \frac{\alpha_f^2 - \beta_f^2}{2\alpha_f \beta_f}} \quad (6.10)$$

where the parameters  $r$ ,  $x$ ,  $\alpha_f$ ,  $\beta_f$  can be experimentally measured.

VII

CONCLUSIONS

Under Task I, the study involving the feasibility of a ferrite loaded conical spiral antenna of reduced size for a given frequency range, several accomplishments have been noted. The usefulness of several techniques of using ferrite as a loading material to reduce the size of the antennas has been explored. Some methods of loading have proved more beneficial than others. A design of such an antenna has been proposed; the predicted performance of this design is within the requirements specified by the Contractor for this task.

Under Task II, a study has been made of arrays utilizing ferrite loaded slot elements. The particular design using a ferrite loaded waveguide with slots of the array cut in the broadside wall of the waveguide was proved impractical for use at frequencies around 300 MHz. This difficulty was due, in a large part, to the lack of low loss ferrite materials at this frequency. A considerable change in viewpoint was taken for the next design. A simple linear array of three ferrite loaded slot elements was utilized. Only the preliminary experimental work has been done so far. This work was sufficient to show that the ferrite loaded slot elements were sufficiently matched in characteristics so as to be useful for an array study. Much of the contemplated purpose of this study including the control of the ferrite loaded elements through magnetic bias remains yet to be done. The accomplishment as described in this report should be considered of a preliminary nature.

The development of a new antenna type of reduced size, the "interdigital array" has been a result of the studies of Task II. This flush mounted antenna will be studied for loading, radiation efficiency, and beam control during the next contract.

Task III has concentrated on studies of ferrite and dielectric rod and tube radiators. It has been found that tube radiators utilizing either ferrite or dielectric are more efficient and have a wider bandwidth than solid rod radiators of the same materials. Detailed comparisons of the mathematical methods used for such an

THE UNIVERSITY OF MICHIGAN  
7848-1-F

antenna have been made. A new mathematical model has been developed. This model predicts more reliably the performance of either the rod or tube radiator. It can be concluded on the basis of the analysis and experimental verification of tube radiators the material having either high permeability or high permittivity or both can be better used if the material is in the form of a hollow tube rather than a solid rod. Some continuance of these studies will be made in the succeeding contract.

Under Task IV, extensive studies have been made of various techniques suitable for constructing antennas of modest size and operable down to a frequency of 30 MHz. The advantages of folding, forming conductor, and loading have been assessed under various conditions. The influence of having multiple segments of an antenna has been studied. A considerable amount of analysis has been made in addition to the experimental effort. Emphasis has been placed upon the tuning to be obtained by various design techniques. A continuance of such studies will be made in the succeeding contract with special emphasis placed upon radiation efficiency of various techniques.

APPENDIX  
A  
GAIN MEASUREMENT BY COMPARISON

In the comparison method of gain measurement the gain of the test antenna can be calculated by the following formula provided the gain of a standard antenna is known:

$$G_t = G_s + C + A_t - A_s + V_t - V_s + L_t - L_s$$

with all terms expressed in db and where:

- C - Polarization mismatch factor
- $G_s$  - Gain of the standard antenna
- $G_t$  - Gain of the test antenna
- $A_t$  - Attenuator setting for the test antenna
- $A_s$  - Attenuator setting for the standard antenna
- $V_t$  - The mismatch loss for the test antenna
- $V_s$  - The mismatch loss for the standard antenna
- $L_t$  - The cable loss for the test antenna
- $L_s$  - The cable loss for the standard antenna

The polarization mismatch factor is obtained by measuring the polarization ratio,  $P$ , in db and converting this to the numerical polarization ratio,  $p$ . Note that  $P$  is always assumed to be a positive logarithm. Furthermore, the gain being measured on the test antenna is assumed to be the maximum gain.

The numerical polarization mismatch factor,  $c$ , is calculated from the numerical polarization ratio,  $r$ , by the formula:

$$c = (p + 1)/p$$

The polarization mismatch factor in db,  $C$ , is calculated from  $c$  and used in the expression for calculating the gain.

Note that the polarization correction factor in db,  $C$ , cannot be greater than 3.01 db (for circular polarization) nor less than 0 db (for linear polarization).

The mismatch loss is calculated by the following formula:

$$V = -10 \log (1 - \Gamma^2)$$

where  $\Gamma$  is the magnitude of the voltage reflection factor.

For the measurements on antenna 232, a dipole was used as the gain standard and it was assumed to be lossless. Thus  $G_t$  was assumed to be 2.16 db. All measurements on the standard dipole and antenna 232 were made with an Anzac H-9 Hybrid that has a specified average insertion loss of 0.5 db. Between the hybrid and antenna 232 were 200 cm of RG-58/U coaxial cable and between the hybrid and the dipole were 128 cm of RG-58/U.

The attenuator settings and reflection coefficients for each antenna at each frequency are given in Table A-1.

TABLE A-1

THE ATTENUATOR SETTINGS AND THE REFLECTION COEFFICIENTS

	170 MHz	196 MHz
Antenna 232 - Vertical Polarization	10 db	12 db
Antenna 232 - Horizontal Polarization	14.5	7.5
Dipole - Horizontal Polarization	34	18
Dipole - Vertical Polarization	33	20
Reflection Coefficient - Antenna 232	0.82	0.70
Reflection Coefficient - Dipole	0.50	0.74

Table A-2 gives the values to be utilized in the gain equation based on the following assumptions:

1) the loss for RG-58/U cable is 6.05 db/100' at 190 MHz and 5.70 db/100' at 170 MHz. This was determined from the data supplied by the Belden wire catalog. (Note that different manufactures claim different attenuations for RG-58/U coaxial cable and there can be a discrepancy of as much as 3 db/100'.)

2) that the reflection coefficient, which was measured at the hybrid with the above stated coaxial cable between the hybrid and the tip of the antennas, is unaltered by losses in this setup (these losses will be taken into account later).

3) the loss in the hybrid is 0.5 db.

The result is that the gain is -4.2 db at 190 MHz and -12.3 db at 170 MHz.

TABLE A-2  
TERMS OF THE GAIN EQUATION

	170 MHz	190 MHz
C	1.3	1.93
$A_t$	14.5	12
$A_s$	34	20
$V_t$	4.84	2.92
$V_s$	1.25	3.44
$L_t$	0.88	0.91
$L_s$	0.74	0.76

When the effects of the cable losses and the hybrid loss on the reflection coefficient are taken into account, the gain at 190 MHz changes to -4.4 db. However, at

170 MHz, correcting the reflection coefficient for the losses produces a value that is slightly greater than unity. Although this is possible in lossy transmission lines, (Stannard, 1967) it is improbable in this case. The more likely explanation is that

1) the losses specified by the manufacturer for the cable and the hybrid are too great and

2) since the true value of the reflection coefficient is very close to one, calculation error plus measurement error produce a corrected value greater than one. The results are summarized in Table A-3.

TABLE A-3  
CORRECTING THE REFLECTION COEFFICIENT  
FOR TRANSMISSION LOSS

	Antenna 232		Dipole	
	170 MHz	190 MHz	170 MHz	190 MHz
Loss	0.88 db	0.91 db	0.74 db	0.76 db
Measured Reflection Coefficient	0.82	0.70	0.50	0.74
Numerical Loss	1.23	1.23	1.19	1.19
Corrected Voltage Reflection Coefficient	1.01	0.86	0.60	0.88
Correction Factor	—	5.85 db	1.94 db	6.48 db

The correction is made by the following formula:

$$\Gamma_T^2 = L^2 \Gamma^2$$

where  $\Gamma_T$  is the true value of the reflection coefficient and L is the numerical value of the loss.

APPENDIX B

DETERMINATION OF COEFFICIENTS AND DERIVATION OF THE  
DETERMINENTAL EQUATION OF THE FERRITE TUBE WAVEGUIDE

The general field components of the hybrid modes are expressed in Eqs. (4.46) to (4.54) in Chapter IV of this report. Both tangential electric and magnetic field components at the boundaries  $\rho=a$  and  $\rho=b$  must be continuous.

At  $\rho=a$ :

$$E_{z1} = E_{z2} : I_n(CW)A_1 = J_n(CV)A_2 + N_n(CV)A_3$$

$$H_{z1} = H_{z2} : I_n(CW)B_1 = J_n(CV)B_2 + N_n(CV)B_3$$

$$E_{\phi 1} = E_{\phi 2} : n \frac{\lambda_o}{\lambda_g} \left[ \frac{I_n(CW)}{CW^2} A_1 + \frac{J_n(CV)}{CV^2} A_2 + \frac{N_n(CV)}{CV^2} A_3 \right]$$

$$= -\eta \left[ \frac{I'_n(CW)}{W} B_1 + \frac{\mu_r J'_n(CV)}{V} B_2 + \frac{\mu_r N'_n(CV)}{V} B_3 \right]$$

$$H_{\phi 1} = H_{\phi 2} : \frac{1}{\eta} \left[ \frac{I'_n(CW)}{W} A_1 + \frac{\epsilon_r J'_n(CV)}{V} A_2 + \frac{\epsilon_r N'_n(CV)}{V} A_3 \right]$$

$$= -n \frac{\lambda_o}{\lambda_g} \left[ \frac{I_n(CW)}{CW^2} B_1 + \frac{J_n(CV)}{CV^2} B_2 + \frac{N_n(CV)}{CV^2} B_3 \right] \quad (B. 1)$$

At  $\rho=b$ :

$$E_{z2} = E_{z3} : K_n(W)A_4 = J_n(V)A_2 + N_n(V)A_3$$

$$H_{z2} = H_{z3} : K_n(W)B_4 = J_n(V)B_2 + N_n(V)B_3$$



$$\begin{aligned}
 E_{\phi 2} = E_{\phi 3} : \quad & n \frac{\lambda_o}{\lambda_g} \left[ \frac{J_n(V)}{V^2} A_2 + \frac{N_n(V)}{V^2} A_3 + \frac{K_n(W)}{W^2} A_4 \right] \\
 & = -\eta \left[ \frac{\mu_r J'_n(V)}{V} B_2 + \frac{\mu_r N'_n(V)}{V} B_3 + \frac{K'_n(W)}{W} B_4 \right] \\
 H_{z2} = H_{z3} : \quad & \frac{1}{\eta} \left[ \frac{\epsilon_r J'_n(V)}{V} A_2 + \frac{\epsilon_r N'_n(V)}{V} A_3 + \frac{K'_n(W)}{W} A_4 \right] \\
 & = -n \frac{\lambda_o}{\lambda_g} \left[ \frac{J_n(V)}{V^2} B_2 + \frac{N_n(V)}{V^2} B_3 + \frac{K_n(W)}{W^2} B_4 \right] . \tag{B. 2}
 \end{aligned}$$

By eliminating  $A_1, B_1, A_4$  and  $B_4$  in (B. 1) and (B. 2) the following four homogeneous equations in the other four constants  $A_2, A_3, B_2$  and  $B_3$  are obtained:

$$\begin{aligned}
 [n\Delta_3 T] A_2 + [nT] A_3 + [C^2 G \Delta_3 (u_r \Delta_1 - \Delta_8)] B_2 + [C^2 G (u_r \Delta_6 - \Delta_8)] B_3 &= 0 \\
 [C^2 F \Delta_3 (\epsilon_r \Delta_1 - \Delta_8)] A_2 + [C^2 F (\epsilon_r \Delta_6 - \Delta_8)] A_3 + [n\Delta_3 T] B_2 + [nT] B_3 &= 0 \\
 [n\Delta_4 T] A_2 + [nT] A_3 + [G \Delta_4 (u_r \Delta_2 - \Delta_5)] B_2 + [G (u_r \Delta_7 - \Delta_5)] B_3 &= 0 \\
 [F \Delta_4 (\epsilon_r \Delta_2 - \Delta_5)] A_2 + [F (\epsilon_r \Delta_7 - \Delta_5)] A_3 + [n\Delta_4 T] B_2 + [nT] B_3 &= 0 , \tag{B. 3}
 \end{aligned}$$

where the  $\Delta$  functions are defined in Eq. (4.56 a) .

If the A's and B's are to correspond to a non-trivial solution the determinant of their coefficients must be zero.

$$\begin{vmatrix}
 n\Delta_3 T & nT & C^2 G \Delta_3 (u_r \Delta_1 - \Delta_8) & C^2 G (u_r \Delta_6 - \Delta_8) \\
 C^2 F \Delta_3 (\epsilon_r \Delta_1 - \Delta_8) & C^2 F (\epsilon_r \Delta_6 - \Delta_8) & n\Delta_3 T & nT \\
 n\Delta_4 T & nT & G \Delta_4 (u_r \Delta_2 - \Delta_5) & G (u_r \Delta_7 - \Delta_5) \\
 F \Delta_4 (\epsilon_r \Delta_2 - \Delta_5) & F (\epsilon_r \Delta_7 - \Delta_5) & n\Delta_4 T & nT
 \end{vmatrix} = 0 . \tag{B. 4}$$

By expanding and rearranging the terms, (B. 4) yields the form of (4. 56). The relations among the A's and B's can be found from (B. 1), (B. 2) and (B. 4). These constants can be expressed conveniently in terms of  $A_2$  using the following relations:

$$A_1 = \frac{J_n(CV)}{I_n(CW)} A_2 + \frac{N_n(CV)}{I_n(CW)} A_3$$

$$B_1 = \frac{J_n(CV)}{I_n(CW)} B_2 + \frac{N_n(CV)}{I_n(CW)} B_3$$

$$A_4 = \frac{J_n(V)}{K_n(W)} A_2 + \frac{N_n(V)}{K_n(W)} A_3$$

$$B_4 = \frac{J_n(V)}{K_n(W)} B_2 + \frac{N_n(V)}{K_n(W)} B_3 \quad , \quad (B. 5)$$

and

$$A_3 = -\frac{A_2}{D} \begin{vmatrix} n\Delta_3 T & C^2 G \Delta_3 (u_r \Delta_1 - \Delta_8) & C^2 G (u_r \Delta_6 - \Delta_8) \\ C^2 F \Delta_3 (\epsilon_r \Delta_1 - \Delta_8) & n\Delta_3 T & nT \\ n\Delta_4 T & G \Delta_4 (u_r \Delta_2 - \Delta_5) & G (u_r \Delta_7 - \Delta_5) \end{vmatrix}$$

$$B_2 = -\frac{A_2}{D} \begin{vmatrix} nT & n\Delta_3 T & C^2 G (u_r \Delta_6 - \Delta_8) \\ C^2 F (\epsilon_r \Delta_6 - \Delta_8) & C^2 F \Delta_3 (\epsilon_r \Delta_1 - \Delta_8) & nT \\ nT & n\Delta_4 T & G (u_r \Delta_7 - \Delta_5) \end{vmatrix}$$

$$B_3 = -\frac{A_2}{D} \begin{vmatrix} nT & C^2 G \Delta_3 (u_{r1} \Delta_1 - \Delta_8) & n \Delta_3 T \\ C^2 F (\epsilon_{r6} \Delta_6 - \Delta_8) & n \Delta_3 T & C^2 F \Delta_3 (\epsilon_{r1} \Delta_1 - \Delta_8) \\ nT & G \Delta_4 (u_{r2} \Delta_2 - \Delta_5) & n \Delta_4 T \end{vmatrix} \quad (B.6)$$

where

$$D = \begin{vmatrix} nT & C^2 G \Delta_3 (u_{r1} \Delta_1 - \Delta_8) & C^2 G (u_{r6} \Delta_6 - \Delta_8) \\ C^2 F (\epsilon_{r6} \Delta_6 - \Delta_8) & n \Delta_3 T & nT \\ nT & G \Delta_4 (u_{r2} \Delta_2 - \Delta_5) & G (u_{r7} \Delta_7 - \Delta_5) \end{vmatrix} \quad (B.7)$$

APPENDIX C

DESIGN CURVES FOR A HELICAL SLOW WAVE STRUCTURE

In designing a small diameter helix to function as a linear slow wave structure, it is essential to know the dependence of the phase velocity reduction factor ( $\lambda_g/\lambda$ ) upon the helix pitch angle ( $\psi$ ). This information may be obtained from the solution of the characteristic equation for a sheath model of a helical transmission line. The characteristic equation for an arbitrary isotropic material loading in the helix core was derived by Li (1958) in his doctoral thesis. For a small diameter helix, the characteristic equation is

$$2 (ka)^2 \left\{ \ln \left( \frac{2}{ka} \right) - \gamma \right\} \left[ \frac{2 + \mu_r (ka)^2 \left\{ \ln(2/ka) - \gamma \right\}}{2 + \epsilon_r (ka)^2 \left\{ \ln(2/ka) - \gamma \right\}} \right] = \mu_r (\beta_0 a)^2 \cot^2 \psi$$

where  $k^2 = \beta^2 - \beta_0^2$ ,  $\beta$  is the wave number in the longitudinal direction,  $\beta_0$  is the free space wave number, "a" is the radius of the helix,  $\psi$  is the pitch angle of the sheath winding, and  $\gamma$  is Eulers constant (0.5772157).

A computer program was written for the IBM 7090 computer at the University of Michigan Computing Center in Fortran II that would solve the characteristic equation and plot the required pitch angle ( $\psi$ ) vs  $\beta_0 a$  for a family of specified phase velocity reduction factors. With the slight modifications that are indicated by comment cards, the main program may be used on any computer system compatible with Fortran II. The subroutine that does

the plotting, however, calls on many local subroutines to use the IBM 763/789 plotter and is not compatible with other systems. Nevertheless, both the main program and the subroutine are included in the event that they may be useful to others wishing to solve the characteristic equation for other ferrites.

Solutions to the characteristic equation for a number of different core loadings are graphed in Figs. C-1 through C-9. The loadings are characterized by the relative permittivity ( $\epsilon_r$ ) and permeability ( $\mu_r$ ) of the core material. The materials which the  $\epsilon_r$  and  $\mu_r$  represent are stated in parentheses. While various engineering implications relating to the core material are discussed in Section 5.2.4, a few mathematical observations will be stated here. Li pointed out that little phase velocity reduction beyond that of an air core ( $\epsilon_r = \mu_r = 1$ ) is obtained with just dielectric loading of small diameter helices. This is illustrated in Figs. C-1 through C-4, where the relatively minor effect of increasing just  $\epsilon_r$  is seen to be more prominent for larger values of  $2\pi a/\lambda$  and smaller values of  $\lambda_g/\lambda$ . On the other hand, the utilization of ferrite loading to increase  $\mu_r$  results in a substantial phase velocity reduction for a specified helix pitch angle. The effect is illustrated in Figs. C-5a, b through C-9a, b, where two scales have been used to facilitate accuracy.

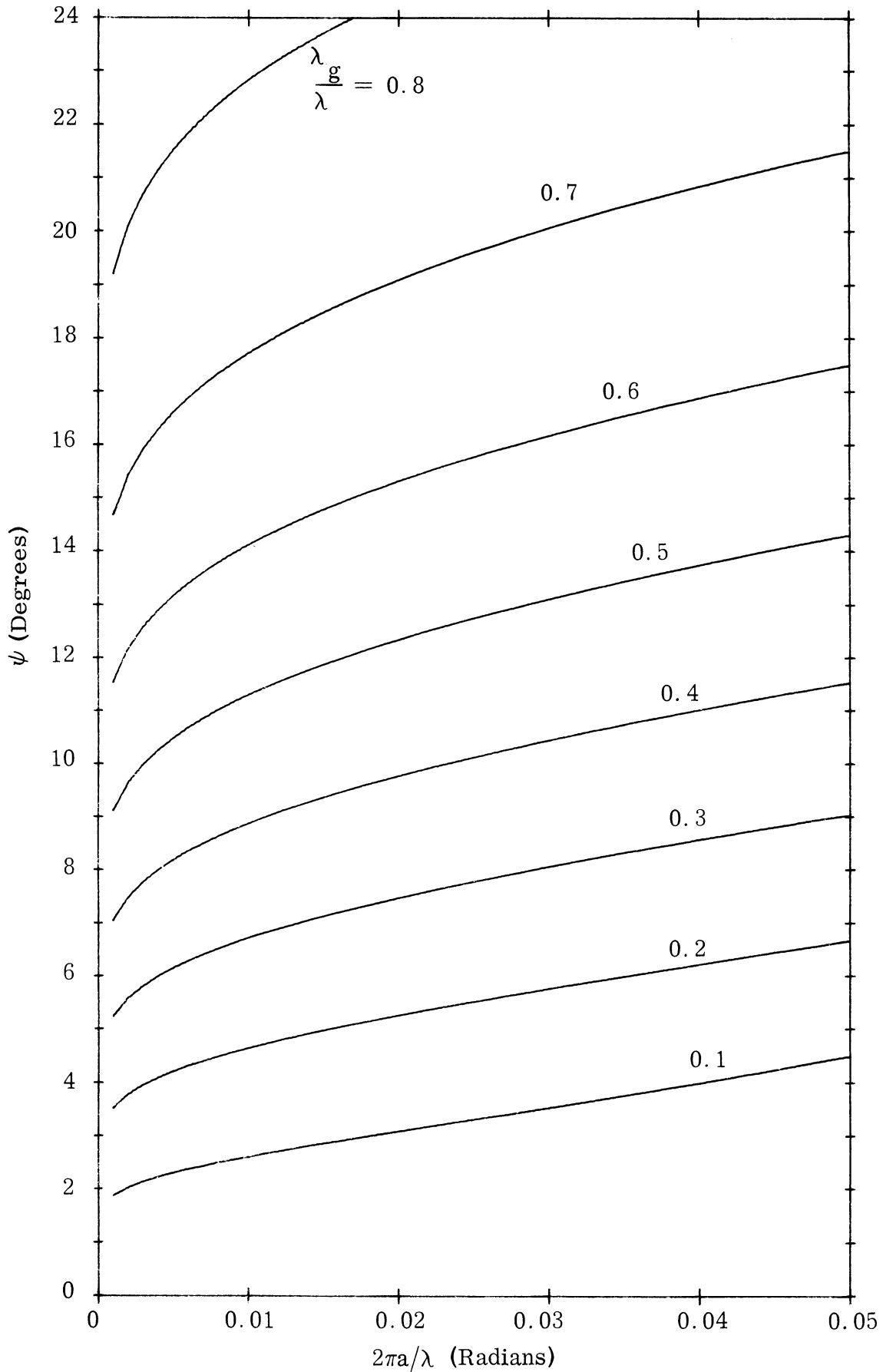


FIG. C-1: SOLUTION OF THE CHARACTERISTIC EQUATION FOR HELIX HAVING CORE PARAMETERS  $\epsilon_r = 1.00$ ,  $\mu_r = 1.00$ ; (Air).

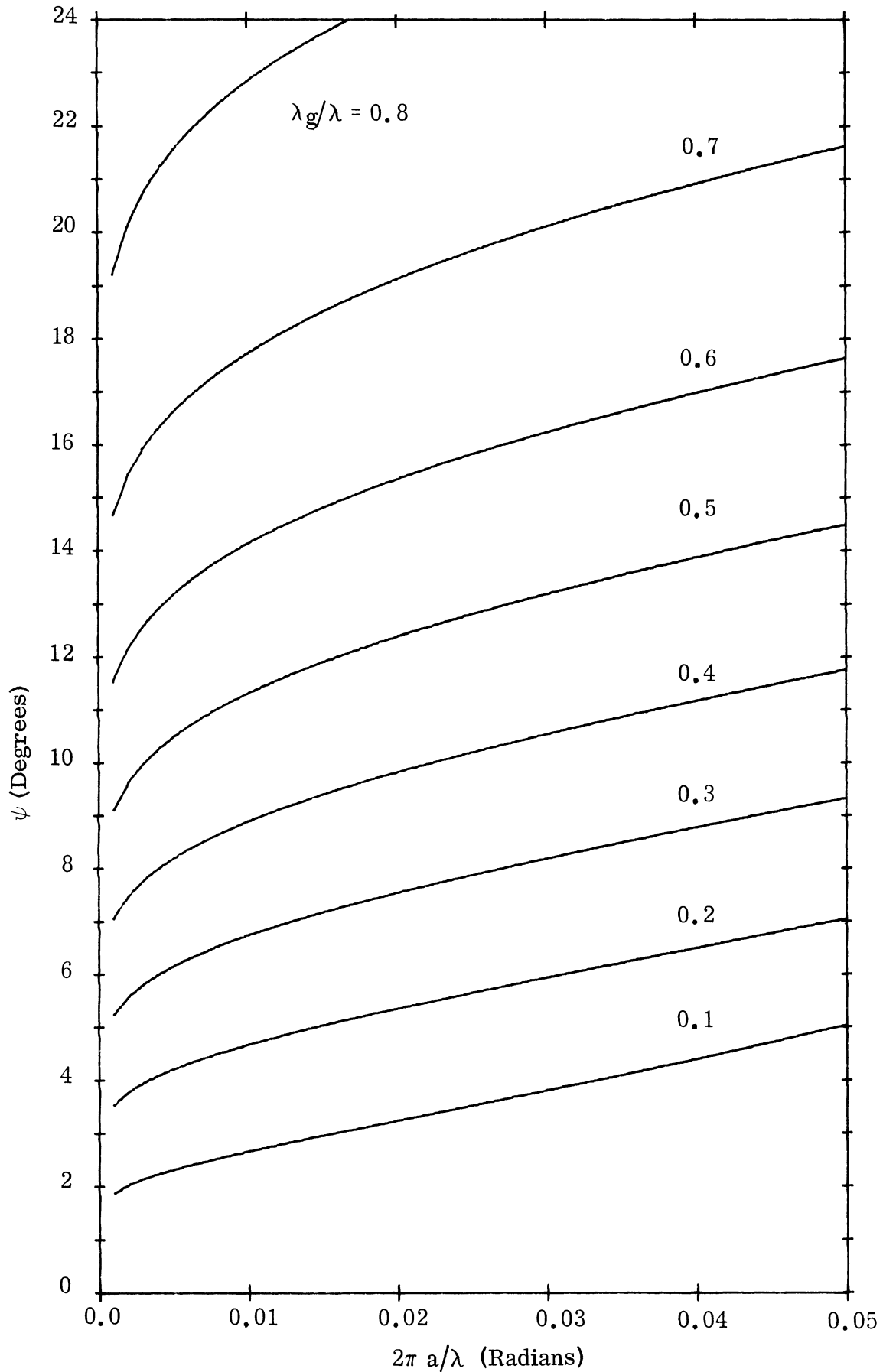


FIG. C-2: SOLUTION OF THE CHARACTERISTIC EQUATION FOR HELIX HAVING CORE PARAMETERS  $\epsilon_r = 3.77$ ,  $\mu_r = 1.00$ ; (EAF-2 Powder Ferrite Biased into Saturation).

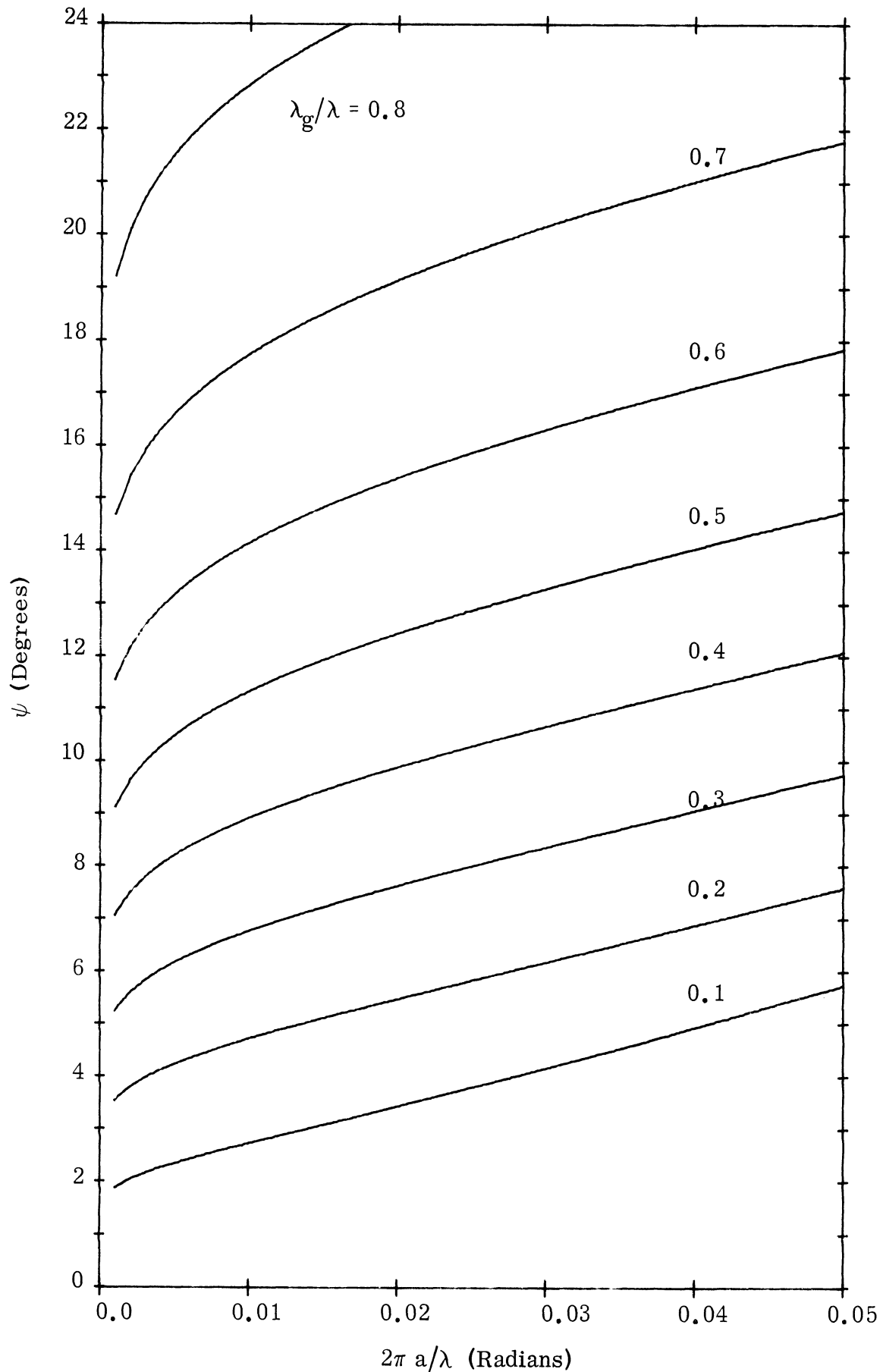


FIG. C-3: SOLUTION OF THE CHARACTERISTIC EQUATION FOR HELIX HAVING CORE PARAMETERS  $\epsilon_r = 7.88$ ,  $\mu_r = 1.00$ ; (Q-3 Ferrite at 150 MHz Biased into Saturation).



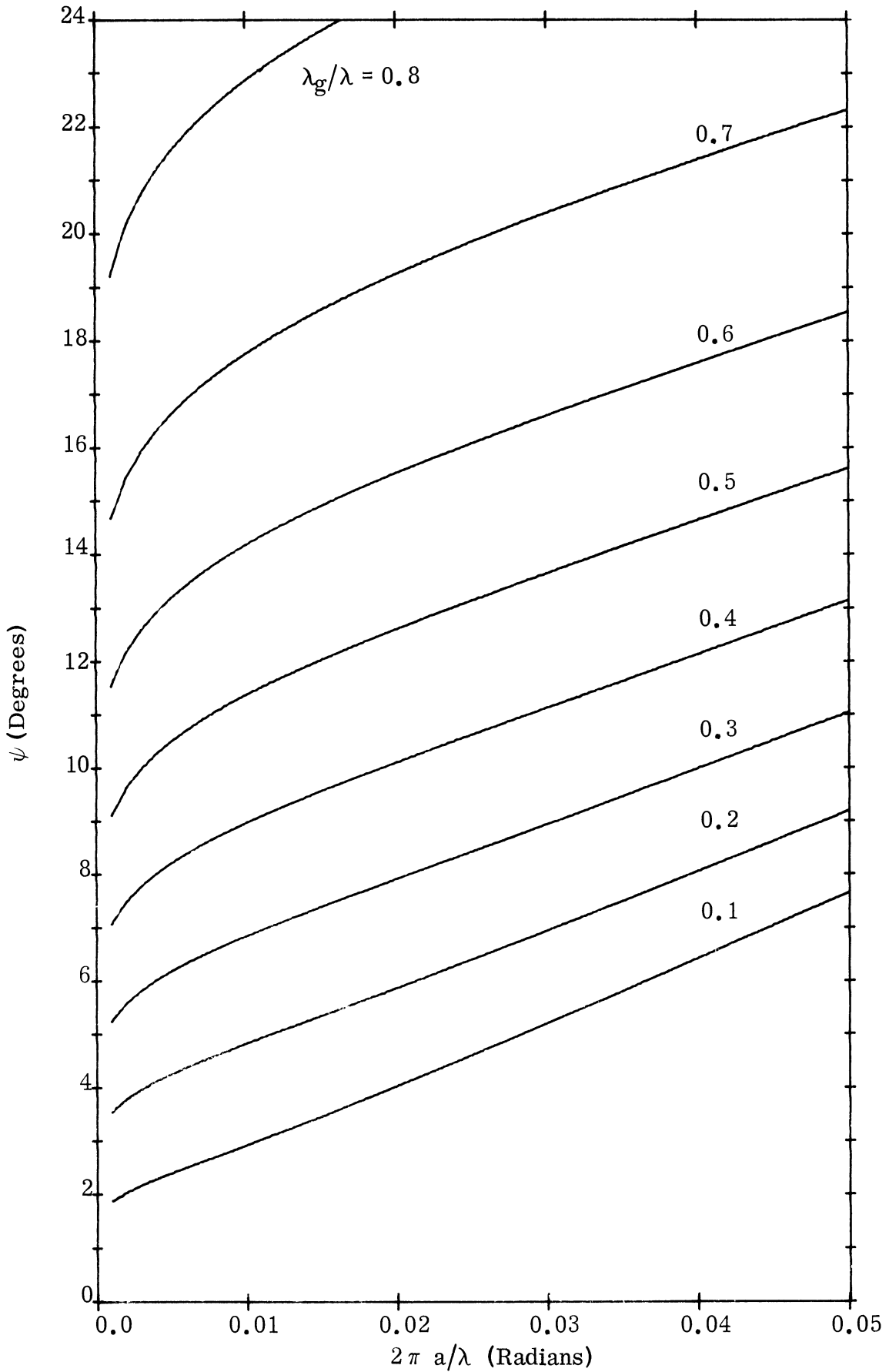


FIG. C-4: SOLUTION OF THE CHARACTERISTIC EQUATION FOR HELIX HAVING CORE PARAMETERS  $\epsilon_r = 22.0$ ,  $\mu_r = 1.00$ ; (Eccosorb CR at 300 MHz Biased into Saturation).

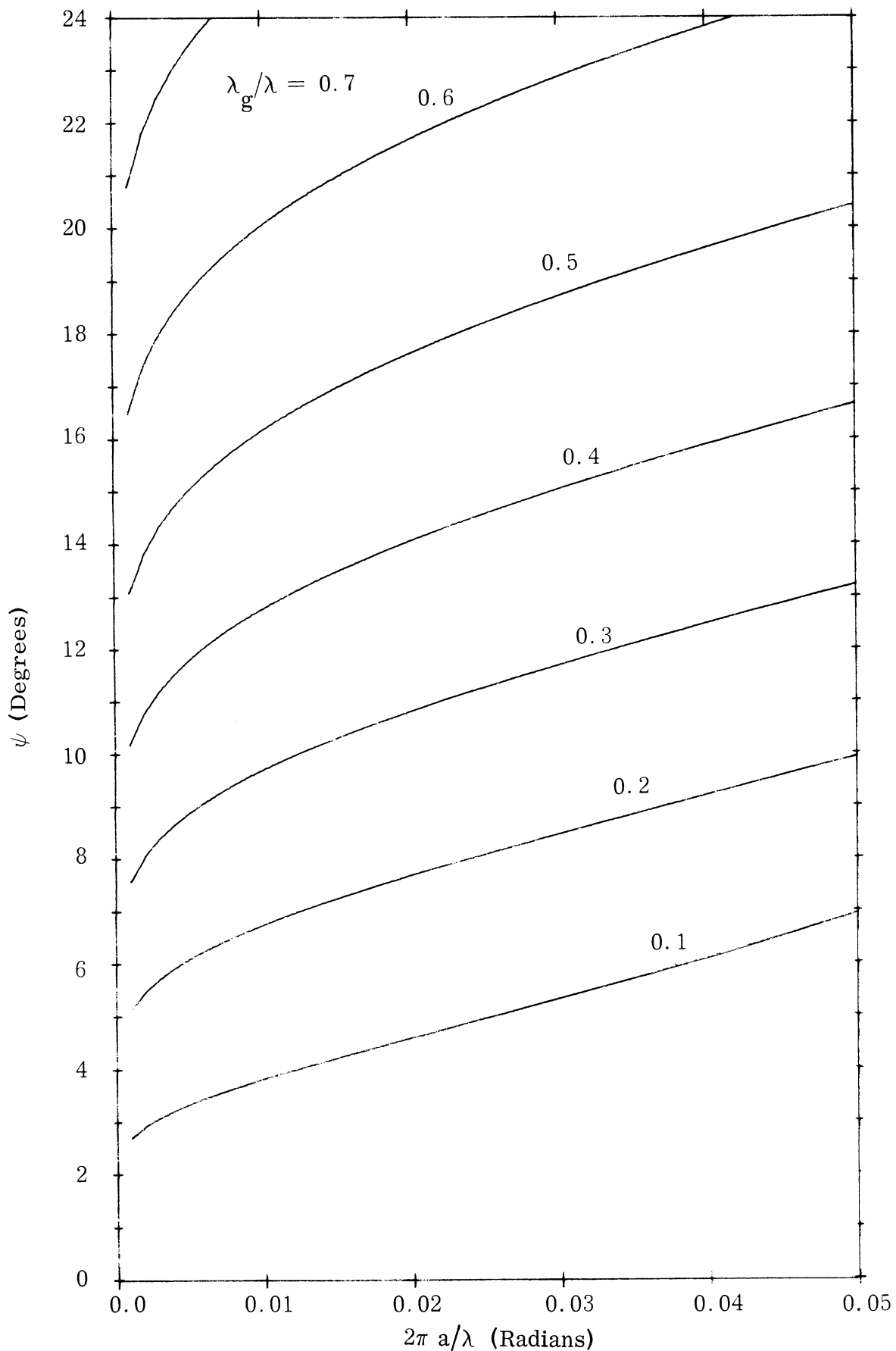


FIG. C-5a: SOLUTION OF THE CHARACTERISTIC EQUATION FOR HELIX HAVING CORE PARAMETERS  $\epsilon_r = 3.77$ ,  $\mu_r = 2.10$ ; (EAF-2 Powder Ferrite).

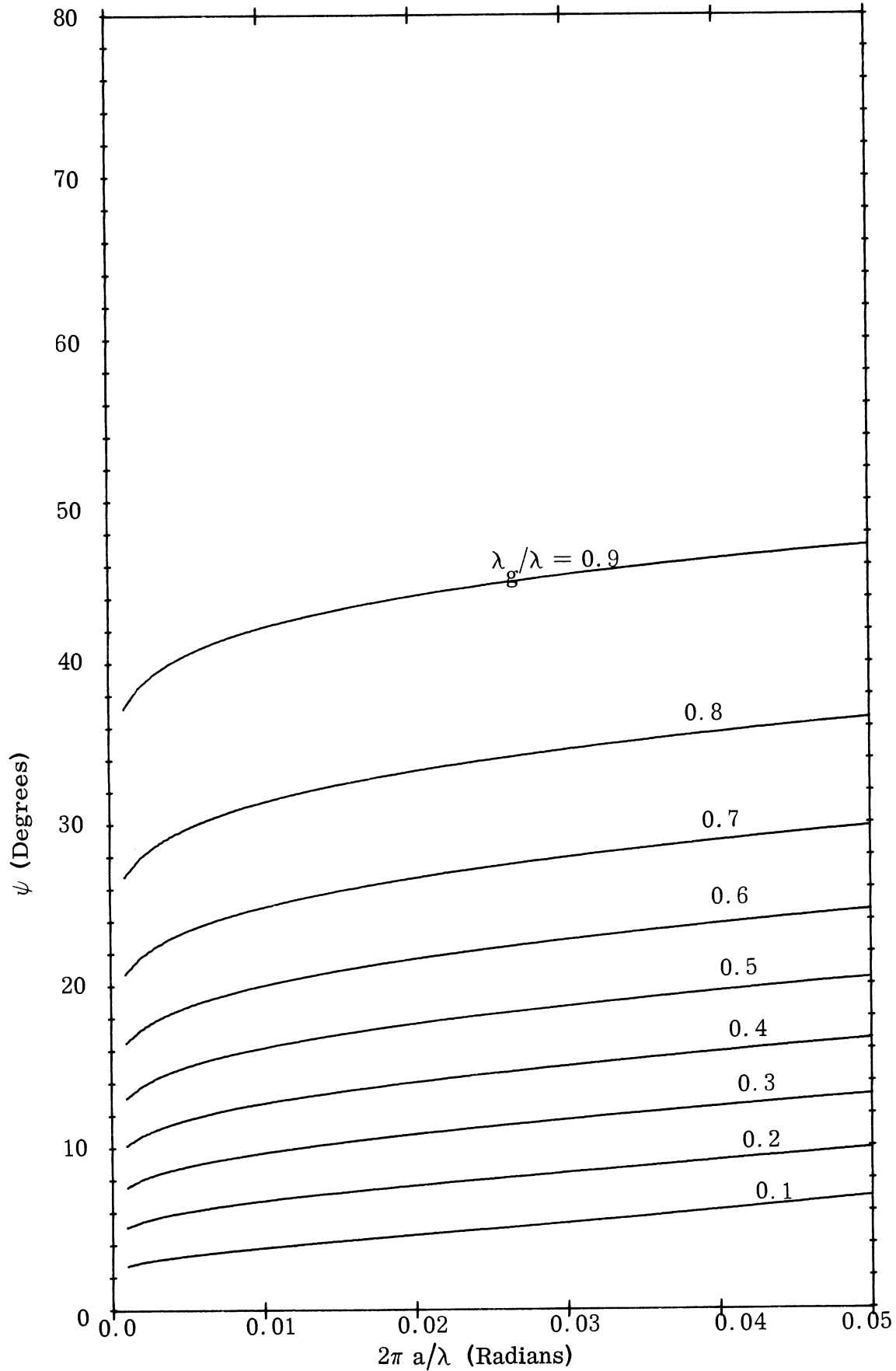


FIG. C-5b: SOLUTION OF THE CHARACTERISTIC EQUATION FOR HELIX HAVING CORE PARAMETERS  $\epsilon_r = 3.77$ ,  $\mu_r = 2.10$ ; (EAF-2 Powder Ferrite).

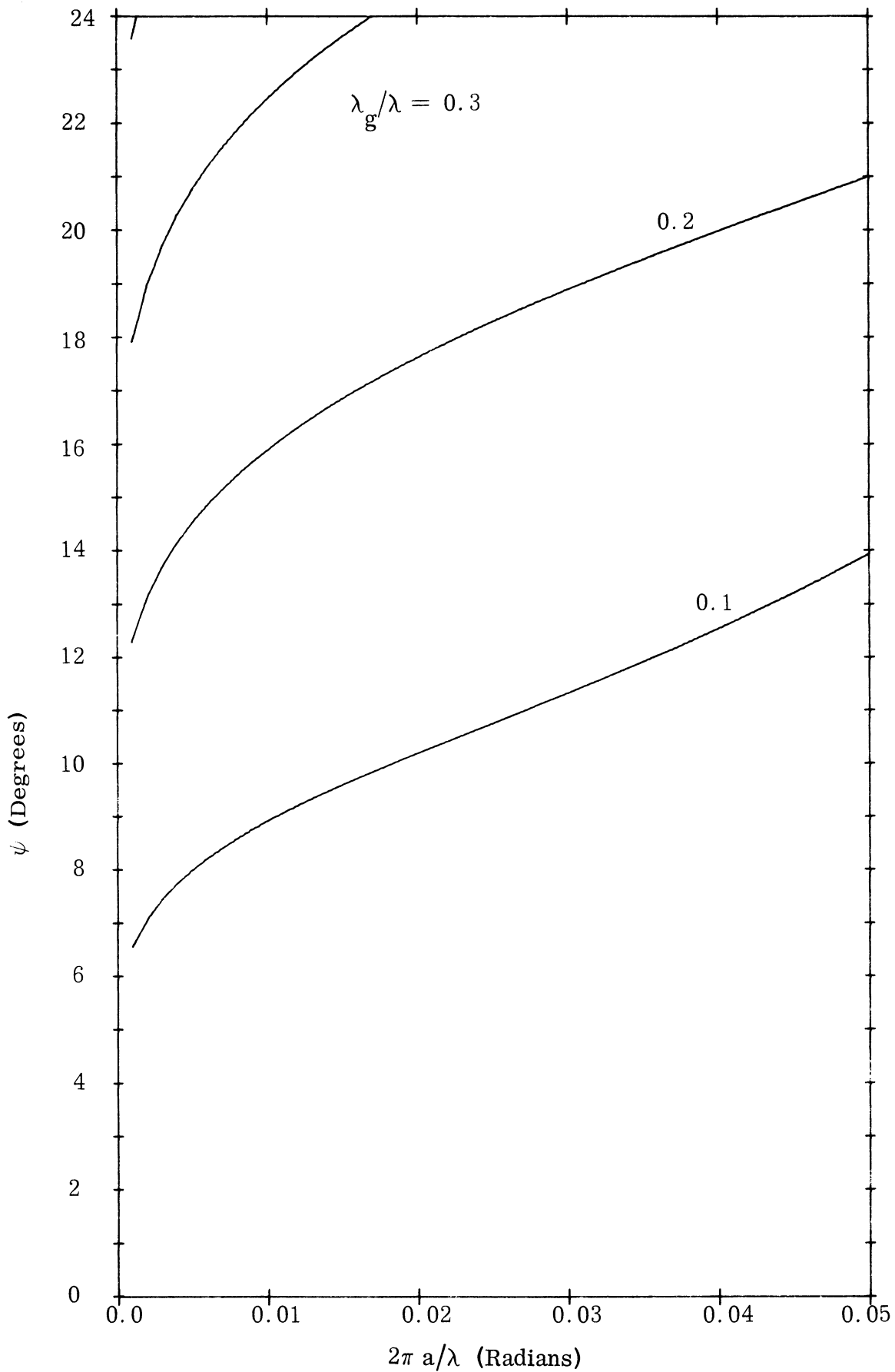


FIG. C-6a: SOLUTION OF THE CHARACTERISTIC EQUATION FOR HELIX HAVING CORE PARAMETERS  $\epsilon_r = 7.96$ ,  $\mu_r = 12.4$ ; (Q-3 Ferrite at 100 MHz).

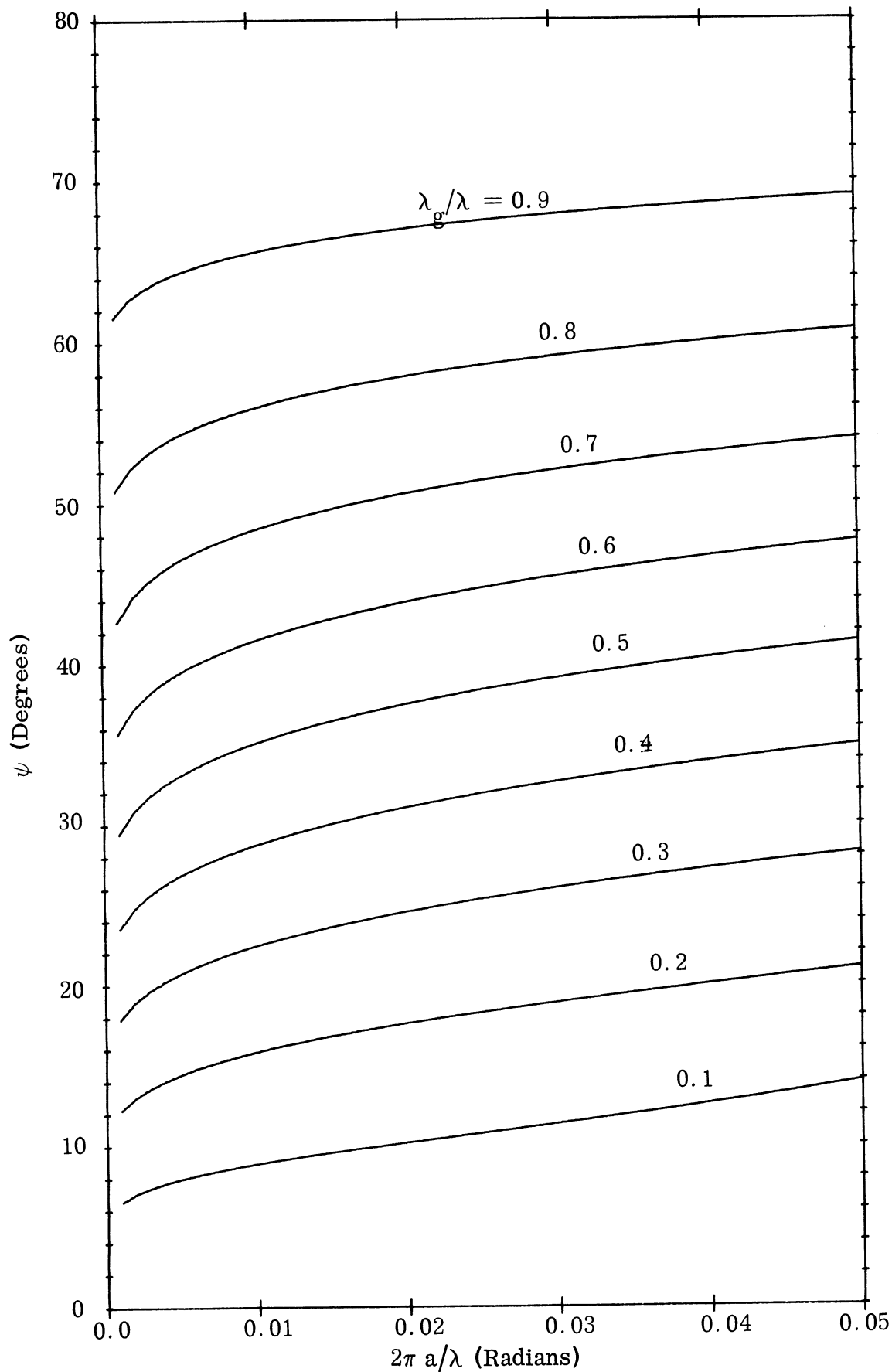


FIG. C-6b: SOLUTION OF THE CHARACTERISTIC EQUATION FOR HELIX HAVING CORE PARAMETERS  $\epsilon_r = 7.96$ ,  $\mu_r = 12.4$ ; (Q-3 Ferrite at 100 MHz).

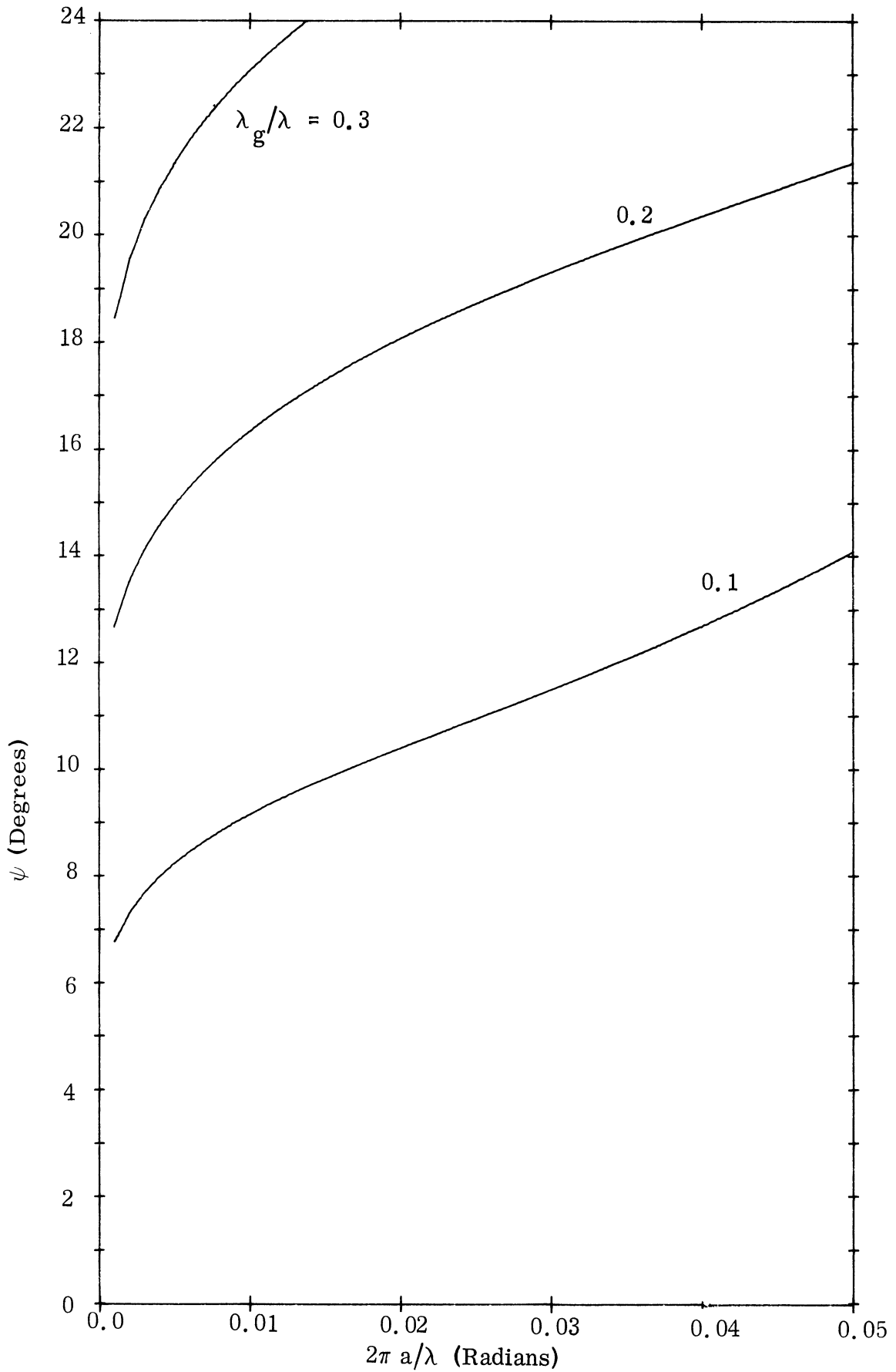


FIG. C-7a: SOLUTION OF THE CHARACTERISTIC EQUATION FOR HELIX HAVING CORE PARAMETERS  $\epsilon_r = 7.88$ ,  $\mu_r = 13.2$ ; (Q-3 Ferrite at 150 MHz).

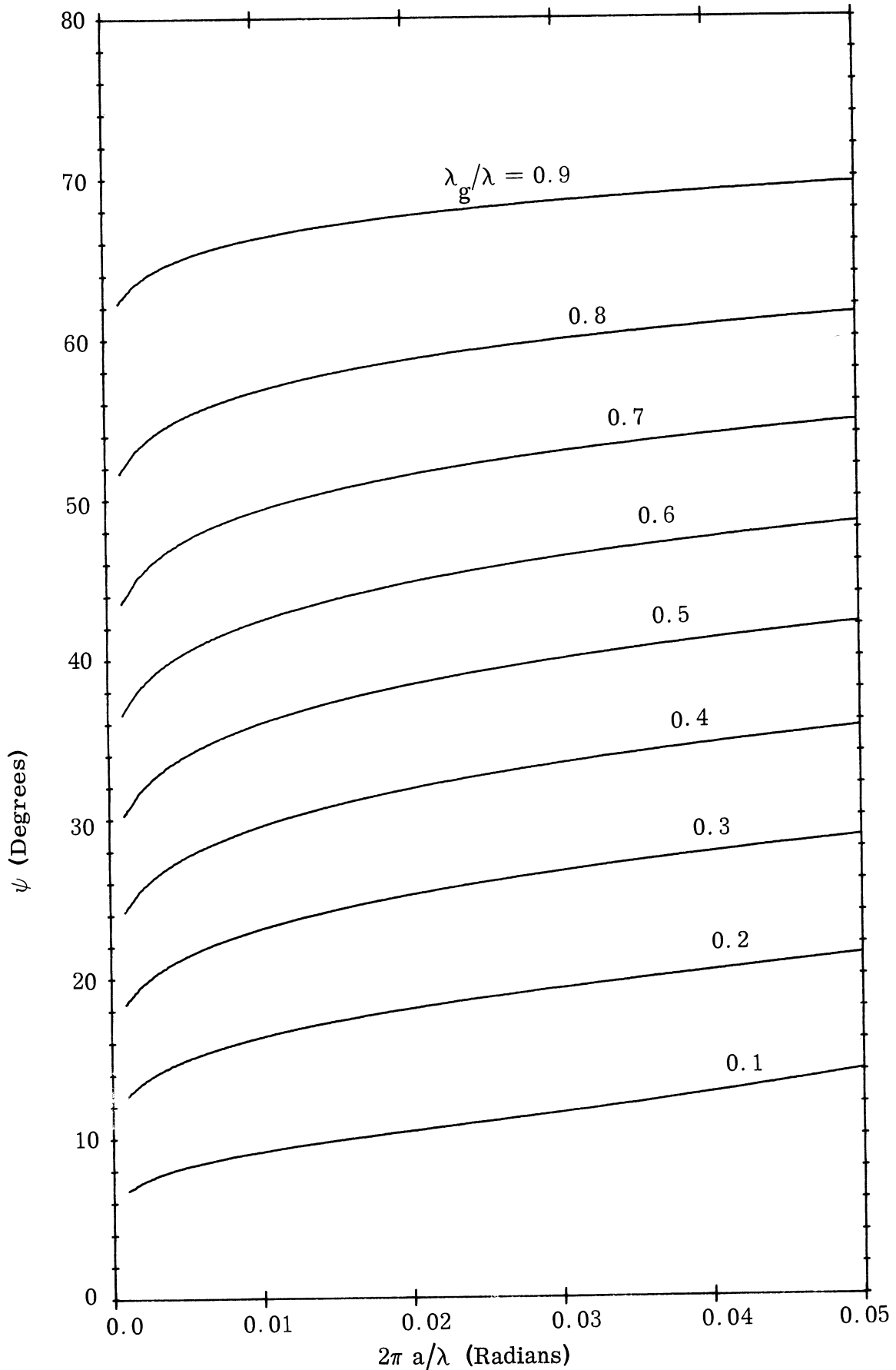


FIG. C-7b: SOLUTION OF THE CHARACTERISTIC EQUATION FOR HELIX HAVING CORE PARAMETERS  $\epsilon_r = 7.88$ ,  $\mu_r = 13.2$ ; (Q-3 Ferrite at 150 MHz).

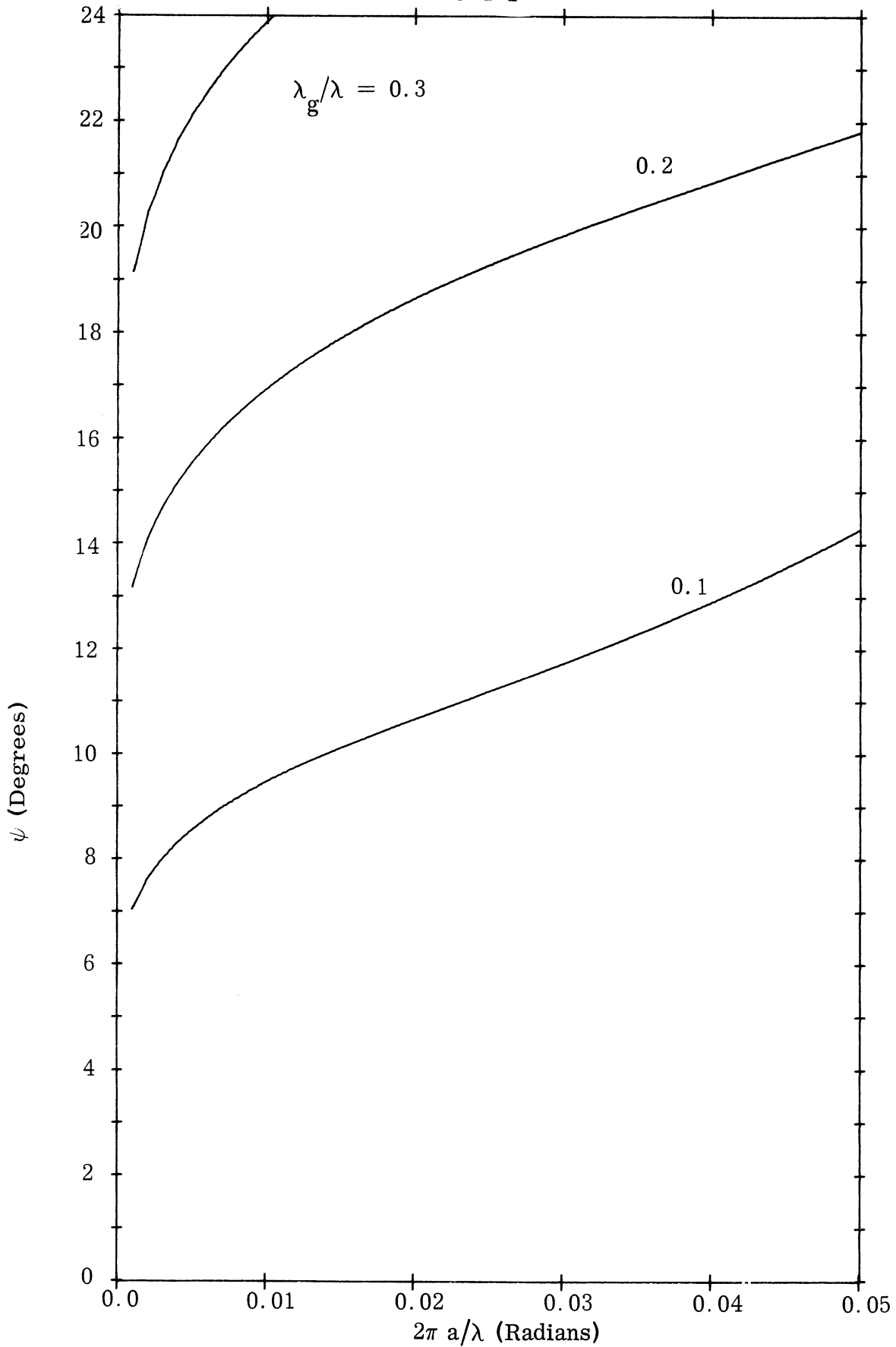


FIG. C-8a: SOLUTION OF THE CHARACTERISTIC EQUATION FOR HELIX HAVING CORE PARAMETERS  $\epsilon_r = 7.81$ ,  $\mu_r = 14.3$ ; (Q-3 Ferrite at 200 MHz).



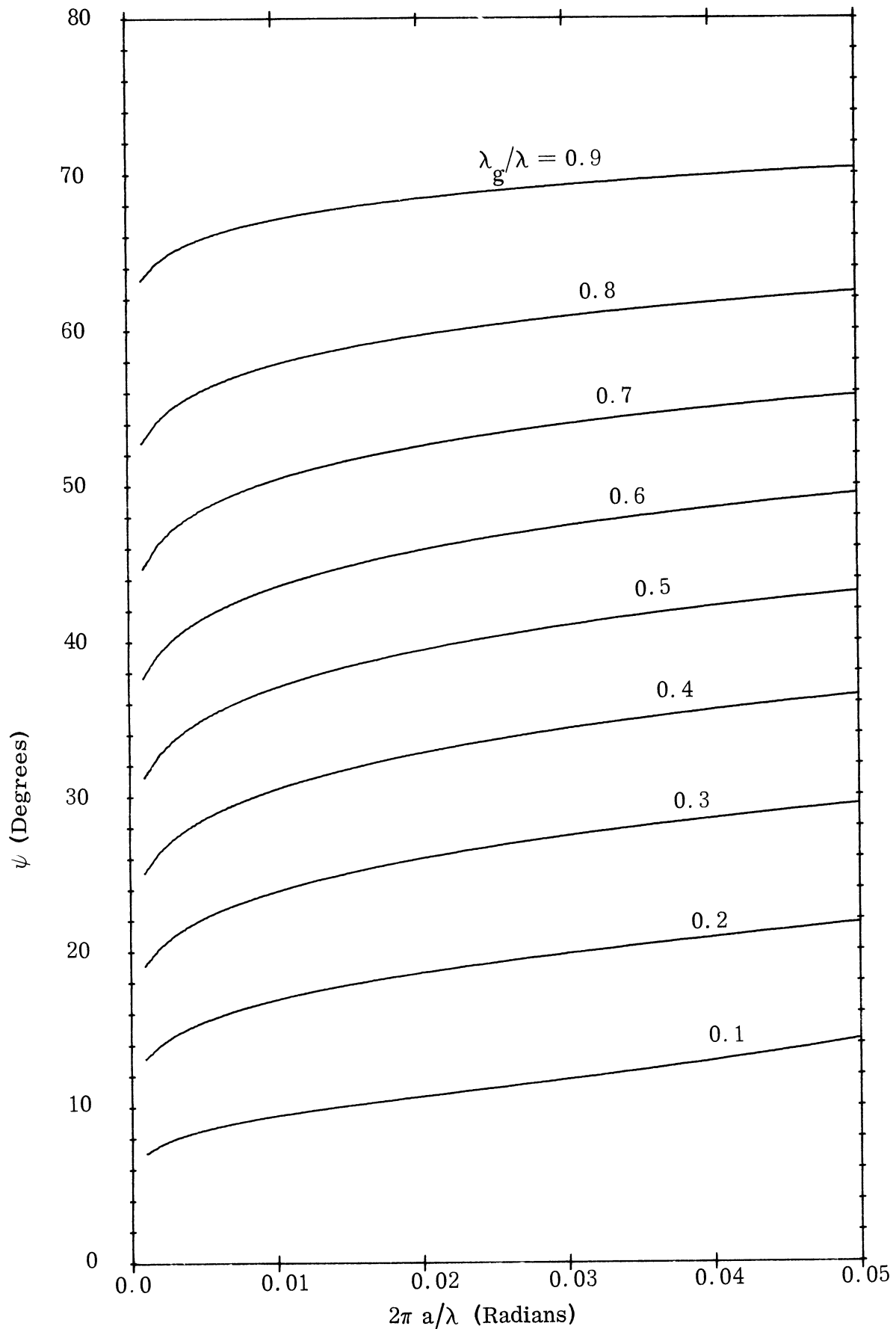


FIG. C-8b: SOLUTION OF THE CHARACTERISTIC EQUATION FOR HELIX HAVING CORE PARAMETERS  $\epsilon_r = 7.81$ ,  $\mu_r = 14.3$ ; (Q-3 Ferrite at 200 MHz).

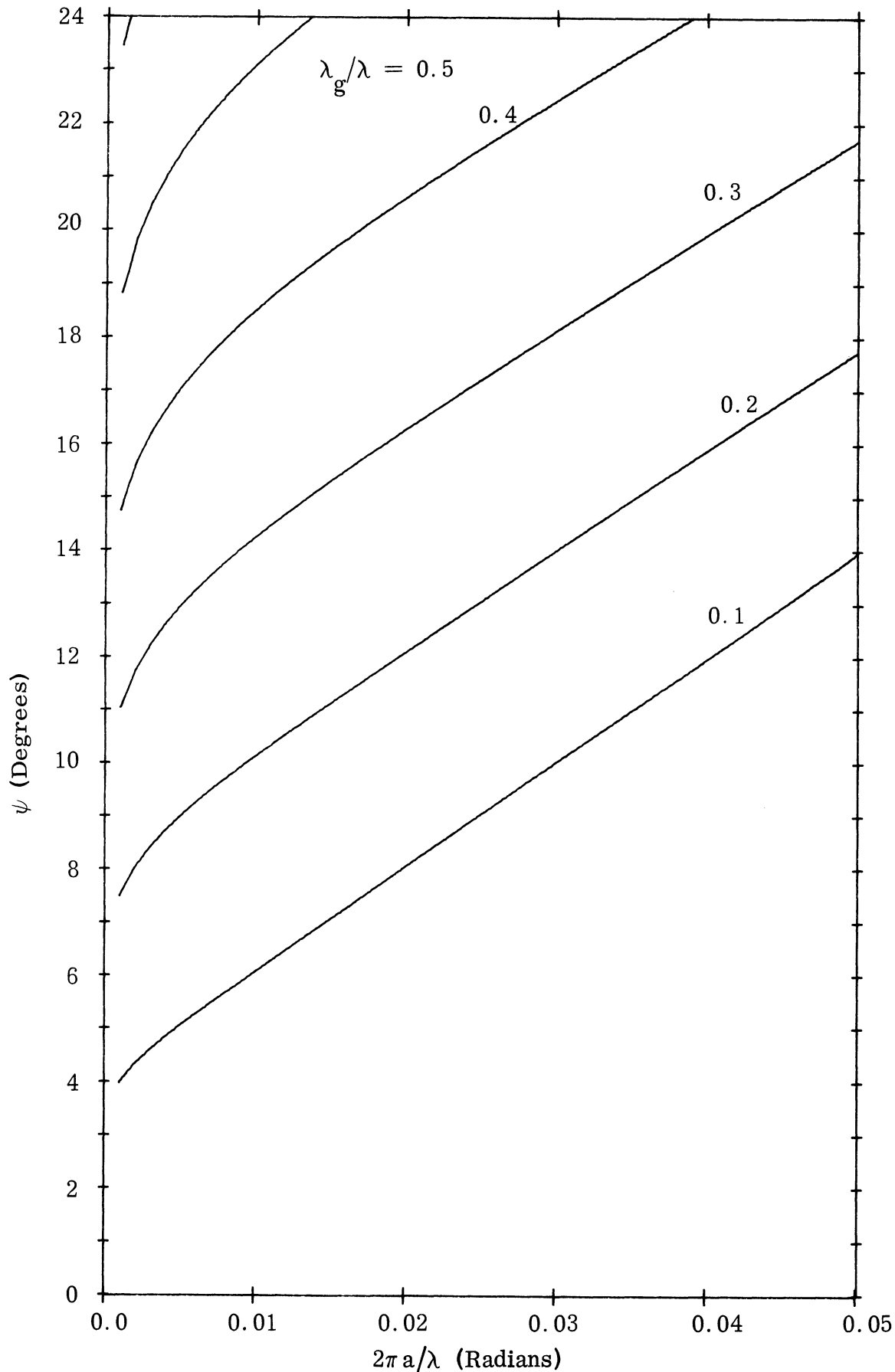


FIG. C-9a: SOLUTION OF THE CHARACTERISTIC EQUATION FOR HELIX HAVING CORE PARAMETERS  $\epsilon_r = 22.0$ ,  $\mu_r = 4.51$ ; (Eccosorb CR at 300 MHz).

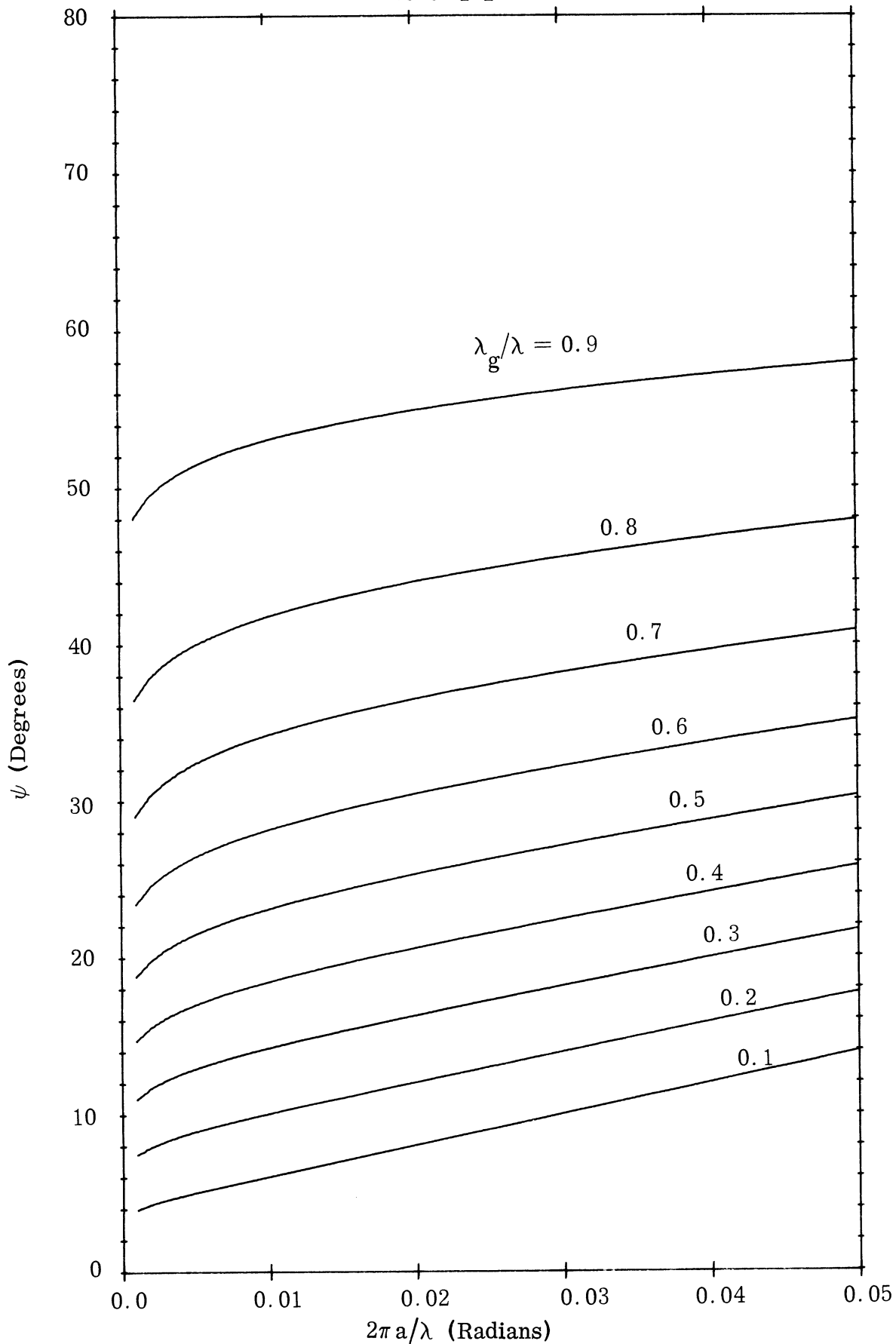


FIG. C-9b: SOLUTION OF THE CHARACTERISTIC EQUATION FOR HELIX HAVING CORE PARAMETERS  $\epsilon_r = 22.0$ ,  $\mu_r = 4.51$ ; (Eccosorb CR at 300 MHz).

```

C      DIMENSION PSI(450), X(450)
C      TAPE 7 IS THE INPUT TAPE, AND TAPE 6 THE OUTPUT TAPE OF THE UNIVERSITY OF
C      MICHIGAN SYSTEM
C
C      READ INPUT TAPE 7,20, RELMU, RELEPS
C      FORMAT (2E10.0)
C      WRITE OUTPUT TAPE 6,22,RELMU,RELEPS
C      FORMAT(32H1THE RELATIVE MU AND EPSILON ARE 1P2E20.8,
1 // 52H R, BETA(0)*A AND PSI ARE PRINTED OUT IN THAT ORDER.)
C      I=1
C      J=1
C      R=0.1
C      B0A=0.001
C      WRITE OUTPUT TAPE 6,46
C      FORMAT(/)
C      BA=B0A/R
C      XKAE2= (BA**2)-(B0A**2)
C
C      SORT IS A LOCAL FUNCTION FOR CALCULATING THE SQUARE ROOT.
C
C      XKA=SQRT(XKAE2)
C
C      ELOG IS A LOCAL FUNCTION FOR CALCULATING THE NATURAL LOGRITHM.
C

```

25 LINES PRINTED

```

80 BRACK=ELUG(2.0/XKA)
90 BRACK=BRACK-0.5772157
100 CT2PSI=(2.0*XKAE2*BRACK*(2.0+(RELMU*XKAE2*BRACK)))/(RELMU*(BOA**2)
110 1*(2.0+(RELEPS*XKAE2*BRACK)))
120 COTPSI=SQRT(CT2PSI)
130 C ATAN IS A LOCAL FUNCTION FOR CALCULATING THE ARCTANGENT.
140 C THE RETURN OF ATAN IS IN RADIANS , STATEMENT 130 CONVERTS THIS TO DEGREES.
150 C
160 PSI(I)=ATAN(1.0/COTPSI)
170 PSI(I)=PSI(I)/(1.745329E-2)
180 X(I)=BOA
190 IF (J-5) 153,140,140
200 WRITE OUTPUT TAPE 6, 150,R,BOA, PSI(I)
210 FORMAT (1P3E20.8)
220 J=0
230 J=J+1
240 I=I+1
250 BOA=BOA+0.001
260 IF (BOA-0.05) 50,50,180
270 R=R+0.1
280 IF (R-0.99)40,195,195
290 CALL GRAPH (X,PSI)
300 GO TO 10
310 END

```

25 LINES PRINTED

THE UNIVERSITY OF MICHIGAN

7848-1-F

```

C THIS SUBROUTINE DOES THE GRAPH USING THE CALPLOT SUBROUTINES.
C PLTXMX IS NOT CALLED FOR SINCE 8.5 INCHES OF GRAPH PAPER IS SUFFICIENT.
C PSCLAE IS NOT CALLED FOR SINCE THE SCALE FACTORS ARE KNOWN APRIORI.
C THESE APRIORI VALUES ARE FED INTO PLTOFS.
C
C SUBROUTINE GRAPH (BOA,PSI)
C DIMENSION PSI(450), BOA(450)
C
C STATEMENT 10 SPECIFIES THE RELATIVE URIGIN.
C
10 CALL PLTOFS(0.0,0.01,0.0,10.0,1.0,1.0)
C
C STATEMENT 30 DRAWS AND LABELS THE X AXIS. 35 DOES THE UPPER X AXIS.
C 40 DRAWS AND LABELS THE Y AXIS. 45 DOES THE RIGHT Y AXIS.
C
30 CALL PAXIS(1.0,1.0,1H,-1,-5.0,0.0,0.0,0.01,1.0)
35 CALL PAXIS(1.0,9.0,1H,-1,-5.0,0.0,0.0,0.01,1.0)
40 CALL PAXIS(1.0,1.0,1H,1,-8.0,90.0,0.0,10.0,0.2)
45 CALL PAXIS(6.0,1.0,1H,1,-8.0,90.0,0.0,10.0,0.2)
C
C SINCE THE NORMAL MODE OF PLOTTING IS LINEAR-RECTANGULAR, THE MODE NEED NOT BE
C DEFINED.
C 50 PLOTS PSI VS. BETA(0)*A USING A SOLID LINE.
C PRSTER, PONRST, AND POFRST ARE CALLED TO PREVENT PLOTTING OUTSIDE
C THE DESIRED PLOTTING REIGUN.
C
47 SWT=PRSTER(1.0,1.0,5.0,8.0)
48 SWT=PONRST(0)
50 DO 60 I=1,9
55 K=1+(I-1)*50
60 CALL PLINE(BOA(K),PSI(K),50,1,0,0,1)
65 SWT=POFRST(0)
C
C 70 INDICATES THE PLOTTING IS ALL FINISHED.
C
70 CALL PLTEND
80 RETURN
END

```

39 LINES PRINTED

## APPENDIX D

## INPUT IMPEDANCE TO A HELICAL DIPOLE

As pointed out in Section 5.3.1, the EMF method is an approximation in that it assumes a sinusoidal current distribution along a linear element. Nevertheless, the results obtained for a normal dipole are known to be sufficiently accurate for most engineering applications. It would thus seem logical to extend the induced EMF method to an analysis of a linear slow wave structure used as a dipole. However, a difficulty arises in that certain integrals which appear due to the generalization have no known closed form solutions. Li (1958) has been able to obtain an approximation to the integrals which allows a tenable closed form expression. His result is discussed below, and then extended to gain further insight into some useful engineering approximations pertinent to linear slow wave structures.

#### D.1 Symmetric Excitation Impedance by the Induced EMF Method

The EMF method was applied by Li (1958) in his Ph. D. thesis to obtain the input impedance of a small diameter helical element. This solution is significant not only in its own right, but also because it is representative of the characteristics of various other linear slow wave

structures. A helical element supports essentially a sinusoidal current distribution in which the axial wave number  $\beta_s$  is controlled by properly choosing the helix pitch angle. The slow wave structure was mathematically modeled using the sheath helix approximation. Although the details of this formulation have been rather carefully studied before preparing this report, the inherent complexity requires that only the primary steps be outlined, the solution quoted, and the limitations discussed.

The input impedance is obtained by the induced EMF method by dividing the complex power contributed to the electromagnetic field through a cylinder enclosing the element by the amplitude squared of the input current. The formulation reduces to an evaluation of the following expression for the input impedance.

$$Z_{11} = \frac{-1}{(I_m \sin \beta_s h)^2} \int_{-h}^h \left[ E_z(z) + E_\phi(z) \cot \psi \right] I_m \sin \beta_s (h - |z|) dz \quad (D.1)$$

$E_z(z)$  and  $E_\phi(z)$  are the longitudinal and traverse components of the electric field on the surface of the enclosing cylinder and are given by

$$E_z(z) = j 30 I_m \frac{\beta_s}{\beta_o} \left[ 2 \frac{e^{-j\beta_o R_o}}{R_o} \cos \beta_s h - \frac{e^{-j\beta_o R_1}}{R_1} - \frac{e^{-j\beta_o R_2}}{R_2} + \frac{\beta_s^2 - \beta_o^2}{\beta_s} \int_{-h}^h \sin \beta_s (h - |z_1|) \frac{e^{-j\beta_o R}}{R} dz_1 \right] \quad (D.2)$$

and

$$E_\phi(z) = -j 60 I_m \frac{\beta_s^2 - \beta_o^2}{\beta_o} \left[ \ln \left( \frac{2}{ka} \right) - \gamma \right] \tan \psi \sin \beta_s (h - |z|) \quad (D.3)$$



where

$$R_0 = \sqrt{a^2 + z^2} \qquad R = \sqrt{a^2 + (z - z_1)^2}$$

$$R_1 = \sqrt{a^2 + (z + h)^2} \qquad R_2 = \sqrt{a^2 + (z - h)^2}$$

$$\gamma = 0.5772 \qquad k^2 = \beta_s^2 - \beta_0^2$$

$\psi$  = helix pitch angle .

The last term in  $E_z$  containing the integral, along with the entire  $E_\phi$  account for the added complexity in extending the EMF method to the helical slow wave structure. Both of these terms are seen to vanish as the phase velocity reduction factor  $p_s$  approaches unity, in which case  $\beta_s \rightarrow \beta_0$ , ( $p_s = \beta_0/\beta_s$ ,  $\beta_0$  being the free space wave number). Finding a suitable closed form approximate solution to the integral term in  $E_z$  is essential to solving the slow wave structure impedance problem.

After some manipulation to facilitate the discussion in the next section, Li's solution yields the following result for the complex input impedance of a small diameter helical slow wave structure.

$$Z_{11} = R + j(X_1 + X_2) \tag{D.4}$$

$$R = \frac{30}{D \sin^2 x} \left\{ 2 [\text{Cin } Ax - \text{Cin } Bx] \right. \\ + \cos 2x [2 \text{Cin } Ax - 2 \text{Cin } Bx - \text{Cin } 2Ax + \text{Cin } 2Bx] \\ + \sin 2x [-2 \text{Si } Ax + 2 \text{Si } Bx + \text{Si } 2Ax - \text{Si } 2Bx] \\ \left. - \frac{4D}{3} \left[ \frac{1}{1 - D^2} (\cos Dx - \cos x)^2 + 2(1 - D^2)(1 - \cos x)^2 \right] \right\} \tag{D.4a}$$

$$\begin{aligned}
 X_1 = & \frac{30}{D \sin^2 x} \left\{ 2 \left[ \text{Si } Ax + \text{Si } Bx - \sin 2x \right] \right. \\
 & + \cos 2x \left[ 2 \text{Si } Ax + 2 \text{Si } Bx - \text{Si } 2Ax - \text{Si } 2Bx \right] \\
 & \left. + \sin 2x \left[ 2 \text{Cin } Ax + 2 \text{Cin } Bx - \text{Cin } 2Ax - \text{Cin } 2Bx \right] \right\} \quad (\text{D.4b})
 \end{aligned}$$

$$X_2 = \frac{-120}{D} \left( \ln \frac{h}{a} - 1 \right) \cot x \quad (\text{D.4c})$$

where:  $A = (1 + p_s)$ ,  $B = (1 - p_s)$ ,  $D = p_s$ ,  $x = \beta_s h$  and  $0 \leq x \leq \pi$ . The functions  $R$ ,  $X_1$  and  $X_2$  have been put into graphical form for easy use and appear in Figs. D-1a, b through D-3a, b\* respectively. The functions  $R$  and  $X_1$  are plotted for the family of  $p_s$  ranging in 0.1 increments from 0.1 to 1.0. Since  $X_2$  is affected by  $p_s$  only as a multiplicative factor, unnecessary duplication was avoided by plotting the product  $X_2 p_s$  for the family of  $h/a$  ranging from 15 to 8000.

A few comments are in order regarding the limitations of this result, along with its applicability to general slow wave structures. First, the evaluation of Eq. (D.1), using Eqs. (D.2) and (D.3), to obtain Eq. (D.4) required the usual assumption that the radius "a" be very small; i. e.,  $a \ll h$ , or  $\lambda$ . In addition, a closed form evaluation of the integral term in Eq. (D.2) required approximations. After dividing the integral into a real and imaginary part, the real part was integrated exactly, and found to approximately cancel the contribution of Eq. (D.3) to the input reactance. This approximation allowed the entire effect of  $E_\phi$  to be removed from the final result, Eq. (D.4). The imaginary part of

\* Each figure is drawn to two scales - a, for an overall presentation, and b, for an expanded view of the ordinate near the origin.

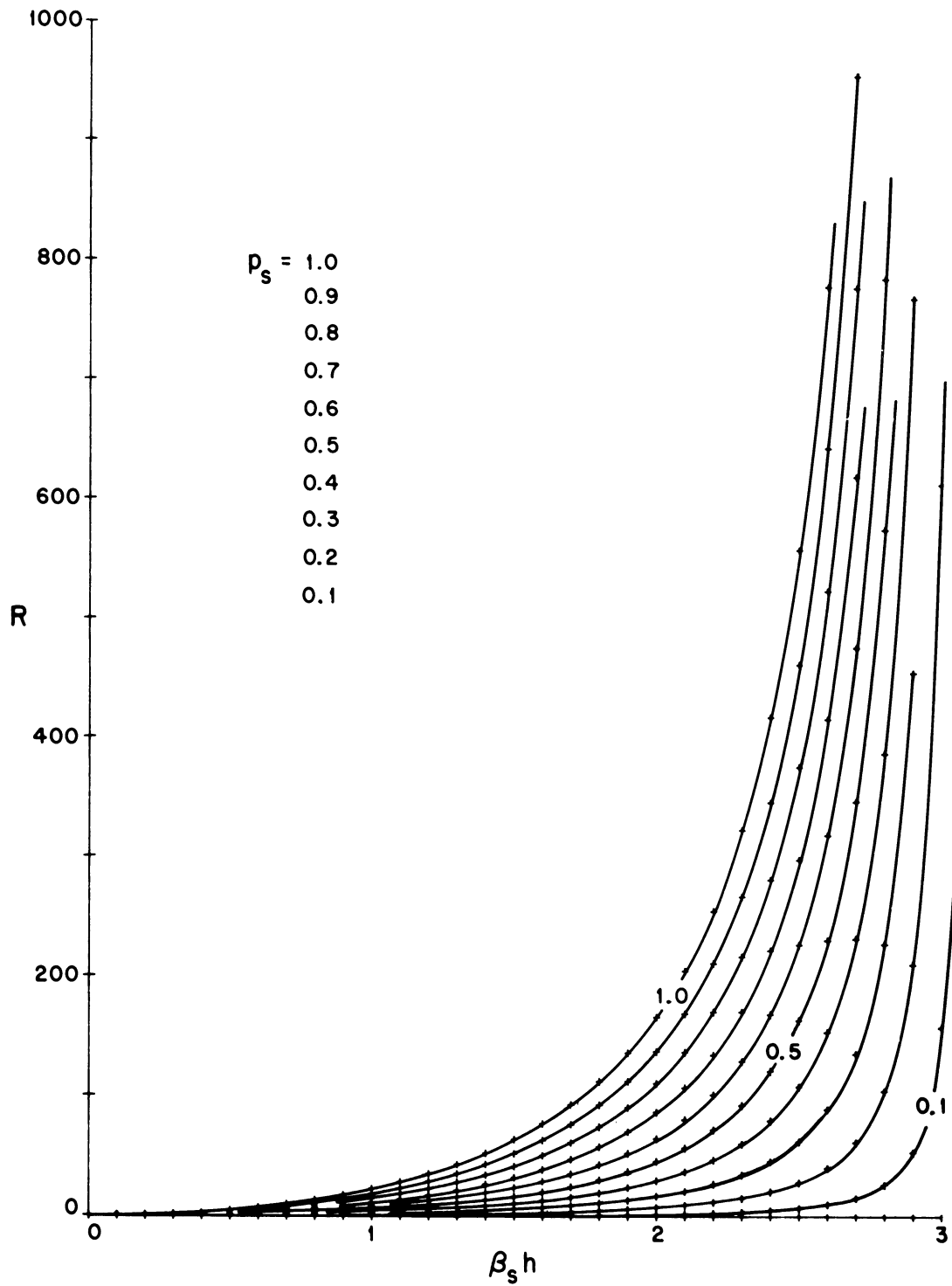


FIG. D-1a:  $R$  VERSUS  $\beta_s h$  FOR THE PARAMETER  $p_s$  (EMF METHOD).

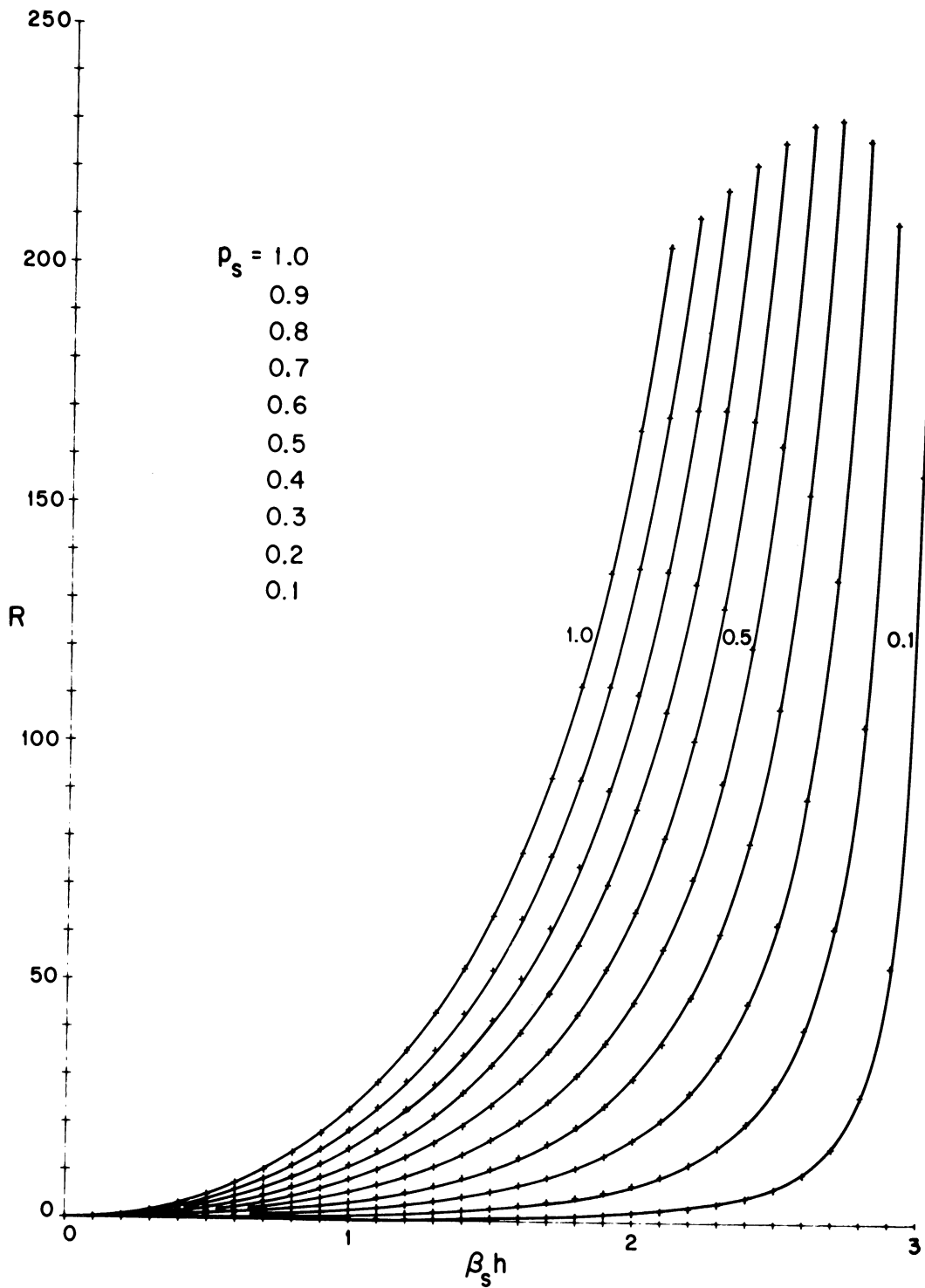


FIG. D-1b: EXPANDED  $R$  VERSUS  $\beta_s h$  FOR THE PARAMETER  $p_s$  (EMF METHOD).

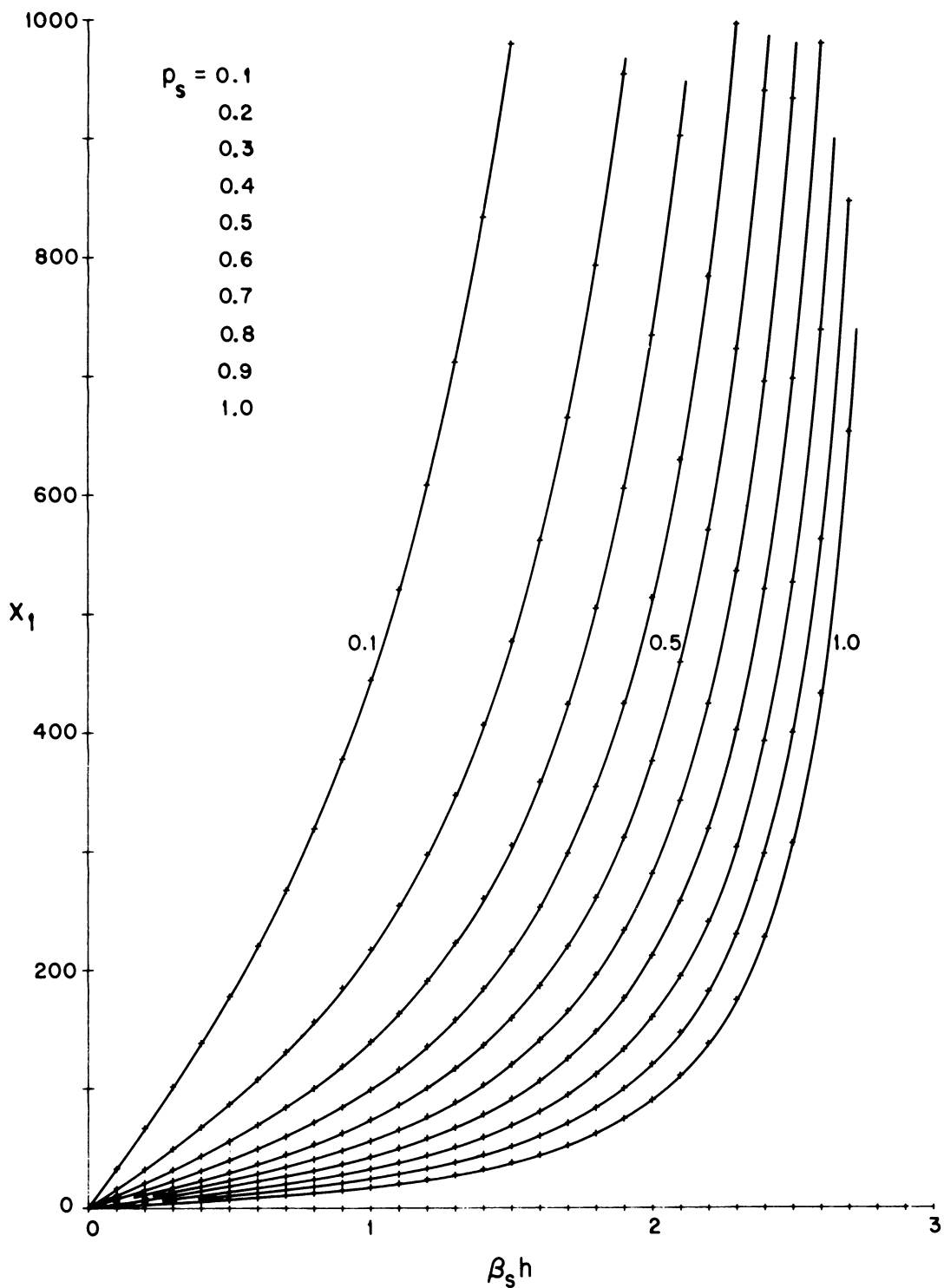


FIG. D-2a:  $X_1$  VERSUS  $\beta_s h$  FOR THE PARAMETER  $p_s$  (EMF METHOD).

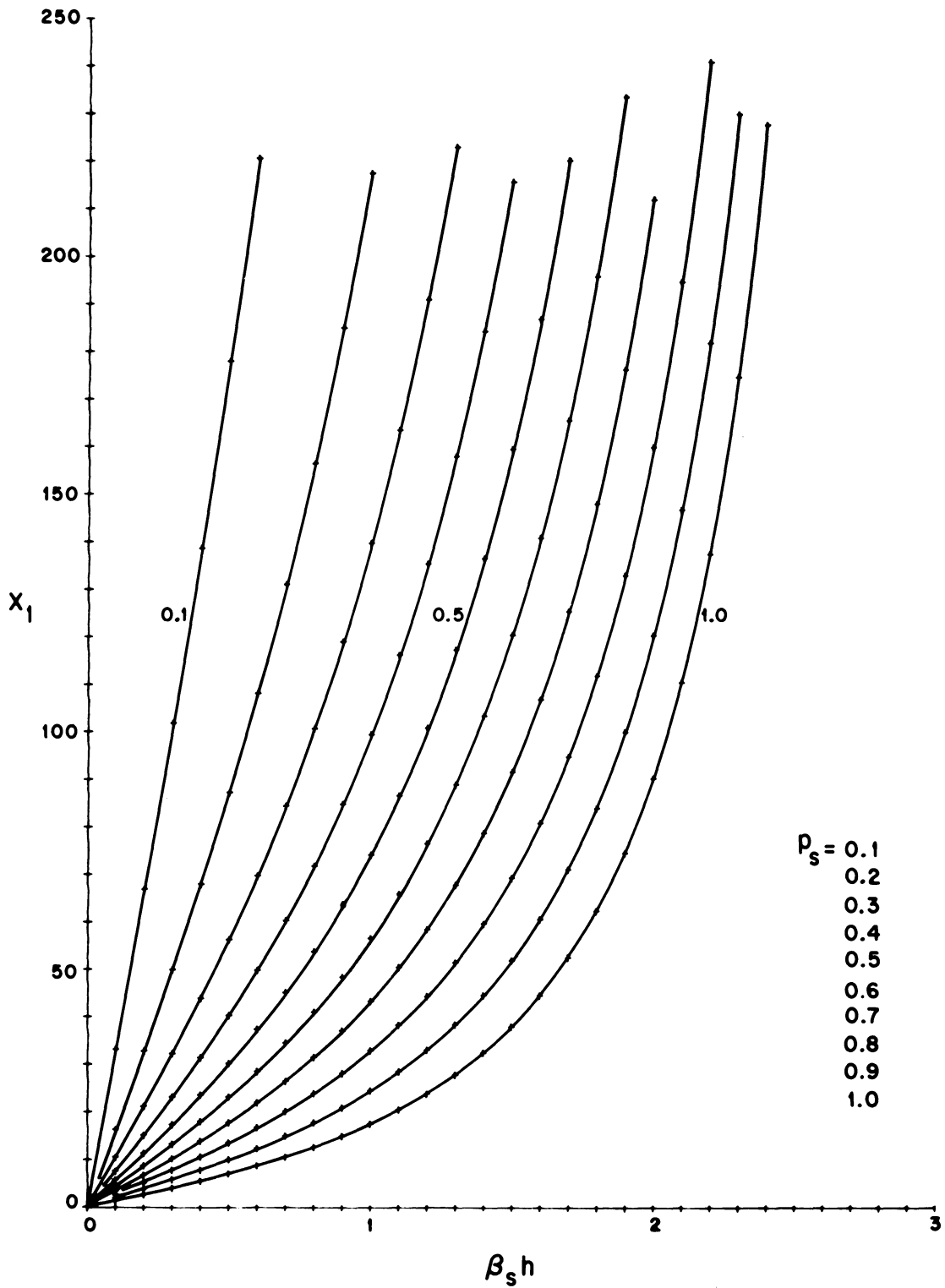


FIG. D-2b: EXPANDED.  $X_1$  VERSUS  $\beta_s h$  FOR THE PARAMETER  $p_s$  (EMF METHOD).

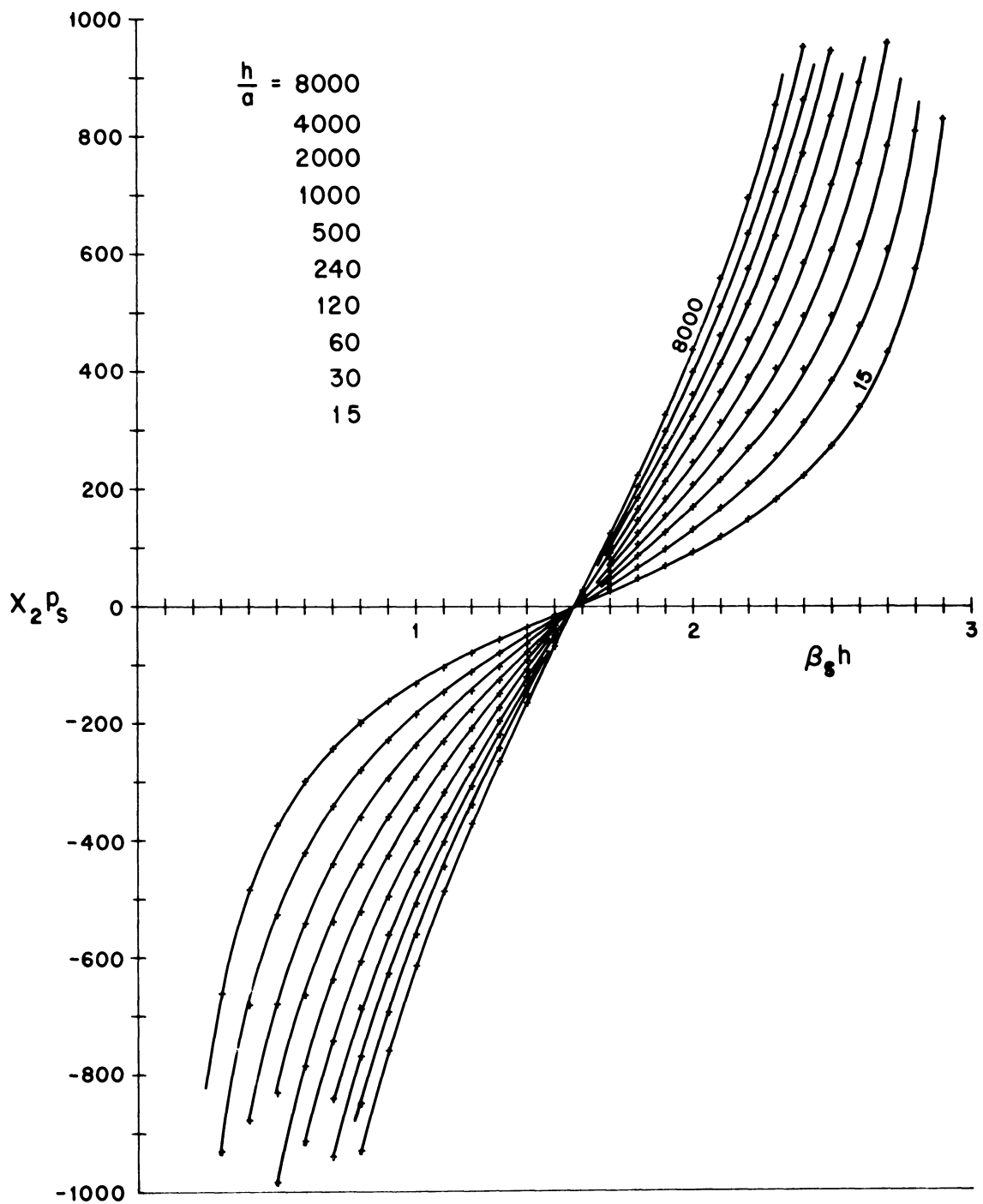


FIG. D-3a:  $X_{2p_s}$  VERSUS  $\beta_s h$  FOR THE PARAMETER  $h/a$  (EMF METHOD).

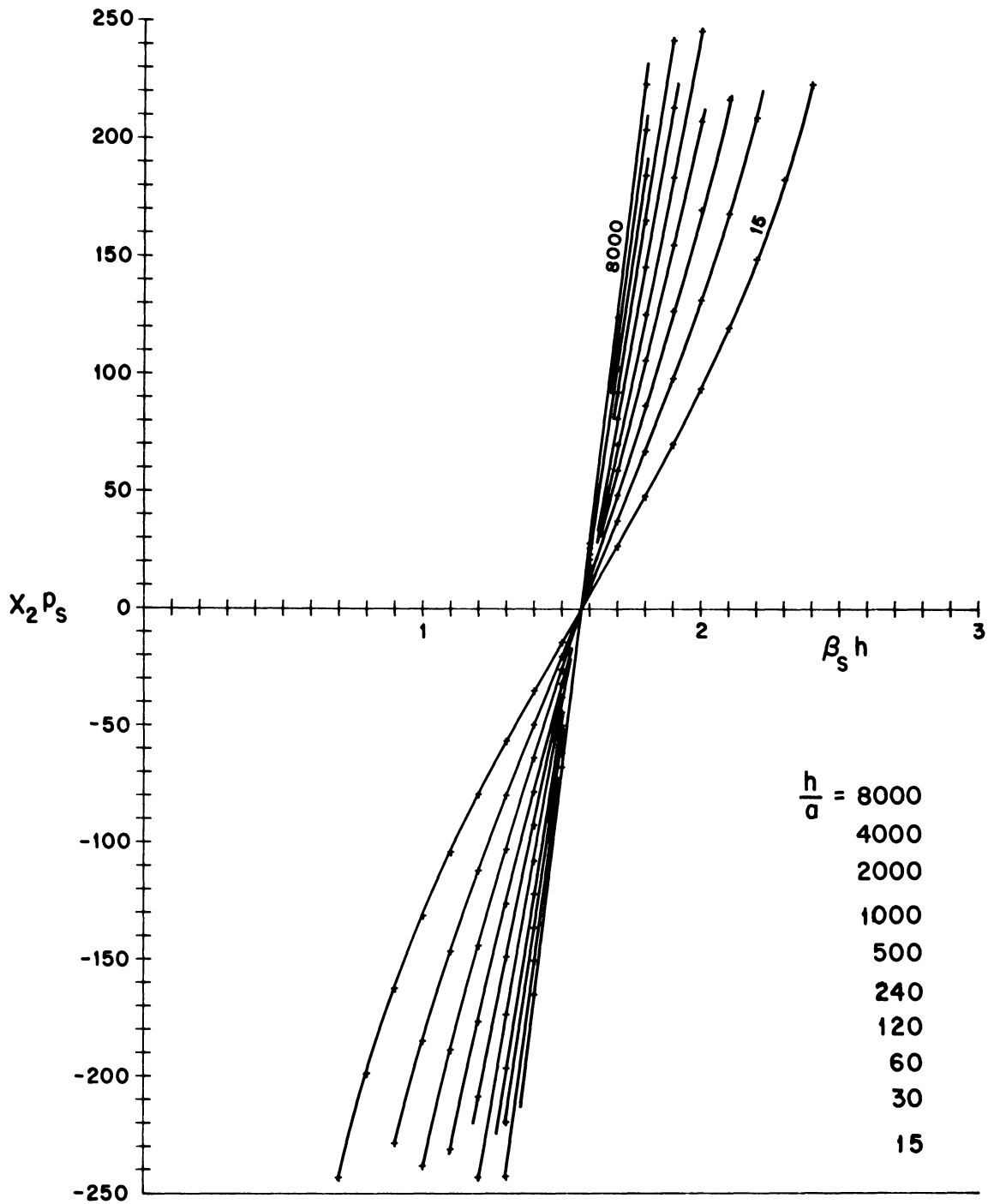


FIG. D-3b: EXPANDED  $X_2 p_s$  VERSUS  $\beta_s h$  FOR THE PARAMETER  $h/a$  (EMF METHOD).



the integral was evaluated using an approximation which becomes poor for  $x > \pi$ . This influence is felt in the last bracketed terms of Eq. (D.4a), which can become unduly large and make  $R$  negative if  $x$  is not restricted. Hence, the impedance expression for the small diameter helical dipole is accurate provided the element is thin and  $0 \leq x \leq \pi$ . Moreover, the expression will adequately describe the behavior of a small diameter helix having a ferrite core. The primary effect of the ferrite core is to decrease the current phase velocity, and hence can be represented through  $p_s$ . The dependence of  $p_s (= \lambda_g/\lambda)$  upon the ferrite core is presented in Appendix C.

#### D.2 Comparison with Transmission Line Analogy

The above separation of input reactance into two components ( $X_1$  and  $X_2$ ) was motivated by a similar technique introduced by Tai in connection with the regular dipole ( $p_s = 1.0$ ) as presented in Chapter 3 of Jasik (1961). Tai factored out the terms appearing in  $X_2$  solely for the mathematical reasons of giving  $X_1$  the properties: a) of having no dependence upon the element thickness, and b) of being regular at the origin (i.e.  $X_1 \rightarrow 0$  as  $\beta_s h \rightarrow 0$ ). It is intended here to propose a physical interpretation to this so far strictly mathematical separation. Observe that  $X_2$  is in the mathematical form of the input impedance for an open circuited length of lossless uniform transmission line having a characteristic impedance given by

$$Z_o = 120(\beta_s/\beta_o)(\ln h/a - 1) \quad . \quad (D.5)$$

Ascribing such an interpretation to the mathematics is of course not new; but, generally the analogy is argued hueristically starting from transmission line theory, dominant mode biconical antenna theory, or the zeroth order

integral equation solution. Here, however, the argument is reversed; a somewhat more credible induced EMF technique reduces formally to a form containing a familiar term; otherwise, this approach would be on somewhat shaky footing. Although it may be rightly argued that the first order integral equation solution is on firm ground, the first order solution obscures the analogy due to an awkward change in its zeroth order functional form, whereas the EMF solution merely introduces additive "correction" terms. This latter notion of  $R$ , and in particular  $X_1$  being viewed as correction terms deserves further explanation. Normally one does not think of  $R$ , given by either the EMF method or equivalently by the Poynting vector method, as being "corrective" since our familiarity with the result relegates it as "basic". However it is "corrective" when compared with the more approximate zeroth order result. More importantly,  $X_1$  is the only readily tractable additive "correction" function available. Despite excellent numerical results from more involved methods, a relatively simple functional expression for the entire reactance is often desirable.

If  $X_1$  is rightly to be considered a correction to  $X_2$ , its corrective effect must be small. Tai's results for the normal dipole ( $p_s = 1.0$ ) showed this to indeed be the case. That this is true for general  $p_s$  is verified by examining Figs. D-2 and D-3. Consider as an example a helical slow wave structure for which  $p_s = 0.5$  and  $h/a = 500$ . Nominal resonance based upon  $X_2 = 0$  would occur at  $\beta_s h = 1.57 (= \pi/2)$ . However, Fig. D-2b indicates that  $X_1 = 177$  for this value of  $\beta_s h$ . Actual resonance is achieved when  $\beta_s h$  is decreased to where  $X_1 + X_2 = 0$ . Using Figs. D-2b and D-3b to determine the required decrease in  $\beta_s h$ , one finds  $X_1 = 148 = -X_2$  at  $\beta_s h = 1.45$ . Hence,  $X_1$  causes only a 7.6 percent correction to the value of  $\beta_s h$  predicted by the use of  $X_2$  alone. In conclusion it may be said that  $X_2$  is a strong

function of frequency, its strength being controlled by the numerical value of  $Z_o$ .  $X_1$  is by comparison a slowly varying function of frequency, its primary influence being a slight lowering of the actual resonant frequency.

There remains the somewhat delicate task of reconciling the above equation for  $Z_o$  as representing in some sense a meaningful expression of characteristic impedance. First, for the case where  $\beta_s = \beta_o$ ,  $Z_o$  reduces to Tai's results. (A typographical error appears in  $X_2$  of Jasik (1961), but has subsequently been noted by Tai (1965)). Throughout the years several differing expressions have appeared to account for characteristic impedance. Siegel and Labus (see Jordan, 1950) initially suggested the form :

$$Z_o = 120 \left( \ln \frac{h}{a} - 1 - \frac{1}{2} \ln \frac{2h}{\lambda} \right) . \quad (D. 6)$$

Later the expression for a biconical line was averaged over the length of a cylindrical antenna to obtain:

$$Z_o = 120 \left( \ln \frac{2h}{a} - 1 \right) . \quad (D. 7)$$

It has been stated by Jordan (1950) that both the above expressions when applied to a short antenna yield calculated values which are consistently higher than measured values. He suggests the use of

$$Z_o = 120 \left( \ln \frac{h}{a} - 1 \right) \quad (D. 8)$$

as an "adjusted" characteristic impedance that is empirically picked to give the closest fit to experimentally measured values. Moreover, still another expression results from equating the zeroth order integral equation solution, which contains the thickness parameter  $\Omega = 2 \ln \frac{2h}{a}$ , to that of an equivalent transmission line. This results in  $Z_o = 60 \Omega$ , or

$$Z_o = 120 \ln \frac{2h}{a} . \quad (D. 9)$$

While a number of slightly different expressions exist for  $Z_0$ , the importance of the numerical differences between them is somewhat over shadowed when one considers the errors introduced by variations due to different feed point terminal conditions. Thus, the degree of uncertainty introduced by measurement technique, and the conditions of actual application suggests that the choice of  $Z_0$  is not too critical. Should somewhat greater precision be desired, it would be best to determine  $Z_0$  from measurement. This way the above uncertainties would to an extent be taken into account.

In conclusion it is seen that the induced EMF method suggests an expression for  $Z_0$  which is identical to Jordan's when  $\beta_s = \beta_0$ . Moreover, the dominant role in describing the impedance behavior is performed by  $X_2$ . Thus, it is suggested that  $R$  and  $X_1$  may be viewed as correction terms to the zeroth order integral equation solution, to within the limitations of the approximate, but generally adequate, induced EMF formulation. This point of view will prove exceedingly useful in Section 5.4, and is a dominant motivation for the present development.

THE UNIVERSITY OF MICHIGAN  
7848-1-F

REFERENCES

- Adams, A. T. (1964), "The Rectangular Cavity Slot Antenna with Homogeneous Isotropic Loading," The University of Michigan Cooley Electronics Laboratory Technical Report 147.
- Adams, A. T. (1967), "Flush Mounted Rectangular Cavity Slot Antennas - Theory and Design," Trans. IEEE, AP-15, No. 3, 342-351.
- Angulo, C. M. and W. S. C. Chang (1958), "The Excitation of a Dielectric Rod by a Cylindrical Waveguide," Trans. IRE, MTT-6, 389-393.
- Barnett, R. I., Jr. (1963), "An All Dielectric Coaxial Waveguide and Antenna," PhD Dissertation, The Ohio State University.
- Beam, R. E., et al (1950), "Investigations of Multi-mode Propagation in Waveguides and Microwave Optics," Northwestern University Microwave Laboratory Report AD 94929.
- Beam, R. E. and P. Andris (1952), "Input Impedance of Folded Dipole Antennas," Proc. NAECON, 8, 678-691.
- Brown, J. and J. O. Spector, (1957), "The Radiating Properties of Endfire Aerials," Proc. IEE, 104B, 27-34.
- Bulgakov, B. M. et al (1960), "Symmetrical Surface Waves in a Helix Waveguide with a Ferrite Medium," Radiotekhnika i Elektronika, 5, No. 11, 1818-1827.
- Chatterjee (1956), "Some Investigations on Dielectric Rod Aerials," J. Indian Inst. Sci., 38, 93-103; (1957), 39, 134-155; (1962), 44, 148-218.
- Chen, Chin-Lin (1967), "Theory of the Balanced Helical Wire Antenna," Radio Science, 2, 127-190.
- Collin, R. C. (1960), Field Theory of Guided Waves, McGraw-Hill Book Company, Inc., New York.
- Duncan, J. W. and R. H. DuHamel (1957), "Launching Efficiency of Wires and Slots for a Dielectric Rod Waveguide," University of Illinois Technical Report No. 24.
- Electronic Engineers Master (1966), United Technical Publications, Garden City, New York.
- Fradin, A. Z. (1961), Microwave Antennas, Pergamon Press, London.
- Ferris, J. E. et al (1966), "Broadband Antenna Techniques Study - Interim Report," The University of Michigan Radiation Laboratory Report 7260-1-T, ECOM-01263-4, AD 488 067.

THE UNIVERSITY OF MICHIGAN  
7848-1-F

- Hach, R. C. (1966), Conductron Corporation (private communication with one of the authors).
- Halliday, D. F. and D. G. Kiely (1947), "Dielectric-Rod Aerials," Referenced in James (1967).
- Hersch, W. (1960), "The Surface Wave Aerial," Proc. IEE, 107C, 202-210.
- Hong, S. and G. G. Rassweiler (1966), "Size Reduction of a Conical Log-Spiral Antenna by Loading with a Magneto-Dielectric Material," Trans. IEEE, AP-14, 650-651.
- James, J. R. (1967), "Theoretical Investigation of Cylindrical Dielectric Rod Antennas," Proc. IEE, 114, 309-319.
- Jasik, H. (1961), Antenna Engineering Handbook, McGraw-Hill Book Company, Inc., New York (Section 3.1).
- Johnson, Walter D. (1950), Transmission Lines and Networks, McGraw-Hill Book Company, New York
- Jordan, E. C. (1950), Electromagnetic Waves and Radiating Systems, Prentice-Hall, New Jersey (pp. 452-473 and 512).
- Kalafus, R. M. and J. A. M. Lyon (1961), "Feasibility of Electrically Small Antennas on an Energy Basis," Eleventh Annual USAF Antenna Research and Development Symposium, October 16-20, Monticello, Illinois.
- Kiely, D. G. (1953), "Dielectric Aerials," Methuen Monograph, London.
- King, R. W. P. (1956), The Theory of Linear Antennas, Harvard University Press, Cambridge, Mass.
- Kraus, J. D. (1950), Antennas, McGraw-Hill Book Company, Inc., New York.
- Lax, B. and K. J. Button (1962), Microwave Ferrites and Ferromagnetics, McGraw-Hill Book Company, Inc., New York.
- Li, T. and R. Beam (1957), "Helical Folded Dipoles and Unipoles," Proc. NEC, XIII, 89-105.
- Li, T. (1958), "The Small-Diameter Helical Antenna and its Input Impedance Characteristics," Ph. D. Dissertation, Northwestern University, Evanston, Illinois.
- Lyon, J. A. M., et al (1965), "Study and Investigation of a UHF-VHF Antenna," The University of Michigan Radiation Laboratory Report 5549-1-F, AFAL-TR-65-64.

THE UNIVERSITY OF MICHIGAN  
7848-1-F

- Lyon, J. A. M. , et al (1966), "Study and Investigation of a UHF-VHF Antenna, " The University of Michigan Radiation Laboratory Report 7140-1-F, AFAL-TR-66-101.
- Mallach, P. (1953), "Notes from Unpublished German Documents, " Central Radio Bureau Library, London (Referenced in Kiely, 1953) .
- Müller, G. E. and W. A. Tyrell (1947), "Polyrod Antennas, " Bell System Tech. J. , 26, 837 .
- Müller, G. E. (1952), "Dielectric Antennas, " The Ohio State University Research Foundation Final Engineering Report 434-6.
- Okubo, G. (1965), "Helix Frequency Scanning Feed, " Microwave J. , 8, No. 12, 39-44.
- Rassweiler, G. (1966), "Helical and Log Conical Helical Antennas Loaded with an Isotropic Material, " The University of Michigan Radiation Laboratory Report 7848-3-Q, AD 806094 (PhD Dissertation).
- Rado, G. T. (1953), "Magnetic Spectra of Ferrites, " Rev. of Modern Phys. , 25 .
- Schelkunoff, S. A. and H. T. Friis (1952), Antennas: Theory and Practice, John T. Wiley and Sons, New York (Sec. 8. 28).
- Shnitkin , H. and S. Levy (1962), "Getting Maximum Bandwidth with Dipole Antennas, " Electronics, 35, 40-42 (August 31 Issue).
- Sichak, W. (1954), "Coaxial Line with Helical Inner Conductor, " Proc. IRE, 42, 1315-1319.
- Silver, S. (1965), Microwave Antenna Theory and Design, Dover Publications, New York.
- Stannard, G. E. (1967), "Calculation of Power on a Transmission Line, " Proc. IEEE, 55, 132 .
- Stephenson, I. T. and P. E. Mays (1966), "Normal-mode Helices as Moderately Super-directive Antennas, " Trans. IEEE, AP-14, 108-110.
- Tai, C. T. (1948), "Coupled Antennas, " Proc. IRE, 56, 487-500.
- Tai, C. T. (1965), "Linear Antennas, " Electronic Industries, 75-78.
- Taylor, T. T. (1955), "Design of Line-source Antennas for Narrow Beamwidth and Low Sidelobes, " Trans. IRE, AP-3, 16-28.
- Turner, E. M. (1966), Air Force Avionics Laboratory, Dayton, Ohio (private communication).
- Venerus, J. C. (1967), Indiana General, Keasley, New Jersey (private communication).
- Walter, C. H. (1965), Traveling Wave Antennas, McGraw-Hill Book Company, Inc. , New York.

THE UNIVERSITY OF MICHIGAN

7848-1-F

- Watson, R. B. and C. W. Horton (1948a) "The Radiation Patterns of Dielectric Rods - Experiment and Theory," J. Appl. Phys., 19, 661 .
- Watson, R. B. and C. W. Horton (1948b), " On the Calculation of Radiation Patterns of Dielectric Rods, " J. Appl. Phys., 19, 836 .
- Wolff, E. A. (1966), Antenna Analysis, John T. Wiley and Sons, New York.
- Wu, Pei-Rin (1967a), "A Study of an Interdigital Array Antenna," The University of Michigan Radiation Laboratory Report 7848-5-Q.
- Wu, Pei-Rin (1967b), "On the Measurement of a Bifilar Complementary Helical Antenna," Trans. IEEE, AP-15, 700 .
- Wu, Pei-Rin (1967c), MIT-Lincoln Laboratory (private communication with one of the authors) .



UNCLASSIFIED

Security Classification

## DOCUMENT CONTROL DATA - R &amp; D

(Security classification of title, body of abstract and indexing annotation must be entered when the overall report is classified)

1. ORIGINATING ACTIVITY (Corporate author) The University of Michigan Radiation Laboratory, Dept. of Electrical Engineering, 201 Catherine Street, Ann Arbor, Michigan 48108		2a. REPORT SECURITY CLASSIFICATION UNCLASSIFIED	
		2b. GROUP	
3. REPORT TITLE  Study and Investigation of a UHF-VHF Antenna			
4. DESCRIPTIVE NOTES (Type of report and inclusive dates) Final Report 1 April 1966 through 28 February 1968			
5. AUTHOR(S) (First name, middle initial, last name) John A. M. Lyon, Nicholas G. Alexopoulos, Chao-Chun Chen, James C. Parker, Jr., Dean L. Smith and Pei-Rin Wu.			
6. REPORT DATE 31 March 1968	7a. TOTAL NO. OF PAGES 304	7b. NO. OF REFS 56	
8a. CONTRACT OR GRANT NO. AF 33(615)-3609	9a. ORIGINATOR'S REPORT NUMBER(S) 7848-1-F		
b. PROJECT NO. 6278	9b. OTHER REPORT NO(S) (Any other numbers that may be assigned this report) AFAL-TR-68-114		
c. Task 627801			
d.			
10. DISTRIBUTION STATEMENT Qualified requestors may obtain copies of this report from DDC. This document is subject to special export controls and transmittal to foreign governments or foreign nationals may be made only with prior approval of AFAL(AVPT), Wright-Patterson AFB, Ohio 45433			
11. SUPPLEMENTARY NOTES		12. SPONSORING MILITARY ACTIVITY Air Force Avionics Laboratory AVWE  Wright-Patterson AFB, Ohio 45433	
13. ABSTRACT This final report describes the results of a program to reduce the size of antennas while still maintaining the usual frequency operating range for each type of antenna involved. The work described has been in part theoretical analysis and in other parts largely experimental. The work has been divided into four tasks. Task I on ferrite loaded conical spirals has dealt with the development of a ferrite loaded conical spiral antenna covering a range from 200 to 600 MHz. Several design procedures have been considered. Under this task an appropriate type of design has resulted which will fulfill the original task requirement. In Task II the objective has been to use ferrite loaded slot elements in an array and to utilize the control possible with such elements associated with a biasing magnetic field. Time has permitted only a preliminary assembly of the array without any complete determination of the functional possibilities. A novel antenna of reduced size, the "interdigital array", has been developed. Under Task III a detailed analysis has been made of ferrite rod antennas. Numerous experiments have been performed. The studies therein indicate that a ferrite tube or hollow rod antenna has more desirable characteristics than the solid rod antenna. Under Task IV detailed studies have been made of various loading and miniaturization techniques suitable for frequencies down to 30 MHz. The studies under this task indicate the influence of the various techniques of winding, loading and fabrication upon the antenna characteristics. The need for further work on some of the tasks is clearly recognized in this report. Much of the required future work is covered in the renewal contract (F33615-68-C-1381).			

DD FORM 1473

1 NOV 65

UNCLASSIFIED

Security Classification

14. KEY WORDS	LINK A		LINK B		LINK C	
	ROLE	WT	ROLE	WT	ROLE	WT
Antennas Ferrite Loading Techniques Physically Small Antennas Helix Antenna Conical Helix Antenna Slot Antennas Interdigital Array Antenna Ferrite Rod Antenna Linear Slow Wave Structures						



UNIVERSITY OF MICHIGAN  
3 9015 03465 8438